

# Transactions of the ASME®

Editor, **LEWIS T. WHEELER**  
**APPLIED MECHANICS DIVISION**

Executive Committee  
(Chair) **D. KRAJCINOVIC**  
**S. KYRIAKIDES**  
**P. D. SPANOS**  
**M. C. BOYCE**  
**W.-K. LIU**

Associate Editors  
**E. ARRUDA (2004)**  
**J. R. BARBER (2003)**  
**R. C. BENSON (2003)**  
**A. A. FERRI (2003)**  
**H. GAO (2003)**  
**V. K. KINRA (2002)**  
**D. A. KOURIS (2002)**  
**A. K. MAL (2004)**  
**B. M. MORAN (2002)**  
**A. NEEDLEMAN (2004)**  
**O. O'REILLY (2004)**  
**N. C. PERKINS (2002)**  
**M.-J. PINDER (2003)**  
**K. R. RAJAGOPAL (2003)**  
**K. T. RAMESH (2003)**  
**K. RAVI-CHANDAR (2003)**  
**W. S. SARIC (2003)**  
**D. A. SIGNER (2003)**  
**T. E. TEZDUYAR (2003)**  
**N. TRIANTAFYLIDIS (2003)**

## BOARD ON COMMUNICATIONS

Chair and Vice-President  
**OZDEN OCHOA**

## OFFICERS OF THE ASME

President, **W. A. WEIBLEN**  
Executive Director, **D. L. BELDEN**  
Treasurer, **R. E. NICKELL**

## PUBLISHING STAFF

Managing Director, Engineering  
**THOMAS G. LOUGHLIN**  
Director, Technical Publishing  
**PHILIP DI VIETRO**  
Managing Editor, Technical Publishing  
**CYNTHIA B. CLARK**  
Managing Editor, Transactions  
**CORNELIA MONAHAN**  
Production Coordinator  
**JUDITH SIERANT**  
Production Assistant  
**MARISOL ANDINO**

Transactions of the ASME, Journal of Applied  
Mechanics (ISSN 0021-8936) is published bimonthly  
(Jan., Mar., May, July, Sept., Nov.)

The American Society of Mechanical Engineers,  
Three Park Avenue, New York, NY 10016.

Periodicals postage paid at New York, NY and additional  
mailing office. POSTMASTER: Send address changes to  
Transactions of the ASME, Journal of Applied Mechanics,  
c/o THE AMERICAN SOCIETY OF MECHANICAL ENGINEERS,  
22 Law Drive, Box 2300, Fairfield, NJ 07007-2300.

CHANGES OF ADDRESS must be received at Society  
headquarters seven weeks before they are to be effective.

Please send old label and new address.

STATEMENT from By-Laws. The Society shall not be  
responsible for statements or opinions advanced in papers or  
... printed in its publications (B7.1, Para. 3).

COPYRIGHT © 2002 by The American Society of Mechanical  
Engineers. For authorization to photocopy material for  
internal or personal use under those circumstances not falling  
within the fair use provisions of the Copyright Act, contact  
the Copyright Clearance Center (CCC), 222 Rosewood Drive,  
Danvers, MA 01923, tel: 978-750-8400, www.copyright.com.

Request for special permission or bulk copying should  
be addressed to Reprints/Permission Department. INDEXED by  
Applied Mechanics Reviews and Engineering Information,  
Inc. Canadian Goods & Services Tax Registration #126148048.

# Journal of Applied Mechanics

Published Bimonthly by The American Society of Mechanical Engineers

**VOLUME 69 • NUMBER 2 • MARCH 2002**

## TECHNICAL PAPERS

- 97 Surface Instability of an Elastic Thin Film Interacting With a Suspended Elastic Plate  
**C. Q. Ru**
- 104 Adherence of a Rectangular Flat Punch Onto a Clamped Plate: Transition From a Rigid Plate to a Flexible Membrane  
**K.-T. Wan and J. Duan**
- 110 Adherence of an Axisymmetric Flat Punch Onto a Clamped Circular Plate: Transition From a Rigid Plate to a Flexible Membrane  
**K.-T. Wan**
- 117 Multimode Approach to Nonlinear Supersonic Flutter of Imperfect Circular Cylindrical Shells  
**M. Amabili and F. Pellicano**
- 130 Stress Field in Finite Width Axisymmetric Wound Rolls  
**Y. M. Lee and J. A. Wickert**
- 139 An Alternative Decomposition of the Strain Gradient Tensor  
**H. Jiang, Y. Huang, T. F. Guo, and K. C. Hwang**
- 142 Normal Indentation of Elastic Half-Space With a Rigid Frictionless Axisymmetric Punch  
**G. Fu and A. Chandra**
- 148 A Simplified Method to Predict the Steady Cyclic Stress State of Creeping Structures  
**K. V. Spiliopoulos**
- 154 A Boundary Element Method Without Internal Cells for Two-Dimensional and Three-Dimensional Elastoplastic Problems  
**X.-W. Gao**
- 161 Effective System Properties and Special Density in Random Vibration With Parametric Excitation  
**S. Krenk, Y. K. Lin, and F. Rüdinger**
- 171 Random Response Analysis of Preisach Hysteretic Systems With Symmetric Weight Distribution  
**Y. Q. Ni, Z. G. Ying, and J. M. Ko**
- 179 In-Plane Wave Propagation Through Elastic Solids With a Periodic Array of Rectangular Defects  
**E. Scarpetta and M. A. Sumbatyan**
- 189 Low Reynolds Number Slip Flow in a Curved Rectangular Duct  
**C. Y. Wang**

## BRIEF NOTES

- 195 Some Properties of  $J$ -Integral in Plane Elasticity  
**Y. Z. Chen and K. Y. Lee**
- 198 Orthotropic Hyperelasticity in Terms of an Arbitrary Molecular Chain Model  
**J. E. Bischoff, E. M. Arruda, and K. Grosh**
- 202 2001 Author Index

(Contents continued on inside back cover)

This journal is printed on acid-free paper, which exceeds the ANSI Z39.48-1992 specification for permanence of paper and library materials. ©™

♻ 85% recycled content, including 10% post-consumer fibers.

## **ANNOUNCEMENTS AND SPECIAL NOTES**

- 208 Information for Authors
- 209 Preparing and Submitting a Manuscript for Journal Production and Publication
- 210 Preparation of Graphics for ASME Journal Production and Publication
- 211 New Reference Format

# Surface Instability of an Elastic Thin Film Interacting With a Suspended Elastic Plate

C. Q. Ru

Department of Mechanical Engineering,  
University of Alberta,  
Edmonton, AB T6G 2G8, Canada  
e-mail: c.ru@ualberta.ca

*This paper studies surface instability of a compliant elastic thin film on a rigid substrate interacting with a suspended elastic plate through van der Waals forces. The analysis is based on a novel method which permits a simple rational expression for the interaction coefficient as a function of the wave number of instability mode. The critical value of the interaction coefficient and the instability mode of the film-plate system can be determined easily by identifying the minimum of the interaction coefficient within an admissible range. When the stability strength of the plate is lower than the film even for the shortest plate-lengths, the interaction coefficient is found to be an increasing function of the wave number, and thus the film-plate system exhibits a long-wave instability mode determined by the suspended plate. In all other cases, the interaction coefficient admits an internal local minimum representing the short-wave mode of the film, and the critical value and instability mode of the film-plate system are determined by the internal local minimum for shorter plates, or by the long-wave mode of the plate for longer plates. Some numerical examples are given to illustrate the results. [DOI: 10.1115/1.1445146]*

## 1 Introduction

Surface morphological instability of a thin liquid layer in various configurations, due to van der Waals forces or electrostatic interaction, has been the topic of extensive research ([1–3]). Very recently, similar issue has been raised for solid thin films. For example, Ghatak et al. [4], Monch and Herminghaus [5], and Shenoy and Sharma [6] studied surface instability of a rubber elastic layer bonded on a rigid substrate and attracted by a rigid plane through van der Waals forces. It is found that the flat surface of the compliant elastic layer becomes unstable when the interaction exceeds a critical value (it is the case when the gap width between the two surfaces is only a few tens of nanometers). In particular, the wavelength of the surface instability mode is proportional to the thickness of the elastic layer, independently of its elastic modulus and the nature of the interaction. This new type of surface instability, governed by a competition between the interaction energy and the elastic strain energy of the layer, is purely elastic in nature and does not rely on the existence of a surface compressive prestress. Therefore, it is essentially different from the known surface instabilities due to surface compressive stress ([7,8]) or stress-assisted surface diffusion ([9,10]). A throughout study of this new type of surface instability is relevant for many physical phenomena and technical problems at microscopic or nanometer scale, such as solid adhesion ([11,12]), wafer bonding ([13,14]), and electrically induced surface patterning ([15,16]).

Here, two important open issues immediately come into question. First, in all of the existing work ([4–6]), the interacting body (such as a metallic plate, of shear modulus higher than 10 GPa) has been treated as rigid body because it is much stiffer than the rubber elastic layer (of shear modulus less than 10 MPa). However, as shown in [5,6] and also in the present paper (see Section 5), the critical value for surface instability of an elastic film fixed on a rigid substrate is determined by its surface compliance  $h/E$ ,

where  $h$  is the thickness of the elastic film, and  $E$  is its Young's modulus. Therefore, the strength of a metallic layer against surface instability would be comparable to or even lower than a rubber elastic film if the thickness of the former is a few orders of magnitude larger than the latter. In this case, the assumption of rigid body is inadequate for the metallic layer, and the system should be treated as two interacting elastic bodies. In doing so, because the individual instability modes of two elastic layers of different thicknesses are different, the incompatibility of the two instability modes could crucially affect the critical value and the instability mode of the system. Hence, the deformability of the interacting body is an issue of practical and theoretical significance.

Second, in many important cases of two interacting elastic layers, one layer is often suspended so that it is traction-free on one of its surfaces and interacts with another elastic layer on a rigid substrate through the other surface. In this case, the attractive forces are supported by some geometrical constraints at the edges which keep the two mutually attracting elastic layers apart, see Fig. 1. Obviously, the instability mode of a suspended elastic layer (modeled as an elastic plate) is substantially different from that of an elastic layer bonded on a rigid substrate. In fact, the former, like the buckling mode of a Euler column, is proportional to the length of the layer, whereas the latter scales with the thickness of the layer, as mentioned before. Hence, the incompatibility between the long-wave mode of the former and the short-wave mode of the latter could have a crucial effect on surface instability of the film-plate system. This offers one of the justifications for the study of surface instability of a suspended elastic plate interacting with an elastic film on a rigid substrate, as shown in Fig. 1.

The problem depicted by Fig. 1 may also be motivated from some other problems of current interest. For example, suspended crossbar array of carbon nanotubes, above a thin dielectric layer deposited on a substrate, has been proposed recently as a promising advance towards carbon nanotube-based electronics ([17,18]). In such a design, suspended nanotubes could deform due to the van der Waals interaction with other adjacent nanotubes and the dielectric layer ([19,20]). Thus, in view of the fact that even small local deformation of carbon nanotubes could crucially affect their electronic performance ([21,22]), the deformation and surface instability of suspended carbon nanotubes (modeled as an elastic strip or beam) due to the van der Waals interaction with an elastic layer on a substrate is of greater interest. Here, it is stressed that

Contributed by the Applied Mechanics Division of THE AMERICAN SOCIETY OF MECHANICAL ENGINEERS for publication in the ASME JOURNAL OF APPLIED MECHANICS. Manuscript received by the ASME Applied Mechanics Division, June 20, 2001; final revision, October 5, 2001. Associate Editor: R. C. Benson. Discussion on the paper should be addressed to the Editor, Prof. Lewis T. Wheeler, Department of Mechanical Engineering, University of Houston, Houston, TX 77204-4792, and will be accepted until four months after final publication of the paper itself in the ASME JOURNAL OF APPLIED MECHANICS.

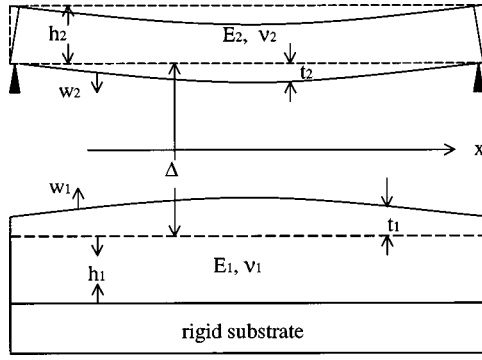


**Fig. 1 Surface instability of an elastic thin film interacting with a suspended elastic plate**

this type of surface instability, which appears on the tensile side of the bent member, is different than buckling-induced wrinkling of carbon nanotubes under bending due to a compressive stress ([23,24]). To our best knowledge, this type of surface instability has not been addressed in the literature, in spite of extensive research on contact mechanics of two elastic bodies in the presence of van der Waals-like forces ([25]) and the related tip-surface instability ([26,27]).

## 2 Description of the Model

Surface instability of an elastic film interacting with a rigid body is analyzed in [5,6] with the conventional method of plane elasticity. It turns out that the analysis of surface instability of two interacting elastic layers would be quite formidable if such a method is adopted. Here, instead, a novel method based on the Kerr-model ([28]) of elastic foundations is suggested. As will be seen below, this new method reduces the original plane-strain problem of two displacement components in two spatial dimensions to one of single displacement component in one spatial dimension, and thus allows one to study surface instability of two interacting elastic layers.

Since surface instability is characterized by the surface normal deflection, and the van der Waals interaction only causes a surface normal stress, the analysis of surface instability could be simplified largely if a relation between the surface normal deflection and the surface normal stress could be found. Motivated by this idea, we have examined the well-known Winkler model for elastic foundations and its various refined versions ([28–30]). We found that only the Kerr's model ([28]) perfectly serves this purpose (for instance, Bharatha and Levinson's model ([30]) cannot achieve this goal). To demonstrate this, let us first consider the lower elastic film fixed on a rigid substrate, shown in Fig. 1. As shown in the Appendix, the (upward) surface deflection  $V_1(x)$  of the elastic film on a rigid substrate can be related to the normal stress  $\sigma(x)$  on its surface by a differential relation

$$\begin{aligned} [1 - ah_1^2 D^2 + bh_1^4 D^4 - eh_1^6 D^6 + gh_1^8 D^8] V_1 \\ = [c - dh_1^2 D^2 + fh_1^4 D^4 - kh_1^6 D^6] \frac{h_1}{E_1} \sigma, \end{aligned} \quad (1)$$

where  $D$  denotes the differential operator  $d/dx$ ,  $h_1$  and  $E_1$  are the thickness of the elastic film and its Young's modulus, and  $a, b, c, d, e, f, g$ , and  $k$  are some dimensionless constants depending on the Poisson's ratio  $\nu_1$  of the elastic film, given by

$$\begin{aligned} a = \frac{1}{1 - \nu_1}, \quad b = \frac{(3 - 4\nu_1)}{12(1 - \nu_1)^2}, \quad c = \frac{(1 - 2\nu_1)(1 + \nu_1)}{(1 - \nu_1)}, \\ d = \frac{(3 - 4\nu_1)(1 + \nu_1)}{3(1 - \nu_1)}, \end{aligned}$$

$$\begin{aligned} e = \frac{(3 - 4\nu_1)}{90(1 - \nu_1)^2}, \quad f = \frac{(3 - 4\nu_1)(1 + \nu_1)}{15(1 - \nu_1)}, \\ g = \frac{(3 - 4\nu_1)}{1260(1 - \nu_1^2)}, \quad k = \frac{2((1 + \nu_1)(3 - 4\nu_1))}{315(1 - \nu_1)}. \end{aligned} \quad (2)$$

In particular, the coefficient  $c$  vanishes when the elastic film is incompressible ( $\nu = 1/2$ ), reflecting the fact that a uniform surface pressure will not cause any normal deflection of an incompressible elastic layer perfectly bonded on a rigid substrate.

Similarly, for a suspended elastic plate (its upper surface is traction-free), as shown in Fig. 1, the (downward) vertical deflection  $V_2(x)$  of its lower surface can be related to the normal stress  $\sigma(x)$  exerted on the lower surface, by a differential relation (see the Appendix for the detailed derivation)

$$[1 - ph_2^2 D^2 + qh_2^4 D^4 - th_2^6 D^6] \frac{h_2}{E_2} \sigma = [rh_2^4 D^4 - sh_2^6 D^6 + uh_2^8 D^8] V_2 \quad (3)$$

where  $h_2$  and  $E_2$  are the thickness of the suspended elastic plate and its Young's modulus, and  $p, q, r, s, t$ , and  $u$  are some dimensionless constants depending on the Poisson's ratio  $\nu_2$  of the suspended elastic plate, given by

$$\begin{aligned} p = \frac{1}{3}, \quad q = \frac{1}{15}, \quad t = \frac{2}{315}, \quad r = \frac{1}{12(1 - \nu_2^2)}, \\ s = \frac{1}{90(1 - \nu_2^2)}, \quad u = \frac{1}{1260(1 - \nu_2^2)}. \end{aligned} \quad (4)$$

Here,  $\sigma$  appearing in (1) and (3) is the same, because the normal stress on the lower surface of the suspended plate is equal to the normal stress on the surface of the elastic film fixed on a rigid substrate. It is noted that Eq. (3) becomes

$$\frac{h_2}{E_2} \sigma = rh_2^4 D^4 V_2 \quad (5)$$

if all higher-order terms are neglected. Evidently, the result (5) is exactly the classic elastic plate equation under a transverse pressure. Hence, Eq. (3) is a high-order modified form of Eq. (5) for a suspended elastic plate under the surface normal stress.

When two elastic layers are brought into contact, van der Waals forces come into play if the gap width between the two surfaces is very small (say, well below 100 nm ([5])). The van der Waals interaction between the two surfaces produces a surface normal stress  $\sigma(\delta)$  whose value at a point  $x$  is a function of the distance  $\delta(x)$  between the two surfaces at that point. For instance, a simple general expression for the van der Waals interaction  $\sigma(\delta)$  between two flat surfaces can be found in [5]. Thus, if the deflections of the layers, prior to and after surface instability, are  $t_1, t_2$  and  $w_1, w_2$ , respectively, that is

$$V_1 = t_1 + w_1, \quad V_2 = t_2 + w_2, \quad (6)$$

thus the surface normal stress  $\sigma$  can be expanded as

$$\sigma(\delta) = \sigma_0 + A(\delta - \delta_0),$$

$$\sigma_0 = \sigma(\delta_0), \quad A = \left. \frac{\partial \sigma}{\partial \delta} \right|_{\delta = \delta_0} < 0,$$

$$\delta_0 = \Delta - (t_1 + t_2), \quad \delta - \delta_0 = -(w_1 + w_2) \quad (7)$$

where  $\Delta$  is the undeformed initial gap between the two surfaces,  $\delta_0$  is the gap prior to surface instability, and  $\sigma_0$  is the normal stress prior to surface instability. Here, it is essential that the van der Waals forces are attractive and  $A < 0$  ([5]), and the interaction acts like a linear spring of a negative spring constant. Hence, the surfaces of two interacting elastic bodies would become unstable when the attractive interaction, characterized by the coefficient  $(-A)$ , is sufficiently strong. Evidently, the present

analysis based on the general interaction law  $\sigma(\delta)$  is valid not only for van der Waals interaction, but also for electrostatic interaction between two oppositely charged solid layers.

Prior to surface instability,  $w_1 = w_2 = 0$  and  $\sigma = \sigma_0$ , and substitution of (6) and (7) into (1) and (3) gives

$$\begin{aligned} & [1 - ah_1^2 D^2 + bh_1^4 D^4 - eh_1^6 D^6 + gh_1^8 D^8] t_1 \\ & = [c - dh_1^2 D^2 + fh_1^4 D^4 - kh_1^6 D^6] \frac{h_1}{E_1} \sigma_0, \\ & [1 - ph_2^2 D^2 + qh_2^4 D^4 - th_2^6 D^6] \frac{h_2}{E_2} \sigma_0 \\ & = [rh_2^4 D^4 - sh_2^6 D^6 + uh_2^8 D^8] t_2 \end{aligned} \quad (8)$$

where  $\sigma_0 = \sigma(\Delta - (t_1 + t_2))$ , as defined by (7). Assuming that the deflections of the elastic layers are small compared to the initial gap  $\Delta$  ([5,6]), the influence of the spatial nonuniformity of the gap  $\delta_0$  on the coefficient  $A$  can be neglected. Thus, throughout the paper, the coefficient  $A$  is assumed to be a constant.

To study surface instability of the film-plate system, we shall focus on the existence condition for a nonzero solution ( $w_1, w_2$ ). The governing equations for  $w_1$  and  $w_2$  can be obtained from Eqs. (1), (3), and (8), as follows:

$$\begin{aligned} & [1 - ah_1^2 D^2 + bh_1^4 D^4 - eh_1^6 D^6 + gh_1^8 D^8] w_1 \\ & = -A \frac{h_1}{E_1} [c - dh_1^2 D^2 + fh_1^4 D^4 - kh_1^6 D^6] (w_1 + w_2), \quad (9) \\ & [rh_2^4 D^4 - sh_2^6 D^6 + uh_2^8 D^8] w_2 \\ & = -A \frac{h_2}{E_2} [1 - ph_2^2 D^2 + qh_2^4 D^4 - th_2^6 D^6] (w_1 + w_2) \end{aligned} \quad (10)$$

where  $A$  is a constant. Here, because the wavelength of surface instability is usually much larger than the gap width between the two surfaces, the effect of the surface energy is small ([5,6]), and thus has been neglected. Therefore, surface instability of the film-plate system occurs when the coupled Eqs. (9) and (10) admit a nonzero solution. As will be seen below, this becomes possible when the interaction coefficient ( $-A$ ) is sufficiently large.

### 3 Instability Mode of a Suspended Elastic Plate

To study surface instability of the film-plate system, it is helpful to first understand the individual instability modes of the elastic film on a rigid substrate and the suspended elastic plate when they are attracted by a rigid flat. Surface instability of an elastic film on a rigid substrate interacting with a rigid flat was studied in [5,6], where it was shown that the critical value of ( $-A$ ) is proportional to the surface compliance  $h/E$  of the film, and the wavelength of the instability mode scales with the film thickness, independently of the length of the film. In particular, when the film on a rigid substrate is incompressible ( $\nu_1 = 1/2$ ), the critical value of ( $-A$ ), denoted by  $(-A)_1$ , is about  $2.07E_1/h_1$  ([5,6]).

For a suspended elastic plate attracted by a rigid plane, the governing equation can be obtained by taking  $E_1 = \infty$  and  $w_1 = 0$  in (9) and (10). Thus, Eq. (10) gives

$$\begin{aligned} & -A [1 - ph_2^2 D^2 + qh_2^4 D^4 - th_2^6 D^6] \frac{h_2}{E_2} w_2 \\ & = [rh_2^4 D^4 - sh_2^6 D^6 + uh_2^8 D^8] w_2. \end{aligned} \quad (11)$$

Let us consider a hinged plate (as shown in Fig. 1) and assume that  $w_2(x) \propto \sin(mx)$ , where  $m$  is a wave number. It follows from (11) that

$$-A = \frac{E_2 [r + sh_2^2 m^2 + uh_2^4 m^4] h_2^3 m^4}{[1 + ph_2^2 m^2 + qh_2^4 m^4 + th_2^6 m^6]}. \quad (12)$$

It can be verified that RHS of (12) is an increasing function of the wave number  $m$ . If the length of the plate is  $L$ , the ratio  $(mL)/\pi$  must be a positive integer to meet the hinged edge conditions. Hence, the minimum of ( $-A$ ) given by (12) is obtained at  $m = \pi/L$ . This means that the suspended plate has a half-wave instability mode, just like the buckling mode of a hinged Euler column. Further, according to the basic assumption of an elastic "plate,"  $(h\pi/L)^2$  should be smaller than unity. Thus, it turns out from (4) and (12) that all higher-order coefficients,  $p, q, s, t$ , and  $u$ , have a negligible effect on surface instability of a suspended plate, and the critical value of a (hinged) suspended plate attracted by a rigid flat is approximately

$$-A_2 \approx \frac{E_2 \pi^4 h_2^3}{12(1 - \nu_2^2) L^4}. \quad (13)$$

Hence, surface instability of a suspended plate is different from a film on a rigid substrate at least in the following three aspects: (1) the critical value of ( $-A$ ) is inversely proportional to  $L^4$  for the former, but independent of  $L$  for the latter; (2) the former has a long-wave mode with the wavelength scaling with the length of the plate, while the latter has a short-wave mode with the wavelength scaling with the film thickness; (3) the higher-order terms of Kerr's model are negligible for the instability of a suspended plate attracted by a rigid body, but essential for a film on a rigid substrate (as illustrated in Section 5). In particular, the ratio of the critical value for a suspended plate to the critical value for a film on a rigid substrate is approximately

$$\lambda = \frac{A_2}{A_1} \approx \frac{E_2 \pi^4 h_1 h_2^3}{24(1 - \nu_2^2) E_1 L^4}, \quad A_1 = -2.07 \frac{E_1}{h_1}. \quad (14)$$

In what follows, surface instability of the film-plate system depicted in Fig. 1 is studied, with an emphasis on the role of the competition between the long-wave mode of the suspended plate and the short-wave mode of the film on a rigid substrate.

### 4 Surface Instability of the Film-Plate System

Let us now consider the condition for the existence of a nonzero solution ( $w_1, w_2$ ). Note that the coefficient ( $-A$ ), as the loading parameter, appears only on RHS of (9) and (10) with the sum ( $w_1 + w_2$ ). To obtain a simple rational expression for ( $-A$ ), let us define  $W_1 = w_1 + w_2$ , and  $W_2 = w_1 - w_2$ . Thus, Eqs. (9) and (10) become

$$\begin{aligned} & 2A [1 - ph_2^2 D^2 + qh_2^4 D^4 - th_2^6 D^6] \frac{h_2}{E_2} W_1 + [rh_2^4 D^4 - sh_2^6 D^6 \\ & + uh_2^8 D^8] W_1 = [rh_2^4 D^4 - sh_2^6 D^6 + uh_2^8 D^8] W_2, \\ & [1 - ah_1^2 D^2 + bh_1^4 D^4 - eh_1^6 D^6 + gh_1^8 D^8] W_1 + 2A \frac{h_1}{E_1} \\ & \times [c - dh_1^2 D^2 + fh_1^4 D^4 - kh_1^6 D^6] W_1 \\ & = -[1 - ah_1^2 D^2 + bh_1^4 D^4 - eh_1^6 D^6 + gh_1^8 D^8] W_2. \end{aligned} \quad (15)$$

Let  $W_1 = X \sin(mx)$  and  $W_2 = Y \sin(mx)$ , where  $X$  and  $Y$  are two undetermined constants and  $m$  is a wave number. Substituting these expressions into (15) yields

$$2AS \frac{h_2}{E_2} X + TX = TY, \quad LX + 2A \frac{h_1}{E_1} RX = -LY, \quad (16)$$

where

$$\begin{aligned} S &= [1 + p\alpha^2 Z + q\alpha^4 Z^2 + t\alpha^6 Z^3], \\ T &= [r\alpha^4 Z^2 + s\alpha^6 Z^3 + u\alpha^8 Z^4], \end{aligned}$$



$$L=[1+aZ+bZ^2+eZ^3+gZ^4], \quad R=[c+dZ+fZ^2+kZ^3],$$

$$Z=h_1^2m^2, \quad \frac{h_2}{h_1}=\alpha. \quad (17)$$

Since the existence of a nonzero solution ( $w_1, w_2$ ) is equivalent to the existence of a nonzero solution ( $W_1, W_2$ ), the condition for surface instability is given by the existence condition for a nonzero solution ( $X, Y$ ). In doing so, a simple rational expression is derived from (16) for the interaction coefficient  $A$  as

$$-A \frac{h_1}{E_1} = \frac{LT}{\beta SL + RT}, \quad (18)$$

where

$$\beta = \frac{\frac{h_2}{E_2}}{\frac{h_1}{E_1}}.$$

It is verified that RHS of (18) approaches zero monotonically when  $Z$  tends to zero.

If the suspended plate is hinged at its edges, we have

$$m = \frac{n\pi}{L}, \quad n=1,2,3 \dots \quad (19)$$

Therefore, the critical value of  $(-A)$  and the instability mode of the film-plate system can be determined easily by identifying the minimum of (18) and the associated value of  $Z$  under the constraint (19). In particular, it follows from (19) the admissible values of  $Z$  are bounded from below by the condition

$$Z=(mh_1)^2 \geq \left(\frac{\pi h_1}{L}\right)^2. \quad (20)$$

Thus, the limit case  $Z=0$  is excluded by condition (20). In what follows, surface instability of the film-plate system is studied by identifying the minimum of (18) within the range bounded by (20). Obviously, the length  $L$  of the suspended plate enters the problem through condition (20).

## 5 Results and Discussions

First, to demonstrate the efficiency of the present method, let us consider the case when the upper plate is rigid and thus  $\beta=0$ . In this case, Eq. (18) gives

$$-A_1 \frac{h_1}{E_1} = \frac{L(Z)}{R(Z)}. \quad (21)$$

For example, when the elastic film is incompressible ( $\nu_1=1/2$ ), it can be verified easily that RHS of (21) has a unique minimum which is about 2.063 and attained at  $(mh_1)^2=4.8$ . Thus, the corresponding critical value of  $(-Ah_1/\mu_1)$  is about 6.19 (where  $\mu$  is the shear modulus and thus  $E=3\mu$  when  $\nu=1/2$ ), which is attained at  $h_1m=2.19$ . These results are in excellent agreement with the values  $(-Ah/\mu)=6.22$  and  $hm=2.12$ , obtained by the conventional method ([5,6]). The present method and the result (21) are much simpler than the conventional method. In particular, the present method is applicable to both incompressible and compressible elastic layers. Here, it should be stated that if a lower-order Kerr-model (1) with  $g=k=0$  is used, the critical value of  $(-Ah/\mu)$  predicted by the present method will be about 7, with  $(mh)=1.7$ . Further, if the lowest-order Kerr model with  $e=f=g=k=0$  is used, the predicted critical value of  $(-Ah/\mu)$  by the present method will be about 9, with  $hm=1.3$ . Therefore, in contrast to a suspended plate attracted by a rigid flat for which the higher-order terms of the Kerr's model (3) have a negligible effect on the critical value and instability mode (see Section 3), the

**Table 1 Special value of  $Z$  below which (18) is lower than its internal local minimum**

	$\beta=0.2$	$=0.1$	$=0.01$	$=0.001$	$=0.0001$
$\alpha=10$	0.03	0.018	0.0047	0.0015	0.00048
$\alpha=100$	0.0003	0.00018	0.00005	$1.5 \times 10^{-5}$	$4.8 \times 10^{-6}$

higher-order terms of the Kerr model (1) for a film on a rigid substrate play an indispensable role in the surface instability of the film.

Now, let us examine surface instability of the film-plate system. Since the effect of Poisson's ratio is less important for both the suspended plate (see (4)) and the film on a rigid substrate ([5,6]), we shall neglect the Poisson's ratio of the suspended elastic plate (thus  $\nu_2=0$ ), and assume that the elastic film on a rigid substrate is incompressible ( $\nu_1=1/2$ ).

**Case I: Stiff Thick Plates.** First, let us examine the case when the suspended plate is much stiffer and also thicker than the compliant film on a rigid substrate. For instance, let  $\alpha=10$  and  $\beta=0.2, 0.1, 0.01, 0.001$ , and  $0.0001$ , respectively. In these cases, it is found that (18) has an internal local minimum, valued around 2.05 to 2.06, within a very narrow range  $Z \in [4.7, 4.8]$ . Apparently, this minimum corresponds to the critical value and instability mode of the film on a rigid substrate given by (21). On the other hand, because (18) approaches zero monotonically when  $Z$  tends to zero, there is a special value of  $Z$  below which (18) is lower than its internal local minimum. The dependency on  $\beta$  of this special value of  $Z$  are shown in Table 1 for  $\alpha=10$ . Hence, if RHS of (20) is larger than this special value, the admissible minimum of (18) restricted by (20) is provided by the internal local minimum. In this case, the critical value and the instability mode of the system are determined by the internal local minimum or, in other words, by the elastic film. On the other hand, if RHS of (20) is smaller than the special value listed in Table 1, the admissible minimum of (18) is provided by the smallest admissible wave-number given by (20) because whose corresponding value of (18) is smaller than the internal local minimum. In this case, the critical value and the instability mode of the system are determined by the suspended plate. Note that RHS of (20) is inversely proportional to  $L^2$ , the above results indicate that the critical value and the instability mode of the film-plate system are determined by the film when the plate is sufficiently short, or by the suspended plate when the plate is sufficiently long.

This conclusion has a simple interpretation. In fact, the special values listed in Table 1 are defined by the condition that the critical value of the plate is equal to the critical value of the film (that is,  $\lambda=1$ ). Thus, this special value of  $Z$  can be estimated by combining  $\lambda=1$  with the lower bound of (20), which yields

$$Z \approx \frac{5\sqrt{\beta}}{\alpha^2}. \quad (22)$$

This result is applicable only when RHS of (22) is smaller than unity, as required by the condition (20). In particular, formula (22) predicts that this special value is inversely proportional to  $\alpha^2$ . To confirm this, this special value of  $Z$  is calculated for  $\alpha=100$  and listed in Table 1. The results of Table 1 confirm that this special value of  $Z$  is inversely proportional to  $\alpha^2$ . Finally, it is stated that, for all cases listed in Table 1, the parameters  $\alpha$  and  $\beta$  satisfy the requirement that RHS of (22) is much smaller than unity.

**Case II: Stiff Thin Plates.** It is noted that the stability strength of the suspended plate is proportional to the cube of its thickness  $h_2$ , while the stability strength of the film on a rigid substrate is inversely proportional to its thickness  $h_1$ . Thus, it is expected that surface instability of the film-plate system relies heavily on the thickness-ratio  $\alpha$ . Hence, another case of physical interest is when the stiff plate is thin compared to the film. First,

**Table 2** Special value of  $Z$  below which (18) is lower than its internal local minimum (when an internal local minimum of (18) does not exist, as indicated by “\*,” the special values of  $Z$  collected here are those below which (18) is lower than 2.06)

	$\beta=0.0001$	$=0.00001$	$=0.000001$	$=0.0000001$	$=0.00000001$
$\alpha=1$	0.05	0.015	0.005	0.0015	0.0005
$\alpha=0.1$	13*	6*	0.8	0.17	0.048

let us consider the cases  $\alpha=1$  and  $\beta \in [10^{-8}, 10^{-4}]$ . It is found that (18) still has an internal local minimum, valued around 2.05 to 2.1, within a narrow range  $Z \in [4.0, 4.8]$ . Apparently, this internal local minimum corresponds to the critical value and instability mode of the film on a rigid substrate given by (21). On the other hand, because (18) approaches zero when  $Z$  tends to zero, there is a special value of  $Z$  below which (18) is lower than the internal local minimum. The dependency on  $\beta$  of this special value of  $Z$  is shown in Table 2 for  $\alpha=1$ . It is verified that the special values listed in Table 2 for  $\alpha=1$  can also be estimated approximately by formula (22).

Furthermore, let us consider the plates even thinner than the film. For example, let us consider  $\alpha=0.1$  and  $\beta \in [10^{-8}, 10^{-4}]$ . Two new phenomena are observed for  $\beta > 0.00001$ . First, in these cases ( $\alpha=0.1$  and  $\beta > 0.00001$ ), the special values of  $Z$  listed in Table 2, below which (18) is lower than 2.05, are no longer smaller than unity. Second, it is found that (18) becomes a monotonic function of  $Z$  even for larger values of  $Z$  and no longer has an internal local minimum. The interpretation is simple: The plate is so thin that its stability strength is always lower than that of the film even when the length of the plate is just few times the plate thickness. In this case, an internal local minimum of (18) is absent, reflecting the fact that the film-plate system always exhibits the long-wave instability mode of the suspended thin plate and the short-wave instability mode of the film will not play any role.

To demonstrate these results clearly, let us plot the sixth root of expression (18) as a function of  $Z^{1/6}$  over a relevant range for several typical cases. First, let us consider thinner plates with  $\alpha=0.5$  and  $\alpha=0.05$ , respectively. The sixth root of expression (18) is plotted against  $Z^{1/6}$  in Figs. 2 and 3 for various values of  $\beta$ . It is seen that, for given  $\alpha$ , (18) has an internal local minimum for smaller values of  $\beta$ , but the internal local minimum disappears for relatively larger values of  $\beta$ . The biggest value of  $\beta$  which admits an internal local minimum of (18) can be estimated roughly by setting RHS of (22) equal to unity.

This phenomenon does disappear for very thick plates. For example, let us consider thicker plates with  $\alpha=1000$  and  $\alpha=10,000$ , respectively. The sixth root of expression (18) is sketched in Figs. 4 and 5 against  $Z^{1/6}$  for various values of  $\beta$ . In

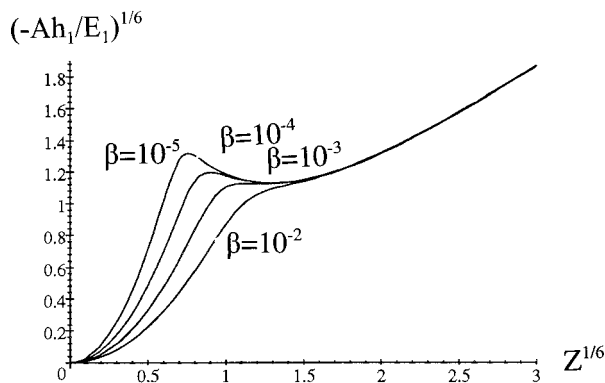


**Fig. 2** The interaction coefficient determined by (18) for thin plates with  $\alpha=0.5$  which shows the dependency on  $\beta$  of the existence of an internal local minimum of (18)

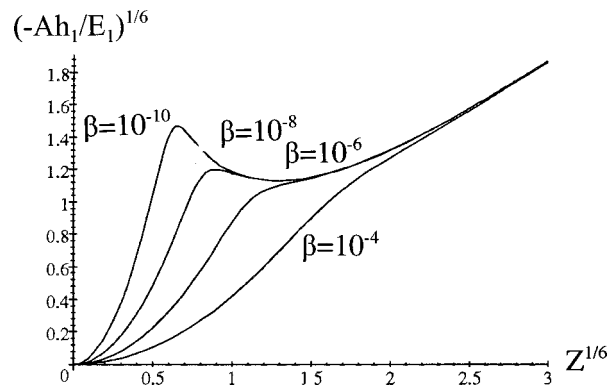


**Fig. 3** The interaction coefficient determined by (18) for thin plates with  $\alpha=0.05$  which shows the dependency on  $\beta$  of the existence of an internal local minimum of (18)

all of the cases shown in Figs. 4 and 5, (18) has an internal local minimum, and thus the critical value and instability mode of the film-plate system are determined by the minor of the internal local minimum and the value of (18) at the admissible lower bound (20). When the length of the plate is sufficiently short, the lower bound (20) is so large that the internal local minimum is lower than the value of (18) at the lower bound. Thus, the film-plate system exhibits the short-wave instability mode of the film. This means that not only the film, but also the plate, will exhibit the short-wave instability mode. On the other hand, if the plate is

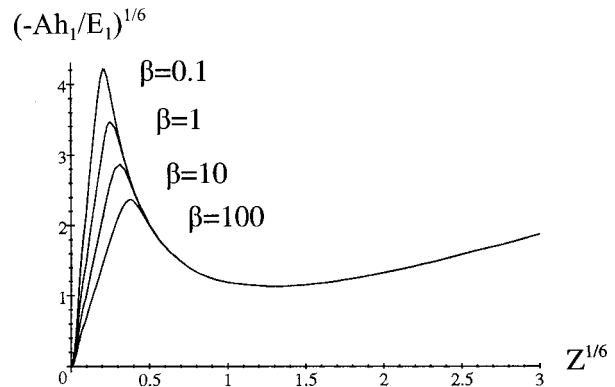


**Fig. 4** The interaction coefficient determined by (18) for thick plates with  $\alpha=1000$  which indicates the existence of an internal local minimum of (18)

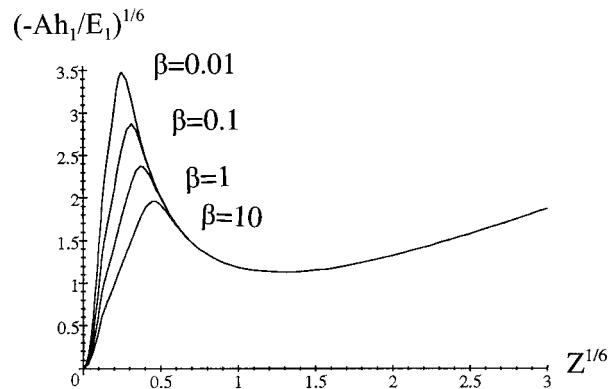


**Fig. 5** The interaction coefficient determined by (18) for thick plates with  $\alpha=10,000$  which indicates the existence of an internal local minimum of (18)

sufficiently long, the lower bound (20) is so small that the internal local minimum is higher than the value of (18) at the lower bound. In this case, the film-plate system exhibits the long-wave mode of the suspended plate. Thus, not only the plate, but also the film, will exhibit the long-wave instability mode of the plate.

## 6 Conclusions

This paper gives a study of surface instability of an elastic film fixed on a rigid substrate interacting with a suspended elastic plate. The analysis is based on a novel method much simpler than the conventional method used for surface instability of an elastic film interacting with a rigid body ([5,6]). The efficiency and accuracy of the present method is demonstrated by excellent agreement between the predicted results and the known data for a special case. The present results show that the competition between the long-wave mode of the suspended plate and the short-wave mode of the film plays a crucial role in surface instability of the film-plate system. In particular, it is found that

(1) when RHS of (22), determined by the geometrical and material parameters of the film-plate system, is larger than or close to unity, the stability strength of the suspended plate is lower than the film on a rigid substrate even for the shortest plate-lengths. In this case, the interaction coefficient given by (18) has no internal local minimum, and thus the film-plate system exhibits the long-wave instability mode of the suspended plate determined by the lower bound (20).

(2) when RHS of (22) is smaller than unity, the interaction coefficient given by (18) has an internal local minimum representing the short-wave mode of the film on a rigid substrate. Thus, the critical value and instability mode of the film-plate system are determined by the film if the plate is short enough, or by the suspended plate if the plate is long enough.

## Acknowledgment

The financial support of the Natural Sciences and Engineering Research Council of Canada (NSERC) is gratefully acknowledged.

## Appendix

The method suggested here is based on a relation between the surface normal deflection and the surface normal stress of an elastic layer (see (1),(2) or (3),(4) in the text). Such a relation is given by Kerr [28] for an elastic layer resting on a frictionless rigid substrate. Here, Kerr's method is used to derive a similar relation for an elastic layer fixed on a rigid substrate, or a suspended elastic layer. To demonstrate this, let us begin with Kerr's expressions for the tangential stress, vertical normal stress, and two displacement components under plane-strain

$$\begin{aligned}\sigma_{xz} = & -\frac{1}{2} [zD^2 \cos(zD) - D \sin(zD)] X_0' \\ & - \left[ \cos(zD) + \frac{1}{2} zD \sin(zD) \right] X_1' \\ & - \frac{1}{2} \left[ z \cos(zD) + \frac{1}{D} \sin(zD) \right] X_2' - \frac{1}{2} \frac{z}{D} \sin(zD) X_3', \\ \sigma_{zz} = & \left[ \cos(zD) + \frac{1}{2} zD \sin(zD) \right] X_0'' \\ & + \left[ \frac{3}{2D} \sin(zD) - \frac{1}{2} z \cos(zD) \right] X_1'' + \frac{z}{2D} \sin(zD) X_2'' \\ & + \frac{1}{2} \left[ \frac{\sin(zD)}{D^3} - \frac{z}{D^2} \cos(zD) \right] X_3'',\end{aligned}$$

$$\begin{aligned}Eu_x = & (1 - \nu^2) \left[ D \cos(zD) X_0 + \sin(zD) X_1 + \frac{1}{D} \cos(zD) X_2 \right. \\ & + \left. \frac{1}{D^2} \sin(zD) X_3 \right] - (1 + \nu) \left[ \left[ \cos(zD) + \frac{1}{2} zD \sin(zD) \right] X_0' \right. \\ & + \left[ \frac{3}{2D} \sin(zD) - \frac{1}{2} z \cos(zD) \right] X_1' + \frac{z}{2D} \sin(zD) X_2' \\ & + \left. \frac{1}{2} \left[ \frac{\sin(zD)}{D^3} - \frac{z}{D^2} \cos(zD) \right] X_3' \right], \\ Eu_z = & (1 - \nu^2) \left[ \sin(zD) X_0' - \frac{1}{D} \cos(zD) X_1' \right. \\ & + \left. \frac{1}{D^2} \sin(zD) X_2' - \frac{1}{D^3} \cos(zD) X_3' \right] \\ & - (1 + \nu) \times \left[ \frac{1}{2} [zD^2 \cos(zD) - D \sin(zD)] X_0 \right. \\ & + \left[ \cos(zD) + \frac{1}{2} zD \sin(zD) \right] X_1 \\ & + \left. \frac{1}{2} \left[ \frac{\sin(zD)}{D} + z \cos(zD) \right] X_2 + \frac{z}{2D} \sin(zD) X_3 \right]\end{aligned}$$

where  $u_x$  and  $u_z$  are the displacements along the  $x$  and  $z$ -axes, respectively,  $z$  is the upward vertical coordinate measured from the surface of the elastic layer,  $E$  and  $\nu$  are the Young's modulus and Poisson ratio of the elastic layer,  $X_i(x)$  ( $i=0, 1, 2, 3$ ) are some unknown functions of  $x$ , and "′" denoted their derivatives. First, for a suspended elastic layer subjected to a normal stress on one of its surfaces, the boundary conditions on the surfaces ( $z=0$ ) and ( $z=-h$ ) are

$$\begin{aligned}\sigma_{xz}(x, -h) = 0, \quad \sigma_{zz}(x, -h) = 0, \quad \sigma_{xz}(x, 0) = 0, \\ u_z(x, 0) = w, \quad \sigma_{zz}(x, 0) = \sigma.\end{aligned}$$

Thus, we have the following five conditions:

$$\begin{aligned}X_1'(x) &= 0, \\ \frac{1}{2} [-hD^2 \cos(hD) + D \sin(hD)] X_0' \\ &+ \frac{1}{2} \left[ -h \cos(hD) - \frac{1}{D} \sin(hD) \right] X_2' \\ &+ \frac{1}{2} \frac{h}{D} \sin(hD) X_3' = 0, \\ \left[ \cos(hD) + \frac{1}{2} hD \sin(hD) \right] X_0'' \\ &+ \frac{h}{2D} \sin(hD) X_2'' \\ &- \frac{1}{2} \left[ \frac{\sin(hD)}{D^3} - \frac{h}{D^2} \cos(hD) \right] X_3'' = 0, \\ X_0'' &= \sigma, \\ -(1 - \nu^2) \frac{1}{D^3} X_3' &= Ew.\end{aligned}$$

One can eliminate  $X_0$ ,  $X_1$ , and  $X_3$  and obtain the two relations



$$\begin{aligned}
& \frac{1}{2} [-h^2 D^2 \cos(hD) + hD \sin(hD)] \sigma \\
& + \frac{1}{2} [-h^2 D \cos(hD) - h \sin(hD)] X_2' \\
& - \frac{1}{2} h^2 D^3 \sin(hD) E^* w = 0, \\
& \left[ \cos(hD) + \frac{1}{2} hD \sin(hD) \right] \sigma + \frac{h}{2} \sin(hD) X_2' \\
& + \frac{1}{2} [D \sin(hD) - hD^2 \cos(hD)] E^* w = 0.
\end{aligned}$$

Thus, eliminating  $X_2$  leads to a simple relation between  $w$  and  $\sigma$  as

$$\begin{aligned}
& \left[ 1 + \sin(hD) \frac{1}{hD} \cos(hD) \right] \sigma \\
& + \frac{1}{2} [\sin(hD) \sin(hD) - h^2 D^2] E^* \frac{w}{h} = 0.
\end{aligned}$$

Equations (3) and (4) in the text can be obtained from the above relation by expanding the trigonometric functions in power series of  $(hD)$  and retaining the first three terms.

Similarly, for an elastic layer fixed on a rigid substrate, the boundary conditions on its surfaces are

$$\begin{aligned}
u_x(x, -h) = 0, \quad u_z(x, -h) = 0, \quad \sigma_{xz}(x, 0) = 0, \\
u_z(x, 0) = w, \quad \sigma_{zz}(x, 0) = \sigma.
\end{aligned}$$

Thus, in a similar way, a simple relation between  $w$  and  $\sigma$  can be found as

$$\begin{aligned}
& \left[ \frac{1}{2} h(1 + \nu) - \sin(hD) \cos(hD) \right] \\
& \times \left[ \frac{1}{2D} (1 + \nu)(3 - 4\nu) \right] \sigma \frac{(1 - \nu^2)}{E} \\
& = \left[ \frac{1}{4} (1 + \nu)(3 - 4\nu) \sin(hD) \sin(hD) \right. \\
& \quad \left. - (1 - \nu^2)(1 - \nu) + \frac{1}{4} (1 + \nu) h^2 D^2 \right] w.
\end{aligned}$$

Equations (1) and (2) in the text can be obtained from the above relation by expanding the trigonometric functions in power series of  $(hD)$  and retaining the first three terms. In particular, the relations (1)–(4) can also be applied to two-dimensional patterning of elastic layers provided  $D^2$  is replaced by  $\nabla^2$ .

## References

- [1] Herminghaus, S., 1999, "Dynamic Instability of Thin Liquid Films Between Conducting Media," *Phys. Rev. Lett.*, **83**, pp. 2359–2362.
- [2] Schall, P. J., and McHugh, J. P., 1999, "The Stability of Two-Layer Inviscid Flow Between an Elastic Layer and a Rigid Boundary," *ASME J. Appl. Mech.*, **66**, pp. 197–203.
- [3] Gorla, R. S. R., 2001, "Rupture of Thin Power-Law Liquid Film on a Cylinder," *ASME J. Appl. Mech.*, **68**, pp. 2294–2297.
- [4] Ghatak, A., Chaudhury, M. K., Shenoy, V., and Sharma, A., 2000, "Meniscus Instability in a Thin Elastic Film," *Phys. Rev. Lett.*, **85**, pp. 4329–4332.
- [5] Monch, W., and Herminghaus, S., 2001, "Elastic Instability of Rubber Films Between Solid Bodies," *Europhys. Lett.*, **53**, pp. 525–531.
- [6] Shenoy, V., and Sharma, A., 2001, "Pattern Formation in a Thin Solid Film With Interactions," *Phys. Rev. Lett.*, **86**, pp. 119–122.
- [7] Biot, M. A., 1963, "Surface Instability of Rubber in Compression," *Appl. Sci. Res.*, **12A**, pp. 168–182.
- [8] Gent, A. N., and Cho, I. S., 1999, "Surface Instability in Compressed or Bent Rubber Blocks," *Rubber Chem. Technol.*, **72**, pp. 253–262.
- [9] Asaro, R. J., and Tiller, W. A., 1972, "Interface Morphology Developing During Stress Corrosion Cracking: Part I. Via Surface Diffusion," *Metall. Trans.*, **3**, pp. 1789–1796.
- [10] Srolovitz, D. J., 1989, "On the Stability of Surfaces of Stressed Solids," *Acta Metall.*, **37**, pp. 621–624.
- [11] Crosby, A. J., Shull, K. R., Lakrout, H., and Creton, C., 2000, "Deformation and Failure Modes of Adhesively Bonded Elastic Layers," *J. Appl. Phys.*, **88**, pp. 2956–2966.
- [12] Chow, T. S., 2001, "Nanoadhesion Between Rough Surfaces," *Phys. Rev. Lett.*, **86**, pp. 4592–4595.
- [13] Gosele, U., and Tong, Q. Y., 1998, "Semiconductor Wafer Bonding," *Annu. Rev. Mater. Sci.*, **28**, pp. 215–241.
- [14] Han, W. Yu, J., and Wang, Q., 2000, "Elastic Deformation of Wafer Surfaces in Bonding," *J. Appl. Phys.*, **88**, pp. 4401–4403.
- [15] Schaffer, E., Albrecht, T. T., Russell, T. P., and Steiner, U., 2000, "Electrically Induced Structure Formation and Pattern Transfer," *Nature (London)*, **403**, pp. 874–877.
- [16] Jacobs, H. O., and Whitesides, G., 2001, "Submicrometer Patterning of Charge in Thin-Film Electrets," *Science*, **291**, pp. 1763–1766.
- [17] Rueckes, T., Kim, K., Joselevich, E., Tseng, G. Y., Cheung, C. L., and Lieber, C. M., 2000, "Carbon Nanotube-Based Nonvolatile Random Access Memory for Molecular Computing," *Science*, **289**, pp. 94–97.
- [18] Collins, P. G., and Avouris, P., 2000, "Nanotubes for Electronics," *Sci. Am.*, **Dec.**, pp. 62–69.
- [19] Hertel, T., Walkup, R. E., and Avouris, P., 1998, "Deformation of Carbon Nanotubes by Surface van der Waals Forces," *Phys. Rev. B*, **58**, pp. 13,870–13,873.
- [20] Yoon, Y., Mazzoni, M. S. C., Choi, H. J., Ihm, J., and Louie, S. G., 2001, "Structural Deformation and Intertube Conductance of Crossed Carbon Nanotube Junctions," *Phys. Rev. Lett.*, **86**, pp. 688–691.
- [21] Rochefort, A., Salahub, D. R., and Avouris, P., 1998, "The Effect of Structural Distortion on the Electronic Structures of Carbon Nanotubes," *Chem. Phys. Lett.*, **297**, pp. 45–50.
- [22] Tomblar, T. W., Zhou, C., Alexseyev, L., Kong, J., Dai, H., Liu, L., Jayanthi, C. S., Tang, M., and Wu, S. Y., 2000, "Reversible Electromechanical Characteristics of Carbon Nanotubes Under Local-Probe Manipulation," *Nature (London)*, **405**, pp. 769–772.
- [23] Falvo, M. R., Clary, G. J., Taylor, R. M., Chi, V., Brooks, F. P., Washburn, S., and Superfine, R., 1997, "Bending and Buckling of Carbon Nanotubes Under Large Strain," *Nature (London)*, **389**, pp. 582–584.
- [24] Ru, C. Q., 2000, "Effective Bending Stiffness of Carbon Nanotubes," *Phys. Rev. B*, **62**, pp. 9973–9976.
- [25] Johnson, K. L., 1996, "Continuum Mechanics Modeling of Adhesion and Friction," *Langmuir*, **12**, pp. 4510–4513.
- [26] Pethica, J. B., and Sutton, A. P., 1988, "On the Stability of a Tip and Flat at Very Small Separation," *J. Vac. Sci. Technol.*, **A6**, pp. 2490–2494.
- [27] Gleyzes, P., Kuo, P. K., and Boccara, A. C., 1991, "Bistable Behavior of Vibrating Tip Near a Solid Surface," *Appl. Phys. Lett.*, **58**, pp. 2989–2991.
- [28] Kerr, A. D., 1984, "On the Formal Development of Elastic Foundation Models," *Ingenieur-Archiv*, **54**, pp. 455–464 (in English).
- [29] Vlasov, V. Z., and Leont'ev, U. N., 1966, *Beams, Plates, and Shells on Elastic Foundations*, Israel Program for Scientific Translations, Jerusalem.
- [30] Bharatha, S., and Levinson, C., 1980, "A Theory of Elastic Foundations," *Arch. Ration. Mech. Anal.*, **74**, pp. 249–266.

**K.-T. Wan<sup>1</sup>**

Department of Engineering  
Science and Mechanics,  
Virginia Polytechnic Institute  
and State University,  
Norris Hall 106, Mail Code 0219,  
Blacksburg, VA 24061  
e-mail: kwan@vt.edu

**J. Duan**

School of Mechanical and  
Production Engineering,  
Nanyang Technology University,  
Nanyang Avenue,  
Singapore 639798

# Adherence of a Rectangular Flat Punch Onto a Clamped Plate: Transition From a Rigid Plate to a Flexible Membrane

*A linear elastic solution is proposed for the adhesion/delamination of a constrained thin film adhered to a rectangular flat punch. As the punch is pulled away by an external load, the film deforms and gradually delaminates until a line contact is left prior to complete separation. This is in sharp contrast with the finite pull-off contact radius as predicted by the classical Johnson-Kendall-Roberts theory for adhesion between solid bodies. In order to portray the transition from a platelike to a membranelike behavior, the film thickness and stiffness are allowed to span a wide range of values. Simple experiments demonstrated the validity of the theory. [DOI: 10.1115/1.1303824]*

## 1 Introduction

Thin film adhesion is an important subject in many fields. For instances, in microelectronics, good adhesion is required between encapsulating polymer films on silicon chip to enhance mechanical reliability, and in biological sciences, cell locomotion requires reasonable adhesion between thin cell membrane and substratum, and agglomeration/division of cells involves cell-cell adhesion/decohesion. It is therefore essential to formulate the adhesive contact mechanics for bodies enclosed by thin films.

Hertz [1] and Boussinesq [2] introduced the classical contact mechanics for a convex solid body indenting on a continuum substrate. Johnson et al. [3] later extended the work to include adhesion at the contact and derived the now-celebrated Johnson-Kendall-Roberts (JKR) theory. Kendall [4] formulated the adhesive contact mechanics of a circular flat punch in contact with an elastic half-space, which was later modified by Maugis [5] to include different punch geometries. Contact mechanics for thin films has attracted much attention lately. Plaut et al. studied the deflection and buckling of a bent elastica in contact with a flat surface ([6]). Wan considered the adherence between an axisymmetric punch and a thin flexible film ([7]). In this paper, we focus on a new configuration: the adhesion between a rectangular flat punch and a thin film constrained at two opposite ends (while the other two ends remain free). The punch is gradually pulled away from the film and thus driving a delamination into the punch-film interface. The film is allowed to span a wide range of thickness and mechanical compliance, rather than being confined to the classical limits of either a plate under pure bending or a membrane under pure stretching. The new elastic model is derived based on a simple energy balance and linear elasticity. Experiments with an interface made by adhering a commercially available pressure-sensitive tape onto an aluminum punch serve to illustrate the theory.

## 2 Theory

Figure 1 shows a thin isotropic film with unit width, thickness,  $h$ , elastic modulus,  $E$ , Poisson's ratio,  $\nu$ , and flexural rigidity  $D = Eh^3/12(1-\nu^2)$ , being adhered onto a rigid substrate with a rectangular opening of length,  $2l$ . A rectangular flat punch is then pulled away from the membrane by an external load,  $F$ , so that the contact area of length,  $2c$ , diminishes until complete separation at the film-substrate interface. The free hanging film on either side of the contact, with an initial length  $(l-c)$ , is strained by a uniform uniaxial membrane stress of  $N$  along the midplane of the films. The debonding angle, a measure of the inclination of the film to the plate, is assumed to be small hereafter. Note that this angle is determined by the geometry and is independent of the film thickness. For simplicity, viscoelasticity of the polymer film is not considered in the present model. It is assumed that only the free-hanging regions  $x \leq (l-c)$  and  $x \geq (l+c)$  experience bending and stretching while the contact region  $(l-c) \leq x \leq (l+c)$  is free from mechanical stresses. We will first consider the elastic deformation of the film as a consequence of the external load without delamination, before proceeding to the delamination mechanics.

**2.1 Constitutive Relation Without Delamination.** The profile  $w(x)$  of the free hanging film is governed by linear elasticity ([8,9])

$$D \frac{d^2 w}{dx^2} = Nw - \frac{Nx}{2} - M_0 \quad (1)$$

where  $M_0$  is the bending moment at  $x=0$ . Equation (1) be rewritten as

$$\frac{d^2 \omega}{d\xi^2} - \beta^2 \omega = -\varphi \xi - m_0 \quad (2)$$

with a set of dimensionless quantities defined as follows:

$$\xi = \frac{x}{l}, \quad \omega = \frac{w}{h}, \quad \lambda = 1 - \frac{c}{l}, \quad m_0 = \frac{M_0 l^2}{Dh},$$

$$\beta = \left( \frac{Nl^2}{D} \right)^{1/2} \quad \text{and} \quad \varphi = \frac{Fl^3}{2Dh}. \quad (3)$$

The parameter  $\beta$  represents the ratio of membrane stress to film rigidity: (i) for a plate,  $D \gg Nl^2$  and  $\beta \rightarrow 0$ ; and for a membrane,  $D \ll Nl^2$  and  $\beta \rightarrow \infty$ . Assuming being clamped at opposite ends, the

<sup>1</sup>To whom correspondence should be addressed.

Contributed by the Applied Mechanics Division of THE AMERICAN SOCIETY OF MECHANICAL ENGINEERS for publication in the JOURNAL OF APPLIED MECHANICS. Manuscript received by the ASME Applied Mechanics Division, Feb. 12, 2001; final revision, Oct. 15, 2001. Associate Editor: K. Ravi-Chandar. Discussion on the paper should be addressed to the Editor, Prof. Lewis T. Wheeler, Department of Mechanical Engineering, University of Houston, Houston, TX 77204-4792, and will be accepted until four months after final publication of the paper itself in the ASME JOURNAL OF APPLIED MECHANICS.

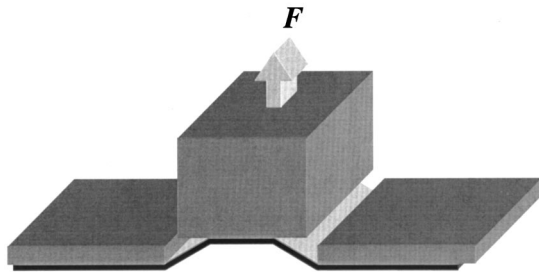
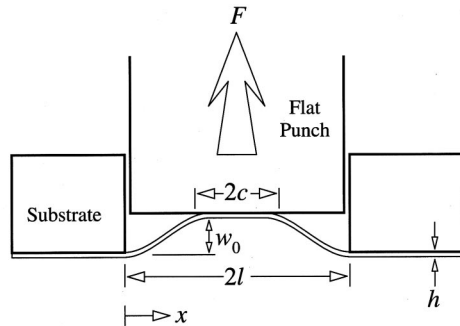


Fig. 1 A rectangular punch adhered onto a thin film constrained at two opposite ends

profile approaches zero gradients at the contact edges because of nonzero bending. There are therefore three boundary conditions:

$$(d\omega/d\xi)=0 \text{ at } \xi=0 \text{ and } \xi=\lambda \quad (4)$$

$$\omega=0 \text{ at } \xi=0 \quad (5)$$

Solving (2) exactly,

$$\omega = \frac{\varphi}{\beta^3} \left\{ -\sinh(\beta\xi) + \left[ \frac{\cosh(\beta\lambda)-1}{\sinh\beta\lambda} \right] [\cosh(\beta\xi)-1] + \beta\xi \right\}. \quad (6)$$

The displacement traveled by the punch is given by

$$\omega_0 = \omega|_{\xi=\lambda} = \frac{\varphi}{\beta} \left\{ \frac{[\cosh(\beta\lambda)-1]^2}{\sinh(\beta\lambda)} - \sinh(\beta\lambda) + \beta\lambda \right\}. \quad (7)$$

The average membrane stress is given by ([8,9]<sup>1</sup>)

$$N = \frac{Eh}{\lambda l(1-\nu^2)} \int_0^{l-c} \frac{1}{2} \left( \frac{dw}{dx} \right)^2 dx. \quad (8)$$

Substituting (6) into (8), the normalized load takes the form of

$$\varphi = \frac{\beta^2}{\sqrt{6}} \frac{\cosh(\beta\lambda/2)}{\left[ 1 + \frac{\cosh(\beta\lambda)}{2} - \frac{3 \sinh(\beta\lambda)}{2\beta\lambda} \right]^{1/2}}. \quad (9)$$

The constitutive relation  $\varphi(\omega_0)$  can be found analytically for a fixed  $\lambda$  by eliminating  $\beta$  from (7) and (9). The exact expression is not given here though it can be obtained by software such as MATHEMATICA and will cover a number of pages. We choose to show  $\varphi(\omega_0)$  in Fig. 2 as a parametric plot for various values of  $\lambda$ , using  $\beta$  as the varying parameter. The limiting cases of plate and membrane are shown as dashed lines. As we suggested earlier ([9]),  $\varphi(\psi_0)$  can be written as  $\varphi \propto \omega_0^n$ , where  $n$  is defined to be

<sup>1</sup>In article 2 of reference [8], the membrane stress is computed for the cylindrical bending of uniformly loaded rectangular plates with simply supported edges (Eq. (5) in [8]). The same expression is valid in the present model.

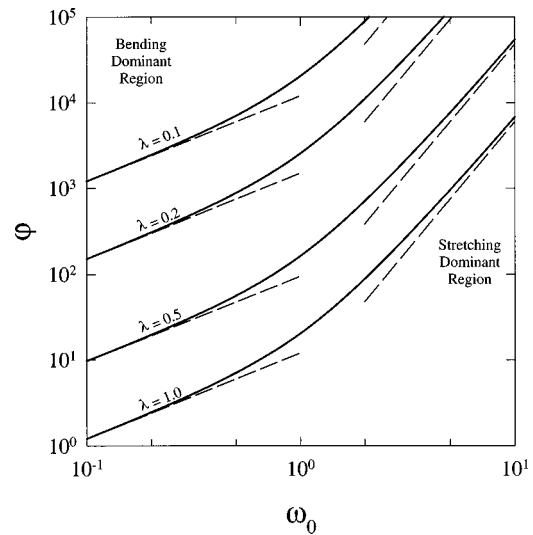


Fig. 2 Constitutive relations for various  $\lambda$  without delamination (solid lines) and the limiting cases of pure bending and stretching (dotted lines). The gradient  $n=1$  in the bending dominant region and becomes 3 in the stretching dominant region. An intermediate transition zone with  $1 \leq n \leq 3$  lies between  $0.1 \leq \omega_0 \leq 10$ .

$$n = \frac{d(\log \varphi)}{d(\log \omega_0)}$$

$$= [\beta\lambda - 2 \tanh(\beta\lambda/2)]$$

$$\times \left[ \frac{36\beta\lambda \cosh(\beta\lambda/2) + 6(\beta\lambda \cosh(3\beta\lambda/2) + (2\beta^2\lambda^2 - 21)\sinh(\beta\lambda/2) - 21 \sinh(3\beta\lambda/2))}{(4\beta^2\lambda^2 - 6)\cosh(\beta\lambda/2) + (2\beta^2\lambda^2 + 6)\cosh(3\beta\lambda/2) + (3\beta\lambda + 2\beta^3\lambda^3)\sinh(\beta\lambda/2) - 9\beta\lambda \sinh(3\beta\lambda/2)} \right] \quad (10)$$

such that  $1 \leq n \leq 3$ , with the lower and upper limits corresponding to platelike and membranelike behavior, respectively.

For a thick and stiff plate,  $\omega(\xi)$  is derived by putting  $\beta=0$  in (2) and integrating with respect to  $\xi$  twice while keeping (4) and (5). Thus, (6) and (7) become

$$\omega = \frac{\varphi}{2} \left( \frac{\lambda \xi^2}{2} - \frac{\xi^3}{3} \right) \text{ or } w = 6w_0 \left( \frac{\lambda x^2}{2l^2} - \frac{x^3}{3l^3} \right) \quad (11)$$

$$\omega_0 = \frac{\varphi \lambda^3}{12} \text{ or } w_0 = \frac{Fl^3 \lambda^3}{24Dh}, \quad (12)$$

respectively, identical to the classical elastic solution ([8,9]). Equation (12) implies that  $n=1$  and  $\varphi \propto \omega_0$  as expected classically. Here the punch displacement is small compared to the film thickness ( $\omega_0 \leq 1$ ) and bending is dominant. As for a thin and flexible membrane, substitution of  $\beta \rightarrow \infty$  reduces (9) to  $\varphi = \beta^3/6^{1/2}$ , and (6) and (7) become

$$\omega = \left( \frac{\varphi}{\beta^2} \right) \xi \text{ or } w = \frac{w_0}{\lambda l} x \quad (13)$$

$$\varphi = \left( \frac{6}{\lambda^3} \right) \omega_0^3 \text{ or } F = \left( \frac{Eh}{1-\nu^2} \right) \left( \frac{w_0}{\lambda l} \right)^3, \quad (14)$$

respectively. Alternatively, (13) and (14) can also be obtained by putting  $\beta \rightarrow \infty$  in (2) and ignoring both  $(d^2\omega/d\xi^2)$  and  $m_0$ . Equation (14) implies that  $n=3$  and  $\varphi \propto \omega_0^3$  ([9,10]). Here  $\omega_0$  is large ( $\omega_0 \gg 1$ ) and stretching prevails over bending. Note that (11) to (14) are consistent with the V-peel configuration where the exter-

nal load is applied in a central line and  $\lambda=1$  [9,11]. The film is now so flexible that virtually no bending moment exists even at the contact edges, resulting in a nonzero debonding angle that violates the boundary condition (4) in the limit.

There is one shortcoming of the above theory. When the entire punch surface is in contact with the film ( $\lambda=0$ ), there is no free-hanging film to store up the elastic energy. There are two seemingly nonphysical consequences: (i) a singular local membrane stress  $\beta$  and (ii) an infinite  $\varphi$  to maintain equilibrium. The ambiguity can be removed by placing the root of rotation at the contact interface, instead of the midplane of the film ([12]). The local stress will then become a function of distance from the contact corner and will be governed by the stress intensity factor ([13]), a subject that is beyond the scope of this paper. The severity of the problem is relaxed when the punch is narrower than the film span, i.e., the initial  $\lambda$  is nonzero.

**2.2 Constitutive Relation With Delamination.** When the punch displacement exceeds a certain threshold, delamination drives into the interface from the two opposite edges shrinking the contact area by  $2l \delta\lambda$ . The mechanical energy release rate (in  $\text{J.m}^{-2}$ ),  $G$ , under a fixed load configuration (constant  $F$ ) is defined to be ([13])

$$G = \frac{1}{2l} \left( \frac{\partial U_c}{\partial \lambda} \right)_{F,n} \quad (15)$$

where the complementary energy is

$$U_c = \int w_0 dF = \frac{n}{1+n} F w_0 \quad (16)$$

using the relation  $\varphi \propto \omega_0^n$ . Defining a normalized quantity  $\Gamma = G(Dh^2/l^4)^{-1}$ , substitution of (7) and (16) into (15) yields

$$\Gamma = \frac{1}{2} \left( \frac{n}{1+n} \right) \varphi \left( \frac{\partial \omega_0}{\partial \lambda} \right) = \frac{1}{2} \left( \frac{n}{1+n} \right) \varphi^2 \left[ \frac{\tanh^2(\beta\lambda/2)}{\beta^2} \right]. \quad (17)$$

At equilibrium,  $G = \gamma$  with  $\gamma$  the adhesion energy of the punch-film interface, or, equivalently,  $\Gamma = \Gamma^* = \gamma(Dh^2/l^4)^{-1}$ . Each  $\Gamma^*$  is therefore determined by a pair of  $\beta$  and  $\lambda$ . The  $\beta$ - $\lambda$  plot can be conformally mapped into a  $\varphi$ - $\omega_0$  space using (7) and (9).<sup>2</sup> Note that an analytical expression for  $\Gamma(\varphi, \omega_0)$  is possible, but a numerical approach is sought.

In the limiting case of a plate, substituting (12) into (16) and (15), or simply putting  $\beta \rightarrow 0$  into (17), four equivalent expressions can be derived:

$$\Gamma = \frac{3}{2} \left( \frac{\varphi \omega_0}{\lambda} \right) = \frac{1}{8} (\varphi \lambda)^2 = 18 \frac{\omega_0^2}{\lambda^4} = \left( \frac{9}{32} \right)^{1/3} (\varphi^2 \omega_0)^{2/3}. \quad (18)$$

At equilibrium ( $\Gamma = \Gamma^*$ ),  $\omega_0 \propto \lambda^2$  and  $\varphi \propto \omega_0^{-1/2}$ , so that as the punch displacement increases, delamination grows and the applied force diminishes from a maximum. In the limit of  $\lambda=1$ ,  $\Gamma = G(Fw_0/2\lambda l)^{-1} = 3/2$ , which is consistent with a V-peel test under pure bending ([19]). Similarly, in a membrane, substitution of (14) into (16) and (15) yields

$$\Gamma = \frac{3}{4} \left( \frac{\varphi \omega_0}{\lambda} \right) = \left( \frac{9}{128} \right)^{1/3} \varphi^{4/3} = \frac{9}{2} \left( \frac{\omega_0}{\lambda} \right)^4. \quad (19)$$

At equilibrium,  $\varphi$  remains constant regardless of the delamination length. In the limit of  $\lambda=1$ ,  $\Gamma = G(Fw_0/2\lambda l)^{-1} = 3/4$ , which is consistent with a V-peel test under pure stretching ([9,14]) and the classical “pull-off” test ([11]).

Figure 3 shows the constitutive relation  $\varphi(\omega_0)$  for various  $\Gamma^*$  (solid lines), and the plate and membrane limits (dashed lines).

<sup>2</sup>For a chosen value of  $\Gamma$ ,  $\beta$  can be found numerically for a fixed  $\lambda$ . With such  $\beta$ , a pair of  $\varphi$  and  $\omega_0$  are found. The entire function  $\varphi(\omega_0)$  can thus be traced for a fixed  $\Gamma$  by iterating a range of  $\lambda$ .

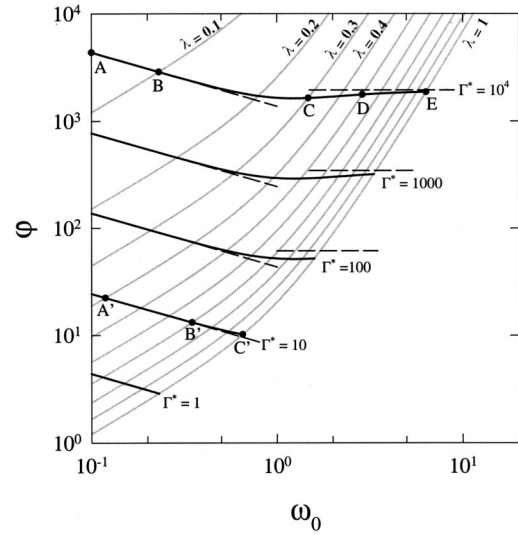


**Fig. 3 Constitutive relations for various  $\lambda$  with delamination (dark solid lines) and without delamination (gray lines). The dotted lines represent the bending and stretching limits. As delamination propagates, the curve ABCDE cuts through all gray curves of different  $\lambda$ . The theoretical pure bending (monotonic decreasing) and pure stretching (horizontal) limits are shown as dashed lines.**

Consider the case where  $\Gamma^* = 10^4$  (curve ABCDE). Starting with point A ( $\lambda=0$ ), delamination propagates into the interface as the punch moves upwards. Along section AB, the film behaves as a plate until point B ( $\lambda=0.1$ ) where it begins to deviate. The section BCD denotes a bending to stretching transition and comprises a local minimum. From C to E, the delamination becomes progressively more membranelike and the slope gradually tends to zero. A line contact ( $\lambda=1$ ) is finally reached at E, before a complete detachment of the punch from the film, or a “pull-off.”<sup>3</sup> Another example is noted for  $\Gamma^*=10$  (curve A'B'C'). Beginning from  $\lambda=0$ , the delamination passes through A' ( $\lambda=0.4$ ), then B' ( $\lambda=0.7$ ), and finally reaches pull-off at C' ( $\lambda=1$ ). The film behaves like a plate throughout the delamination process, with virtually no trace of stretching. Thus for all  $\Gamma^*$  below 10, the film is essentially platelike and  $\varphi(\omega_0)$  is always monotonically decreasing. It is interesting to note that  $\lambda=1$  at “pull-off” always. Figure 4 shows the critical force  $\varphi^\dagger$  and punch displacement  $\omega_0^\dagger$  at pull-off as monotonically increasing functions of  $\Gamma^*$ . The limiting pull-off parameters are such that for a plate, (18) requires

$$F^\dagger = \left[ \frac{8E\gamma}{3l^2(1-\nu^2)} \right]^{1/2} h^{3/2} \quad (20)$$

$$w_0^\dagger = \left[ \frac{2l^4\gamma(1-\nu^2)}{3E} \right]^{1/2} \frac{1}{h^{3/2}} \quad (21)$$

and for a membrane, (19) requires

$$F^\dagger = \left[ \frac{512E\gamma^3}{27(1-\nu^2)} \right]^{1/4} h^{1/4} \quad (22)$$

$$w_0^\dagger = \left[ \frac{8l^4\gamma(1-\nu^2)}{3E} \right] \frac{1}{h^{1/4}}. \quad (23)$$

<sup>3</sup>In the literature, “pull-off” usually refers to the event of complete separation under a fixed load configuration. In this paper, we adopt a loose definition to include both fixed load and fixed grips.



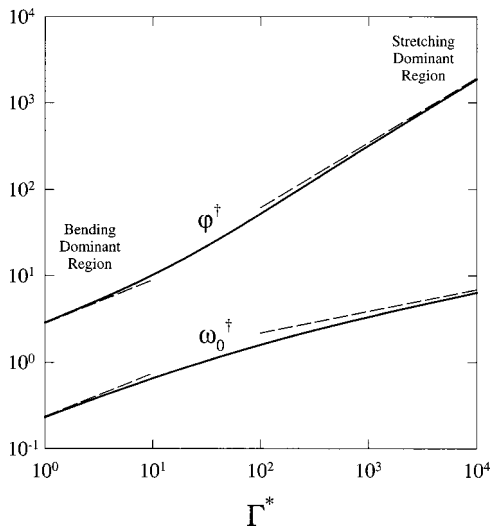


**Fig. 4** The normalized critical force  $\varphi^\dagger$  and normalized punch displacement  $\omega_0^\dagger$  at “pull-off” as functions of a normalized adhesion strength  $\Gamma^*$ , along with the pure bending and pure stretching limits (dashed lines).

Thus,  $F^\dagger$  is always a monotonically increasing function of  $h$  while  $w_0^\dagger$  is monotonically decreasing.

### 3 Experiment

The aim of the following experiment was to demonstrate the delamination mechanics, rather than to measure the interface energy. As a simple illustration, a model interface was constructed by adhering a commercially available pressure-sensitive adhesive (PSA) tape onto an aluminum plate/punch. PSA was used because of the ease in sample preparation. Some remarks are worth noting. First it is well known that the actual interface energy of a PSA is small compared to the interfacial resistance against delamination growth ([15,16]). In the following experiments and analysis,  $\gamma$  (or  $\Gamma^*$ ) refers to the latter rather than the former. Secondly, the tape was a “composite” with a backing polymer sheet coated with a thin adhesive layer. However, since the elastic energy was stored mainly in the polymer film instead of the adhesive, and that the interlayer adhesion in a multilayer film (see later) was much stronger than the punch-film interface, the composite characteristics was ignored.

A model interface was fabricated as follows (Fig. 1). A rectangular opening (50 mm  $\times$  65 mm) was machined into an aluminum plate (100 mm  $\times$  150 mm and 6 mm thick). A sticky tape of 5 mm wide and 50  $\mu$ m thick, with an elastic modulus of  $700 \pm 140$  MPa and Poisson’s ratio of 0.3, was then adhered to the back of the substrate. A polished flat aluminum punch (49.2 mm  $\times$  52 mm) was brought into adhesive contact with the film via the rectangular opening. The small ratio of the film width to the substrate opening (1:10) was intentional so as to minimize the effects due to the anticlastic geometry of the front. The punch was then pulled away vertically from the film in a fixed grips configuration at cross-head speeds of  $v=1, 2$ , and 5 mm.min $^{-1}$ . A universal testing machine recorded the load as a function of the punch displacement. Experiments were repeated for multilayer films to investigate the effects due to changes in thickness. The adhesive strength was measured by a standard 90 deg peel test to be  $\gamma=60 \pm 10$  J.m $^{-2}$ . For comparison purposes, a “weak” interface with an adhesion strength much less than 60 J.m $^{-2}$  was fabricated by spraying the adhesive side of the film with mould release agent before adhesion.

Typical data of  $F(w_0)$  are shown in Fig. 5 for (a) 1, 2, and 3 layers at  $v=1$  mm.min $^{-1}$ , (b) single layer at  $v=1, 2$  and 5

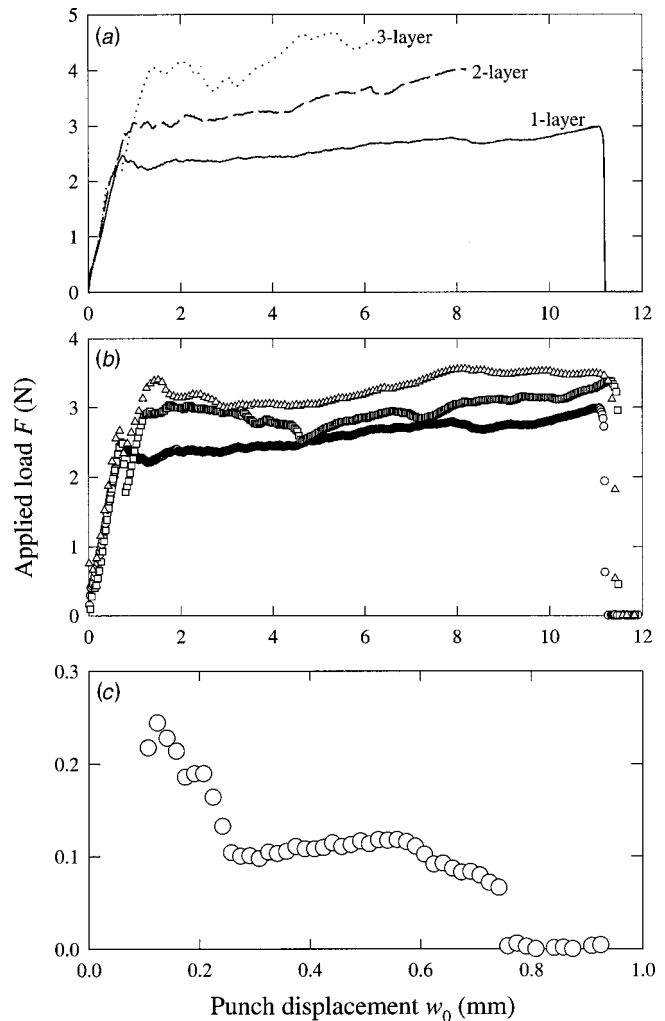


**Fig. 5** Typical data of  $F(w_0)$  for (a) cross-head speed of 1 mm.min $^{-1}$  and 1 (solid curve), 2 (dashed curve) and 3 (dotted curve) layers of film, (b) single layer at cross-head speed of 1 mm.min $^{-1}$  (circles), 2 mm.min $^{-1}$  (squares), and 5 mm.min $^{-1}$  (triangles) and (c) single layer at cross-head speed of 1 mm.min $^{-1}$  for a weak interface. Note the change of scale in (c).

mm.min $^{-1}$ , and (c) single layer at  $v=1$  mm.min $^{-1}$  for the weak interface. In Figs. 5(a) and 5(b), as the punch moved away,  $F$  increased before reaching a plateau. The fluctuation in  $F$  was the result of surface roughness, air pockets inevitably trapped at the interface, antielastic geometry of the crack front, and stick-slip behavior during crack propagation. The plateau force was larger in case of a thicker film, but was essentially independent of the cross-head speed. The minor difference due to different speeds could be the consequence of viscoelastic behavior of the polymer film. The strong interface led to a  $\omega_0^\dagger$  and  $\Gamma^*$  in the order of 100 and  $10^9$ , respectively, which was well within the stretching dominant region and the membrane limit is sufficient to account for the delamination process (c.f. (19)). On the other hand, in Fig. 5(c), delamination in the weak interface showed a comparatively large initial  $F$  that decreased gradually towards a plateau prior to pull off. Here  $\omega_0$  and  $\Gamma^*$  were in the order of  $10^0$  and  $10^6$ , respectively, which fell in the bending-stretching transition where an initial decrease in external load was expected.

A pull-off event with a line contact was observed in all measurements. Figures 6(a) and 6(b) show the measured  $F^\dagger$  and  $w_0^\dagger$  as functions of film thickness, respectively. It was apparent that both  $F^\dagger$  and  $w_0^\dagger$  were independent of the cross-head speed and at thicker film led to a lower  $F^\dagger$  and a higher  $w_0^\dagger$ . Theoretical curves



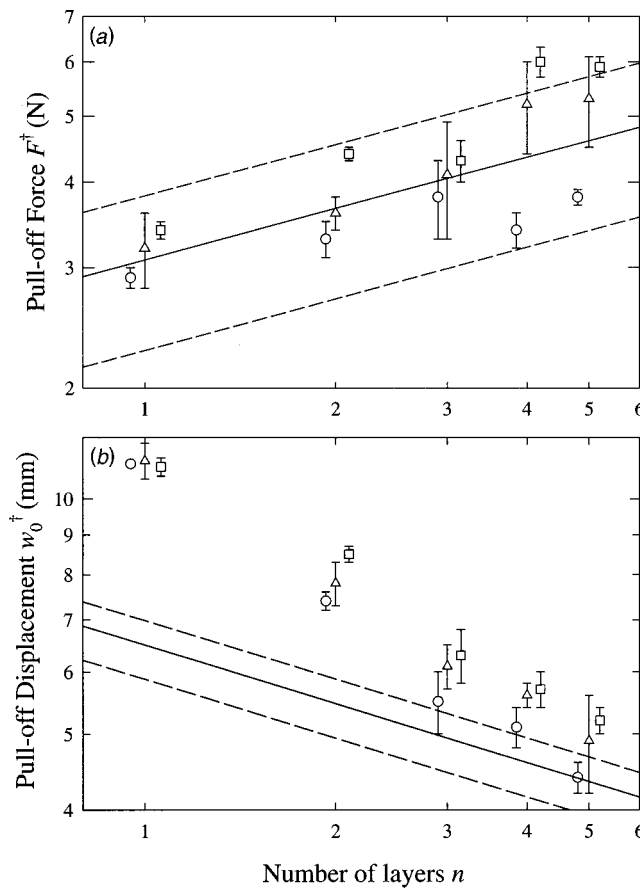


**Fig. 6 (a) The measured pull-off force  $F^*$  and (b) pull-off punch displacement  $w_0^*$  as a function of number of film layers in log-log plots for cross head speeds of 1 mm.min<sup>-1</sup> (circles), 2 mm.min<sup>-1</sup> (triangles) and 5 mm.min<sup>-1</sup> (squares). The theoretical curves with  $\gamma=60 \text{ J.m}^{-2}$  (solid lines), and the upper and lower limits (dashed lines) for  $\Delta\gamma=10 \text{ J.m}^{-2}$  are also shown.**

according to (22) and (23) with  $\gamma=60 \pm 10 \text{ J.m}^{-2}$  were also shown for comparison. A significant deviation from theory was noted in  $w_0^*$ , especially for a single layer film. This could be the result of a slight plastic yielding of the film. Yielding was minimal in thick films.

#### 4 Discussion

There are some distinct differences between our new model and the classical adherence of a flat punch on an elastic half-space studied by Kendall [4] and Maugis [5]. When a flat rigid punch is pulled away from a continuum substrate, an abrupt destruction of the entire interface occurs once a critical external load is reached. On the other hand, in a punch-film configuration, a gradual and stable shrinkage of the contact area is predicted until complete detachment. The underlying reason is the presence of a stress field induced by the punch on the continuum substrate in the former, and its replacement by bending/stretching of the film in the latter. The damage done to the adhered as a result of pull-off is expected to be minimal in a constrained film because of the zero contact area at pull-off. The rule is not exclusive, however. For instance, in case of a constrained film adhered onto an axisymmetric flat punch ([7]), a finite residual contact circle at pull-off is expected, alluding to the similar prediction by the JKR theory.

The new model has an impact in many biological systems. For instance, a capsule encapsulated by a thin membrane (e.g., a red blood cell) adheres itself to a substratum (e.g., a blood vessel wall), and detaches itself in the presence of internal forces (e.g.,

cell locomotion) or external forces (e.g., osmotic pressure) ([17]). Here the roles played by the film and the punch are juxtaposed, in that, the punch (or substratum) is now stationary while the membranous cell in motion moves into and out of contact. When a cell comes into adhesive contact with a rigid substrate, the cell wall “stretches” itself in the noncontact area and “bends” towards the contact circle. Bruinsma [18], Albersdörfer et al. [19], and Kloboucek et al. [20] discussed such observation and showed that the cell profile immediately outside the contact circle was given by

$$w(x) = \left( \frac{\lambda}{R_c} \right) \left\{ x - \lambda \left[ 1 - \exp \left( - \frac{x}{\lambda} \right) \right] \right\} \quad (24)$$

with  $\lambda$  the capillary length and  $R_c$  the radius of curvature. In close scrutiny, (24) is consistent with and in fact equivalent to (6). Both (6) and (24) comprise a linear term corresponding to stretching and an exponential term (replacing all hyperbolic functions in (6) by exponential) due to bending. It is important to note that the theoretical profile is correct only in a one-dimensional rectangular contact but may not be applicable to a two-dimensional axisymmetric situation (e.g., a spherical capsule). In fact, we showed earlier that the contact mechanics is quite different in a case of a circular punch on a thin flexible constrained film ([7]).

#### 5 Conclusion

We have derived the adhesive contact mechanics of a rectangular flat punch on a constrained film, which was demonstrated by the simple experiment of sticky tapes adhered onto an aluminum substrate. A pull-off event is expected when the contact area shrinks down to a line and the external force reaches a critical threshold. This new model should be used in adherence between a thin film and a solid, instead of the classical punch-elastic half-space theory. Our new model is expected to have implications in thin-walled biological capsules.

#### Acknowledgment

This research was supported by NTU Academic Research Fund #RG 48/99. The authors are grateful to Dr. Lam Yee Cheong, Dr. Kuo-Kang Liu, and Dr. Kin Liao of NTU for discussions, and to the referees for useful suggestions.

#### References

- [1] Hertz, H., 1896, *Miscellaneous Papers by H. Hertz*, Jones and Schott (eds.), Macmillian, London.
- [2] Boussinesq, J., 1885, *Application des potentiels à l'étude de l'équilibre et du mouvement des solides élastiques*, Gauthier-Villars, Paris.
- [3] Johnson, K. L., Kendall, K., and Roberts, A. D., 1971, “Surface Energy and the Contact of Elastic Solids?” *Proc. R. Soc. London, Ser. A*, **324**, pp. 301–313.
- [4] Kendall, K., 1971, “The Adhesion and Surface Energy of Elastic Solids,” *J. Phys. D*, **4**, pp. 1186–1195.
- [5] Maugis, D., 2000, *Contact, Adhesion and Rupture of Elastic Solids*, Springer, New York.
- [6] Plaut, R. H., Suhrman, S., Dillard, D. A., Williams, B. E., and Watson, L. T., 1999, “Deflections and Buckling of a Bent Elastica in Contact With a Flat Surface,” *Int. J. Solids Struct.*, **36**, pp. 1209–1229.
- [7] Wan, K.-T., 2001, “Adherence of an Axial Symmetric Flat Punch on a Thin Flexible Membrane,” *J. Adhes.*, **75**, pp. 369–380.
- [8] Timoshenko, S. P., and Woinowsky-Krieger, S., 1959, *Theory of Plates and Shells*, 2nd Ed., McGraw-Hill, New York.
- [9] Wan, K.-T., 1999, “Fracture Mechanics of a V-Peel Adhesion Test—Transition From a Bending Plate to a Stretching Membrane,” *J. Adhes.*, **70**, pp. 197–207.
- [10] Wan, K.-T., and Liao, K., 1999, “Measuring Mechanical Properties of Thin Flexible Films by a Shaft-Loaded Blister Test,” *Thin Solid Films*, **352**, pp. 167–172.
- [11] Gent, A. N., and Kaang, S., 1986, “Pull-Off Forces for Adhesive Tapes,” *J. Appl. Polym. Sci.*, **32**, pp. 4689–4700.
- [12] Kinloch, A. J., Lau, C. C., and Williams, J. G., 1994, “The Peeling of Flexible Laminates,” *Int. J. Fract.*, **66**, pp. 45–70.
- [13] Atkins, A. G., and Mai, Y. W., 1985, *Elastic and Plastic Fracture*, Ellis Horwood/John Wiley, Chichester, UK.
- [14] Williams, J. G., 1997, “Energy Release Rates for the Peeling of Flexible Membranes and the Analysis of Blister Tests,” *Int. J. Fract.*, **87**, pp. 265–288.

- [15] Kinlock, A. J., 1987, *Adhesion and Adhesives: Science and Technology*, Chapman and Hall, New York.
- [16] Skeist, I., 1977, *Handbook of Adhesives*, Van Nostrand Reinhold, New York.
- [17] Liu, K. K., and Wan, K.-T., 2001, "A New Model to Characterize Cell-Substrate Adhesion in the Presence of Osmosis," *Med. Biol. Eng. Comput.*, **38**, pp. 690–691.
- [18] Bruinsma, R., Goulian, M., and Pincus, P., 1994, "Self Assembly of Membrane Junctions," *Biophys. J.*, **67**, pp. 746–750.
- [19] Albersdörfer, A., Feder, T., and Sachmann, E., 1997, "Adhesion-Induced Domain Formation by Interplay of Long-Range Repulsion and Short-Range Attraction Force: A Model Membrane Study," *Biophys. J.*, **73**, No. 1, pp. 245–257.
- [20] Kloboucek, A., Behrisch, A., Faix, J., and Sackmann, E., 1999, "Adhesion-Induced Receptor Segregation and Adhesion Plaque Formation: A Model Membrane Study," *Biophys. J.*, **77**, pp. 2311–2328.

# Adherence of an Axisymmetric Flat Punch Onto a Clamped Circular Plate: Transition From a Rigid Plate to a Flexible Membrane

K.-T. Wan

Department of Engineering  
Science and Mechanics,  
Virginia Polytechnic Institute  
and State University,  
Norris Hall 106, Mail Code 0219,  
Blacksburg, VA 24061  
e-mail: kwan@vt.edu

*A clamped circular film is adhered to a rigid cylindrical punch. An external force pulls the punch away causing delamination at the punch-plate interface. The deflections of the film are discussed for a range of film thickness and stiffness, detailing the continuous transition from a plate under bending to a membrane under stretching. An equilibrium theory of delamination mechanics is derived based on an energy balance. A complete separation at the punch-film interface, or the "pull-off" event, is predicted when the contact circle shrinks to approximately 0.18 of the film diameter. The values and trends, presented in dimensionless normalized form here, should have implications in biological and colloidal sciences in relation to thin-walled capsules and in electronics in relation to thin encapsulating films. [DOI: 10.1115/1.1433477]*

## 1 Introduction

Thin film adhesion is an important subject in biology ([1]), electronics ([2]), and colloids ([3]). Most up-to-date studies are based on the celebrated Johnson-Kendall-Roberts (JKR) adhesion theory and its various modified forms ([4,5]), which proved to be very useful in describing the adhesive contact between a rigid punch and an elastic half-space ([6–8]). One shortcoming is that the theory is confined to rigid solid bodies and therefore the application to bodies comprising thin flexible films is doubtful. For instance, adhesion of membranous biological capsules does not develop the Hertzian stress field at the contact circle required by the JKR theory (e.g., an erythrocyte cell with a wall thickness of 100 Å and elastic modulus of roughly 1.0 MPa adhered onto a rigid substrate ([9]), and formation of adhesion plaque in cell locomotion ([10])). A new adhesive contact mechanics is therefore needed. We earlier constructed a one-dimensional model for the adhesion between a rigid rectangular punch and a thin film of different thickness ([11]). A two-dimensional model was also derived for the adhesion between an axisymmetric punch and a membranelike film under pure stretching, where a "pull-off" event was predicted when the contact circle shrank to roughly 0.19 of the film diameter ([12]). In this paper, we attempt to re-derive the two-dimensional model, but relax the constraint of pure membrane. Films spanning a range of thickness and stiffness, and the resulting mixed bending and stretching modes of elastic deformation will be considered.

Historically, large elastic deformation of circular plate was studied extensively: (i) clamped plates under uniform pressure, as discussed in the classical works by Hencky, Nadai, and Way (all summarized in Timoshenko and Woinowsky-Krieger [13]) and more recent studies by Mansfield [14], Sheplak [15], and Wan [16]; (ii) clamped plates under central point load, as discussed by

Malyshev [17], Williams [18], Chia [19], and Wan [20]; and (iii) clamped annular plates subjected to axisymmetrical line load around a central hole, where series or numerical solutions are available ([19,21]). It is, however, difficult to manipulate series solutions to formulate analytical adhesion mechanics. In this paper, we will derive an exact analytical model based on linear elasticity, an average membrane stress approximation and a simple energy balance, similar to the various forms of blister tests we derived earlier ([16,22–24]). The exact but nonlinear extension will be left for future work.

## 2 The Constitutive Relation Without Delamination

Figure 1 shows a thin isotropic film adhered onto a rigid plate with a central circular opening of radius  $a$ . The film possesses a flexural rigidity  $D = Eh^3/12(1-\nu^2)$  with an elastic modulus,  $E$ , Poisson's ratio,  $\nu$ , and thickness,  $h$ . A cylindrical flat punch of radius,  $a$ , is brought into an adhesive contact with the exposed film via the hole. An external force,  $F$ , is applied vertically to pull the punch a distance  $w_0$  away from the film. The elastic membrane stress thus developed in the film causes an axisymmetric delamination to drive into the punch-film interface. The contact circle of radius,  $c$ , shrinks until the punch completely separates from the film at "pull-off."<sup>1</sup> For simplicity, the midplane of the film is taken to be the neutral plane in the following discussion.

The constitutive relation without delamination is derived as follows. Within the contact circle ( $r < c$ ), the film profile  $w(r)$  conforms to the planar punch geometry. In the noncontact annulus ( $c \leq r \leq a$ ),  $w$  is governed by the von Karman plate theory for large deflection ([13]):

$$\frac{d}{dr} \left[ \frac{1}{r} \frac{d}{dr} \left( r \frac{dw}{dr} \right) \right] = \frac{1}{D} \left[ \frac{F}{2\pi r} + N_r \left( \frac{dw}{dr} \right) \right] \quad (1)$$

$$\frac{d}{dr} (N_r + N_t) + \frac{Eh}{2r} \left( \frac{dw}{dr} \right)^2 = 0 \quad (2)$$

<sup>1</sup>Here "pull-off" refers to either fixed load or fixed grips, as we suggested earlier ([11]).

Contributed by the Applied Mechanics Division of THE AMERICAN SOCIETY OF MECHANICAL ENGINEERS for publication in the ASME JOURNAL OF APPLIED MECHANICS. Manuscript received by the ASME Applied Mechanics Division, February 12, 2001; final revision, October 15, 2001. Associate Editor: K. Ravi-Chandar. Discussion on the paper should be addressed to the Editor, Prof. Lewis T. Wheeler, Department of Mechanical Engineering, University of Houston, Houston, TX 77204-4792, and will be accepted until four months after final publication of the paper itself in the ASME JOURNAL OF APPLIED MECHANICS.

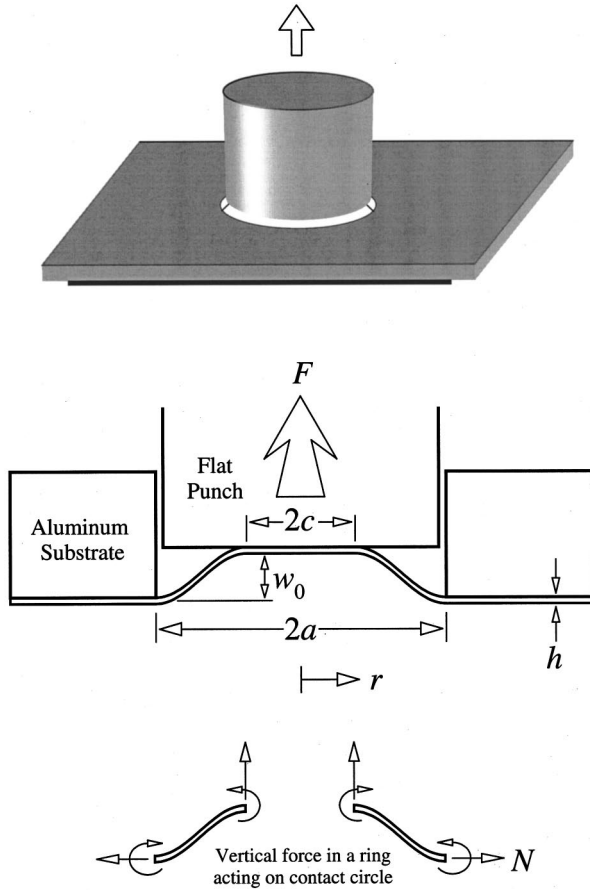


**Fig. 1 Sketch of a circular cylindrical flat punch adhered onto a thin membrane constrained at the circular rim. A free-body diagram showing the external force, bending moments and tensile membrane stress.**

$$N_t = \frac{d}{dr}(rN_r) \quad (3)$$

where  $N_r = \sigma_r/h$  and  $N_t = \sigma_t/h$  are, respectively, the radial and tangential membrane stresses. The set of nonlinear equations can only be solved numerically ([19]). To obtain an analytical solution, we assume  $N_r \approx N_t \approx N$  for small strain so that the new configuration is the same as exerting an in-plane tensile load around the plate circumference. Now, (1) only is to be solved, (2) is satisfied in the first approximation since  $dw/dr \approx 0$ , and (3) is automatically satisfied. It is convenient to normalize (1) by the dimensionless quantities as follows:

$$\xi = \frac{r}{a}, \quad W = \frac{w}{h}, \quad \zeta = \frac{c}{a}, \quad \zeta^2 = \frac{\pi c^2}{\pi a^2},$$

$$\beta = \sqrt{\frac{Na^2}{D}}, \quad \varphi = \frac{Fa^2}{2\pi Dh}, \quad \theta = \frac{dW}{d\xi} = \frac{a}{h} \frac{dw}{dr}. \quad (4)$$

The parameter  $\beta$  denotes the important ratio of stretching stress to bending rigidity such that (i) when  $\beta \rightarrow 0$ , the film is platelike and allows bending only, and (ii) when  $\beta \rightarrow \infty$ , the film is membrane-like and allows stretching only. Therefore, (1) is recast as follows:

$$\xi^2 \frac{d^2 \theta}{d\xi^2} + \xi \frac{d\theta}{d\xi} - (1 + \beta^2 \xi^2) \theta = \varphi \xi \quad (5)$$

which is a linear modified Bessel differential equation. The boundary conditions are

$$\text{at } \xi=1, \quad \theta=0 \text{ and } W=0 \quad (6)$$

$$\text{at } \xi=\zeta, \quad \theta=0. \quad (7)$$

An exact solution to (5) is found to be

$$\theta = \varphi \left[ C_1 I_1(\beta \xi) + C_2 K_1(\beta \xi) - \frac{1}{\beta^2 \xi} \right] \quad (8)$$

where

$$C_1 = \frac{1}{\beta^2} \left[ \frac{K_1(\beta \zeta) - K_1(\beta)/\zeta}{I_1(\beta)K_1(\beta \zeta) - I_1(\beta \zeta)K_1(\beta)} \right] \quad (9)$$

$$C_2 = \frac{1}{\beta^2} \left[ \frac{I_1(\beta \zeta) - I_1(\beta)/\zeta}{K_1(\beta)I_1(\beta \zeta) - K_1(\beta \zeta)I_1(\beta)} \right]. \quad (10)$$

The functions  $I_i(x)$  and  $K_i(x)$  are the  $i$ th order of the first and second kind modified Bessel functions, respectively. The profile is found by integrating (8) with respect to  $\xi$  from  $\zeta$  to 1,

$$W = \frac{\varphi}{\beta^2} \{ C_1 \beta [I_0(\beta \xi) - I_0(\beta)] - C_2 \beta [K_0(\beta \xi) - K_0(\beta)] - \log \xi \}. \quad (11)$$

The central deflection, or punch displacement, is given by  $W_0 = W|_{\xi=\zeta}$ . Figure 2 shows the normalized profiles ( $W/W_0$ ) as a function of  $\xi$  for  $\zeta=0.1$  and  $\beta=1, 10, 100$ . Note that the slope at  $\xi=1$  and  $\xi=\zeta$  are always zero. The elastic energy is stored in the noncontact annulus of area  $\pi(a^2 - c^2) = \pi a^2(1 - \zeta^2)$ . The average membrane stress is found by ([11,25])

$$N = \frac{Eh}{a^2(1-\nu^2)} \times \frac{1}{1-\zeta^2} \int_c^a \frac{1}{2} \left( \frac{dw}{dr} \right)^2 r dr \quad (12)$$

or, in a normalized form,

$$\beta^2 = \frac{6}{1-\zeta^2} \int_{\zeta}^1 \theta^2 \xi d\xi. \quad (13)$$

Substituting (8) into (13),

$$\varphi = \beta^2 \left\{ \frac{1 - \zeta^2}{6[g(\beta) - g(\beta \zeta)]} \right\}^{1/2} \quad (14)$$

where

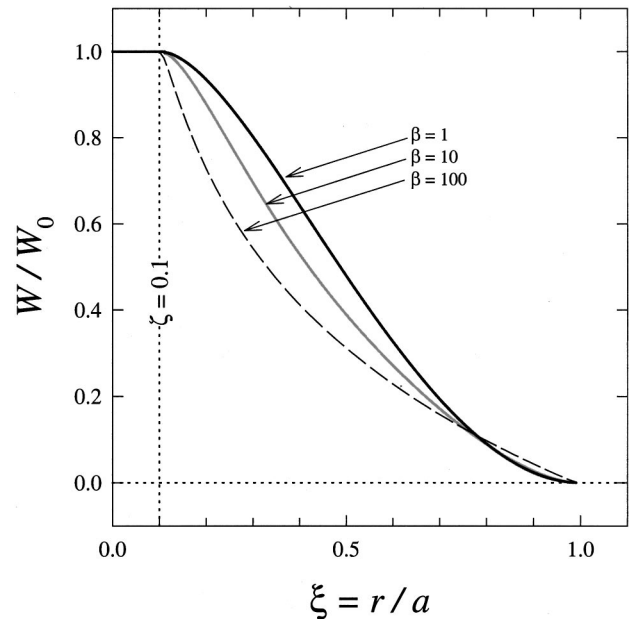


**Fig. 2 Film profiles for  $\zeta=0.1$  and  $\beta=1, 10, 100$ . Note that the gradients at the outer and inner circles are zero at small  $\beta$ .**

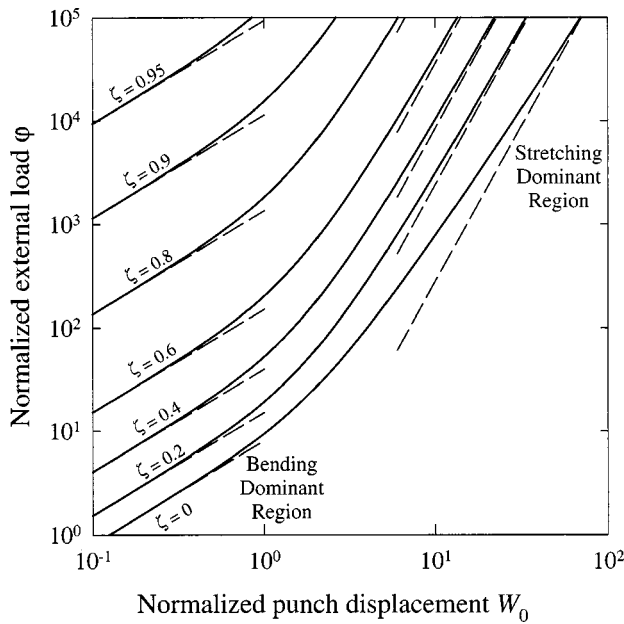


**Fig. 3 Constitutive relation  $\varphi(W_0)$  for various  $\zeta$  as indicated. The pure bending and pure stretching limits are shown as dashed lines. There exists an intermediate bending-stretching transition region.**

$$g(x) = C_1^2 \frac{x^2}{2} \left[ \left( 1 + \frac{1}{x^2} \right) I_1(x)^2 - \left( I_0(x) - \frac{I_1(x)}{x} \right)^2 \right] + C_2^2 \frac{x^2}{2} \left[ K_1(x)^2 - K_0(x)^2 - \frac{2K_0(x)K_1(x)}{x} \right] + \frac{1}{\beta^2} \log(x) - \frac{2}{\beta} [C_1 I_0(x) - C_2 K_0(x)] + 2C_1 C_2 \left\{ \frac{x^2}{2} [I_0(x)K_0(x) + I_1(x)K_1(x)] - x I_1(x)K_0(x) \right\}. \quad (15)$$

The constitutive relation  $\varphi(W_0)$  can now be found analytically by eliminating  $\beta$  from (11) and (14), though the very involved function is not given here explicitly.<sup>2</sup> Since both  $\varphi$  and  $W_0$  are functions of  $\beta$ , we choose to show  $\varphi(W_0)$  in Fig. 3 as a parametric plot by varying  $\beta$  for fixed  $\zeta$ , as suggested earlier in the one-dimensional model ([11]). For convenience, the function is recast into

$$\varphi \propto W_0^n \quad (16)$$

with

$$n = \frac{d(\log \varphi)}{d(\log W_0)} = \left( \frac{W_0}{\varphi} \right) \left[ \frac{\partial \varphi}{\partial \beta} \middle/ \frac{\partial W_0}{\partial \beta} \right]. \quad (17)$$

An analytical function  $n(W_0)$  can be derived by substituting (11) and (14) into (17), but is not given here. Figure 4 shows a parametric plot for  $n(W_0)$  by varying  $\beta$ .

Two limiting cases are of interest here. For a pure plate with a small  $W_0$  and  $\beta \sim 0$ , (5) becomes an equi-dimensional ordinary differential equation and (11) collapses to

$$W = W_0 \left[ \frac{(1 - \zeta^2)(1 - \zeta^2 + \zeta^2 \log \zeta^2) - \zeta^2 \log \zeta^2 (1 - \zeta^2 + \log \zeta^2)}{(1 - \zeta^2)^2 - \zeta^2 \log \zeta^2 \log \zeta^2} \right] \quad (18)$$

with

$$W_0 = \frac{f_1(\zeta)}{8} \varphi \quad (19)$$

where

$$f_1 = 1 - \zeta^2 - \frac{\zeta^2 \log \zeta^2 \log \zeta^2}{1 - \zeta^2}. \quad (20)$$

Here  $n=1$  and  $\varphi(W_0)$  is linear. Equation (19) is shown as dashed lines in the bending dominant region in Fig. 3. In the case of a central point contact with  $\zeta=0$  and  $f_1(\zeta)=1$ , (18) reduces to the familiar classical solution for a circular plate ([13]):

$$W = \frac{\varphi}{8} (1 - \zeta^2 + \zeta^2 \log \zeta^2). \quad (21)$$

For a pure membrane with a large  $W_0$  and  $\beta \rightarrow \infty$ , (11) reduces to

$$W = W_0 \left( \frac{\log \xi}{\log \zeta} \right) \quad (22)$$

where

$$W_0 = \left[ \frac{f_2(\zeta)}{24} \right]^{1/3} \varphi^{1/3} \quad (23)$$

with

$$f_2 = (1 - \zeta^2) \log \zeta^2 \log \zeta^2. \quad (24)$$

Now  $n=3$  and  $\varphi(W_0)$  becomes cubic. Equation (23) is shown as dashed lines in the stretching dominant region in Fig. 3. In the case of  $\zeta=0$ , the contact circle reduces to a point and the profile becomes an inverted cusp, in reminiscent of the shaft-loaded blister test ([23]). In the case of mixed bending and stretching in a film of intermediate thickness and stiffness, the transition zone spans roughly two decades from  $W_0=0.1$  to 10 and  $1 \leq n \leq 3$ .

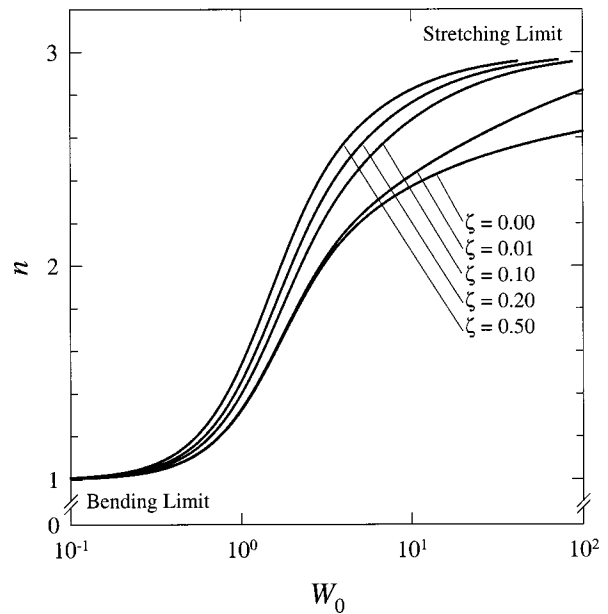


**Fig. 4 Gradient of the constitutive relation  $n$  as a function of  $W_0$  for various  $\zeta$  as indicated. When bending dominates at small  $W_0$ ,  $n \approx 1$ ; and when stretching prevails at large  $W_0$ ,  $n \approx 3$ . In the intermediate region ( $0.1 < W_0 < 10$ ),  $n$  lies between 1 and 3.**

<sup>2</sup>The lengthy solution can be found by MATHEMATICA and covers many pages.



### 3 Thermodynamics of Thin Film Adhesion/Delamination

The thermodynamics of delamination can be constructed as follows. The potential energy of the external load,  $U_P$ , the elastic energy stored in the elastic membrane,  $U_E$ , and surface energy of the contact circle,  $U_S$ , are defined as

$$U_P = -Fw_0 \quad (25)$$

$$U_E = \int Fdw_0 = \left(\frac{1}{n+1}\right)Fw_0 \quad (26)$$

$$U_S = -(\pi c^2)\gamma \quad (27)$$

using (16), where  $\gamma$  is the adhesion energy of the punch-film interface. Following the formulation suggested by Maugis [8], the enthalpy,  $H$ , for fixed load (constant  $\varphi$ ) and the internal energy,  $U$ , for fixed grips (constant  $W_0$ ) are given by

$$H = U_P + U_E + U_S \quad (28)$$

$$U = U_E + U_S. \quad (29)$$

Four normalized quantities are defined as follows:

$$\begin{aligned} \tilde{H} &= \frac{H}{(2\pi D h^2/a^2)}, \quad \tilde{U} = \frac{U}{(2\pi D h^2/a^2)} \\ \Gamma &= \frac{G}{(2D h^2/a^4)}, \quad \Gamma^* = \frac{\gamma}{(2D h^2/a^4)}. \end{aligned} \quad (30)$$

At delamination, a mechanical energy release rate is defined as

$$G = -\frac{\partial}{\partial(\pi c^2)}(U_P + U_E) \Big|_F = \frac{\partial U_E}{\partial(\pi c^2)} \Big|_{W_0} \quad (31)$$

or, in a normalized form,

$$\Gamma = -\left(\frac{n}{n+1}\right)\varphi \frac{\partial W_0}{\partial(\zeta^2)}. \quad (32)$$

Note that  $G$  (or  $\Gamma$ ) is identical in fixed grips and fixed grips configurations. The crack driving force, or “motif” ([8]), is defined the gradient of either  $\tilde{H}$  or  $\tilde{U}$  such that

$$(\Gamma - \Gamma^*) = \frac{\partial \tilde{H}}{\partial(\zeta^2)} = \frac{\partial \tilde{U}}{\partial(\zeta^2)}. \quad (33)$$

The contact circle expands when  $\Gamma < \Gamma^*$ , diminishes when  $\Gamma > \Gamma^*$ , and stays stationary at equilibrium when  $\Gamma = \Gamma^*$ . The stability of the system is determined by  $[\partial\Gamma/\partial(\zeta^2)]$  such that a negative quantity corresponds to a stable equilibrium, positive for an unstable equilibrium (i.e., a spontaneous crack growth), and zero for a neutral equilibrium. The delamination mechanics is illustrated by the two limiting cases as follows.

For a pure plate, substituting  $n=1$  into (28) and (29) so that

$$\tilde{H} = -\frac{f_1}{16}\varphi^2 - \zeta^2\Gamma^* \quad (34)$$

$$\tilde{U} = \frac{4}{f_1}W_0^2 - \zeta^2\Gamma^*. \quad (35)$$

Figure 5(a) shows a family of curves ( $\tilde{H}/\Gamma^*$ ) as a function of  $\zeta^2$ . Each curve possesses a local maximum, denoting an unstable equilibrium. The equilibrium curve is found by substituting (19) into (32),

$$\Gamma = -\frac{\varphi^2}{16} \left[ \frac{df_1}{d(\zeta^2)} \right] = \chi|_{\beta=0}(\varphi W_0) \quad (36)$$

with

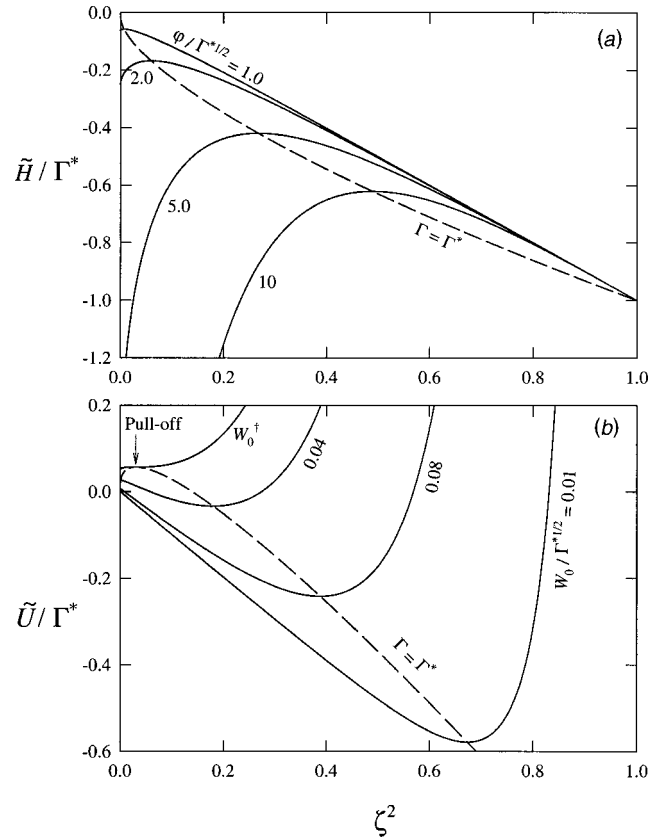


**Fig. 5** A pure plate. (a) The enthalpy ( $\tilde{H}/\Gamma^*$ ) as a function of contact area  $\zeta^2$  under fixed load for  $[\varphi/(\Gamma^*)^{1/2}] = 1, 2, 5$  and 10. The dashed line joining the maximum of each curve represents the unstable equilibrium. (b) The internal energy ( $\tilde{U}/\Gamma^*$ ) as a function of contact area  $\zeta^2$  under fixed grips for  $[W_0/(\Gamma^*)^{1/2}] = 0.01, 0.04, 0.08, 0.112761$ . The dashed line represents the stable delamination process. Pull-off occurs at the point of inflexion at  $W_0^\dagger$ .

$$\chi|_{\beta=0} = \frac{(1 - \zeta^2 + \log \zeta^2)^2}{2(1 - \zeta^2)(1 - 2\zeta^2 + \zeta^4 - \zeta^2 \log \zeta^2 \log \zeta^2)} \quad (37)$$

which is shown as a dashed curve in Fig. 5(a). If we now start with a full punch-film contact with  $\zeta = 1$  and slowly raise  $\varphi$  from zero, no delamination is expected since  $\tilde{H}$  is always a local minimum at  $\zeta = 1$ . Theoretically, it requires an infinite external load to initiate delamination. If any delamination is to occur, an energy barrier must be overcome. Any deviation from the unstable equilibrium will lead to either spontaneous increase of the contact area towards  $\zeta = 1$  or decrease towards  $\zeta = 0$ . Figure 5(b) shows a family of ( $\tilde{U}/\Gamma^*$ ) as a function of  $\zeta^2$ . Each curve possesses a local minimum, denoting a stable equilibrium. Substituting (32) into (33),

$$\Gamma = 4W_0^2 \left[ \frac{d(1/f_1)}{d(\zeta^2)} \right]_{W_0} \quad (38)$$

which is identical to (36). Starting with  $\zeta = 1$  at  $W_0 = 0$ , if we gradually raise  $W_0$ , the equilibrium point will move towards a decreasing  $\zeta$ , i.e., delamination. At  $W_0^\dagger = 0.112761(\Gamma^*)^{1/2}$  when  $\zeta^\dagger = 0.175754$  and  $\varphi^\dagger = 1.54548$ , the local minimum of  $\tilde{U}$  is replaced by a point of inflexion. Further increase of  $W_0$  results in a complete separation between the punch and the film, or “pull-off.”

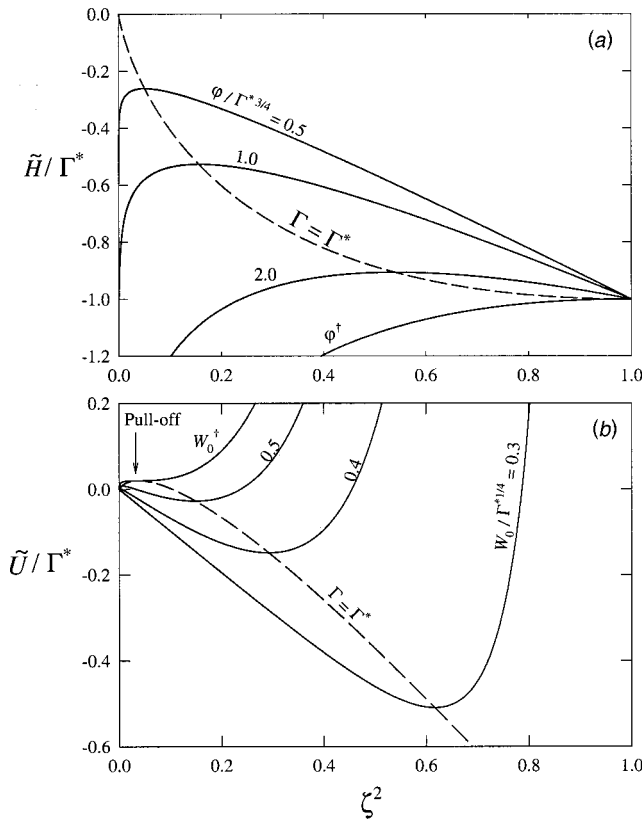


**Fig. 6** A pure membrane. (a) The enthalpy ( $\tilde{H}/\Gamma^*$ ) as a function of contact area  $\zeta^2$  under fixed load for  $[\varphi/(\Gamma^*)^{3/4}] = 0.5, 1.0, 2.0$  and 2.74636. The dashed line joining the maximum of every curve represents the unstable equilibrium. Spontaneous delamination occurs at  $\varphi^\dagger$ . (b) The internal energy ( $\tilde{U}/\Gamma^*$ ) as a function of contact area  $\zeta^2$  under fixed grips for  $[W_0/(\Gamma^*)^{1/4}] = 0.3, 0.4, 0.5$  and 0.562441. The dashed line represents the delamination process. Pull-off occurs at the point of inflexion at  $W_0^\dagger$ .

For a pure membrane under stretching only, Figs. 6(a) and 6(b) show  $(\tilde{H}/\Gamma^*)$  and  $(\tilde{U}/\Gamma^*)$ , respectively, as functions of  $\zeta^2$ . Substituting (23) into (32) to be

$$\Gamma = \chi|_{\beta \rightarrow \infty}(\varphi W_0) \quad (39)$$

with

$$\chi|_{\beta \rightarrow \infty} = \frac{2 - 2\zeta^2 - \zeta^2 \log \zeta^2}{4\zeta^2(1 - \zeta^2) \log(1/\zeta^2)} \quad (40)$$

which is identical to Williams's solution ([25]). Under a fixed load, the punch-film interface is stable at  $\zeta=1$  until  $\varphi$  reaches  $\varphi^\dagger = 2.74636(\Gamma^*)^{3/4}$ . At this point,  $\tilde{H}$  is a monotonically increasing function of  $\zeta$  and delamination occurs spontaneously until  $\zeta=0$ . Under fixed grips, delamination grows in a stable manner until "pull-off" happens at  $W_0^\dagger = 0.562441(\Gamma^*)^{1/4}$  when  $\zeta^\dagger = 0.194545$  and  $\varphi^\dagger = 0.413392(\Gamma^*)^{3/4}$ .

The thermodynamics of thin film delamination with intermediate film thickness and stiffness under mixed bending and stretching is similar to the above description and will be illustrated in the next section.

#### 4 The Constitutive Relation With Delamination

For a fixed  $\Gamma^*$ ,  $\varphi(W_0)$  with delamination can be found by substituting (11) into (32) to obtain  $\Gamma(\beta, \zeta)$  and then conformally mapped into a  $\varphi - W_0$  space using a method introduced earlier ([11]). To illustrate the theory,  $\Gamma^* = 10^4$  is chosen and the corre-

sponding  $\varphi(W_0)$  is shown in Fig. 7. Curve AMP represents the pure plate limit. Along the stable delamination branch AM, the punch moves gradually away from the substrate, while the external force decreases. At the "pull-off" point M at  $\zeta^\dagger$  where  $(dW_0/d\varphi) = 0$ , the delamination becomes spontaneous, resulting in a complete separation of the film from the punch, i.e., the "pull-off" event (c.f., Fig. 5(b)). Branch MP shows a positive  $(d\varphi/dW_0)$  and is therefore unstable and physically inaccessible. Note that the curve terminates at P on the bending limit. Curve JKL represents the pure membrane limit. Delamination is stable

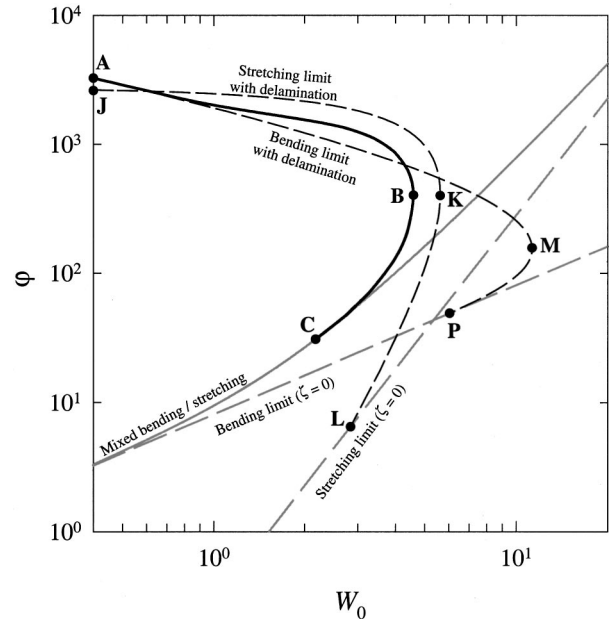


**Fig. 7** Curve ABC shows the constitutive relation with delamination for  $\Gamma^* = 10^4$ . The solid gray line is the mixed bending-stretching constitutive relation without delamination for a central point load ( $\zeta=0$ ). The two dashed gray curves AMP and JKL show the bending and stretching limits, respectively.

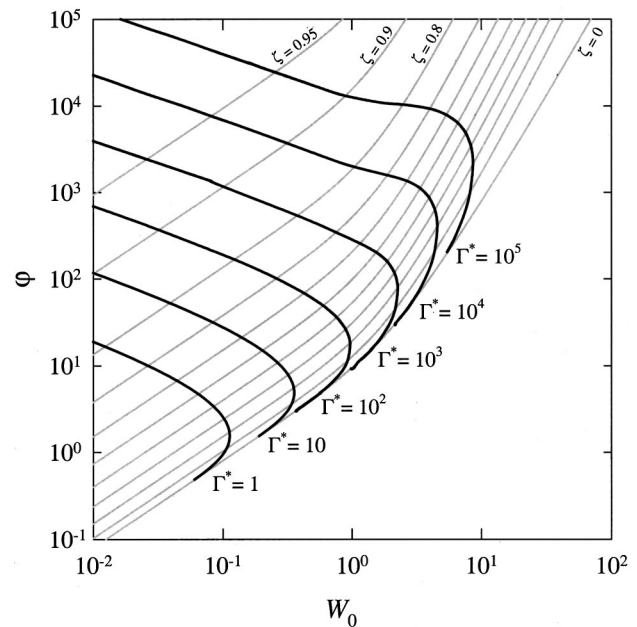


**Fig. 8** Constitutive relations with delamination for various  $\Gamma^*$  as indicated (solid lines), along with the no-delamination relations for  $\zeta=0$  to 0.9 with an interval of 0.1 and  $\zeta=0.95$  (gray lines).

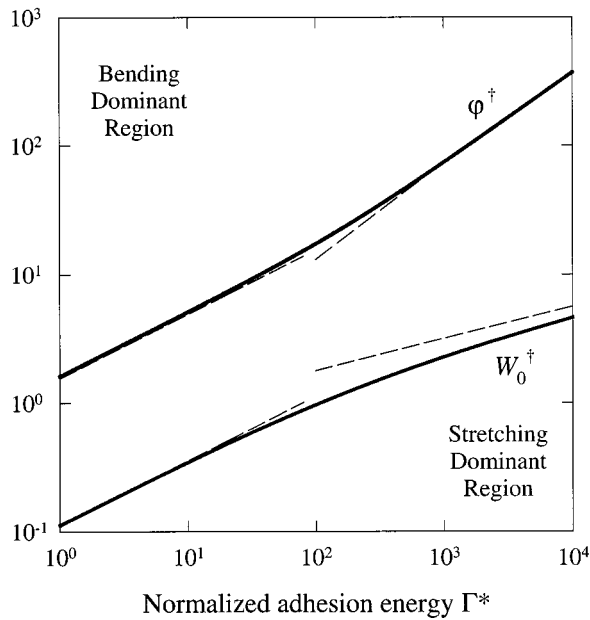


**Fig. 9** The critical load  $\varphi^\dagger$  and punch displacement  $W_0^\dagger$  at pull-off as functions of  $\Gamma^*$  (solid lines), along with the bending and stretching limits (dashed lines).

along branch JK and nonphysical along branch KL. Point K is the “pull-off” point at  $\zeta^\dagger$  (c.f., Figure 6(b)). The curve terminates at L on the stretching limit. Curve ABC represents the constitutive relation for a real film under mixed bending and stretching. At small  $W_0 \sim 1$ , bending prevails and  $\varphi(W_0)$  follows closely AMP. When  $W_0$  exceeds 1, membrane stretching becomes more dominant and  $\varphi(W_0)$  is forced to deviate towards JKL. Pull-off occurs at point B. The branch BC is nonphysical, and the curve terminates at C. Figure 8 shows a family of  $\varphi(W_0)$  for various  $\Gamma^*$ . All

curves begin with a platelike behavior at small  $W_0$  and eventually terminate on the nondelamination curve  $\varphi(W_0)$  with  $\zeta=0$ . For  $\Gamma^* < 10^2$ ,  $\varphi(W_0)$  lies mainly in the bending dominant region where stretching is negligible. For  $\Gamma^* > 10^2$ ,  $\varphi(W_0)$  deviates from pure bending and approaches the stretching limit.

The pull-off radius depends weakly on  $\beta$  and is confined to a narrow range of  $0.175754 \leq \zeta^\dagger \leq 0.194545$  (or,  $\zeta^\dagger \approx 0.18$ ). Figure 9 shows  $\varphi^\dagger$  and  $W_0^\dagger$  at pull-off as monotonic increasing functions of  $\Gamma^*$ , along with the two limits.

## 5 Discussion

It is interesting to compare our axisymmetric punch-film model with the one-dimensional rectangular punch-film model ([11]), Kendall’s adhesion models for circular flat punch with an elastic half-space and thin film ([7]) and JKR adhesion theory of solid sphere to rigid substrate ([4]). The comparison is summarized in Table 1.

The rectangular punch-film model ([11]) has similar nondelamination constitutive equations to the axisymmetric punch, in that, both are linear in the bending limit, cubic in the stretching limit and a transition around  $W_0 \approx 1$ . Significant difference lies in the “pull-off” event. The rectangular contact in the one-dimensional geometry reduces to zero, i.e., a line contact, in a stable manner, while the axisymmetric contact in the two-dimensional geometry is finite and vanishes abruptly in an unstable manner. One interesting implication is that of an elliptical punch with a conic eccentricity  $e$ , where  $e=0$  corresponds to a circular punch and  $e=1$  to a rectangular punch. As  $e$  increases from 0 to 1, there are two consequences: (i) the ratio of contact area at pull-off to punch area decreases from a maximum of  $(0.18)^2 = 0.0324$  to zero, and (ii) the degree of stability at pull-off increases.

When a rigid cylindrical punch is pulled away from an elastic half-space ([7]), the adhesive contact circle remains identical to the punch dimension until critical pull-off force is reached. The critical force and punch displacement at pull-off are identical for both fixed load and fixed grips configurations. This is in contrast with the punch-film model where a stable delamination and finite contact radius at pull-off are expected under fixed grips.

**Table 1** Comparison between various theories

	Present model	Wan	Kendall	JKR / Maugis
Geometry	Rigid cylindrical punch to film constrained at periphery	Rigid rectangular punch to film constrained at edges	Rigid cylindrical punch to substrate	Sphere to rigid flat substrate
Pull-off force $F^\dagger$	<u>Pure plate:</u> Fixed load: <i>infinite</i> Fixed grips: $1.98216 \left( \frac{Eh^3\gamma}{1-\nu^2} \right)^{1/2}$ <u>Pure membrane:</u> Fixed load: $5.51277 \left( \frac{Eh\gamma^3 a^4}{1-\nu^2} \right)^{1/4}$ Fixed grips: $0.83100 \left( \frac{Eh\gamma^3 a^4}{1-\nu^2} \right)^{1/4}$	<u>Pure plate:</u> Fixed load: <i>infinite</i> Fixed grips: $\left[ \frac{8Eh^3\gamma}{3l^2(1-\nu^2)} \right]^{1/2}$ <u>Pure membrane:</u> Fixed load: $\left[ \frac{512Eh\gamma^3}{27(1-\nu^2)} \right]^{1/4}$ Fixed grips: $\left[ \frac{512Eh\gamma^3}{27(1-\nu^2)} \right]^{1/4}$	Elastic half space: $\left( \frac{8\pi Ea^3\gamma}{1-\nu^2} \right)^{1/2}$ Thin film: $\pi a^2 \left( \frac{2\kappa\gamma}{h} \right)^{1/2}$ where $\kappa$ is the bulk modulus of the film.	Fixed load: $\frac{3}{2} \pi R\gamma$ Fixed grips: $\frac{5}{6} \pi R\gamma$ where $R$ is the radius of sphere.
Pull-off radius $a^\dagger$	<u>Pure plate:</u> Fixed load: $a$ Fixed grips: $0.175754 a$ <u>Pure membrane:</u> Fixed load: $a$ Fixed grips: $0.194545 a$	<u>Pure plate:</u> Fixed load: film area. Fixed grips: line contact <u>Pure membrane:</u> Fixed load: line contact Fixed grips: line contact	Fixed load: $a$ Fixed grips: $a$ (N.B.) Here $a$ is the radius of cylindrical punch.	Fixed load: $0.63 a$ Fixed grips: $0.30 a$ (N.B.) Here $a$ is the contact radius at zero applied load.
References		[11]	[7]	[4], [8]

When a solid sphere of radius  $R$  is brought into adhesive contact with a rigid flat under zero external force, the contact radius is found by the Johnson-Kendall-Roberts theory to be  $a = [9\pi\gamma R^2(1-\nu^2)/4E]^{1/3}$  ([4]). Ignoring the weight of the sphere, a finite force is required for pull-off at a finite contact radius. Here the pull-off parameters for fixed load are different from that for fixed grips (see Table 1). Since the pull-off event is unstable, the two adhering solids should theoretically jump into contact if they were brought into close proximity, provided that an effective long-range force is present in the gap. Our model of axisymmetric punch-film system implies  $a^\dagger \approx 0.18a$ . A “jump into contact” event is also expected when a solid probe (cylindrical punch) is brought to a distance less than  $w_0^\dagger$  from a free hanging film. Our previous study predicted the “jump” for a film of zero rigidity ([12]) and the present work further extends the claim to include all film stiffness and thickness. The new model portrays a different mechanism for interaction and assemblies of colloidal thin-walled capsules as compared to the conventional solid-solid adhesion theory ([26]).

It is worthwhile to remark several limitations of the present model:

(i) Buckling at film center. In a pure plate-like film, buckling at the center is expected for small  $\zeta$ . It is ignored here so that the contact circle is not subject to any compression or shearing and thus elastic fracture mechanics is valid. If such contact stress is accounted for, then the “pull-off” parameters  $\zeta^\dagger$ ,  $\varphi^\dagger$ , and  $W_0^\dagger$  will deviate from the predicted values. Effects of buckling diminish as film thickness and stiffness decrease.

(ii) Neutral axis is hitherto taken to be along the midplane of film. The approximation is valid when  $(h/a) \approx 0$ . In reality, only the contact edge is fixed at the punch-film interface. Similar to the conventional 90 deg peel test, an alternating stress field ahead of the contact circle or crack front is expected due to elastic foundations ([8]). The effects due to a significant  $(h/a)$  ratio is discussed by Zheng et al. [27]. When this is accounted for, a *finite* pull-off force is expected in a pure plate under fixed load.

(iii) The range of the attractive intermolecular force at the interface is hitherto assumed to be negligible. If the force is long range in nature (e.g., Coulombic), the thin annulus immediately circumscribing the contact circle will experience a force at a distance. The film profile and the contact mechanics in turn will be altered correspondingly. The presence of such a “cohesive zone” is evident when two surfaces are in close proximity, e.g., crack-tip region ([27]).

## 6 Conclusion

An elastic solution for an axisymmetric punch in adhesive contact with a thin film was derived. A “pull-off” event similar to the JKR theory was predicted. The new theory is important in modeling adhesion between solid bodies and membranes. The film profile prediction serves as a guide to possible empirical measurements.

## Acknowledgments

This research was supported by Nanyang Technological University (Singapore) Academic Research Fund #RG 48/99. The author is grateful to Dr. Yee Cheong Lam, Dr. Kuo-Kang Liu, and Dr. Kin Liao of NTU for helpful discussions.

## References

- [1] Sackmann, E., 1994, “Intra- and Extracellular Macromolecular Networks: Physics and Biological Function,” *Macromol. Chem. Phys.*, **195**, pp. 7–28.
- [2] Ohring, M., 1992, *The Materials Science of Thin Films*, Academic Press, San Diego, CA.
- [3] Derjaguin, B. V., 1989, *Theory of Stability of Colloids and Thin Films*, Consultants Bureau, New York.
- [4] Johnson, K. L., Kendall, K., and Roberts, A. D., 1971, “Surface Energy and the Contact of Elastic Solids,” *Proc. R. Soc. London, Ser. A*, **A324**, pp. 301–313.
- [5] Johnson, K. L., and Greenwood, J. A., 1997, “An Adhesion Map for the Contact of Elastic Spheres,” *J. Colloid Interface Sci.*, **192**, pp. 326–333.
- [6] Johnson, K. L., 1958, “A Note on the Adhesion of Elastic Solids,” *Br. J. Appl. Phys.*, **9**, pp. 199–200.
- [7] Kendall, K., 1971, “The Adhesion and Surface Energy of Elastic Solids,” *J. Phys. D*, **4**, pp. 1186–1195.
- [8] Maugis, D., 2000, *Contact, Adhesion and Rupture of Elastic Solids*, Springer, New York.
- [9] Liu, K. K., and Wan, K.-T., 2001, & “A New Model to Characterize Cell-Substrate Adhesion in the Presence of Osmosis,” *Med. Biol. Eng. Comput.*, **38**, pp. 690–691.
- [10] Kloboucek, A., Behrisch, A., Faix, J., and Sackmann, E., 1999, “Adhesion-Induced Receptor Segregation and Adhesion Plaque Formation: A Model Membrane Study,” *Biophys. J.*, **77**, pp. 2311–2328.
- [11] Wan, K.-T., and Duan, J., 2002, “Adherence of a Rectangular Flat Punch Onto a Clamped Plate-Transition From a Rigid Plate to a Flexible Membrane,” *ASME J. Appl. Mech.*, **69**, pp. 104–109.
- [12] Wan, K.-T., 2001, “Adherence of an Axial Symmetric Flat Punch on a Thin Flexible Membrane,” *J. Adhes.*, **75**, pp. 369–380.
- [13] Timoshenko, S. P., and Woinowsky-Krieger, S., 1959, *Theory of Plates and Shells*, 2nd Ed., McGraw-Hill, New York, pp. 1–17.
- [14] Mansfield, E. H., 1994, *The Bending and Stretching of Plates*, Pergamon Press, New York.
- [15] Sheplak, M., and Dugundji, J., 1998, “Large Deflection of Clamped Circular Plates Under Initial Tension and Transitions to Membrane Behavior,” *ASME J. Appl. Mech.*, **65**, pp. 107–115.
- [16] Wan, K.-T., and Lim, S. C., 1998, “The Bending to Stretching Transition of a Pressurized Blister Test,” *Int. J. Fract.*, **92**, pp. L43–L47.
- [17] Malyshev, B. M., and Saganik, R. L., 1965, “The Strength of Adhesive Joints Using the Theory of Cracks,” *Int. J. Fract. Mech.*, **1**, pp. 114–128.
- [18] Williams, M. L., 1969, “The Continuum Interpretation for Fracture and Adhesion,” *J. Appl. Polym. Sci.*, **13**, pp. 29–40.
- [19] Chia, C. Y., 1980, *Nonlinear Analysis of Plates*, McGraw-Hill, New York.
- [20] Wan, K.-T., and Mai, Y. W., 1995, “Fracture Mechanics of a Shaft-Loaded Blister of Thin Flexible Membrane on Rigid Substrate,” *Int. J. Fract.*, **74**, pp. 181–197.
- [21] Yang, W. H., and Hsu, K. H., 1971, “Indentation of a Circular Membrane,” *ASME J. Appl. Mech.*, **93**, pp. 227–230.
- [22] Wan, K.-T., 1999, “Fracture Mechanics of a V-Peel Adhesion Test—Transition From a Bending Plate to a Stretching Membrane,” *J. Adhes.*, **70**, pp. 197–207.
- [23] Wan, K.-T., 1999, “Fracture Mechanics of a Shaft-Loaded Blister Test—Transition From a Bending Plate to a Stretching Membrane,” *J. Adhes.*, **70**, pp. 209–219.
- [24] Wan, K.-T., and Liao, K., 1999, “Measuring Mechanical Properties of Thin Flexible Films by a Shaft-Loaded Blister Test,” *Thin Solid Films*, **352**, pp. 167–172.
- [25] Williams, J. G., 1997, “Energy Release Rates for the Peeling of Flexible Membranes and the Analysis of Blister Tests,” *Int. J. Fract.*, **87**, pp. 265–288.
- [26] Kendall, K., Alford, N. McN., and Birchall, J. D., 1987, “Elasticity of Particle Assemblies as a Measure of the Surface Energy of Solids,” *Proc. R. Soc. London, Ser. A*, **A412**, pp. 269–283.
- [27] Zheng, M., Su, Y. J., Chen, L. Q., and Zhang, T. Y., 1999, “Frictional Effects of Interface Bonding Energy in Blister Testing,” *Theor. Appl. Fract. Mech.*, **32**, No. 2, pp. 75–80.
- [28] Barenblatt, G. I., 1962, “The Mathematical Theory of Equilibrium Cracks in Brittle Fracture,” *Adv. Appl. Mech.*, **7**, pp. 55–129.



# Multimode Approach to Nonlinear Supersonic Flutter of Imperfect Circular Cylindrical Shells

**M. Amabili**

Dipartimento di Ingegneria Industriale,  
Università di Parma,  
Parco Area delle Scienze 181/A,  
Parma I-43100, Italy

**F. Pellicano**

Dipartimento di Scienze dell'Ingegneria,  
Università di Modena e Reggio Emilia,  
Via Campi 213/B,  
Modena, I-41100, Italy

*The aeroelastic stability of simply supported, circular cylindrical shells in supersonic flow is investigated by using both linear aerodynamics (first-order piston theory) and nonlinear aerodynamics (third-order piston theory). Geometric nonlinearities, due to finite amplitude shell deformations, are considered by using the Donnell's nonlinear shallow-shell theory, and the effect of viscous structural damping is taken into account. The system is discretized by Galerkin method and is investigated by using a model involving up to 22 degrees-of-freedom, allowing for travelling-wave flutter around the shell and axisymmetric contraction of the shell. Asymmetric and axisymmetric geometric imperfections of circular cylindrical shells are taken into account. Numerical calculations are carried out for a very thin circular shell at fixed Mach number 3 tested at the NASA Ames Research Center. Results show that the system loses stability by travelling-wave flutter around the shell through supercritical bifurcation. Nonsimple harmonic motion is observed for sufficiently high post-critical dynamic pressure. A very good agreement between theoretical and existing experimental data has been found for the onset of flutter, flutter amplitude, and frequency. Results show that onset of flutter is very sensible to small initial imperfections of the shells. The influence of pressure differential across the shell skin has also been deeply investigated. The present study gives, for the first time, results in agreement with experimental data obtained at the NASA Ames Research Center more than three decades ago. [DOI: 10.1115/1.1435366]*

## 1 Introduction

The first reported occurrence of flutter instability on circular cylindrical shells appears to have been on the V-2 rocket. Since that time, the study of the aeroelastic stability of cylindrical shells in axial flow is fundamental in the design of skin panels on aerospace vehicles, high-performance aircraft, and missiles. A fundamental contribution to studies on this topic is due to the introduction of the piston theory by Ashley and Zartarian in 1956 ([1]).

Many interesting studies have investigated the shell stability in supersonic flow by using a linear shell model, and among others, Dowell [2], Olson and Fung [3], Barr and Stearman [4], and Ganapathi et al. [5] predicted the onset of flutter instability. Experiments ([3,6]) have indicated that the oscillation amplitude of flutter is of the same order of the shell thickness; therefore, a nonlinear shell theory should be used in order to predict accurately the flutter amplitude. Extensive reviews of works on aeroelasticity of plates and shells were written by Dowell [7] and Bismarck-Nasr [8]; a few nonlinear studies on shells and curved panels were included. A specific review on nonlinear panel flutter was written by Mei et al. [9], including five studies on curved plates. Many experimental results on aeroelastic stability of circular cylindrical shells in axial air-flow were collected in the paper by Horn et al. [6].

Only a few researchers used a nonlinear shell model to investigate the aeroelastic stability of cylindrical shells and curved panels in axial supersonic and hypersonic flow. Librescu [10,11] studied the stability of shallow panels and finite-length circular cylindrical shells by using Donnell's nonlinear shallow-shell

theory and a simple mode expansion without considering the companion mode (a second standing-wave mode described angularly by  $\sin(n\theta)$ , the orientation of which is at  $\pi/(2n)$  with respect to the original one, described by  $\cos(n\theta)$ ,  $n$  being the number of nodal diameters) nor the interaction with the axisymmetric modes. The absence of the companion mode does not permit travelling-wave flutter. Expansions neglecting the axisymmetric modes are not able to capture the correct nonlinear response of circular shells and are only suitable for curved panels. The theory developed by Librescu [10,11] is also suitable for composite shells and nonlinear terms in the supersonic flow pressure calculated by the third-order piston theory were included. No results on limit-cycle amplitudes were given. Results obtained by Librescu can also be found in his book ([12]).

Olson and Fung [13] modeled simply supported shells using a simplified form of Donnell's nonlinear shallow-shell theory and a simple two-mode expansion without considering the companion mode but including an axisymmetric term. In their study, the supersonic flow was modeled by using the linear piston theory. In subsequent studies, Evensen and Olson [14,15] also considered the companion mode, therefore employing a four-degree-of-freedom mode expansion. This expansion allows the study of travelling-wave flutter, where nodal lines are travelling circumferentially around the shell; this phenomenon is similar to travelling waves predicted and measured for large-amplitude forced vibrations of circular cylindrical shells. However, similarly to Evensen's ([16]) expansion for the flexural shell displacement, these expansions are not moment-free at the ends of the shell, as they should be for classical simply supported shells, and the homogeneous solution for the stress function is neglected. Evensen and Olson [14,15] investigated periodic solutions by using the harmonic balance method and solved the nonlinear algebraic equations only for some special cases. The results obtained are different, from the qualitative point of view, with respect to those of Olson and Fung [13]; this is due to the different order of the

Contributed by the Applied Mechanics Division of THE AMERICAN SOCIETY OF MECHANICAL ENGINEERS for publication in the ASME JOURNAL OF APPLIED MECHANICS. Manuscript received by the ASME Applied Mechanics Division, March 7, 2001; final revision, October 1, 2001. Associate Editor: D. A. Siginer. Discussion on the paper should be addressed to the Editor, Prof. Lewis T. Wheeler, Department of Mechanical Engineering, University of Houston, Houston, TX 77204-4792, and will be accepted until four months after final publication of the paper itself in the ASME JOURNAL OF APPLIED MECHANICS.



perturbation approach used. Olsson [17] added to the problem the effect of a particular temperature field on the material properties by using a simple two-mode expansion.

Carter and Stearman [18] and Barr and Stearman [4,19] performed a series of theoretical and experimental studies on the supersonic flutter of circular cylindrical shells by including geometric imperfections; however, the theoretical analysis was linear. They also introduced an improved linear piston theory to describe the shell-flow interaction for Mach numbers  $M > 1.6$ .

Amabili and Pellicano [20] studied the aeroelastic stability of simply supported, circular cylindrical shells without imperfections in supersonic flow. Nonlinearities caused by the large-amplitude shell motion were considered by using Donnell's nonlinear shallow-shell theory, and the effect of viscous structural damping was taken into account. Two different in-plane constraints were applied to the shell edges: (i) zero axial force and (ii) zero axial displacement. The linear piston theory was applied to describe the fluid-structure interaction by using two different formulations, taking into account or neglecting the curvature correction term. The system was discretized by Galerkin method and was investigated by using a model involving seven degrees-of-freedom, allowing for travelling-wave flutter of the shell and shell axisymmetric contraction; modes with up to two streamwise half-waves were considered. Results show that the system loses stability by travelling-wave flutter. A good agreement between theoretical calculations and experimental data reported in reference ([3]) was found for flutter amplitudes.

Bolotin [21] treated the nonlinear flutter of curved plates in his book on nonconservative problems. Dowell [22,23] investigated the nonlinear flutter of curved plates of shallow curvature by using a modified Donnell's nonlinear shallow-shell theory. Both simply supported and clamped plates were considered. The linear piston theory was used to describe the fluid-structure interaction. Six modes, with different numbers of streamwise waves, were included in the mode expansion. Limit-cycle amplitudes were calculated and the effect of an internal pressurization was investigated. The effect of the curvature in the flow direction was analyzed; results show that streamwise curvature is dramatically destabilizing for the onset of flutter. Vol'mir and Medvedeva [24] investigated the nonlinear flutter of circular cylindrical panels with initial deflection and axial loads in supersonic flow. They used Donnell's nonlinear shallow-shell theory to model the panel dynamics and linear piston theory to model the fluid-structure interaction. The numerical solution was obtained by using the finite difference method. A more recent study on the influence of curvature on supersonic flutter of simply supported panels is due to Krause and Dinkler [25]; in this study the curvature of the panel is in the direction of the flow. Krause and Dinkler used the finite element method to discretize the structure taking into account von Kármán (analogous to Donnell) geometric nonlinearities; imperfections were used to describe the curvature of the panel. The third-order piston theory was used to model the fluid-structure interaction. They found that the flutter boundary is much lower for largely curved panels than for flatter panels; they also predicted chaotic flutter motion.

Hypersonic flutter of simply supported, orthotropic curved panels was studied by Bein et al. [26] and Nydick et al. [27] by using Donnell's nonlinear shallow-shell theory, the Galerkin method, and direct integration of the equations of motion. Expansion of flexural displacement involving modes up to eight longitudinal half-waves and one circumferential half-wave showed convergence of the solution. First-order piston theory, third-order piston theory, Euler equations, and Navier-Stokes equations were used to describe the fluid-structure interaction with hypersonic flow; significant differences were found by using different models. Non-simple harmonic motion with modulations of amplitude was observed for sufficiently high post-critical dynamic pressure. An

extensive experimental study on supersonic flutter of flat and slightly curved panels at Mach number 2.81 was performed by Anderson [28].

The studies developed in the past for the stability of circular cylindrical shells in flow do not agree sufficiently well with experimental results, as pointed out by Horn et al. [6]. In particular, for subsonic Mach numbers, highly divergent and catastrophic instabilities have been measured experimentally for clamped-clamped copper shells excited by a fully developed turbulent flow ([6]). This kind of instability has recently been explained by Amabili et al. by using a nonlinear shell model and potential flow in cases of both internal ([29]) and external and annular subsonic flow ([30]). Numerical results obtained are in agreement with experimental data reported in reference ([31]).

A review of studies on the nonlinear dynamics of shells, which are closely related to the present study, was recently written by Amabili and Paidoussis [32] and is avoided here for brevity.

The nonlinear stability of simply supported, circular cylindrical shells in supersonic axial flow is investigated in the present study by using an improved structural and aerodynamic model with respect to the analysis ([20]) recently developed by the same authors of the present paper. In particular, both linear aerodynamics (first-order piston theory) and nonlinear aerodynamics (third-order piston theory) are used. Geometric nonlinearities, due to finite amplitude shell deformations, are considered by using Donnell's nonlinear shallow-shell theory, and the effect of viscous structural damping is taken into account. Asymmetric and axisymmetric geometric imperfections of the circular cylindrical shells and static pressure are taken into account. The system is discretized by Galerkin projections and is investigated by using a model involving up to 22 degrees-of-freedom, allowing for travelling-wave flutter of the shell and shell axisymmetric contraction.

Numerical calculations are performed for a copper circular shell, fabricated by electroplating and tested in the  $8 \times 7$  ft supersonic wind tunnel, at fixed Mach number 3, at the NASA Ames Research Center ([3,13]) in 1964. During the experiments, it was observed that the pertinent streamwise wavelengths of interest are very large with respect to the boundary layer thickness, suggesting that the influence of the boundary layer is probably negligible. In this study, a program for the continuation of solution of nonlinear differential equations is used to obtain the bifurcation diagrams. Moreover, direct integration of the equations of motion is used for comparison and investigation of amplitude modulated motion arising by a Neimark-Sacker bifurcation of the periodic orbit.

## 2 Equation of Motion, Boundary Conditions, and Mode Expansion

A cylindrical coordinate system  $(O; x, r, \theta)$  is chosen, with the origin  $O$  placed at the center of one end of the shell. The displacements of points in the middle surface of the shell are denoted by  $u$ ,  $v$ , and  $w$ , in the axial, circumferential, and radial directions, respectively;  $w$  is taken positive inwards. Initial imperfections of the circular cylindrical shell associated with zero initial tension are denoted by the radial displacement  $w_0$ ; only radial initial imperfections are considered. By using Donnell's nonlinear shallow-shell theory, the equation of motion for finite-amplitude transverse dynamic deformation of a thin, imperfect, circular cylindrical shell is given by ([33–35])

$$D \nabla^4 w + c h \dot{w} + \rho h \ddot{w} = p - p_m + \frac{1}{R} \frac{\partial^2 F}{\partial x^2} + \frac{1}{R^2} \left[ \frac{\partial^2 F}{\partial \theta^2} \left( \frac{\partial^2 w}{\partial x^2} + \frac{\partial^2 w_0}{\partial x^2} \right) - 2 \frac{\partial^2 F}{\partial x \partial \theta} \left( \frac{\partial^2 w}{\partial x \partial \theta} + \frac{\partial^2 w_0}{\partial x \partial \theta} \right) + \frac{\partial^2 F}{\partial x^2} \left( \frac{\partial^2 w}{\partial \theta^2} + \frac{\partial^2 w_0}{\partial \theta^2} \right) \right], \quad (1)$$

where  $D = Eh^3/[12(1 - \nu^2)]$  is the flexural rigidity,  $E$  the Young's modulus,  $\nu$  the Poisson ratio,  $h$  the shell thickness,  $R$  the mean shell radius,  $\rho$  the mass density of the shell,  $c$  the damping parameter,  $p$  the radial aerodynamic pressure applied to the surface of the shell as a consequence of the external supersonic flow (positive inward), and  $p_m$  is the pressure differential across the shell skin (positive outward). The overdot denotes a time derivative and  $F$  is the in-plane Airy stress function. Here  $F$  is given by the following compatibility equation ([33–35]):

$$\begin{aligned} \frac{1}{Eh} \nabla^4 F = & -\frac{1}{R} \frac{\partial^2 w}{\partial x^2} + \frac{1}{R^2} \left[ \left( \frac{\partial^2 w}{\partial x \partial \theta} \right)^2 \right. \\ & \left. + 2 \frac{\partial^2 w}{\partial x \partial \theta} \frac{\partial^2 w_0}{\partial x \partial \theta} - \left( \frac{\partial^2 w}{\partial x^2} + \frac{\partial^2 w_0}{\partial x^2} \right) \frac{\partial^2 w}{\partial \theta^2} - \frac{\partial^2 w}{\partial x^2} \frac{\partial^2 w_0}{\partial \theta^2} \right]. \end{aligned} \quad (2)$$

In Eqs. (1) and (2), the biharmonic operator is defined as  $\nabla^4 = [\partial^2/\partial x^2 + \partial^2/(R^2 \partial \theta^2)]^2$ . Donnell's nonlinear shallow-shell equations are accurate only for modes of large number  $n$  of circumferential waves; specifically,  $1/n^2 \ll 1$  must be satisfied, so that  $n \geq 5$  is required in order to have fairly good accuracy. Donnell's nonlinear shallow-shell equations are obtained by neglecting the in-plane inertia, transverse shear deformation and rotary inertia, giving accurate results only for very thin shells, that is  $h \ll R$ . In plane displacements are infinitesimal, i.e.,  $|u| \ll h$ ,  $|v| \ll h$ , whereas  $w$  is of the same order of the shell thickness. The predominant nonlinear terms are retained but other secondary effects, such as the nonlinearities in curvature strains, have been neglected; in particular, the curvature changes are expressed by linear functions of  $w$  only. These approximations give good accuracy to study flutter problems.

The forces per unit length in the axial and circumferential directions, as well as the shear force, are given by ([36])

$$N_x = \frac{1}{R^2} \frac{\partial^2 F}{\partial \theta^2}, \quad N_\theta = \frac{\partial^2 F}{\partial x^2}, \quad N_{x\theta} = -\frac{1}{R} \frac{\partial^2 F}{\partial x \partial \theta}. \quad (3)$$

The strain-displacement relations are

$$\begin{aligned} (1 - \nu^2) \frac{N_x}{Eh} = & -\frac{\nu w}{R} + \frac{1}{2} \left( \frac{\partial w}{\partial x} \right)^2 + \frac{\partial w}{\partial x} \frac{\partial w_0}{\partial x} + \frac{\nu}{2} \left( \frac{\partial w}{\partial \theta} \right)^2 \\ & + \nu \frac{\partial w}{R \partial \theta} \frac{\partial w_0}{R \partial \theta} + \frac{\partial u}{\partial x} + \frac{\nu}{R} \frac{\partial v}{\partial \theta}, \end{aligned} \quad (4)$$

$$\begin{aligned} (1 - \nu^2) \frac{N_\theta}{Eh} = & -\frac{w}{R} + \frac{\nu}{2} \left( \frac{\partial w}{\partial x} \right)^2 + \nu \frac{\partial w}{\partial x} \frac{\partial w_0}{\partial x} + \frac{1}{2} \left( \frac{\partial w}{\partial \theta} \right)^2 \\ & + \frac{\partial w}{R \partial \theta} \frac{\partial w_0}{R \partial \theta} + \nu \frac{\partial u}{\partial x} + \frac{1}{R} \frac{\partial v}{\partial \theta}, \end{aligned} \quad (5)$$

$$\begin{aligned} (1 - \nu^2) \frac{N_{x\theta}}{Eh} = & 2(1 - \nu) \left[ \frac{1}{R} \frac{\partial w}{\partial x} \frac{\partial w}{\partial \theta} + \frac{1}{R} \frac{\partial w}{\partial x} \frac{\partial w_0}{\partial \theta} + \frac{1}{R} \frac{\partial w_0}{\partial x} \frac{\partial w}{\partial \theta} \right. \\ & \left. + \frac{1}{R} \frac{\partial u}{\partial \theta} + \frac{\partial v}{\partial x} \right]. \end{aligned} \quad (6)$$

In this study, attention is focused on a finite, simply supported (with zero axial load), circumferentially closed circular cylindrical shell of length  $L$ . The following boundary conditions are imposed:

$$w = w_0 = 0, \quad (7a)$$

$$M_x = -D \{ (\partial^2 w / \partial x^2) + \nu [\partial^2 w / (R^2 \partial \theta^2)] \} = 0 \quad \text{at } x = 0, L, \quad (7b)$$

and

$$\partial^2 w_0 / \partial x^2 = 0 \quad \text{at } x = 0, L. \quad (7c)$$

$$N_x = 0 \quad \text{at } x = 0, L \quad (8a)$$

and

$$v = 0 \quad \text{at } x = 0, L, \quad (8b)$$

where  $M_x$  is the bending moment per unit length; moreover,  $u$ ,  $v$ , and  $w$  must be continuous in  $\theta$ .

The radial displacement  $w$  is expanded by using the linear shell eigenmodes for zero flow as the base and can be written as follows:

$$\begin{aligned} w(x, \theta, t) = & \sum_{m=1}^{M_1} \sum_{n=1}^N [A_{m,n}(t) \cos(n\theta) + B_{m,n}(t) \sin(n\theta)] \sin(\lambda_m x) \\ & + \sum_{m=1}^{M_2} A_{m,0}(t) \sin(\lambda_m x), \end{aligned} \quad (9a)$$

where  $n$  is the number of circumferential waves,  $m$  is the number of longitudinal half-waves,  $\lambda_m = m\pi/L$  and  $t$  is the time;  $A_{m,n}(t)$ ,  $B_{m,n}(t)$ , and  $A_{m,0}(t)$  are the modal coordinates that are unknown functions of  $t$  ( $A_{m,0}$  is related to axisymmetric modes). The integers  $N$ ,  $M_1$ , and  $M_2$ , which give the number of modes used in the Galerkin expansion, must be selected with care in order to have the required accuracy and acceptable dimension of the nonlinear problem. In the numerical calculations, different expansions have been used and compared. The maximum number of degrees-of-freedom used in the numerical calculations for Eq. (9) is 22. It is observed, for symmetry reasons, that the nonlinear interaction among linear modes of the chosen base involves only the asymmetric modes ( $n > 0$ ) having a given  $n$  value, the asymmetric modes having a multiple eliminate  $k \times n$  of circumferential waves, where  $k$  is an integer, and axisymmetric modes ( $n = 0$ ). For the latter case, only modes with an odd  $m$  value of longitudinal half-waves have been considered because they are the most important, as previously observed in other studies on nonlinear vibrations of shells ([29,37,38]). Asymmetric modes having up to six longitudinal half-waves ( $M_1 = 6$ ) and modes having  $n$  and  $2 \times n$  circumferential waves have been considered in the numerical calculations. Axisymmetric modes play an important role in nonlinear oscillations; moreover, they are fundamental to study the effect of pressurization. This is the reason why they are included in the present model; in all the numerical calculations  $M_2 = 11$  is used (only odd  $m$  values). The form of the radial displacement used in the numerical calculation is

$$\begin{aligned} w(x, \theta, t) = & \sum_{m=1}^{4 \text{ or } 6} \sum_{k=1}^{1 \text{ or } 2} [A_{m,kn}(t) \cos(kn\theta) \\ & + B_{m,kn}(t) \sin(kn\theta)] \sin(\lambda_m x) \\ & + \sum_{m=1}^6 A_{(2m-1),0}(t) \sin(\lambda_{(2m-1)} x). \end{aligned} \quad (9b)$$

Smaller expansions have been used for comparison purposes.

The presence of couples of modes having the same shape but different angular orientations, the first one described by  $\cos(n\theta)$  and the other by  $\sin(n\theta)$ , in the periodic response of the shell leads to the appearance of travelling-wave flutter around the shell in angular direction. This phenomenon is related to the axial symmetry of the system. The travelling-wave flutter represents a fundamental difference *vis-à-vis* the linear approach to shell flutter.

The initial radial imperfection  $w_0$  is expanded in the same form of  $w$ , i.e., in a double Fourier series satisfying the boundary conditions (7a,c) at the shell edges

$$\begin{aligned} w_0(x, \theta) = & \sum_{m=1}^{\tilde{M}_1} \sum_{n=1}^{\tilde{N}} [\tilde{A}_{m,n} \cos(n\theta) + \tilde{B}_{m,n} \sin(n\theta)] \sin(\lambda_m x) \\ & + \sum_{m=1}^{\tilde{M}_2} \tilde{A}_{m,0} \sin(\lambda_m x), \end{aligned} \quad (10)$$

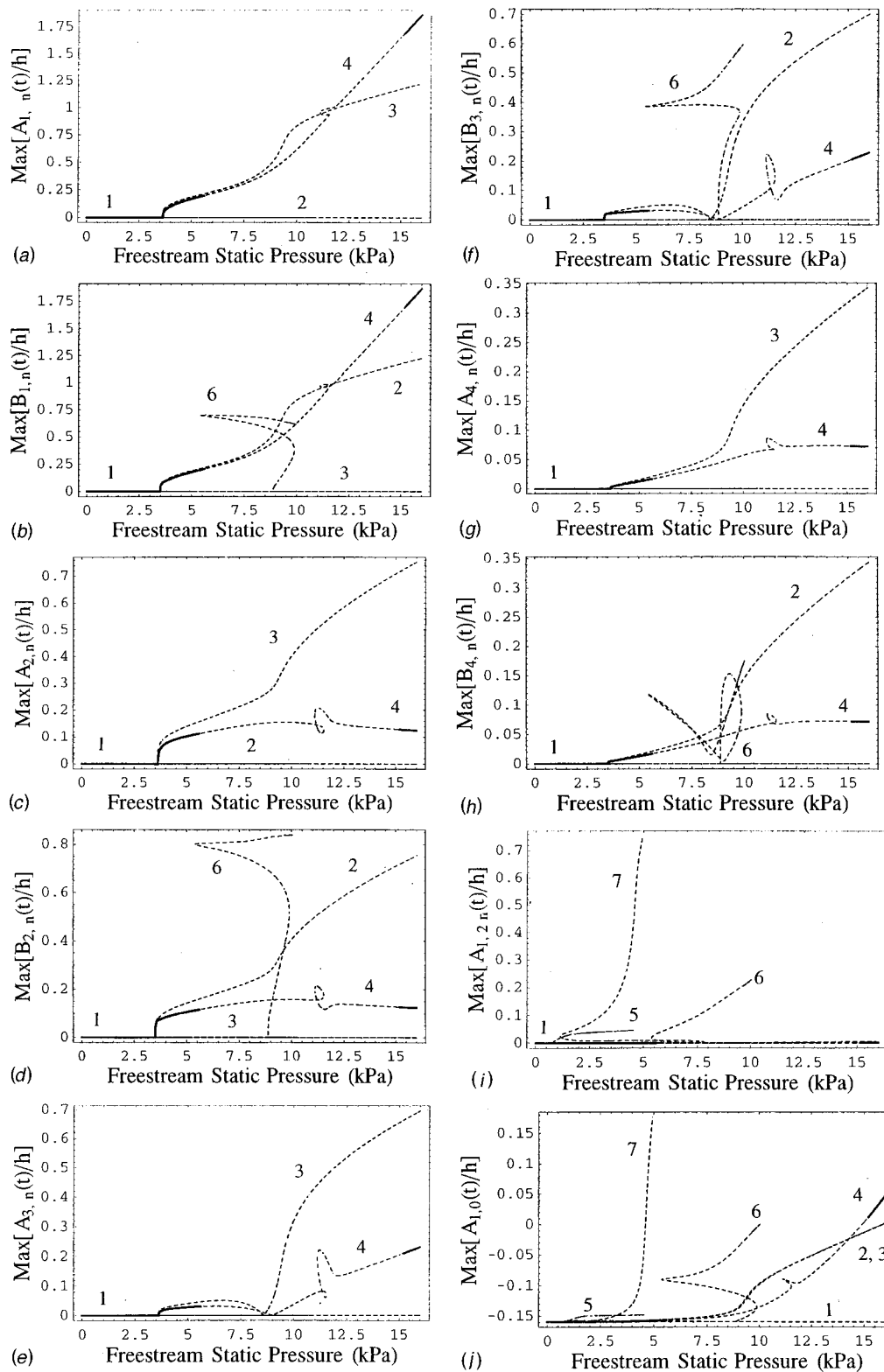


**Fig. 1** Amplitude of oscillatory solutions versus the freestream static pressure;  $n=23$ , linear piston theory. —, stable branches; ---, unstable branches. (a) Maximum amplitude of the first longitudinal mode  $A_{1,n}(t)/h$ ; (b) maximum amplitude of the first longitudinal mode  $B_{1,n}(t)/h$ ; (c) maximum amplitude of the second longitudinal mode  $A_{2,n}(t)/h$ ; (d) maximum amplitude of the second longitudinal mode  $B_{2,n}(t)/h$ ; (e) maximum amplitude of the third longitudinal mode  $A_{3,n}(t)/h$ ; (f) maximum amplitude of the third longitudinal mode  $B_{3,n}(t)/h$ ; (g) maximum amplitude of the fourth longitudinal mode  $A_{4,n}(t)/h$ ; (h) maximum amplitude of the fourth longitudinal mode  $B_{4,n}(t)/h$ ; (i) maximum amplitude of the first mode with  $2n$  circumferential waves  $A_{1,2n}(t)/h$ ; (j) maximum amplitude of the first axisymmetric mode  $A_{1,0}(t)/h$ .

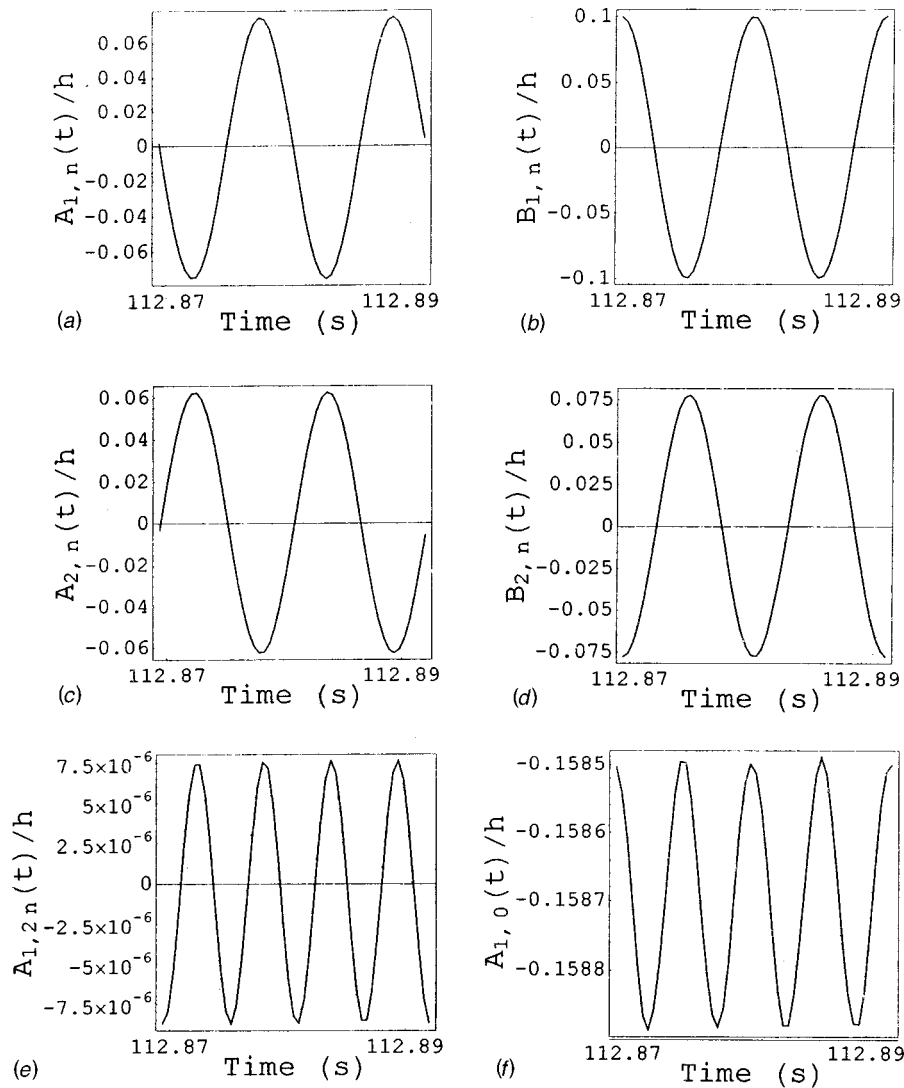


**Fig. 2 Time histories of the shell for  $p_{\infty}=3800$  Pa;  $n=23$ , linear piston theory. (a) Amplitude of the first longitudinal mode  $A_{1,n}(t)/h$ ; (b) amplitude of the first longitudinal mode  $B_{1,n}(t)/h$ ; (c) amplitude of the second longitudinal mode  $A_{2,n}(t)/h$ ; (d) amplitude of the second longitudinal mode  $B_{2,n}(t)/h$ ; (e) amplitude of the first longitudinal mode with  $2n$  circumferential waves  $A_{1,2n}(t)/h$ ; (f) amplitude of the axisymmetric mode  $A_{1,0}(t)/h$ .**

where  $\tilde{A}_{m,n}$ ,  $\tilde{B}_{m,n}$ , and  $\tilde{A}_{m,0}$  are the modal amplitudes of imperfections;  $\tilde{N}$ ,  $\tilde{M}_1$ , and  $\tilde{M}_2$  are integers indicating the number of terms in the expansion. Seven terms in the expansion of imperfections are considered in the numerical calculations: (i) asymmetric imperfection having the same shape of the fluttering mode with one ( $\tilde{A}_{1,n}$ ,  $\tilde{B}_{1,n}$ ), two ( $\tilde{A}_{2,n}$ ,  $\tilde{B}_{2,n}$ ), and three ( $\tilde{A}_{3,n}$ ,  $\tilde{B}_{3,n}$ ) longitudinal half-waves; (ii) axisymmetric imperfection with one longitudinal half-wave ( $\tilde{A}_{1,0}$ ). Additional terms can be inserted; those with  $2n$  circumferential waves can be significant.

### 3 Stress Function and Solution

The expansion used for the radial displacement  $w$  satisfies identically the boundary conditions given by Eqs. (7a, b); moreover, it

satisfies exactly the continuity of the circumferential displacement  $v$ ,

$$\int_0^{2\pi} \frac{\partial v}{\partial \theta} d\theta = \int_0^{2\pi} \left[ \frac{1}{Eh} \left( \frac{\partial^2 F}{\partial x^2} - \nu \frac{\partial^2 F}{R^2 \partial \theta^2} \right) + \frac{w}{R} - \frac{1}{2} \left( \frac{\partial w}{R \partial \theta} \right)^2 - \frac{\partial w}{R \partial \theta} \frac{\partial w_0}{R \partial \theta} \right] d\theta = 0, \quad (11)$$

as it has been verified after calculation of the stress function  $F$  from Eq. (2).

The boundary conditions for the in-plane displacements, Eqs. (8), give very complex expressions when transformed into equations involving  $w$ . Therefore they are modified into simpler integral expressions that satisfy Eqs. (8) on the average ([36]). Specifically, the following conditions are imposed:

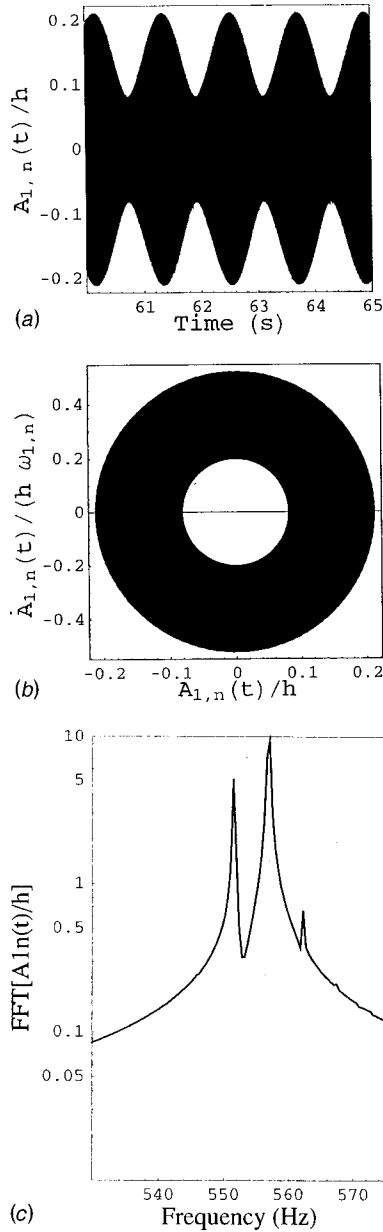


**Fig. 3 Flutter response of the shell for  $p_\infty=7000$  Pa;  $n=23$ , linear piston theory. (a) Time history of the first longitudinal mode  $A_{1,n}(t)/h$ ; (b) phase-plane plot of the first longitudinal mode  $A_{1,n}(t)/h$ ; (c) spectrum of the first longitudinal mode  $A_{1,n}(t)/h$ .**

$$\int_0^{2\pi} N_x R d\theta = 0, \quad \text{at } x=0, L \quad (12)$$

$$\int_0^{2\pi} \int_0^L N_{x\theta} dx R d\theta = 0. \quad (13)$$

Equation (12) ensures a zero axial force  $N_x$  on the average at  $x=0, L$ ; Eq. (13) is satisfied when  $v=0$  on the average at  $x=0, L$  and  $u$  is continuous in  $\theta$  on the average. Substitution of Eqs. (8) by Eqs. (12) and (13) simplifies computations, although it introduces an approximation (it can easily be shown that the boundary conditions are exactly satisfied at  $N$  discrete points, where  $n$  is the number of circumferential waves).

When the expansions of  $w$  and  $w_0$ , Eqs. (9) and (10), are substituted in the right-hand side of Eq. (2), a partial differential equation for the stress function  $F$  is obtained, the solution of which may be written as

$$F = F_h + F_p, \quad (14)$$

where  $F_h$  is the homogeneous and  $F_p$  is the particular solution. The particular solution is given by

$$\begin{aligned} F_p = & \sum_{m=1}^{2M} \sum_{n=1}^{2N} (F_{mn1} \sin m\eta \sin n\theta + F_{mn2} \sin m\eta \cos n\theta \\ & + F_{mn3} \cos m\eta \sin n\theta + F_{mn4} \cos m\eta \cos n\theta) \\ & + \sum_{n=1}^{2N} (F_{0n3} \sin n\theta + F_{mn4} \cos n\theta) \\ & + \sum_{m=1}^{2M} (F_{m02} \sin m\eta + F_{m04} \cos m\eta), \end{aligned} \quad (15)$$

where  $N$  is the same as in Eq. (9a),  $M$  is the maximum of  $M_1$  and  $M_2$ ,  $\eta = \pi x/L$  and the functions of time  $F_{mnj}$ ,  $j=1, \dots, 4$ , have a long expression not reported here; they have been obtained by using the *Mathematica* computer program ([39]) for symbolic manipulations. The homogeneous solution may be assumed to have the form ([29])

$$\begin{aligned} F_h = & \frac{1}{2} \bar{N}_x R^2 \theta^2 + \frac{1}{2} x^2 \left\{ \bar{N}_\theta - \frac{1}{2\pi RL} \int_0^L \int_0^{2\pi} \left[ \frac{\partial^2 F_p}{\partial x^2} \right] R d\theta dx \right\} \\ & - \bar{N}_{x\theta} x R \theta, \end{aligned} \quad (16)$$

where  $\bar{N}_x$ ,  $\bar{N}_\theta$ , and  $\bar{N}_{x\theta}$  are the average in-plane force (per unit length) resultants, as a consequence of the in-plane constraints on the average, defined as

$$\bar{N}_\# = \frac{1}{2\pi L} \int_0^{2\pi} \int_0^L N_\# dx d\theta, \quad (17)$$

where the symbol  $\#$  must be replaced by  $x$ ,  $\theta$ , and  $x\theta$ . Boundary conditions (12, 13) allow us to express the in-plane restraint stresses  $\bar{N}_x$ ,  $\bar{N}_\theta$ , and  $\bar{N}_{x\theta}$ , see Eqs. (4)–(6), in terms of  $w$ ,  $w_0$ , and their derivatives. Simple calculations give

$$\bar{N}_x = 0, \quad (18a)$$

$$\begin{aligned} \bar{N}_\theta = & \frac{Eh}{2\pi R} \left\{ -2 \sum_{m=1}^{M_2} \frac{A_{m,0}(t)}{m} [1 - (-1)^m] + \frac{\pi}{4R} \sum_{n=1}^{\hat{N}} \sum_{m=1}^{\hat{M}} n^2 \right. \\ & \times [A_{m,n}^2(t) + B_{m,n}^2(t) + 2A_{m,n}(t)\tilde{A}_{m,n}(t) \\ & \left. + 2B_{m,n}(t)\tilde{B}_{m,n}(t)] \right\}, \end{aligned} \quad (18b)$$

$$\bar{N}_{x\theta} = 0, \quad (18c)$$

where  $\hat{N}$  is the maximum of  $N$  and  $\tilde{N}$ , and  $\hat{M}$  is the maximum of  $M_1$  and  $\tilde{M}_1$ . Equation (16) is chosen in order to satisfy the boundary conditions imposed. Moreover, it satisfies Eqs. (3) on the average as a consequence of (i) the contribution of  $F_p$  to  $\bar{N}_\theta$  being  $(2\pi RL)^{-1} \int_0^L \int_0^{2\pi} [\partial^2 F_p / \partial x^2] R d\theta dx$ , and (ii) contributions of  $F_p$  to  $\bar{N}_x$  and  $\bar{N}_{x\theta}$  being zero.

By use of the Galerkin method, up to 22 second-order, ordinary, coupled nonlinear differential equations are obtained for the variables  $A_{m,n}(t)$ ,  $B_{m,n}(t)$ , and  $A_{m,0}(t)$ , by successively weighting the single original Eq. (1) with the functions that describe the shape of the modes retained in Eq. (9b). These equations have very long expressions containing quadratic and cubic nonlinear



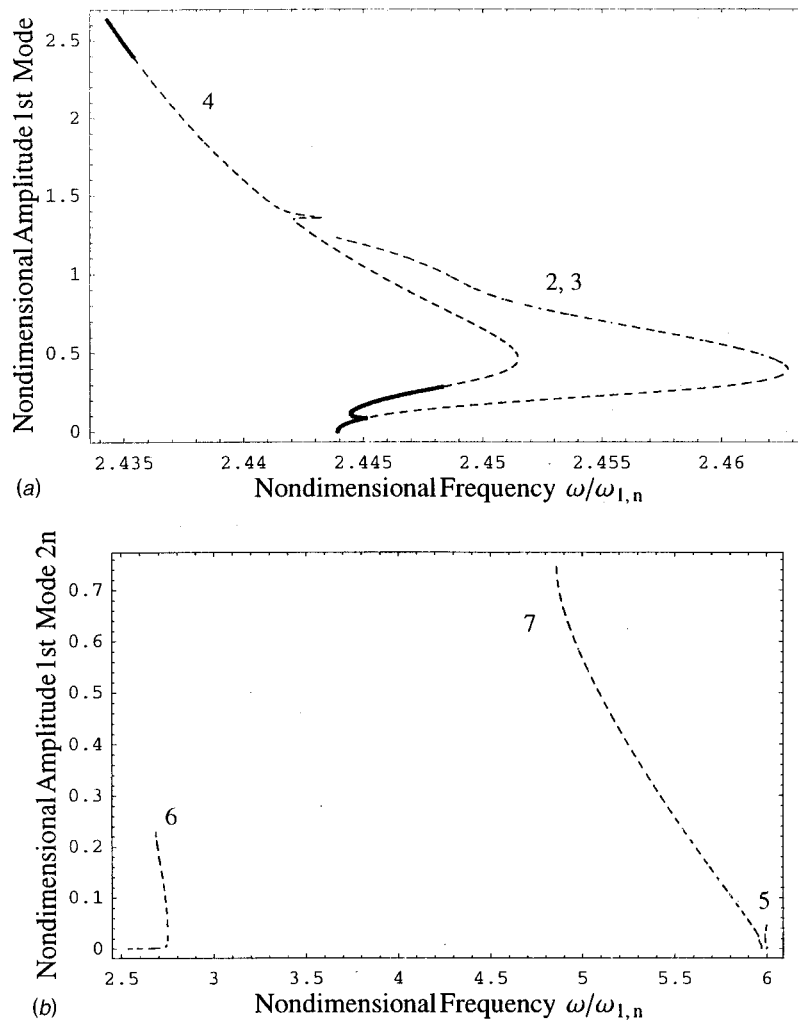


**Fig. 4 Nondimensional flutter amplitude versus nondimensional flutter frequency;  $\omega_{1,n} = 2\pi \times 226.3$  rad/s. —, stable branches; ---, unstable branches. (a) Amplitude of the first longitudinal mode with  $n$  circumferential waves; (b) amplitude of the first longitudinal mode with  $2n$  circumferential waves.**

terms. The Galerkin projection of the equation of motion (1), including the pressure load, has been performed by using the *Mathematica* computer software ([39]).

#### 4 Linear and Third-Order Piston Theory

The fluid-structure interaction used in the present study is based on the piston theory ([1]). As discussed in the Introduction, the configuration investigated is related to experiments performed by Olson and Fung [3,13], where the pertinent streamwise wavelengths of interest are very large with respect to the boundary layer thickness (see Fig. 5 in [3]), suggesting that the influence of the boundary layer is probably negligible ([13]).

According to piston theory ([1]), the radial aerodynamic pressure  $p$  applied to the surface of the shell can be obtained by analogy with the instantaneous isentropic pressure on the face of a piston moving with velocity  $Z$  into a perfect gas which is confined in a one-dimensional channel; this pressure is given by

$$p = p_{\infty} \left( 1 + \frac{\gamma - 1}{2} \frac{Z}{a_{\infty}} \right)^{2\gamma/(\gamma - 1)}, \quad (19)$$

where  $\gamma$  is the adiabatic exponent,  $p_{\infty}$  is the freestream static pressure,  $V_{\infty}$  is the freestream velocity, and  $a_{\infty}$  is the freestream speed of sound. In the analogy, the piston velocity  $Z$  is replaced by the  $Z = V_{\infty} \partial(w + w_0)/\partial x + \partial w/\partial t$  in order to obtain the radial

aerodynamic pressure  $p$  applied to the surface of the shell as a consequence of the external supersonic flow. Equation (19) can be expanded into Taylor series for the variable  $Z/a_{\infty}$  close to zero; the third-order expansion, neglecting higher-order terms, gives ([1,9,10,12,27])

$$p = -\gamma p_{\infty} \left\{ \left[ M \frac{\partial(w + w_0)}{\partial x} + \frac{1}{a_{\infty}} \frac{\partial w}{\partial t} \right] + \frac{\gamma + 1}{4} \left[ M \frac{\partial(w + w_0)}{\partial x} + \frac{1}{a_{\infty}} \frac{\partial w}{\partial t} \right]^2 + \frac{\gamma + 1}{12} \left[ M \frac{\partial(w + w_0)}{\partial x} + \frac{1}{a_{\infty}} \frac{\partial w}{\partial t} \right]^3 \right\}. \quad (20a)$$

The linear terms  $p_1$  in Eq. (20a) can be substituted with a more accurate expression obtained by linearized potential flow theory ([4,40])

$$p_1 = -\frac{\gamma p_{\infty} M^2}{(M^2 - 1)^{1/2}} \left\{ \frac{\partial(w + w_0)}{\partial x} + \frac{1}{M a_{\infty}} \left[ \frac{M^2 - 2}{M^2 - 1} \right] \frac{\partial w}{\partial t} - \frac{w + w_0}{2(M^2 - 1)^{1/2} R} \right\}. \quad (20b)$$

In Eq. (20b), the last term is the curvature correction term and is neglected in some studies of shell stability based on the piston theory. Except for the curvature correction term, Eq. (20b) re-

**Table 1 Critical freestream static pressure giving onset of flutter calculated for different expansions of the radial displacement  $w$ , Eq. (9a);  $n=23$ ,  $p_m=3452 \text{ N/m}^2$ . The result for five modes has been taken from Amabili and Pellicano [20]. Case (i) with 22 modes: expansion given in Eq. (9b) with the options of a maximum of four longitudinal half-waves and  $k=1,2$ . Case (ii) with ten modes: elimination from case (i) of all the modes having  $\sin(kn\theta)$  and  $k=1$  only. Case (iii) with nine modes: elimination from case (ii) of the axisymmetric mode with 11 longitudinal half-waves. Case (iv) with five modes: expansion retaining only  $A_{1,n}$ ,  $A_{2,n}$ ,  $A_{1,0}$ ,  $A_{3,0}$ ,  $A_{5,0}$ .**

	Case (i)	Case (ii)	Case (iii)	Case (iv)
Expansion (number of modes)	22	22	10	5
Piston theory	3rd order linear	linear	linear	linear
Critical $p_\infty$ (Pa)	3614.4	3614.4	3746.7	4077.7 ([20])

duces to the linear part of Eq. (20a) for sufficiently high Mach numbers; Eq. (20b) is more accurate for low supersonic speed and can be used for  $M > 1.6$ .

In the present study, Eq. (20b) is used for linear aerodynamics (referred as linear piston theory in Section 5) and Eq. (20a), with the linear terms modified according to Eq. (20b), for nonlinear aerodynamics (third-order piston theory).

## 5 Numerical Results

Numerical results have been obtained for a case experimentally studied by Olson and Fung [3] and theoretically investigated by Olson and Fung [13], Evensen and Olson [14,15], Carter and Stearman [18], Barr and Stearman [19], and Amabili and Pellicano [20]. The shell and the airflow have the following characteristics:  $R=0.2032 \text{ m}$ ,  $L=0.39116 \text{ m}$ ,  $R/h=2000$ ,  $E=110.32 \times 10^9 \text{ Pa}$ ,  $\rho=8905.37 \text{ kg/m}^3$ ,  $\nu=0.35$ ,  $\gamma=1.4$ ,  $a_\infty=213.36 \text{ m/s}$  and  $M=3$ ; the freestream stagnation temperature is  $48.9^\circ\text{C}$ . A structural modal damping coefficient  $\zeta_{1,n}=0.0005$ , which is compatible with the test shell ([14,15]), is assumed; for other modes  $\zeta_x = \zeta_{1,n} \omega_{1,n} / \omega_x$ . The test shell is extremely thin, fabricated with copper by electroplating, and was tested in the  $8 \times 7 \text{ ft}$  supersonic wind tunnel at the NASA Ames Research Center. The experimental boundary conditions at the shell edges were quite complex ([3]). In particular, the test shell was soldered to two copper end rings, mounted over O-ring seals to allow thermal expansion. In the present calculations they have been simulated with simply supported edges; actual boundary conditions were between simply supported and clamped edges.

**5.1 Shell Without Geometric Imperfections.** In this subsection, the shell is considered without geometric imperfections. Initially calculations have been performed for a number  $n=23$  circumferential waves and pressure differential across the shell skin  $p_m=3447.5 \text{ N/m}^2$ , in order to allow comparison with previous studies ([13–15,20]). The effect of  $p_m$  has been taken into account by using the nonlinear equations, without the linearization used in previous studies ([13–15,18–20]); therefore the static axisymmetric deformation due to pressurization has been taken into account. The freestream static pressure  $p_\infty$  has been used as bifurcation parameter instead of the Mach number  $M$ . In fact, experimental data available for comparison from the supersonic wind tunnel tests ([3,19]) were collected varying  $p_\infty$  and keeping  $M$  constant. As a consequence that the flight velocity  $U=Ma_\infty$  and that  $a_\infty=\sqrt{\gamma p_\infty/\rho_\infty}$ , the flight velocity  $U$  can be easily related to the freestream static pressure  $p_\infty$ .

Solutions of the nonlinear equations of motion have been obtained numerically by using (i) the *Auto* computer program ([41]) for continuation of the solution and bifurcation of ordinary differential equations, based on a collocation method, and (ii) direct integration of the equations of motion. The *Auto* computer program is not able to detect surfaces coming out from a bifurcation point, but it can detect branches. As a consequence that, for the axisymmetry, the system does not possess a preferential angular coordinate  $\theta$  to locate the deformation, in the present case surfaces come out from bifurcation points. In order to use *Auto*, a bifurcation analysis was performed introducing a small perturbation to

the linear part of the system. This approach is analogous to having a very small difference in the stiffness of the system for the couple of modes described by the generalized coordinates  $A_{1,n}$  and  $B_{1,n}$ . This perturbation allows normal bifurcation analysis, as line branches now emerge from bifurcation points instead of surfaces. A perturbation of 0.2 percent to the linear frequency of the mode corresponding to  $B_{1,n}$  has been used in the present case, so that differences with respect to the actual systems are almost negligible. Direct integration of the equations of motion by using Gear's BDF method (routine DIVPAG of IMSL) has also been performed to check the results and obtain the time behavior. Adams Gear algorithm has been used due to the high dimension of the dynamical system. Indeed, when a high-dimensional phase space is analyzed, the problem can present stiff characteristics, due to the presence of different time scales in the response. In simulations with adaptive step-size Runge Kutta methods, spurious nonstationary and divergent motions, incoherent with AUTO solutions, were obtained. Therefore the Adams Gear method, designed for stiff equations, was used.

The bifurcation curves for all the most important modal coordinates versus the freestream static pressure  $p_\infty$  are shown in Fig. 1 for the aerodynamic pressure given by linear piston theory. In this case, 22 modes have been used. The expansion is the one in Eq. (9b) with the options of a maximum of four longitudinal half-waves and  $k=1,2$ .

In Fig. 1 the curves correspond to the flutter amplitudes of the shell (excluding branch 1 that is relative to the trivial equilibrium position). Results show that the perfect shell loses stability for

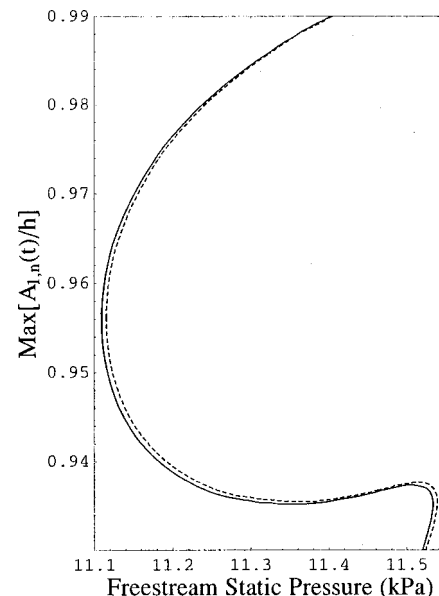


**Fig. 5 Amplitude of oscillatory solutions versus the freestream static pressure;  $n=23$ . —, third-order piston theory; ---, linear piston theory.**

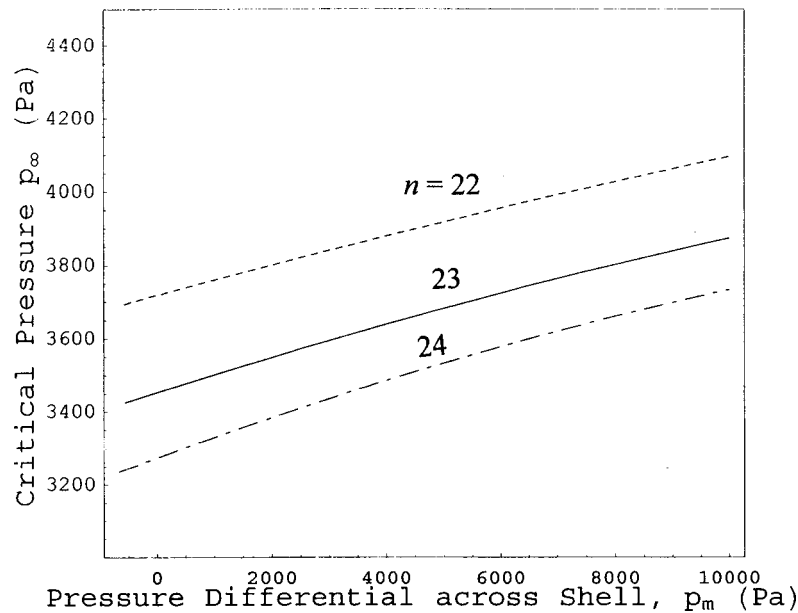


Fig. 6 Critical freestream static pressure versus the pressure differential across the shell skin  $p_m$  for three different numbers of circumferential waves: ---,  $n=22$ ; —,  $n=23$ , - · - · -,  $n=24$

$p_\infty = 3614$  Pa through Hopf bifurcation. Branches 2 and 3 correspond to standing-wave flutter that loses stability very soon through bifurcation. Branch 4, which is the attractive solution, represents a travelling-wave flutter around the shell circumference, as can be shown by observing the time histories of the system obtained by direct integration of the equations of motion for  $p_\infty = 3800$  Pa, reported in Fig. 2. It can be observed in Figs. 2(a, b) that the phase shift between  $A_{1,n}(t)$  and  $B_{1,n}(t)$  is  $\vartheta_2 - \vartheta_1 = \pi/2$ ; the same phase shift is observed in Figs. 2(c, d) for

modes having two longitudinal half-waves. Moreover, the amplitude of the couple of modes with the same number of longitudinal wave number  $m$  is the same, giving pure travelling-wave flutter. It is to be noted that, excluding a very small range of  $p_\infty$  after the onset of instability due to the perturbation introduced, all the stable flutter is a travelling wave around the circumference, as observed in the experiments by Olson and Fung [3] and predicted by Evensen and Olson [14,15] and Amabili and Pellicano [20]. Figures 2(e, f) show that generalized coordinates  $A_{1,2n}$  and

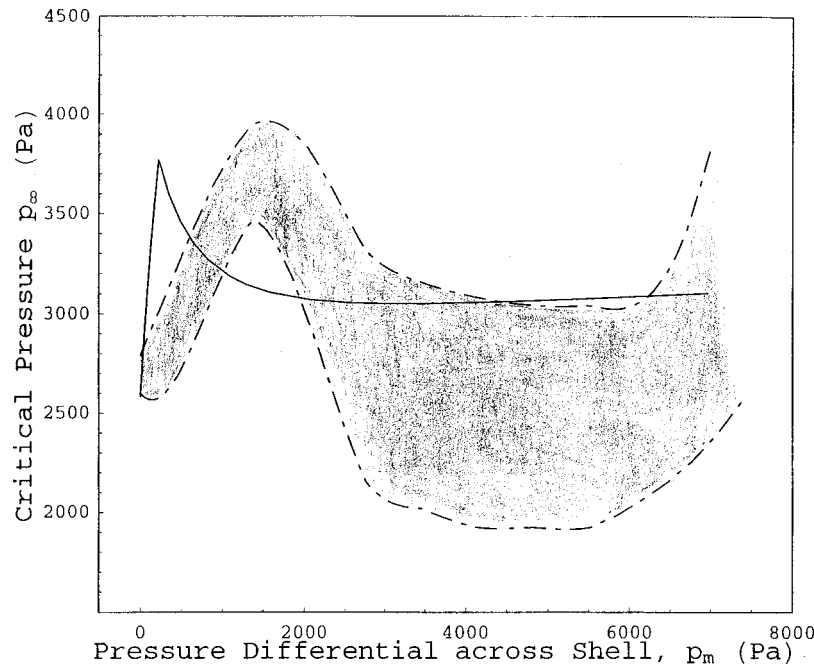
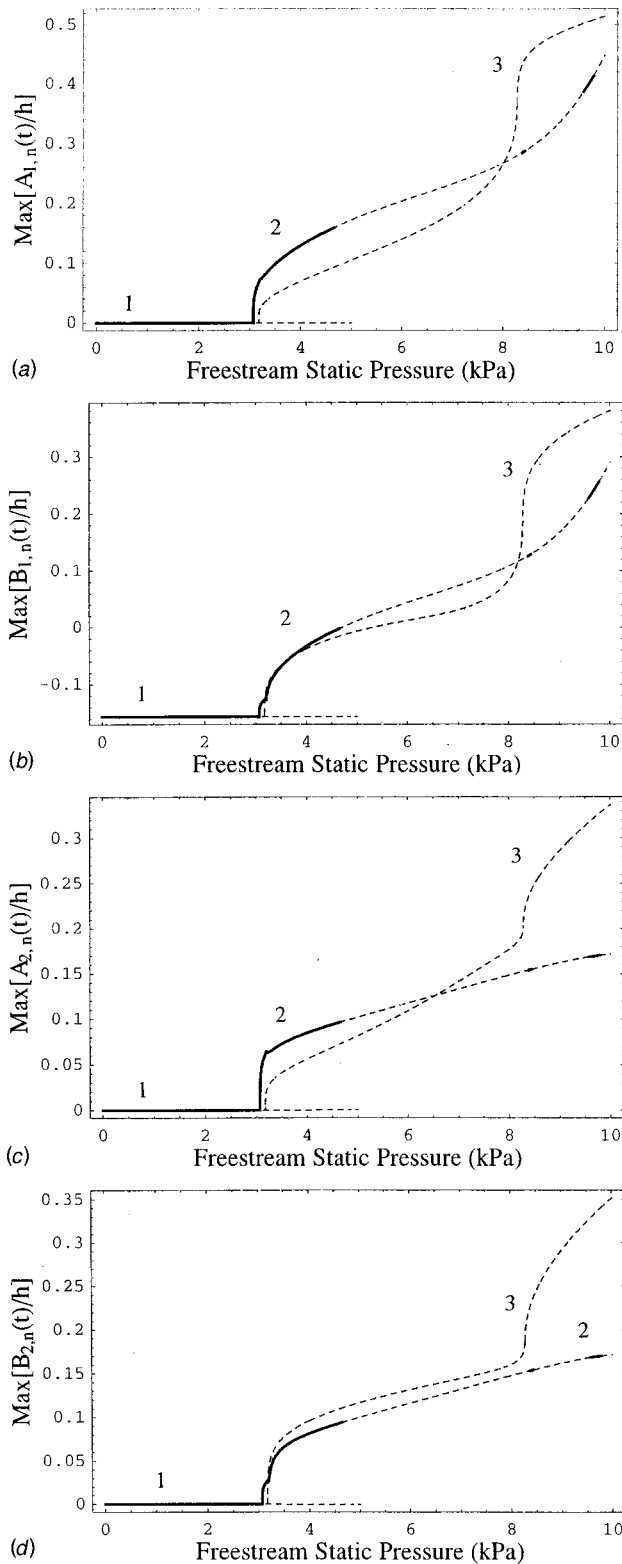


Fig. 7 Critical freestream static pressure versus the pressure differential across the shell skin  $p_m$ : —, theoretical results for imperfect shell,  $\bar{B}_{1,24} = 0.18h$ ,  $\bar{A}_{3,24} = 0.0966h$ ,  $\bar{A}_{1,0} = 2.46h$ , and  $n=24$ ; the gray area delimited by - - - - - represents the experimental data ([19]).



**Fig. 8 Amplitude of oscillatory solutions versus the freestream static pressure;  $n=24$ ,  $p_m=5000$  Pa; imperfect shell ( $\bar{B}_{1,24}=0.18h$ ,  $\bar{A}_{3,24}=0.0966h$ ,  $\bar{A}_{1,0}=2.46h$ ), linear piston theory. —, stable branches; ---, unstable branches. (a) Maximum amplitude of the first longitudinal mode  $A_{1,n}(t)/h$ ; (b) maximum amplitude of the first longitudinal mode  $B_{1,n}(t)/h$ ; (c) maximum amplitude of the second longitudinal mode  $A_{2,n}(t)/h$ ; (d) maximum amplitude of the second longitudinal mode  $B_{2,n}(t)/h$ .**

$A_{1,0}$  have a flutter frequency which is twice the one shown in Figs. 2(a–d). A similar phenomenon has been observed for nonlinear harmonic vibrations of shells ([37,38]).

Branch 4 in Fig. 1 loses stability for  $p_\infty=5600$  Pa through a Neimark-Sacker (torus) bifurcation ([42]) and regains stability at  $p_\infty=15190$  Pa through a second Neimark-Sacker bifurcation. In the range comprised between these two values, there is a quasi-periodic flutter oscillation characterized by amplitude modulations, as shown in Fig. 3 for  $p_\infty=7000$  Pa. For this value of  $p_\infty$ , amplitude modulations are particularly large when compared with those observed for different values of  $p_\infty$ . Figures 3(a) and 3(b) show the amplitude modulation and the trajectory in the phase space; the trajectory fills completely a portion of the plane. This means that the system evolves on a two-dimensional torus, where the trajectory is not closed, giving rise to a quasi-periodic orbit. This happens when the frequencies of oscillations are in an irrational ratio. The effect on the spectrum of the shell oscillation is a splitting of the flutter frequency into several closely and equally spaced frequencies (peaks). This feature can be observed on the spectrum, Fig. 3(c), where two principal peaks, very close to each other, are visible. Amplitude-modulated flutter was also observed in experiments, see Fig. 6(c) of reference ([3]). It can also be observed in Fig. 1 that branch 4 presents a curious curve for  $p_\infty$  comprised between 11,100 and 11,500 Pa. Branches 5, 6, and 7 are always unstable; moreover, branches 5 and 7 present strong subcritical bifurcations and are associated with modes with  $2n$  circumferential waves, see Fig. 1(i). In particular, branch 7 could be very dangerous because highly divergent. However, it is completely unstable and not attractive, i.e., a repeller. The presence of multiple unstable orbits makes the phase trajectory very complex.

The flutter frequency, nondimensionalized with respect to the natural frequency  $\omega_{1,n}$  ( $n=23$ ) of the unpressurized shell, is shown in Fig. 4. Results show that the flutter frequency of branch 4, the most important one, is almost constant; similar result is also found for branches 2 and 3.

Table 1 shows the effect of different expansions of the radial displacement  $w$  on the critical freestream static pressure associated with onset of flutter. In particular, the effect of modes with  $2n$  circumferential waves and modes with angular function  $\sin(n\theta)$  is negligible on the onset of flutter. However, the contribution of the latter ones on the nonlinear flutter response is fundamental, as previously discussed. Several qualitative and quantitative differences have been found between the present results and those obtained by Amabili and Pellicano [20] for the same case with a seven-degree-of-freedom model. The flutter observed in reference ([20]) was always a simple-harmonic oscillation of smaller amplitude; the difference is mainly due to the different number of longitudinal modes included in the expansions of  $w$  and to the different way of considering pressurization. Table 1 gives the quantitative difference between the onset of flutter predicted in reference ([20]) and the one calculated in the present study.

Results obtained by using the third-order piston theory are almost coincident with those obtained with the linear piston theory in the present case. In Fig. 5, a comparison of the results obtained by using the two theories is shown with only a zoom of the bifurcation diagram (see Fig. 1) in order to appreciate the small difference.

Figure 6 shows the critical freestream static pressure associated with onset of flutter versus the pressure differential across the shell skin  $p_m$  for three numbers of circumferential waves:  $n=22, 23, 24$ . Figure 6 shows that the onset of flutter is actually observed for  $n=24$ ; however, the difference with respect to  $n=23$  is very small. The effect of pressurization of the shell has a small stabilizing effect. The last result disagrees with experimental data obtained by Olson and Fung [3,19]. The introduction of



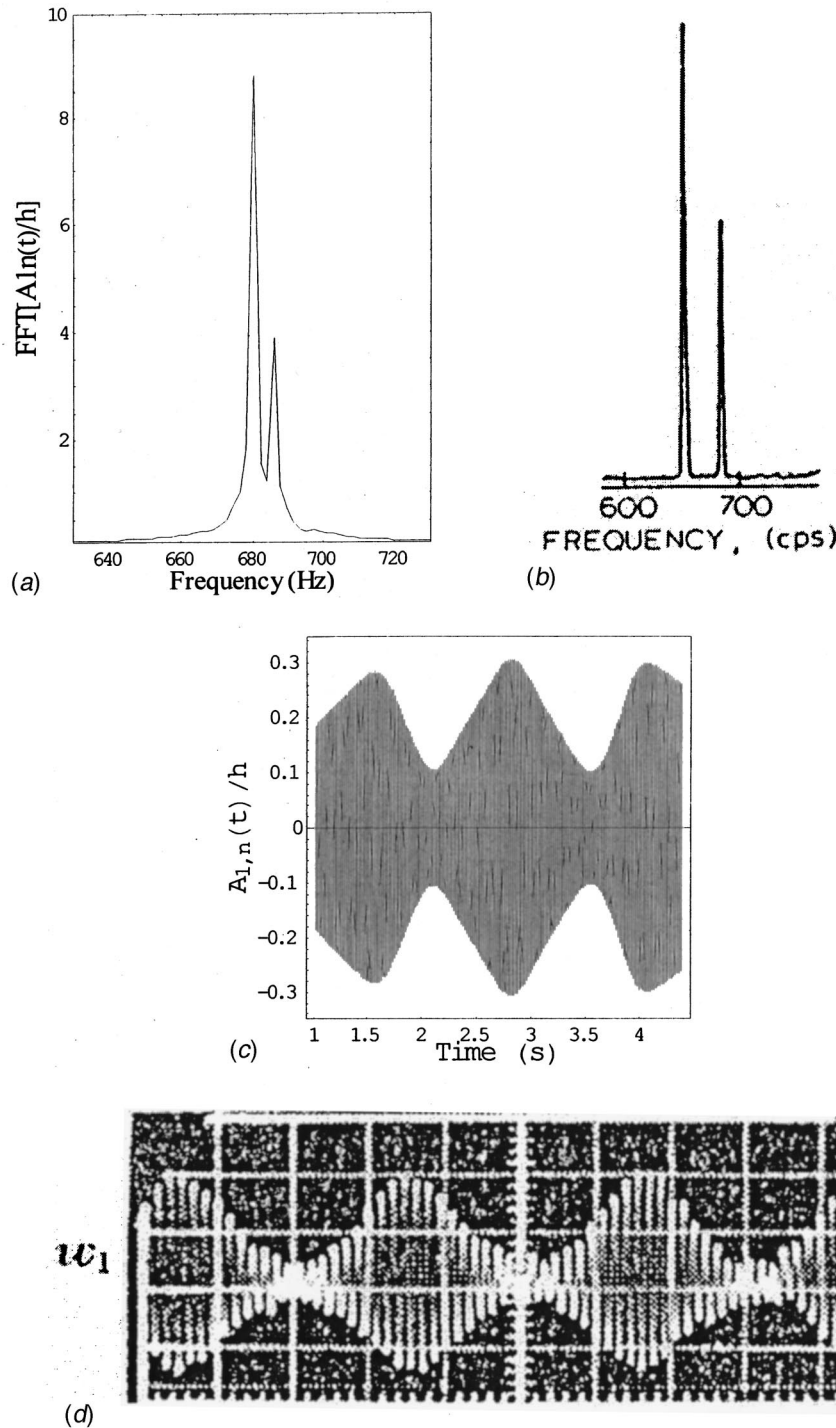


Fig. 9 Flutter response of the shell for  $p_{\infty}=6500$  Pa;  $n=24$ ,  $p_m=5000$  Pa; imperfect shell ( $\bar{B}_{1,24}=0.18h$ ,  $\bar{A}_{3,24}=0.0966h$ ,  $\bar{A}_{1,0}=2.46h$ ), linear piston theory. (a) Time history of the first longitudinal mode  $A_{1,n}(t)/h$ ; (b) experimental time history ([3]); (c) spectrum of the first longitudinal mode  $A_{1,n}(t)/h$ ; (d) experimental spectrum ([3]).

geometric imperfections is needed to better reproduce experimental results.

It can be observed that the shell used in calculations has a softening nonlinearity ([20]). However, as a consequence that at the onset of flutter there is a coalescence of the natural frequency of two shell modes with different number of longitudinal half-waves, supercritical bifurcations arise for the stable branches 2, 3, and 4. In fact, recently it has been shown ([43]) that the passage

from softening to hardening nonlinearity of a shell usually happens in correspondence of internal resonances between modes of the shells, e.g. when two modes have an integer ratio (one, two, or three) between their natural frequency.

**5.2 Shell With Geometric Imperfections.** Results show that onset of flutter is very sensitive to small initial imperfections. In particular, asymmetric imperfections are ironed out by the

pressurization of the shell, whereas the axisymmetric ones are not. This is in agreement with what predicted for buckling of circular shells by Hutchinson [44]. However, asymmetric imperfections change more significantly than axisymmetric modes the natural frequency of the first asymmetric modes, which are the most important to predict flutter boundary.

Calculations have been performed with different combinations of asymmetric and axisymmetric imperfections. However, for sake of brevity, all the results reported in this section are relative to the shell having the following geometric imperfections:  $\bar{B}_{1,24} = 0.18h$ ,  $\bar{A}_{3,24} = 0.0966h$ , and  $\bar{A}_{1,0} = 2.46h$ ; all the other coefficients in Eq. (10) are zero. Considering that  $h$  is about 0.1 mm, the asymmetric imperfections are almost imperceptible and the axisymmetric imperfection, which plays a much smaller role, is compatible with the soldered connection of the shell to end rings, giving deflection inwards. Calculations have been performed by linear piston theory and 18 modes have been used in the expansion of  $w$ . The expansion is the one in Eq. (9b) with the option of a maximum of six longitudinal half-waves and  $k = 1$ .

The solution of the linear eigenvalue problem for the shell without flow shows that imperfections having an odd number of longitudinal half-waves slightly reduce the natural frequencies of modes with an odd number of longitudinal half-waves and increase more substantially the frequency of modes with an even number of longitudinal half-waves. Moreover, imperfections having an angular orientation (e.g., described by  $\cos(n\theta)$ ) have a significant effect only on the same orientation.

Figure 7 shows the flutter boundary versus the pressure differential across the shell skin for the imperfect shell. Experimental results obtained at the NASA Ames Research Center in 1964 ([3,19]) are also shown for comparison. The computed results are in satisfactory agreement with the experiments. In particular, the onset of flutter initially increases quickly with the pressure differential  $p_m$  up to a maximum. This part of the curve is associated with a Hopf bifurcation arising from merging of the frequencies of modes with two and three longitudinal half-waves; these modes are the first to merge, i.e., to give flutter, for the imperfect shell. The second part of the curve, on the right of the maximum, is associated with a Hopf bifurcation arising from merging of the frequencies of modes with one and two longitudinal half-waves; for increased pressure  $p_m$  these modes are the first to merge, as has been obtained for the perfect shell.

It can be observed that the maximum of the computed curve in Fig. 7 is moved on the left with respect to experiments. Actually imperfections should be studied on a statistical basis since data on the specimens used in the experiments are not available. Moreover, imperfections having different numbers of circumferential waves with respect to the fluttering mode should be considered. However, the imperfections introduced reproduce the experimental results of Olson and Fung who observed that ([3]): (i) small internal pressurization was very stabilizing; (ii) moderate pressurization reduced stability to the unpressurized level; (iii) high internal pressure completely stabilized the shell. In particular, observation (ii) was very surprising at that time. This observed behavior is well explained by asymmetric imperfections that are ironed out by moderate pressurization of the shell.

In Fig. 8 the curves correspond to maximum flutter amplitudes of the shell (excluding branch 1) for the same imperfect shell studied in Fig. 7 for  $p_m = 5000$  Pa; only the generalized coordinates  $A_{1,n}$ ,  $B_{1,n}$ ,  $A_{2,n}$ , and  $B_{2,n}$  are represented for brevity. With respect to Fig. 1, all branches (excluding branch 1) correspond to travelling-wave flutter. The shell loses stability by Hopf bifurcation at  $p_\infty = 3067$  Pa; a second Hopf bifurcation arises at  $p_\infty = 3176$  Pa. The increased pressurization  $p_m$  and the presence of imperfections reduce the flutter amplitudes with respect to Fig. 1. The flutter amplitudes obtained in Fig. 8 are in excellent agreement with experimental results described by Olson and Fung [3] where a flutter amplitude of about  $0.5h$  rms is reported at  $x/L = 0.72$ , corresponding to about  $0.7h$  for simple-harmonic oscilla-

tions. The attractive solution is branch 2, and corresponds to travelling-wave flutter with and without amplitude modulations, according to the stability of the simple periodic oscillation indicated in Fig. 8. In particular, for  $4662 < p_\infty < 8373$  Pa, i.e., between two Neimark-Sacker bifurcations, for  $8418 < p_\infty < 9598$  Pa and for  $p_\infty > 9783$  (up to the upper limit 10,000 Pa computed) travelling-wave flutter with amplitude modulations arises. The flutter frequency has only small variations, similar to Fig. 4, around 677 Hz; this value is also in very good agreement with experimental results, as shown in Fig. 7 in reference ([3]).

A comparison between theoretical and experimental results for flutter with amplitude modulations is given in Fig. 9. The experimental results are taken from reference ([3]) where no information is given on the values of  $p_m$  and  $p_\infty$  for which these experimental data were recorded. However, even if it is not possible to say that these theoretical and experimental results correspond exactly to the same conditions, it was observed that the flutter frequency does not change significantly with  $p_m$  and  $p_\infty$ ; Fig. 9 shows that calculations and experiments are in good agreement.

It seems to us that a numerical model capable of reproducing quantitatively the experimental results obtained at the NASA Ames Research Center in 1964 has been developed for the first time in the present paper.

## 6 Conclusions

Results show that the prediction of the onset of flutter of pressurized circular shells requires knowledge of the amount of axisymmetric imperfections. In fact, asymmetric imperfections are ironed out by the pressure, whereas the axisymmetric ones are not.

Numerical results have been obtained at Mach number 3. In this case, the results obtained by using the linear and the third-order piston theories are almost identical.

The predicted nature of flutter was a travelling-wave around the circumference and the amplitude of the order of the shell thickness, giving mild flutter, in agreement with existing experimental results. In particular, both harmonic and amplitude-modulated flutter has been predicted, in agreement with experimental data; flutter changes from harmonic to amplitude-modulated through Neimark-Sacker (torus) bifurcations. It is very important to observe that the nature of the Hopf bifurcation is supercritical for all the calculations performed for Mach number  $M = 3$ . This is also in agreement with the experiments available that show mild supersonic flutter with amplitude gradually increasing with the freestream static pressure (i.e., with the flight speed). Differently, for subsonic incompressible flow, highly catastrophic subcritical divergence was always observed by Amabili et al. [29,30].

The influence of pressure differential across the shell skin has also been investigated in detail. The present study gives, for the first time, numerical results in agreement with experimental data obtained at the NASA Ames Research Center more than three decades ago.

## Acknowledgments

The authors acknowledge the financial support of the COFIN 2000 granting program of the Italian Ministry for University and Scientific Research (MURST) and the Italian Space Agency (ASI).

## References

- [1] Ashley, H., and Zartarian, G., 1956, "Piston Theory—A New Aerodynamic Tool for the Aeroelastician," *J. Aeronaut. Sci.*, **23**, pp. 1109–1118.
- [2] Dowell, E. H., 1966, "Flutter of Infinitely Long Plates and Shells. Part II: Cylindrical Shell," *AIAA J.*, **4**, pp. 1510–1518.
- [3] Olson, M. D., and Fung, Y. C., 1966, "Supersonic Flutter of Circular Cylindrical Shells Subjected to Internal Pressure and Axial Compression," *AIAA J.*, **4**, pp. 858–864.
- [4] Barr, G. W., and Stearman, R. O., 1970, "Influence of a Supersonic Flowfield on the Elastic Stability of Cylindrical Shells," *AIAA J.*, **8**, pp. 993–1000.

- [5] Ganapathi, M., Varadan, T. K., and Jijen, J., 1994, "Field-Consistent Element Applied to Flutter Analysis of Circular Cylindrical Shells," *J. Sound Vib.*, **171**, pp. 509–527.
- [6] Horn, W., Barr, G. W., Carter, L., and Stearman, R. O., 1974, "Recent Contributions to Experiments on Cylindrical Shell Panel Flutter," *AIAA J.*, **12**, pp. 1481–1490.
- [7] Dowell, E. H., 1970, "Panel Flutter: A Review of the Aeroelastic Stability of Plates and Shells," *AIAA J.*, **8**, pp. 385–399.
- [8] Bismarck-Nasr, M. N., 1992, "Finite Element Analysis of Aeroelasticity of Plates and Shells," *Appl. Mech. Rev.*, **45**, pp. 461–482.
- [9] Mei, C., Abel-Motagaly, K., and Chen, R., 1999, "Review of Nonlinear Panel Flutter at Supersonic and Hypersonic Speeds," *Appl. Mech. Rev.*, **52**, pp. 321–332.
- [10] Librescu, L., 1965, "Aeroelastic Stability of Orthotropic Heterogeneous Thin Panels in the Vicinity of the Flutter Critical Boundary. Part I: Simply Supported Panels," *Journal de Mécanique* **4**, pp. 51–76.
- [11] Librescu, L., 1967, "Aeroelastic Stability of Orthotropic Heterogeneous Thin Panels in the Vicinity of the Flutter Critical Boundary. Part II," *Journal de Mécanique* **6**, pp. 133–152.
- [12] Librescu, L., 1975, *Elastostatics and Kinetics of Anisotropic and Heterogeneous Shell-Type Structures*, Noordhoff, Leiden, The Netherlands.
- [13] Olson, M. D., and Fung, Y. C., 1967, "Comparing Theory and Experiment for the Supersonic Flutter of Circular Cylindrical Shells," *AIAA J.*, **5**, pp. 1849–1856.
- [14] Evensen, D. A., and Olson, M. D., 1967, "Nonlinear Flutter of a Circular Cylindrical Shell in Supersonic Flow," *NASA TN D-4265*.
- [15] Evensen, D. A., and Olson, M. D., 1968, "Circumferentially Travelling Wave Flutter of a Circular Cylindrical Shell," *AIAA J.*, **6**, pp. 1522–1527.
- [16] Evensen, D. A., 1967, "Nonlinear Flexural Vibrations of Thin-Walled Circular Cylinders," *NASA TN D-4090*.
- [17] Olsson, U., 1978, "Supersonic Flutter of Heated Circular Cylindrical Shells With Temperature-Dependent Material Properties," *AIAA J.*, **16**, pp. 360–362.
- [18] Carter, L. L., and Stearman, R. O., 1968, "Some Aspects of Cylindrical Shell Panel Flutter," *AIAA J.*, **6**, pp. 37–43.
- [19] Barr, G. W., and Stearman, R. O., 1969, "Aeroelastic Stability Characteristics of Cylindrical Shells Considering Imperfections and Edge Constraint," *AIAA J.*, **7**, pp. 912–919.
- [20] Amabili, M., and Pellicano, F., 2001, "Nonlinear Supersonic Flutter of Circular Cylindrical Shells," *AIAA J.*, **39**, pp. 564–573.
- [21] Bolotin, V. V., 1963, *Nonconservative Problems of the Theory of Elastic Stability*, MacMillan, New York.
- [22] Dowell, E. H., 1969, "Nonlinear Flutter of Curved Plates," *AIAA J.*, **7**, pp. 424–431.
- [23] Dowell, E. H., 1970, "Nonlinear Flutter of Curved Plates, II," *AIAA J.*, **8**, pp. 259–261.
- [24] Vol'mir, S., and Medvedeva, S. V., 1973, "Investigation of The Flutter of Cylindrical Panels in a Supersonic Gas Flow," *Sov. Phys. Dokl.*, **17**, pp. 1213–1214.
- [25] Krause, H., and Dinkler, D., 1998, "The Influence of Curvature on Supersonic Panel Flutter," *Proceedings of the 39th AIAA/ASME/ASCE/AHS/ASC Structures, Structural Dynamics and Materials Conference*, Long Beach, CA, AIAA, Washington, DC, pp. 1234–1240.
- [26] Bein, T., Friedmann, P. P., Zhong, X., and Nydick, I., 1993, "Hypersonic Flutter of a Curved Shallow Panel With Aerodynamic Heating," *34th AIAA/ASME/ASCE/AHS/ASC Structures, Structural Dynamics and Materials Conference*, Apr. 19–22, La Jolla, CA, AIAA, Washington, DC, pp. 1–15.
- [27] Nydick, I., Friedmann, P. P., and Zhong, X., 1995, "Hypersonic Panel Flutter Studies on Curved Panels," *Proceedings of the 36th AIAA/ASME/ASCE/AHS/ASC Structures, Structural Dynamics and Materials Conference*, Vol. 5, Apr. 10–13, New Orleans, LA, AIAA, Washington, DC, pp. 2995–3011.
- [28] Anderson, W. J., 1962, "Experiments on the flutter of flat and slightly curved panels at Mach Number 2.81," AFOSR 2996, Graduate Aeronautical Laboratories, California Institute of Technology, Pasadena, CA.
- [29] Amabili, M., Pellicano, F., and Paidoussis, M. P., 1999, "Non-Linear Dynamics and Stability of Circular Cylindrical Shells Containing Flowing Fluid. Part I: Stability," *J. Sound Vib.*, **225**, pp. 655–699.
- [30] Amabili, M., Pellicano, F., and Paidoussis, M. P., 2001, "Non-Linear Stability of Circular Cylindrical Shells in Annular and Unbounded Axial Flow," *ASME J. Appl. Mech.*, **68**, pp. 827–834.
- [31] El Chebair, A., Paidoussis, M. P., and Misra, A. K., 1989, "Experimental Study of Annular-Flow-Induced Instabilities of Cylindrical Shells," *J. Fluids Struct.*, **3**, pp. 349–364.
- [32] Amabili, M., and Paidoussis, M. P., 2001, "Review of Studies on Geometrically Nonlinear Vibrations and Dynamics of Circular Cylindrical Shells and Panels, With and Without Fluid-Structure Interaction," *Appl. Mech. Rev.*, submitted for publication.
- [33] Watawala, L., and Nash, W. A., 1983, "Influence of Initial Geometric Imperfections on Vibrations of Thin Circular Cylindrical Shells," *Comput. Struct.*, **16**, pp. 125–130.
- [34] Hui, D., 1984, "Influence of Geometric Imperfections and In-Plane Constraints on Nonlinear Vibrations of Simply Supported Cylindrical Panels," *ASME J. Appl. Mech.*, **51**, pp. 383–390.
- [35] Yamaki, N., 1984, *Elastic Stability of Circular Cylindrical Shells*, North-Holland, Amsterdam.
- [36] Dowell, E. H., and Ventres, C. S., 1968, "Modal Equations for the Nonlinear Flexural Vibrations of a Cylindrical Shell," *Int. J. Solids Struct.*, **4**, pp. 975–991.
- [37] Amabili, M., Pellicano, F., and Paidoussis, M. P., 1999, "Non-Linear Dynamics and Stability of Circular Cylindrical Shells Containing Flowing Fluid, Part II: Large Amplitude Vibrations Without Flow," *J. Sound Vib.*, **228**, pp. 1103–1124.
- [38] Amabili, M., Pellicano, F., and Paidoussis, M. P., 2000, "Non-Linear Dynamics and Stability of Circular Cylindrical Shells Containing Flowing Fluid, Part III: Truncation Effect Without Flow and Experiments," *J. Sound Vib.*, **237**, pp. 617–640.
- [39] Wolfram, S., 1999, *The Mathematica Book*, 4th Ed., Cambridge University Press, Cambridge, UK.
- [40] Krumhaar, H., 1963, "The Accuracy of Linear Piston Theory When Applied to Cylindrical Shells," *AIAA J.*, **1**, pp. 1448–1449.
- [41] Doedel, E. J., Champneys, A. R., Fairgrieve, T. F., Kuznetsov, Y. A., Sandstede, B., and Wang, X., 1998, *AUTO 97: Continuation and Bifurcation Software for Ordinary Differential Equations (With HomCont)*, Concordia University, Montreal, Canada.
- [42] Wiggins, S., 1990, *Introduction to Applied Nonlinear Dynamical Systems and Chaos*, Springer-Verlag, New York.
- [43] Pellicano, F., Amabili, M., and Paidoussis, M. P., 2001, "Effect of the Geometry on the Nonlinear Vibration of Circular Cylindrical Shells," *Int. J. Non-Linear Mech.*, submitted for publication.
- [44] Hutchinson, J., 1965, "Axial Buckling of Pressurized Imperfect Cylindrical Shells," *AIAA J.*, **3**, pp. 1461–1466.



# Stress Field in Finite Width Axisymmetric Wound Rolls

**Y. M. Lee**

Associate Mem. ASME

**J. A. Wickert**

Fellow ASME

Department of Mechanical Engineering,  
Carnegie Mellon University,  
Pittsburgh, PA 15213-3890

*A model is developed for predicting the stress field within a wound roll of web material, in which the radial, circumferential, transverse, and shear stresses can vary in both the roll's radial and cross-web (transverse) directions. As has been the case in previous wound roll stress analyses based on one-dimensional models, the present approach accounts for the anisotropic and nonlinear material properties of the layered web material, and the incremental manner in which the roll is wound. In addition, the present development accounts for arbitrary cross-sectional geometry and material of the core, and the presence of nonuniform tension across the web's width during winding. The solution is developed through an axisymmetric, two-dimensional, finite element analysis which couples individual models of the core and layered web region substructures. The core's stiffness matrix at the core-web interface provides a mixed boundary condition for the web region's first layer. In several parameter studies, variations of the stress components in the roll's radial and cross-width directions are discussed and compared with predictions of the simpler companion one-dimensional model. The character of the stress field at the web region's free edges and along the core-web interface, and the possibility of stress concentration or singularity existing there, are also discussed. [DOI: 10.1115/1.1429934]*

## 1 Introduction

Continuous sheets of metal, paper, polymer, and other thin materials are encountered in diverse products and industries. Such "web" materials are flexible mechanical structures that are transported under tension and at high speed during their production and processing. In short, wound rolls formed around a central core are common in manufacturing environments, and are generally the most economical and practical format for material storage and transportation.

The stress field within a roll develops incrementally as the first layer is wrapped onto a core, followed by the addition of many more discrete layers. The resulting stresses determine to a large extent the roll's quality, and can contribute to such failure modes as core collapse, interlayer buckling, and starring. While solutions to such problems can be engineered through empiricism and cut-and-try efforts, the roll's state of stress preferably meets certain design criteria. For instance, the circumferential stress within a web layer at a given point in the roll can be tensile or compressive, but excessive compression can lead to local buckling. Likewise, desirable radial stresses are large enough to prevent individual layers from slipping relative to one another, but not so great as to cause surface damage.

Research pertaining to the stress analysis of wound rolls has a rich history and has emphasized the development of one-dimensional models wherein the core and web are each treated as being infinitely wide. Those models account for anisotropic and nonlinear material properties, the bulk compliance of the core, and the roll's layered structure. Uniform mechanical properties and tension across the width are likewise specified, and a key assumption used in such one-dimensional models is the specification of core stiffness being uniform across the roll's width, a restriction that is re-examined here.

Altmann [1] treated each web layer as an orthotropic pseudoelastic material, and developed a linear wound roll model with

solutions that could be expressed in the form of easily computed integrals. Motivated by applications in magnetic tape data storage, Tramosch [2,3] investigated the viscoelastic characteristics of polymeric substrates, and developed a linear, anisotropic, and time-dependent model to examine stress relaxation in wound rolls. Yagoda [4] demonstrated that the circumferential stress in the vicinity of the core depends strongly on its stiffness. In short, a soft core does not substantially resist the compression afforded by the web layers, in turn generating high compressive circumferential stresses near the core-web interface and facilitating defects. Connolly and Winarski [5] surveyed the Altmann and Tramosch formulations, presented parameter studies in Poisson ratio, radial modulus, winding tension, core radius and thickness, and evaluated such environmental factors as temperature and humidity.

Each of the aforementioned studies specified that the layered region in the wound roll had linear, albeit anisotropic, elastic properties. However, at the bulk level, the elastic modulus in the layered web region's radial direction is known to be a nonlinear function of the radial stress. Even for such seemingly well-understood materials as sheet steel or aluminum, the wound roll stress problem is intrinsically nonlinear, with the roll being properly viewed as a composite, anisotropic, and nonlinear structure ([6]). Hakiel [7] and Willett and Poesch [8] represented the layered region's effective bulk radial modulus as a polynomial function of the radial stress, and approached the solution through finite difference methods. Other processes that contribute to bulk material nonlinearity include air entrainment within the roll ([9,10]) and asperity compliance at the surfaces of the individual web layers.

Wound roll stress analysis is also governed by the effects of wound-in tension loss, viscoelastic response, and the finite deformation of materials that are substantially soft in the roll's radial direction. Good et al. [11] accounted for tension losses within centerwound rolls of highly compressible materials due to reduced interior radius. With corrected values for the wound-in tension, a modified and more accurate stress model was developed based on Hakiel's approach. Zabarar et al. [12] considered the deformation history of magnetic tape during winding and developed a hypoelastic finite element model which accounts for variable loading rates. Qualls and Good [13] extended previous linear analyses of viscoelastic winding mechanics by accounting for the roll's nonlinear bulk radial modulus. Benson [14] developed an alternative approach to the wound roll problem by accounting for the geo-

Contributed by the Applied Mechanics Division of THE AMERICAN SOCIETY OF MECHANICAL ENGINEERS for publication in the ASME JOURNAL OF APPLIED MECHANICS. Manuscript received by the ASME Applied Mechanics Division, Oct. 2, 2000; final revision, June 5, 2001. Associate Editor: J. R. Barber. Discussion on the paper should be addressed to the Editor, Professor Lewis T. Wheeler, Department of Mechanical Engineering, University of Houston, Houston, TX 77204-4792, and will be accepted until four months after final publication of the paper itself in the ASME JOURNAL OF APPLIED MECHANICS.



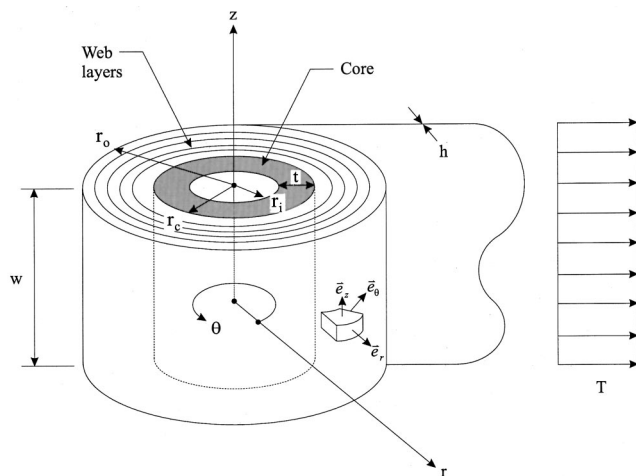


**Fig. 1 Schematic of a finite width wound roll comprising the inner core and wound web regions**

metric nonlinearity that arises when web layers are highly compliant. In that approach, finite radial displacements within the roll were treated by monitoring the position of material particles using a lap index, rather than radius, so as to mark the same material location regardless of the deformation level.

These modeling issues play an important part in wound roll stress analyses, and challenge the development of efficient numerical methods to predict stresses that can vary in more than one spatial dimension. Some so-called two-dimensional wound roll models have been examined by Hakiel [15], Kedl [16], and Cole and Hakiel [17] with a view toward understanding such width-wise variations as the outside roll's radius, winding tension, and stress field due to changes in material thickness. In those views, width-wise variations were modeled under the assumptions that the roll could be partitioned across its width into strips or segments that do not couple, and that within each segment, the stresses and displacements are width-independent and can be calculated through a one-dimensional analysis.

The wound roll examined in the present study comprises core and web regions of finite width, as depicted in Fig. 1. Aside from core stiffness, the winding tension, material thickness, and elastic properties can in principle also be nonuniform. Such realistic attributes are not captured in a one-dimensional model, and it is an objective of this investigation to develop the methodology to assess their importance. To the extent that the radial compliance of the core varies along the axis of its generator, the innermost web layer is subjected to a stiffness boundary condition that varies across the web's width. In what follows, by accounting for differential core compliance, transverse stress, and shear stress, the model is capable of predicting the manner in which the wound roll's stress field varies in both the roll's radial and cross-web directions. In several parameter studies, the extent to which stresses vary in the cross-width direction is discussed, and the results are compared with those obtained from the simpler one-dimensional model. Of further interest are the character of the stress field at the web's free edges and along the core-web interface, and the possibility of stress concentration or singularity existing at those points.

## 2 Core and Wound Roll Model

**2.1 Geometry and Boundary Conditions.** Figure 1 depicts a prototypical roll of finite width  $w$  which is formed by winding continuous web material at specified tension  $T$  onto a core. Shown illustratively in Fig. 1 as a hollow cylinder, the core has inner radius  $r_i$ , wall thickness  $t$ , and coordinates  $r-\theta-z$  centered in the roll. In what follows, the core is treated as having an arbitrary

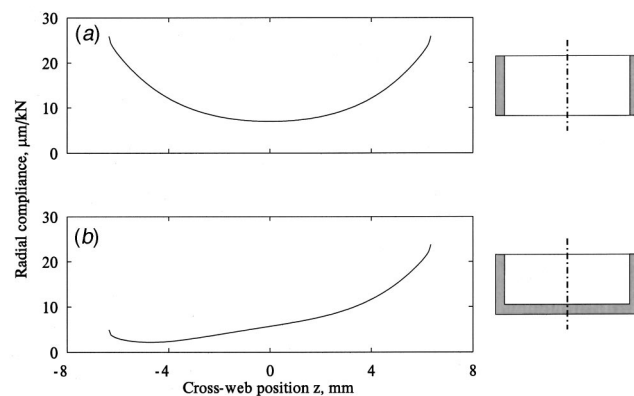


**Fig. 2 Collocated point radial compliance of (a) hollow cylindrical and (b) cup-shaped cores. The parameter values are as specified in Table 1 (plastic).**

but axisymmetric geometry, so that the modeled problem has somewhat greater generality than that depicted in Fig. 1. The web itself has thickness  $h$ , and it is wound layer-by-layer into a cylindrical shape having outer radius  $r_o$  and inner radius  $r_c$  common with the core. As an incrementally layered structure, the web region is a composite with bulk anisotropic properties, and is formed from  $N$  individual layers that have been shrunk-fit onto one another.

The materials and elastic properties of the core and layered web regions in Fig. 1 generally differ. For two core designs, Fig. 2 depicts the manner in which the core's compliance changes in the roll's width-wise direction. Each core has properties and dimensions as specified in Table 1 (plastic). The collocated point compliance is recorded in Fig. 2 with respect to the core's radial direction. The hollow cylindrical core in Fig. 2(a) has a symmetric stiffness distribution in  $z$ , with the compliance at the core's free edges being some three times greater than at the centerline. For the cup-shaped core shown in Fig. 2(b), the asymmetric stiffness profile varies nearly tenfold between the closed and open ends. To the extent that the core's compliance establishes one boundary condition that is afforded to the layered web region, it is problem-

**Table 1 Baseline parameter values used in the case studies**

Core		
Modulus, $E$	3.5 (plastic)	GPa
	70 (aluminum)	GPa
Poisson ratio, $\nu$	0.43 (plastic)	—
	0.33 (aluminum)	—
Outer radius, $r_o$	25.0	mm
Width, $w$	12.7	mm
Thickness, $t$	2.5	mm

### Web

Tension, $T$	1.0	N
Number of layers, $NL$	3000	—
Width, $w$	12.7	mm
Thickness, $h$	10.0	$\mu\text{m}$
Bulk modulus, $E_r$ ( $ \sigma_r  < 4$ MPa)	$10 \sigma_r ^3 - 120 \sigma_r ^2 + 590 \sigma_r  + 7$	MPa
Circumferential modulus, $E_\theta$	7	GPa
Transverse modulus, $E_z$	9	GPa
Shear modulus, $G_{rz}$	100	MPa
Poisson ratio, $\nu_{\theta z} = \nu_{\theta r} = \nu_{zr}$	0.3	—

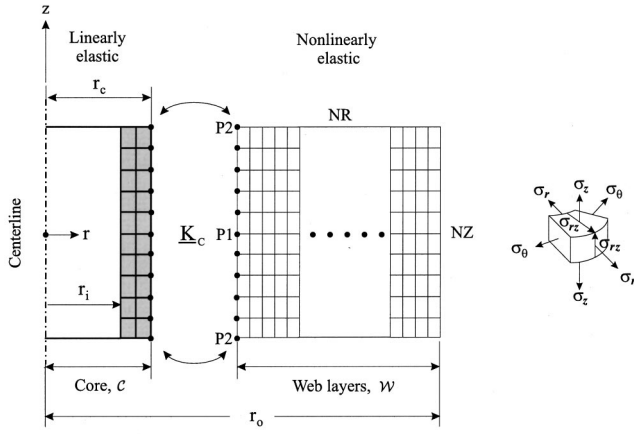


**Fig. 3 Axisymmetric finite element model used to determine wound roll stresses  $\sigma_r$ ,  $\sigma_\theta$ ,  $\sigma_z$ , and  $\sigma_{rz}$ , shown illustratively for a hollow cylindrical core**

atic of one-dimensional wound roll models that such gradients and their influence on the roll's stress field cannot be captured.

Stress components  $\sigma_r$ ,  $\sigma_\theta$ ,  $\sigma_z$ , and  $\sigma_{rz}$  within the core and web regions are each functions of  $r$  and  $z$ , and equilibrium solutions are subject to certain displacement and traction boundary conditions. For instance, rigid-body motion of a hollow cylindrical core is suppressed by specifying that transverse displacement vanishes at the center  $(r_i, 0)$  of the inner core's surface. As each layer is added to the roll, traction conditions over the boundary are imposed as follows:

- inner core surface  $r=r_i$ ,  $z \in [-w/2, w/2]$ , and  $z \neq (r_i, 0)$ :  $\sigma_r = \sigma_{rz} = 0$ ,
- upper and lower core surfaces  $z = \pm w/2$  and  $r \in [r_i, r_c]$ :  $\sigma_z = \sigma_{rz} = 0$ ,
- upper and lower web surfaces  $z = \pm w/2$  and  $r \in [r_c, r_o]$ :  $\sigma_z = \sigma_{rz} = 0$ ,
- outer web surface  $r=r_o$  and  $z \in [-w/2, w/2]$ :  $\sigma_{rz} = 0$  and  $\sigma_r = T/(w(r_c + (n-1)h))$

where  $n$  ( $1 \leq n \leq NL$ ) is the integer index of the current layer, and  $NL$  is the total number of layers on the fully formed roll.

**2.2 Substructure Stiffness Matrices.** In order to account for realistic core geometry and designs, the wound roll is separated into substructures  $\mathcal{C} = \{(r, \theta, z): r < r_c, 0 < \theta < 2\pi, -w/2 < z < w/2\}$  over the core and  $\mathcal{W} = \{(r, \theta, z): r_c < r < r_o, 0 < \theta < 2\pi, -w/2 < z < w/2\}$  over the layered web region, as indicated in Fig. 3. Each substructure is discretized locally through finite element, and they couple through the interfacial core-web stiffness matrix  $\mathbf{K}_C$ . Unit loads are applied sequentially to those nodes in the core substructure's model which are located along the core-web interface, and the corresponding nodal displacements are recorded. Inversion of the flexibility matrix so obtained, formed of displacement vectors in  $r$  and  $z$ , provides matrix  $\mathbf{K}_C$  of dimension  $2(NZ + 1) \times 2(NZ + 1)$ , where  $NZ$  is the number of elements allocated in  $z$  along the core's axis. Because of the potential variety of core materials and geometry,  $\mathbf{K}_C$  is analyzed by using a commercial finite element package. In that manner, the present method is applicable to designs having arbitrary shape in  $z$ , and isotropic, orthotropic, or anisotropic material properties. For illustration in the case studies which follow, two prototypical core designs—cylindrical and cup-shaped—are considered, each having isotropic properties.

In terms of the layered web region, the equilibrium requirements, constitutive equations and conditions of compatibility are represented in terms of the displacement field  $\mathbf{u} = \{u, w\}^T$  as  $\mathbf{A}\mathbf{u} = \mathbf{0}$ , where  $\mathbf{A}$  is a matrix differential operator, and  $\mathbf{u}(r, z)$  and

$w(r, z)$  are the radial and transverse displacements in  $\mathcal{W}$ , respectively. The stress field is determined through the method of weighted residuals, and the weak form of the equilibrium conditions is given by the volume integral

$$\delta \int_{\mathcal{W}} \mathbf{u}^T \mathbf{A} \mathbf{u} d\mathcal{W} = 0 \quad (1)$$

which provides governing equations over  $\mathcal{W}$ , the rectangular cross-section  $\mathcal{A} = \{(r, z): r_c < r < r_o \text{ and } -w/2 < z < w/2\}$ , and the boundary  $\delta\mathcal{A} = \{(r, z): r = r_c \text{ or } r = r_o \text{ and } -w/2 < z < w/2\} \cup \{r_c < r < r_o \text{ and } z = \pm w/2\}$ . Those conditions become

$$\int_{\mathcal{W}} \delta \mathbf{u} \left( \frac{1}{r} (r \sigma_r)_{,r} - \frac{\sigma_\theta}{r} + \sigma_{rz,z} \right) + \delta w \left( \frac{1}{r} (r \sigma_{rz})_{,r} + \sigma_{z,z} \right) d\mathcal{W} = 0 \quad (2)$$

or

$$2\pi \int_{\mathcal{A}} \delta u ((r \sigma_r)_{,r} - \sigma_\theta + r \sigma_{rz,z}) + \delta w ((r \sigma_{rz})_{,r} + r \sigma_{z,z}) d\mathcal{A} = 0, \quad (3)$$

and

$$2\pi \int_{\mathcal{A}} \left( r \sigma_r (\delta u)_{,r} + r \sigma_\theta \left( \frac{\delta u}{r} \right) + r \sigma_z (\delta w)_{,z} + r \sigma_{rz} ((\delta u)_{,z} + (\delta w)_{,r}) \right) d\mathcal{A} - 2\pi \int_{\delta\mathcal{A}} (\delta u (\sigma_r n_r + \sigma_{rz} n_z) + \delta w (\sigma_{rz} n_r + \sigma_z n_z)) r d\delta\mathcal{A} = 0, \quad (4)$$

or

$$2\pi \int_{\mathcal{A}} (\delta \epsilon^T \boldsymbol{\sigma}) r d\mathcal{A} - 2\pi \int_{\delta\mathcal{A}} (\delta \mathbf{u}^T \mathbf{t}) r d\delta\mathcal{A} = 0 \quad (5)$$

where  $\mathbf{n} = \{n_r, n_z\}^T$  is the unit normal, strains  $\boldsymbol{\epsilon} = \{\epsilon_r, \epsilon_\theta, \epsilon_z, \gamma_{rz}\}^T$ , stresses  $\boldsymbol{\sigma} = \{\sigma_r, \sigma_\theta, \sigma_z, \sigma_{rz}\}^T$ , and tractions  $\mathbf{t} = \{\sigma_r n_r + \sigma_{rz} n_z, \sigma_{rz} n_r + \sigma_z n_z\}^T$ .

Equation (5) is discretized locally by using four node, rectangular, axisymmetric finite elements, each having eight degrees-of-freedom. The displacement field within each element is given by

$$\mathbf{u}^e = \sum_{j=1}^4 N_j \mathbf{a}_j^e \quad (6)$$

in terms of shape functions  $N_j = (a \pm (r - r_m))(b \pm z)/(4ab)$  and nodal displacements  $\mathbf{a}_j^e = \{u_j^e, w_j^e\}^T$ . Here  $r_m$ ,  $2a$ , and  $2b$  are the mean radius, width, and height of each element, respectively, as in Fig. 3. The discretized (5) then becomes

$$\sum_{i=1}^{NE} \delta \mathbf{u}_i^{eT} \left( 2\pi \int_{\mathcal{A}^e} \mathbf{B}_i^T (\mathbf{D}_i (\mathbf{B}_i \mathbf{a}_i^e - \boldsymbol{\epsilon}_{0i}) + \boldsymbol{\sigma}_{0i}) d\mathcal{A}^e - 2\pi \int_{\delta\mathcal{A}^e} \mathbf{N}_i^T \mathbf{t}_i r d\delta\mathcal{A}^e \right) = 0 \quad (7)$$

where  $NE = NR \times NZ$  is the total number of elements with  $NR$  in the radial direction,  $\mathbf{D}_i$  is the elasticity matrix,  $\mathbf{B}_i = \{\boldsymbol{\theta}\} \{N_i\}$  is the derivative of the strain-displacement relations with  $[\boldsymbol{\theta}] = [\partial/\partial r, 0; 1/r, 0; 0, \partial/\partial z; \partial/\partial z, \partial/\partial r]$ , and  $\boldsymbol{\epsilon}_{0i}$  and  $\boldsymbol{\sigma}_{0i}$  are the initial strain and stress in the  $i$ th element.

Since  $\delta \mathbf{u}_i^{eT}$  in Eq. (7) is arbitrary, solutions satisfy  $\mathbf{K}_i^e \mathbf{a}_i^e = \mathbf{f}_i^e$  in terms of the  $8 \times 8$  elemental stiffness matrix

$$\mathbf{K}_i^e = 2\pi \int_{\mathcal{A}^e} \mathbf{B}_i^T \mathbf{D}_i \mathbf{B}_i d\mathcal{A}^e \quad (8)$$

and the  $8 \times 1$  elemental load vector

$$\mathbf{f}_i^e = 2\pi \int_{\delta\mathcal{A}^e} \mathbf{N}_i^T \mathbf{t}_i r d\delta\mathcal{A}^e + 2\pi \int_{\mathcal{A}^e} \mathbf{B}_i^T \mathbf{D}_i \boldsymbol{\epsilon}_{0i} d\mathcal{A}^e - 2\pi \int_{\mathcal{A}^e} \mathbf{B}_i^T \boldsymbol{\sigma}_{0i} d\mathcal{A}^e. \quad (9)$$

As the  $n$ th layer is incrementally added to the roll, the  $2(n+1)(NZ+1) \times 2(n+1)(NZ+1)$  stiffness matrix over  $\mathcal{W}$  is determined through  $\mathbf{K}_W = \sum_{i=1}^N \mathbf{K}_i^e$ , prior to the specification of boundary conditions. Likewise, the  $2(n+1)(NZ+1) \times 1$  vector of nodal loads becomes  $\mathbf{F} = \sum_{i=1}^N \mathbf{f}_i^e$ . Summation here indicates the assembly of elemental matrices or vectors by the addition of overlapping terms at adjoining nodes, which requires a connectivity matrix relating the local elemental nodes to the global structural ones. The procedure is described in detail by Zienkiewicz and Taylor [18]. The structure-level stiffness matrix of the entire wound roll  $\mathcal{R}$  having boundary conditions as specified above becomes  $\mathbf{K}_R = \mathbf{K}_C + \mathbf{K}_W$ , where assembly of the matrices corresponding to the interfacial nodes along  $r = r_c$  is implied.

In this manner, the equilibrium conditions are expressed by the system of simultaneous nonlinear algebraic equations  $\mathbf{K}_R(\mathbf{a})\mathbf{a} = \mathbf{F}$ . As discussed in the following section, nonlinearity arises from the stress-dependent bulk properties in  $\mathcal{W}$ , namely  $\mathbf{K}_W = \mathbf{K}_W(\boldsymbol{\sigma}_r)$ .

**2.3 Web Region Elasticity Matrix.** The elasticity matrix  $\mathbf{D}_i$  for each element  $i$  within  $\mathcal{W}$  is an important aspect of the wound roll stress model. With each layer or group of layers having polar orthotropy, some ten material constants—moduli  $E_\theta$  and  $E_z$ , bulk radial  $E_r$ , and bulk shear  $G_{rz}$  moduli, and Poisson ratios  $\nu_{\theta z}$ ,  $\nu_{\theta r}$ ,  $\nu_{zr}$ ,  $\nu_{z\theta}$ ,  $\nu_{r\theta}$ , and  $\nu_{rz}$ —are needed to specify properties in the web region. Even for typical, not to mention exotic materials, numerical values for those parameters are known with varying degrees of certainty, and it is problematic to estimate some of the parameters. For instance, the moduli  $E_\theta$  and  $E_z$ , and ratios  $\nu_{\theta z}$  and  $\nu_{z\theta}$ , can be readily measured. Since parameters  $\nu_{\theta r}$  and  $\nu_{zr}$  relate in-plane loads to out-of-plane displacements, they are challenging to measure for an already thin web layer. The specific  $E_r(\sigma_r)$  dependence can be determined experimentally through standard compression testing of a stack of web material having representative dimensions ([6,8]). By fitting a polynomial curve, for instance, to the measured data, a functional expression for the bulk-level radial modulus can be obtained.

Accurate numerical values for ratios  $\nu_{r\theta}$  and  $\nu_{rz}$ , however, are generally not available. Their measurement requires the application of compressive forces across the layer's thickness dimension,

with the measurement of corresponding displacements or strains in  $\theta$  and  $z$ . In practice, however, such compression plate fixtures invariably restrict in-plane expansion through frictional contact. Thus, conventionally in the analysis of wound roll stresses and with an acknowledged view towards expediency,  $\nu_{r\theta}$  and  $\nu_{rz}$  are approximated on the basis of a material symmetry condition. Specifically, to the extent the roll deforms elastically and in a path-independent manner,

$$\nu_{r\theta} = \nu_{\theta r} \frac{E_r}{E_\theta}, \quad \nu_{rz} = \nu_{zr} \frac{E_r}{E_z}, \quad \nu_{z\theta} = \nu_{\theta z} \frac{E_z}{E_\theta}, \quad (10)$$

the latter of which can be directly measured in principle. For the sample polymeric material in Table 1, these conditions provide the approximations  $\nu_{z\theta} = 0.233$ , and at  $\sigma_r = 1$  MPa compression,  $\nu_{r\theta} = 0.021$  and  $\nu_{rz} = 0.016$ . However, because of interlayer slippage and other effects, real web materials and rolls exhibit some degree of asymmetry along the loading-unloading path. As a result, the condition (10) is not strictly applicable and should be viewed as a physically motivated approximation. In the authors' measurements on certain polymers, for instance, at identical values of  $\sigma_r$ ,  $E_r$  values which differ by 50–100 percent between the loading and unloading portions of a compression test have been observed. To the extent that  $E_r$  is already typically much smaller than  $E_z$  and  $E_\theta$ , the  $\nu_{r\theta}$  and  $\nu_{rz}$  values calculated through Eq. (10) are likewise small, and Benson [14] has suggested specifying  $\nu_{r\theta} = \nu_{rz} \approx 0$ . On the other hand, aside from the small differences in numerical values between application of the (questionable) material symmetry condition and the specification of (arbitrary) small values for  $\nu_{r\theta}$  and  $\nu_{rz}$ , application of Eq. (10) does have the pleasing attribute that mathematical symmetry of  $\mathbf{K}_W$  is preserved. On balance, and from that standpoint of computational efficiency, the material symmetry condition is used here in determining  $\nu_{r\theta}$ ,  $\nu_{rz}$ , and  $\nu_{z\theta}$ , even while recognizing the limitations of that approximation.

With respect to the shear modulus,  $G_{rz}$  can in principle be determined experimentally by loading a stack of material in  $z$  under prescribed compressive stress, in conjunction with an angular distortion. The value so measured would be valid up to the point at which interlayer slippage began. Lacking such available measured data for  $G_{rz}$  in the literature, in case studies here,  $G_{rz}$  is specified to be constant (100 MPa) near the value (130 MPa)  $E_r/(2(1+\nu_{rz}))$  at  $\sigma_r = -1$  MPa. Subsequent parameter studies with various values of  $G_{rz}$  in the range 25–400 MPa have demonstrated that the wound roll stresses are generally insensitive to  $G_{rz}$ , with variations less than five percent, except for  $\sigma_{rz}$  which varies with  $G_{rz}$  in a substantially proportional manner.

With these considerations in mind,  $\mathbf{D}_i$  becomes

$$\mathbf{D}_i = C_0 \begin{bmatrix} E_r(1 - E_z/E_\theta)\nu_{\theta z}^2 & (E_\theta\nu_{r\theta} + E_z\nu_{rz}\nu_{\theta z}) & E_z(\nu_{r\theta}\nu_{rz}) & 0 \\ E_\theta(1 - (E_z/E_r)\nu_{rz}^2) & E_z(E_r\nu_{\theta z} + E_\theta\nu_{r\theta}\nu_{rz})/E_r & 0 & 0 \\ E_z(1 - (E_\theta/E_r)\nu_{r\theta}^2) & 0 & 0 & 0 \\ \text{Symmetric} & & & G_{rz}/C_0 \end{bmatrix} \quad (11)$$

where

$$C_0^{-1} = 1 - 2(E_z/E_r)\nu_{r\theta}\nu_{\theta z}\nu_{rz} - \nu_{rz}^2(E_z/E_r) - \nu_{\theta z}^2(E_z/E_\theta) - \nu_{r\theta}^2(E_\theta/E_r). \quad (12)$$

**2.4 Computation and Iteration.** The equilibrium equations are written  $g(\mathbf{a}) = \mathbf{K}_R(\mathbf{a})\mathbf{a} - \mathbf{F}$  in terms of the nodal displacements, and roots are found through Newton-Raphson iteration. As each layer or group of layers is added to the stratified  $\mathcal{W}$ , a truncated

Taylor expansion is used to linearize about either an initial estimate at  $n = 1$  or the converged result  $\mathbf{a}^*$  obtained from a previous iterate.

Computation begins by evaluating  $\mathbf{K}_R$  at an initial estimate of the stress field. In the first iteration, the nodal displacements become  $\mathbf{a}_1 = \mathbf{K}_R^{-1}(\mathbf{a}^*)\mathbf{F}$ . The vector of imbalanced nodal loads in the second iteration becomes  $\Delta\mathbf{f}_2 = \mathbf{K}_R(\mathbf{a}_1)\mathbf{a}_1 - \mathbf{F}$ . The incremental nodal displacements  $\Delta\mathbf{a}$  in the second iteration are  $\Delta\mathbf{a}_2 = \mathbf{K}_R^{-1}(\mathbf{a}_1)\Delta\mathbf{f}_2$ , and the cumulative displacements at that stage

become  $a_2 = a_1 + \Delta a_2$ . Generally, at the  $j$ th iteration, the imbalanced load, incremental displacement, and cumulative displacement fields are calculated through

$$\Delta f_{j+1} = K_R(a_j)a_j - F \quad (13)$$

$$\Delta a_{j+1} = K_R^{-1}(a_j)\Delta f_{j+1} \quad (14)$$

$$a_{j+1} = a_j + \Delta a_{j+1}. \quad (15)$$

For each system of locally linearized equilibrium conditions, a preconditioned gradient method is used to determine the  $\Delta a_j$ , and convergence is identified by evaluating the norm  $\eta = (\sum \Delta a_j^2 / \sum a_j^2)^{1/2}$ . If  $\eta$  falls below a specified tolerance, say  $10^{-3}$  as in the case studies below, iteration is terminated.

With the nodal displacements so obtained, the stresses within element  $i$  of the wound roll are incremented by

$$\Delta \sigma_{ni} = D_i(B_i a_i - \epsilon_{0i}) + \sigma_{0i} \quad (16)$$

as the  $n$ th layer is added. In turn, the cumulative stress

$$\sigma_{ni} = \sigma_{(n-1)i} + \Delta \sigma_{ni} \quad (17)$$

is represented in terms of  $\sigma_{ni}$  and the stresses  $\sigma_{(n-1)i}$  developed by the first through  $(n-1)$ st layers.

### 3 Comparisons and Convergence

Results obtained from the present analysis are benchmarked against the one-dimensional model of Hakiel [7], which does include the effects of nonlinear radial modulus and uniform core compliance. Parameter values are as specified in Table 1, and for a hollow cylindrical core, Hakiel's "effective core modulus" was calculated through

$$E_c = \frac{E(1 - (r_c - t)^2/r_c^2)}{(1 + \nu)(r_c - t)^2/r_c^2 + (1 - \nu)} \quad (18)$$

where  $E$  and  $\nu$  are the core's modulus and Poisson ratio. Aside from discretization, in Hakiel [7] equilibrium is only approximately satisfied since  $E_r$  is calculated based on the stress state as the previous, not the current, layer was added, and is specified to be a constant as each layer is added. For slightly greater accuracy here, the modulus is calculated based on the stress state at the current iteration.

A comparison of  $\sigma_r$  and  $\sigma_\theta$  for the two solutions is shown in Fig. 4, where values calculated along the roll's centerline  $z=0$  are shown for the two-dimensional model ( $NR=100$  and  $NZ=80$ ). The two-dimensional model, which does not assume conditions of plane strain or neglect Poisson coupling as does the one-dimensional model, predicts larger values of the radial stress by some 15 percent, with peak values of  $-1.76$  and  $-2.02$  MPa for the two models, respectively. The maximum occurs in each case near  $r=32$  mm. In terms of  $\sigma_\theta$ , the two solutions are in close agreement along the centerline with maximum deviation at the core-web interface of less than ten percent.

In a one-dimensional model, no free edge exists along the core-web interface, and in particular, no free surface of dissimilar bonded materials exists, as is the case in a two-dimensional model (points P2, for instance, in Fig. 3). For linear, isotropic, homogeneous materials, such configurations are associated with stress concentration or even singularity, and the corner stress can be non-singular, or of order  $\rho^{-\lambda}$ , or  $\log \rho$ , where  $\rho$  is the radial distance from the corner and  $\lambda$  is an exponent, depending on material properties and the type of loading ([19]). In addition, in related problems of elastic inclusions within a half-space or infi-

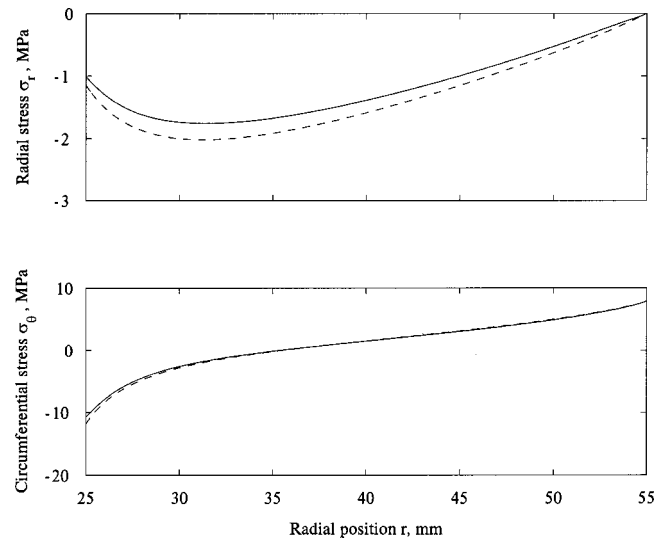


**Fig. 4 Comparison of the radial and circumferential stresses along centerline  $z=0$  as determined through the present (—) and one-dimensional (---; Hakiel [7]) models. The parameter values are as specified in Table 1 (plastic, hollow core).**

nite plate, the strength of the singularity depends on the ratios of the (differing) material properties of the inclusion and the surrounding material ([20]).

Dundurs [21] demonstrated that the influence of the elastic constants for two isotropic edge-bonded materials is set by the two variables  $\alpha = (\bar{E}_1 - \bar{E}_2)/(\bar{E}_1 + \bar{E}_2)$  and  $\beta = (\mu_1(\kappa_2 - 1) - \mu_2(\kappa_1 - 1))/(\mu_1(\kappa_2 + 1) + \mu_2(\kappa_1 + 1))$ , where  $\bar{E}_j = E_j$  and  $k_j = (3 - \nu_j)/(1 + \nu_j)$  for plane stress or  $\bar{E}_j = E_j/(1 - \nu_j^2)$  and  $\kappa_j = 3 - 4\nu_j$  for plane strain. In that formulation,  $E_j$ ,  $\nu_j$ , and  $\mu_j$  ( $j=1,2$ ) are the elastic moduli, Poisson ratios, and shear moduli, of the two edge-bonded regions, and the corner stress is characterized by the numerical value of the determinant quantity  $\alpha(\alpha - 2\beta)$ . For strictly positive values, stresses at the corner are singular at order  $\rho^{-\lambda}$ ; for strictly negative values, the stresses are finite and nonsingular; and for vanishing determinant, the stresses can be singular of order  $\log \rho$ , depending on the applied loads ([19]).

For anisotropic materials, the character of the free-edge corner stresses in ideally bonded quarter-spaces of dissimilar materials has been investigated by Wang and Choi [22,23]. That solution was developed through Lekhnitskii stress potentials, and an eigenfunction expansion was developed to obtain the stress field near the free edge. Alternative approaches have included enriched finite element and boundary integral methods which offer computational efficiency ([24]). The nature of the free-edge corner stress singularity in composite laminates remains an open issue, and the present two-dimensional model can be viewed as a tool for exploring the presence of stress concentration or singularity at the edges of the core-web interface.

With solutions here based on finite element, the presence of a singularity is only suggested by high stress gradients and/or slow convergence rates under successive mesh refinements. Such calculations identify whether stresses converge uniformly at edges of the core-web interface and enable stress concentration factors to be quantified, or whether the stresses do not converge or converge slowly, in which case singularity is possible. For properties as specified in Table 1, Fig. 5 depicts convergence of  $\sigma_r$  in the roll's first layer for the cases of plastic and aluminum cores. In each case, the radial stress converges quickly at point P1 ( $z=0$ ) in Fig. 3, and for the plastic core,  $\sigma_r$  also converges by  $NZ=40$  at points P2 ( $z=\pm w/2$ ), namely, edges of the interface. However, with an aluminum core, the radial stress at P2 has not converged with



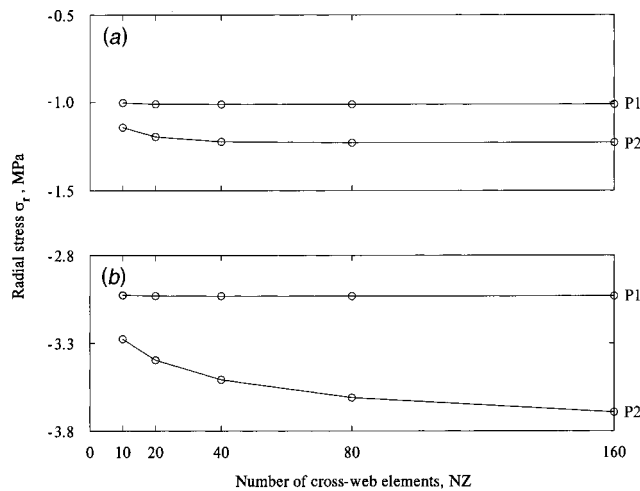


**Fig. 5** Convergence of  $\sigma_r$  at points P1 and P2 in Fig. 3 for (a) plastic and (b) aluminum cores. The radial stress converges well along the roll's centerline in each case, and at the edge of the core-web interface for the plastic material.

successive mesh refinements even at  $NZ=160$ . This material-dependent behavior is analogous to that observed in studies of other edge-bonded regions.

When stresses are finite and converged at P2, stress concentration factors between the roll's nominal centerline stresses and those at the core-web interface's edge can be identified. The cross-web variation of  $\sigma_r$  in the first layer is shown in Fig. 6 for both plastic and aluminum cores. In Fig. 6(a) for the hollow plastic core, the stress at the edges is some  $K=1.22$  times greater than the centerline value, which could be a useful quantity in analyzing wound roll defects. In Fig. 6(b), the shaded zones denote the regions where the stresses have not converged to three significant digits at  $NZ=160$ . Even in that case, however, the influence of the potential singularity is localized since the stress solution has satisfactorily converged over 90 percent of the roll's width.

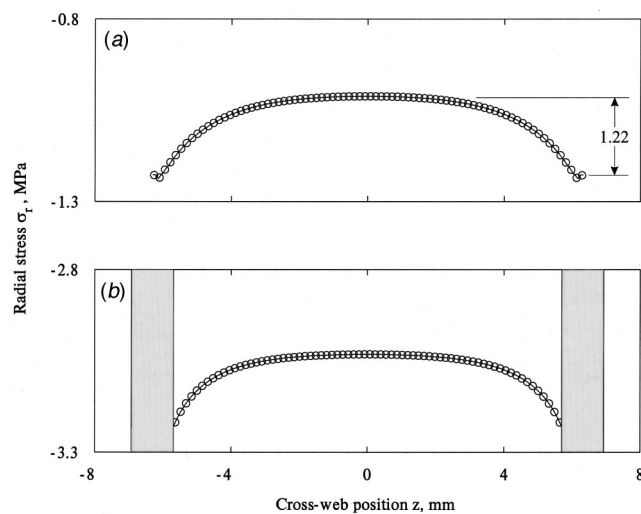


**Fig. 6** Cross-web variation of  $\sigma_r$  along the core-web interface for hollow (a) plastic and (b) aluminum cores;  $NZ=80$  (○ ○ ○ ○), and  $NZ=160$  (—). The shaded zones in (b) denote regions where the stresses have not converged to three significant digits.

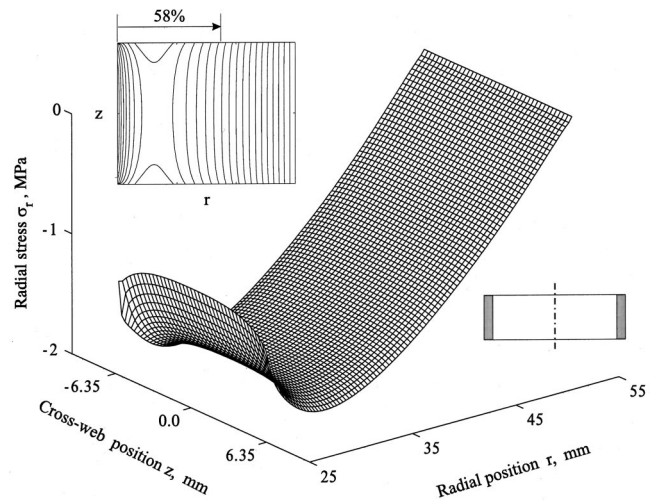


**Fig. 7** Surface and contour representations of the radial and cross-web variation of  $\sigma_r$ ;  $NR=100$ ,  $NZ=80$ . The parameter values are as specified in Table 1 (plastic, hollow core).

#### 4 Discussion and Further Applications

**4.1 Stress Field With a Hollow Core.** Figures 7–9 depict variations of the four stress components as functions of  $r$  and  $z$  for a wound roll having hollow core, dimensions, and properties as specified in Table 1. In Fig. 7, the maximum compressive radial stress of 1.89 MPa occurs at  $(31.6, \pm 6.35)$  mm. The cross-width variation of  $\sigma_r$  diminishes with radial distance from the core. In the region  $r=25\sim 30$  mm, for instance, the cross-width variation in  $\sigma_r$  is greater than ten percent. For the inner 58 percent of the layered region, the cross-width variation is greater than five percent but becomes smaller at larger distances from the core in accordance with St. Venant's principle.

The circumferential stress is tensile at  $r_o$ , vanishes near  $r=35$  mm, and is compressive at radial locations nearer to core, and with negligible cross-width variation. In an axisymmetric structure,  $\sigma_\theta$  depends only on radial displacement, which in turn

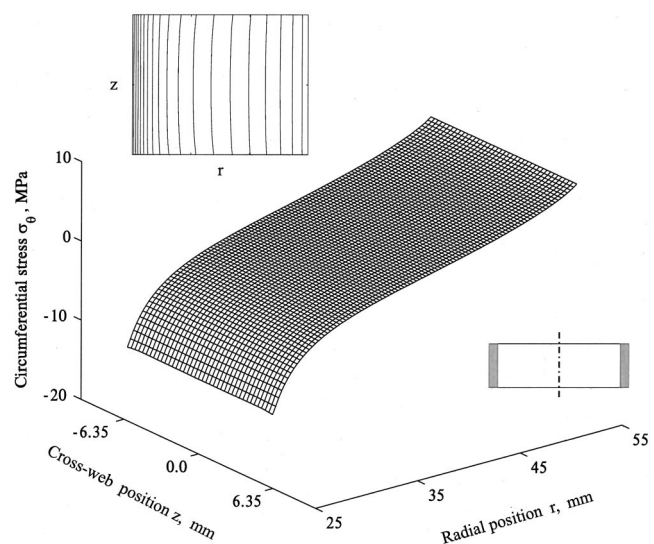


**Fig. 8** Surface and contour representations of the radial and cross-web variation of  $\sigma_\theta$ ;  $NR=100$ ,  $NZ=80$ . The parameter values are as specified in Table 1 (plastic, hollow core).



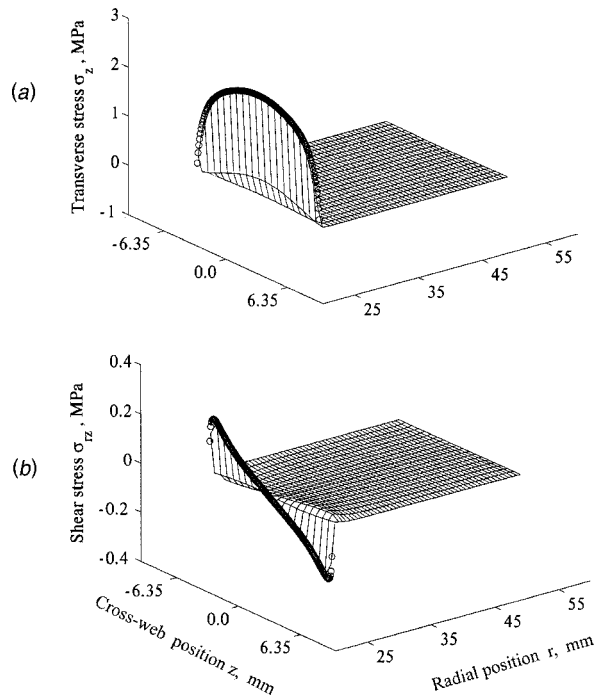


**Fig. 9** Radial and cross-web variations of (a)  $\sigma_z$  and (b)  $\sigma_{rz}$ ;  $NZ=80$  (surface) and  $NZ=160$  (○ ○ ○ ○; first layer only). The parameter values are as specified in Table 1 (plastic, hollow core).

is almost uniform for the chosen core design and with uniform winding tension. The maximum compressive value for  $\sigma_\theta$  of 10.9 MPa occurs at the core-web interface.

In Fig. 9, the transverse and shear stresses are significant only near the core-web interface, and rapidly fall to almost zero elsewhere. The localized character of  $\sigma_z$  and  $\sigma_{rz}$  is attributed primarily to Poisson coupling in the core. Away from the interface, Poisson coupling is negligible because  $\nu_{rz}$  and  $\nu_{\theta z}$  are small, and the stresses are likewise small. Although the solutions for  $\sigma_z$  and

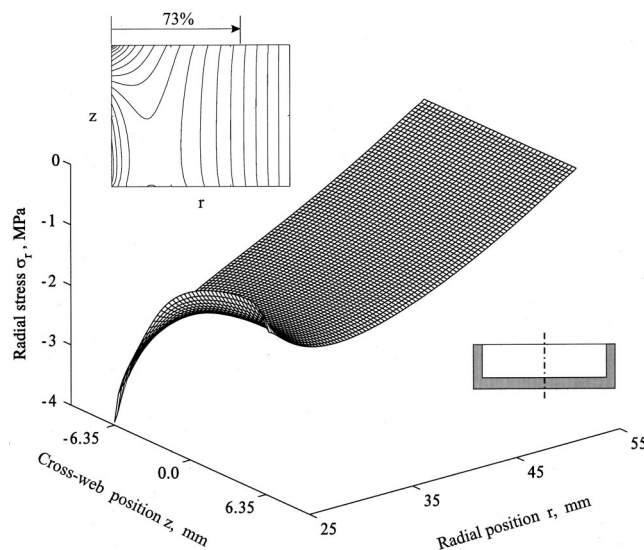


**Fig. 10** Surface and contour representations of the radial and cross-web variation of  $\sigma_r$ ;  $NR=100$ ,  $NZ=80$ . The parameter values are as specified in Table 1 (plastic, cup-shaped core).

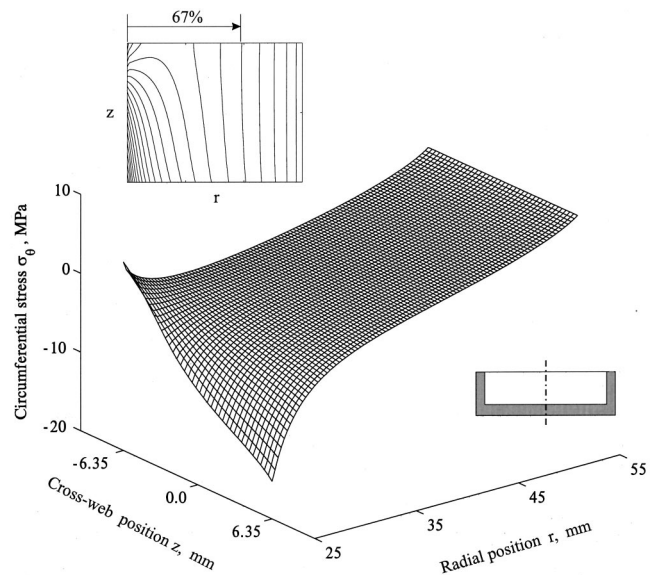


**Fig. 11** Surface and contour representations of the radial and cross-web variation of  $\sigma_\theta$ ;  $NR=100$ ,  $NZ=80$ . The parameter values are as specified in Table 1 (plastic, cup-shaped core).

$\sigma_{rz}$  are highly localized, their solutions have converged in Fig. 9, where results for  $NZ=80$  (surface) are compared in the first web layer with the results for  $NZ=160$  (data points).

In the foregoing analysis, adjacent layers are assumed to remain in contact with no lateral slippage. With an assumed coefficient of friction of, say  $\mu=0.3$ , that assumption can be re-examined by comparing the magnitudes of  $\sigma_{rz}$  and  $\mu\sigma_r$ . Over the entire web domain,  $\sigma_{rz}$  is smaller, providing internal consistency at least with respect to this no-slippage assumption.

**4.2 Stress Field With a Cup-Shaped Core.** When the core is cup-shaped with wall thickness, width, outer radius, and plastic material properties as specified in Table 1, Figs. 10 and 11 depict the radial and circumferential stresses as functions of  $r$  and  $z$ . In the roll's first layer, the compressive radial stress varies between

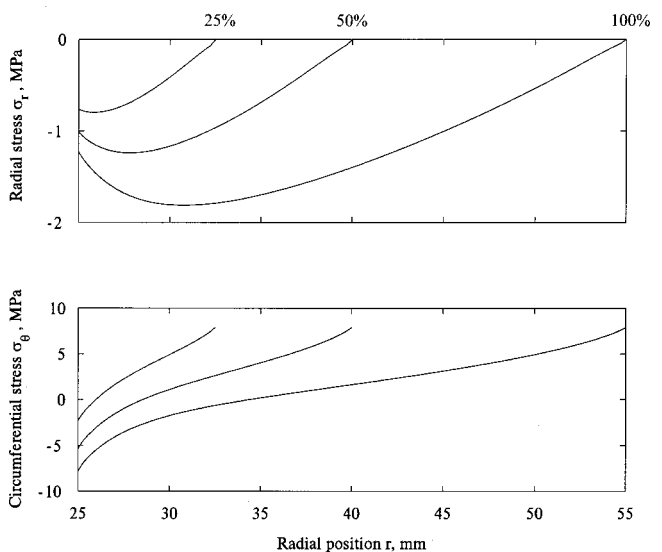


**Fig. 12** Variations of  $\sigma_r$  and  $\sigma_\theta$  along the roll's centerline with increasing numbers of web layers: 25 percent, 50 percent, and 100 percent of a full roll;  $NR=100$ ,  $NZ=80$ . The parameter values are as specified in Table 1 (plastic, cup-shaped core).

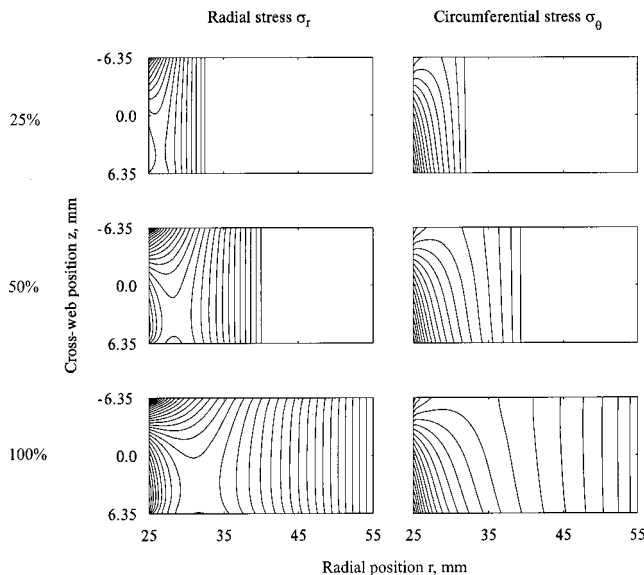


**Fig. 13 Radial and cross-web variations of  $\sigma_r$  and  $\sigma_\theta$  with increasing numbers of web layers: 25 percent, 50 percent, and 100 percent of a full roll;  $NR=100$ ,  $NZ=80$ . The parameter values are as specified in Table 1 (plastic, cup-shaped core).**

3.95 MPa at the closed stiff end to 0.89 MPa near the open compliant side. Although the gradient for  $\sigma_r$  near the stiff edge is steep, the solution has converged to three significant digits. The circumferential stress varies along the core-web interface from 3.92 MPa (tension) at the closed end to 15.2 MPa (compression) at the core's compliant side. Cross-web variations of  $\sigma_r$  and  $\sigma_\theta$  for this geometry are more significant than for the hollow cylindrical core, and because  $\sigma_\theta$  is not always compressive along the core-web interface, winding defects could potentially be generated in  $\mathcal{W}$  on only one face of the roll.

In the region  $r=25\sim 40$  mm, cross-width variation of  $\sigma_r$  is greater than ten percent, and the cross-width variation for the radial and circumferential stresses is greater than five percent over some 73 percent and 67 percent of the roll, respectively. Contours of  $\sigma_r$  and  $\sigma_\theta$  are shown as insets in Figs. 10 and 11. In this example, the stress gradients in  $z$  near the core are sufficiently large that the stress field would not be well approximated by a one-dimensional model imposing uniform width-wise core stiffness.

**4.3 Variable Roll Radius.** Since the stress field in a wound roll depends on the overall number of layers in the roll, Fig. 12 depicts a comparison of  $\sigma_r$  and  $\sigma_\theta$  along the centerline for different numbers of wound-on layers, corresponding to quarter-full, half-full, and full rolls on a cup-shaped core. Similarly, Fig. 13 shows contour representations of  $\sigma_r$  and  $\sigma_\theta$  for these cases. The compressive radial and circumferential stresses each grow as  $NL$  increases. The compressive radial stress is maximized at P2 (closed stiff end) along the core-web interface and becomes more compressive with increasing  $NL$ . The cross-web variation for the radial stress is greater than five percent over more than 70 percent of the web region for each of the three rolls.

In terms of  $\sigma_\theta$ , the cross-web variation for the quarter and half-full rolls exceeds 26 percent and six percent, respectively, over the entire roll, excluding the outermost layer at which the boundary condition of specified tension is applied. For quarter-full, half-full, and full rolls, the  $\sigma_r$  values along the core-web interface are (−1.87, −3.01, −3.95) MPa at the closed end; (−0.76, −1.00, −1.21) MPa at the centerline; and (−0.77, −1.05, −1.20) MPa at the open end. Likewise, the  $\sigma_\theta$  values at those points are (6.20, 5.01, 3.92) MPa, (−2.37, −5.47, −8.03) MPa, and (−7.94, −12.12, −15.21) MPa, demonstrating the presence

of significant cross-width variation. In each case,  $\sigma_\theta$  varies further from tension to compression across the roll's width.

## 5 Summary

The width-wise variation of stresses in wound rolls is investigated by using a two-dimensional, axisymmetric, finite element model. The present analysis relaxes assumptions made in previous one-dimensional models in which the roll was specified to be infinitely wide and with uniform core stiffness, winding tension, and material properties. By separating the wound roll into two regions—the core and layered web substructures—general core geometry and designs can be accommodated, analyzed, and optimized.

In several case studies with different materials and core geometry, the radial and cross-web variations of the  $\sigma_r$ ,  $\sigma_\theta$ ,  $\sigma_z$ , and  $\sigma_{rz}$  stress components, as well as stress concentration or potential singularity at the free edges of the core-web interface, are investigated. The transverse and shear stress in these examples are significant only near the core-web interface and are attributed to Poisson coupling and strain mismatch between material properties. The model can be used for quantifying stress concentration at edges of the core-web interface, and for identifying material combinations and core designs for which certain stress components are expected to be finite or singular. The model can further be applied to investigate the stress state in the presence of nonuniform winding tension or material thickness across the web's width, and those areas are subjects of current investigation.

## Acknowledgment

This work was supported in part by Imation Corporation and the National Science Foundation.

## References

- [1] Altmann, H. C., 1968, "Formulas for Computing the Stresses in Center-Wound Rolls," *J. Tech. Assoc. Paper Pulp Indust.*, **51**, pp. 176–179.
- [2] Trampusch, H., 1965, "Relaxation of Internal Forces in a Wound Reel of Magnetic Tape," *ASME J. Appl. Mech.*, **32**, pp. 865–873.
- [3] Trampusch, H., 1967, "Anisotropic Relaxation of Internal Forces in a Wound Reel of Magnetic Tape," *ASME J. Appl. Mech.*, **34**, pp. 888–894.
- [4] Yagoda, H. P., 1980, "Resolution of a Core Problem in Wound Rolls," *ASME J. Appl. Mech.*, **47**, pp. 847–854.
- [5] Connolly, D., and Winarski, D. J., 1984, "Stress Analysis of Wound Magnetic Tape," *ASLE Tribology and Mechanics of Magnetic Storage Media*, Special Publication 16, ASLE, pp. 172–182.
- [6] Pfeiffer, J. D., 1979, "Prediction of Roll Defects from Roll Structure Formula," *J. Tech. Assoc. Paper Pulp Indust.*, **62**, pp. 83–88.
- [7] Hakiel, Z., 1987, "Nonlinear Model for Wound Roll Stresses," *J. Tech. Assoc. Paper Pulp Indust.*, **70**, pp. 113–117.
- [8] Willett, M. S., and Poesch, W. L., 1988, "Determining the Stress Distributions in Wound Reels of Magnetic Tape Using a Nonlinear Finite-Difference Approach," *ASME J. Appl. Mech.*, **55**, pp. 365–371.
- [9] Bourgin, P., and Bouquerel, F., 1993, "Winding Flexible Media: A Global Approach," *Adv. Inf. Storage Syst.*, **5**, pp. 493–512.
- [10] Keshavan, M. B., and Wickert, J. A., 1997, "Air Entrainment During Steady State Web Winding," *ASME J. Appl. Mech.*, **64**, pp. 916–922.
- [11] Good, J. K., Pfeiffer, J. D., and Giachetto, R. M., 1992, "Losses in Wound-on Tension in the Centerwinding of Wound Rolls," *Web Handling*, ASME AMD-149, ASME, New York, pp. 1–12.
- [12] Zabaras, N., Liu, S., Koppuzha, J., and Donaldson, E., 1994, "A Hypoelastic Model for Computing the Stresses in Center-Wound Rolls of Magnetic Tape," *ASME J. Appl. Mech.*, **61**, pp. 290–295.
- [13] Qualls, W. R., and Good, J. K., 1997, "An Orthotropic Viscoelastic Winding Model Including a Nonlinear Radial Stiffness," *ASME J. Appl. Mech.*, **64**, pp. 201–208.
- [14] Benson, R. C., 1995, "A Nonlinear Wound Roll Model Allowing for Large Deformation," *ASME J. Appl. Mech.*, **62**, pp. 853–859.
- [15] Hakiel, Z., 1992, "On the Effect of Width Direction Thickness Variations in Wound Rolls," *Second International Conference on Web Handling*, Oklahoma State University, pp. 79–98.
- [16] Kedli, D. M., 1992, "Using a Two Dimensional Winding Model to Predict Wound Roll Stresses That Occur due to Circumferential Steps in Core Diameter or to Cross-Web Caliper Variation," *Second International Conference on Web Handling*, Oklahoma State University, pp. 99–112.
- [17] Cole, A., and Hakiel, Z., 1992, "A Nonlinear Wound Roll Stress Model Accounting for Widthwise Web Thickness Nonuniformities," *Web Handling*, ASME AMD-149, ASME, New York, pp. 13–24.

- [18] Zienkiewicz, O. C., and Taylor, R. L., 1989, *The Finite Element Method*, Vols. 1 and 2, McGraw-Hill, New York.
- [19] Bogy, D. B., 1970, "On the Problem of Edge-Bonded Elastic Quarter-Planes Loaded at the Boundary," *Int. J. Solids Struct.*, **6**, pp. 1287–1313.
- [20] Folias, E. S., 1989, "On the Stress Singularities at the Intersection of a Cylindrical Inclusion With the Free Surface of a Plate," *Int. J. Fract.*, **39**, pp. 25–34.
- [21] Dundurs, J., 1967, "Effect of Elastic Constants on Stress in a Composite Under Plane Deformation," *J. Compos. Mater.*, **1**, pp. 310–322.
- [22] Wang, S. S., and Choi, I., 1982, "Boundary Layer Effects in Composite Laminates: Part I—Free-Edge Stress Singularities," *ASME J. Appl. Mech.*, **49**, pp. 541–548.
- [23] Wang, S. S., and Choi, I., 1982, "Boundary Layer Effects in Composite Laminates: Part II—Free-Edge Stress Solutions and Basis Characteristics," *ASME J. Appl. Mech.*, **49**, pp. 549–560.
- [24] Tsamasphyros, G., 1987, "Methods for Combination of Finite Element and Singular Integral Equation Methods," *Comput. Methods Appl. Mech. Eng.*, **60**, pp. 45–56.

**H. Jiang**

Failure Mechanics Laboratory,  
Department of Engineering Mechanics,  
Tsinghua University,  
Beijing 100084, China

**Y. Huang**

Department of Mechanical and  
Industrial Engineering,  
University of Illinois,  
Urbana, IL 61801

**T. F. Guo**

**K. C. Hwang<sup>1</sup>**

Failure Mechanics Laboratory,  
Department of Engineering Mechanics,  
Tsinghua University,  
Beijing 100084, China

# An Alternative Decomposition of the Strain Gradient Tensor

*An alternative decomposition of the strain gradient tensor is proposed in this paper in order to ensure that the deviatoric strain gradient vanishes for an arbitrary volumetric strain field, which is consistent with the physical picture of plastic deformation. The theory of mechanism-based strain gradient (MSG) plasticity is then modified accordingly based on this new decomposition. The numerical study of the crack-tip field based on the new theory shows that the crack tip in MSG plasticity has the square-root singularity, and the stress level is much higher than the HRR field in classical plasticity.*

[DOI: 10.1115/1.1430666]

## 1 Introduction

Fleck and Hutchinson [1] proposed a phenomenological theory of strain gradient plasticity in order to characterize the size dependence observed in the micron and submicron scale experiments ([2–9]). The strain gradient tensor  $\eta_{ijk} = u_{k,ij}$  is decomposed into a volumetric part  $\eta_{ijk}^H$  and a deviatoric part  $\eta_{ijk}'$ ,  $\eta_{ijk} = \eta_{ijk}^H + \eta_{ijk}'$ , where  $u_k$  is the displacement, and  $\eta_{ijk}^H = 1/4 (\delta_{ik} \eta_{jpp} + \delta_{jk} \eta_{ipp})$  ([10]). Within the same theoretical framework ([1]), Gao, Huang and co-workers ([11,12]) developed the mechanism-based strain gradient (MSG) plasticity theory from the Taylor model in dislocation mechanics, and the theory agrees very well with the micro-indentation, microtorsion, and microbend experiments ([13,14]).

Hwang and Inoue [15] investigated the strain gradient effect for the following displacement field:

$$\begin{aligned} u_1 &= A(x_1^2 - x_2^2 - x_3^2) + 2Bx_1x_2 + 2Cx_1x_3, \\ u_2 &= 2Ax_1x_2 + B(-x_1^2 + x_2^2 - x_3^2) + 2Cx_2x_3, \\ u_3 &= 2Ax_1x_3 + 2Bx_2x_3 + C(-x_1^2 - x_2^2 + x_3^2), \end{aligned} \quad (1)$$

where  $A$ ,  $B$ , and  $C$  are constants. It gives a pure volumetric strain field,  $\varepsilon_{ij} = 2(Ax_1 + Bx_2 + Cx_3)\delta_{ij}$ , i.e., the deviatoric strain field  $\varepsilon'_{ij}$  vanishes. The strain gradient field, however, is not pure volumetric because the deviatoric strain gradient field does not vanish,  $\eta'_{ijk} \neq 0$ . It is quite puzzling that a pure volumetric strain field gives a deviatoric strain gradient field because the former implies no plastic deformation (since plastic deformation is always deviatoric) while the latter represents the plastic deformation associated with the geometrically necessary dislocations ([11]). It should be pointed out that the above puzzle between the volumetric strain field and deviatoric strain gradient field does not apply to the flow theories of strain gradient plasticity ([1,16–19]) because of the clear distinction between the plastic strain and the total strain. It

does not affect the deformation theory of MSG plasticity ([11,12]) either since the theory assumes material incompressibility.

An alternative decomposition of the strain gradient tensor is proposed in this study,

$$\eta_{ijk} = \bar{\eta}_{ijk}^H + \bar{\eta}_{ijk}', \quad (2)$$

which gives a vanishing deviatoric part  $\bar{\eta}_{ijk}'$  for an arbitrary volumetric strain field. The theory of MSG plasticity ([11,12]) is then generated accordingly to include the elastic deformation. Finally, we study the crack-tip field with the elastic-plastic theory of MSG plasticity, and show that the stress field around the crack tip has the square-root singularity.

## 2 Decomposition of the Strain Gradient Tensor

Because the strain gradient tensor can be expressed in terms of the strain,  $\eta_{ijk} = \varepsilon_{ik,j} + \varepsilon_{jk,i} - \varepsilon_{ij,k}$ , a natural way to define the deviatoric strain gradient is to replace the strain by its deviatoric part  $\varepsilon'_{ij} (= \varepsilon_{ij} - 1/3 \varepsilon_{kk} \delta_{ij})$  in the above relation, i.e.,

$$\bar{\eta}_{ijk} = \varepsilon'_{ik,j} + \varepsilon'_{jk,i} - \varepsilon'_{ij,k}, \quad (3)$$

which clearly vanishes for a purely volumetric strain field [e.g., (1)]. The corresponding volumetric part of the strain gradient tensor becomes

$$\bar{\eta}_{ijk}^H = \eta_{ijk} - \bar{\eta}_{ijk}' = \frac{1}{3} \varepsilon_{pp,j} \delta_{ik} + \frac{1}{3} \varepsilon_{pp,i} \delta_{jk} - \frac{1}{3} \varepsilon_{pp,k} \delta_{ij}. \quad (4)$$

The above decomposition is different from the existing strain gradient theories ([1,11,12]), and it ensures that the deviatoric and volumetric part of the strain gradient field result from the deviatoric and volumetric strain fields, respectively.

The higher-order stress, which is the work conjugate of the strain gradient tensor, is decomposition differently,  $\tau_{ijk} = \bar{\tau}_{ijk}^H + \bar{\tau}_{ijk}'$ , such that the virtual work done by the higher-order stress can be separated into the hydrostatic and deviatoric parts

$$\delta w = \tau_{ijk} \delta \eta_{ijk} = \bar{\tau}_{ijk}^H \delta \bar{\eta}_{ijk}^H + \bar{\tau}_{ijk}' \delta \bar{\eta}_{ijk}'. \quad (5)$$

This requires the cross terms  $\bar{\tau}_{ijk}^H \delta \bar{\eta}_{ijk}'$  and  $\bar{\tau}_{ijk}' \delta \bar{\eta}_{ijk}^H$  to vanish, which gives the unique decomposition of the higher-order stress as

$$\bar{\tau}_{ijk}' = \tau_{ijk} - \bar{\tau}_{ijk}^H, \quad (6)$$

<sup>1</sup>To whom all correspondence should be addressed.

Contributed by the Applied Mechanics Division of THE AMERICAN SOCIETY OF MECHANICAL ENGINEERS for publication in the ASME JOURNAL OF APPLIED MECHANICS. Manuscript received by the ASME Applied Mechanics Division, January 18, 2001; final revision, July 18, 2001. Editor: M. Ortiz. Discussion on the paper should be addressed to the Editor, Prof. Lewis T. Wheeler, Department of Mechanical Engineering, University of Houston, Houston, TX 77204-4792, and will be accepted until four months after final publication of the paper itself in the ASME JOURNAL OF APPLIED MECHANICS.

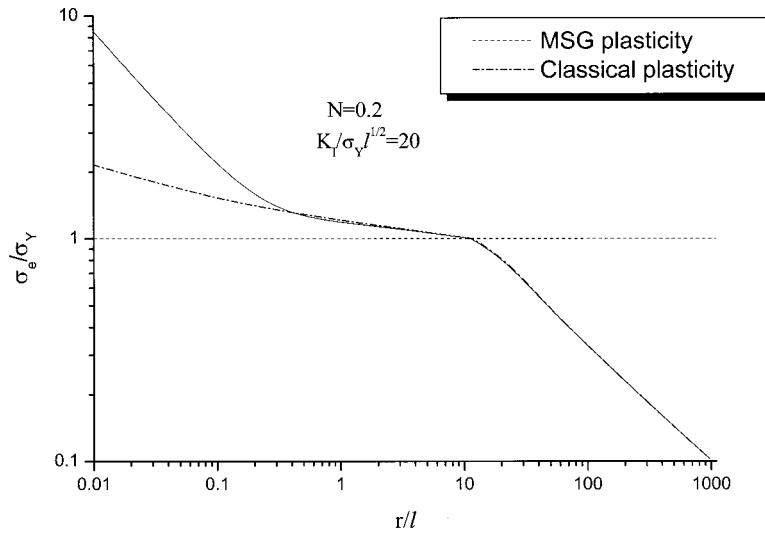


**Fig. 1 The effective stress  $\sigma_e$  normalized by the uniaxial yield stress  $\sigma_Y$  versus the normalized distance to the crack tip,  $r/l$ , ahead of the crack tip, where  $l$  is the intrinsic material length in strain gradient plasticity; the plastic work hardening exponent  $N=0.2$ , Poisson's ratio  $\nu=0.3$ , the ratio of yield stress to elastic modulus  $\sigma_Y/E=0.2$  percent, and the remotely applied elastic stress intensity factor  $K_I/\sigma_Y l^{1/2}=20$**

$$\bar{\tau}_{ijk}^H = \frac{1}{3} \delta_{ik} \left( \tau_{jpp} - \frac{1}{2} \tau_{ppi} \right) + \frac{1}{3} \delta_{jk} \left( \tau_{ipp} - \frac{1}{2} \tau_{ppi} \right). \quad (7)$$

Unlike other strain gradient theories ([1,11,12]), the decomposition of the higher-order stress  $\tau_{ijk}$  is different from that of the strain gradient  $\eta_{ijk}$ .

### 3 The Elastic-Plastic Theory of Mechanism-Based Strain Gradient Plasticity

Let  $\sigma = \sigma_{\text{ref}} f(\varepsilon)$  be the uniaxial stress-strain relation, and  $\sigma_{\text{ref}}$  be a reference stress in uniaxial tension. The flow stress  $\sigma$  in MSG plasticity is established from Taylor model in dislocation mechanics as ([13])

$$\sigma = \sqrt{\sigma_{\text{ref}}^2 f^2(\varepsilon) + 18\alpha^2 \mu^2 b \eta} = \sigma_{\text{ref}} \sqrt{f^2(\varepsilon) + l \eta}, \quad (8)$$

where  $\varepsilon = \sqrt{2/3} \varepsilon'_{ij} \varepsilon'_{ij}$  is the effective strain,  $\mu$  the shear modulus,  $b$  the Burgers vector,  $\alpha$  (0.1~0.5) an empirical material constant in the Taylor dislocation model, and the effective strain gradient  $\eta$  is determined by three dislocation models ([11]) for an incompressible solid as  $\eta = 1/2 \sqrt{\eta'_{ijk} \eta'_{ijk}}$ . Here the deviatoric strain gradient tensor  $\eta'_{ijk}$  is the same as  $\bar{\eta}'_{ijk}$  in (3) for an incompressible solid, therefore a natural generalization of  $\eta$  for an elastic-plastic (compressible) solid is

$$\eta = \frac{1}{2} \sqrt{\bar{\eta}'_{ijk} \bar{\eta}'_{ijk}}. \quad (9)$$

The parameter  $l$  in (8) is the intrinsic material length in strain gradient plasticity given by

$$l = 18\alpha^2 \left( \frac{\mu}{\sigma_{\text{ref}}} \right)^2 b, \quad (10)$$

which is on the order of a few microns.

Following the same multiscale approach ([11]), we have established the constitutive law for the elastic-plastic theory of MSG plasticity based on the alternative decomposition of the strain gradient tensor in (2)–(4).

$$\sigma_{ij} = K \varepsilon_{kk} \delta_{ij} + \frac{2\sigma}{3\varepsilon} \varepsilon'_{ij}, \quad (11)$$

$$\tau_{ijk} = l_\varepsilon^2 \left[ \frac{K}{24} (\delta_{ik} \eta_{jpp} + \delta_{jk} \eta_{ipp}) + \frac{\sigma}{\varepsilon} (\Lambda_{ijk} - \Pi_{ijk}) + \frac{\sigma_{\text{ref}}^2 f(\varepsilon) f'(\varepsilon)}{\sigma} \Pi_{ijk} \right], \quad (12)$$

where  $K$  is the elastic bulk modulus;  $\sigma$  is the flow stress in (8);

$$\Lambda_{ijk} = \frac{1}{72} (2 \bar{\eta}'_{ijk} + \bar{\eta}'_{kji} + \bar{\eta}'_{kij}), \quad \Pi_{ijk} = \frac{\varepsilon'_{mn}}{54\varepsilon^2} (\varepsilon'_{ik} \bar{\eta}'_{jmn} + \varepsilon'_{jk} \bar{\eta}'_{imn}); \quad (13)$$

$l_\varepsilon = 10(\mu/\sigma_Y)b$ , and  $\sigma_Y$  is the initial yield stress in uniaxial tension.

### 4 Crack-Tip Singularity in MSG Plasticity

We use the finite element method for the elastic-plastic theory of MSG plasticity to investigate the mode I crack-tip field and crack-tip singularity. A semi-infinite crack in an infinite elastic-plastic solid remains traction-free on the crack face. The elastic  $K$  field is imposed on the remote boundary. The plastic work-hardening exponent  $N=0.2$ , the ratio of yield stress to Young's Modulus  $\sigma_Y/E=0.2$  percent and Poisson's ratio  $\nu=0.3$ . Details of the numerical analysis are omitted in this paper.

Figure 1 shows the normalized Von Mises effective stress,  $\sigma_e/\sigma_Y$ , versus the nondimensional distance to the crack tip,  $r/l$ , ahead of the crack tip, where  $\sigma_Y$  is the yield stress and  $l$  is the intrinsic material length in strain gradient plasticity. The results are presented for both the elastic-plastic theory of MSG plasticity and the classical theory of plasticity (i.e., without strain gradient effects). The remote applied stress intensity factor is  $K_I/\sigma_Y l^{1/2} = 20$ . The horizontal line of  $\sigma_e/\sigma_Y = 1$  separates the elastic and plastic zones. Outside the plastic zone, both curves emerge to the same straight lines with the slope of  $-1/2$ , corresponding to the elastic  $K$  field with the square-root singularity. Within the plastic zone, the two curves are also essentially the same at a distance larger than  $0.4l$  to the crack tip. Within  $0.4l$  to the crack tip, MSG plasticity theory predicts significantly larger stresses than their counterparts in classical plasticity. Moreover, classical plasticity theory gives a straight line with the slope of  $-N/(N+1)$ , corresponding to the HRR field ([20,21]), while MSG plasticity theory



gives another straight line of slope  $-1/2$ , corresponding to the square-root singularity. In other words, stresses have the square-root singularity around a crack tip in MSG plasticity.

## 5 Concluding Remarks

We have proposed an alternative decomposition of the strain gradient tensor in order to ensure that the deviatoric strain gradient tensor vanishes for an arbitrary volumetric strain field  $\varepsilon_{ij} = \varepsilon(\mathbf{x})\delta_{ij}$ . This is consistent with the physical picture of plastic deformation since a pure volumetric strain field does not correspond to any plastic deformation (and therefore no dislocation activities) such that the deviatoric strain gradient should vanish since the latter is related to the density of geometrically necessary dislocations. We have modified the theory of mechanism-based strain gradient (MSG) plasticity ([11–13]) according to this new decomposition of the strain gradient tensor. We have then used the finite element method to investigate the crack-tip field in MSG plasticity, and have established that the crack tip has the square-root singularity. Within a distance on the order of microns to crack tip, the stress level predicted by MSG plasticity is significantly higher than the HRR field for classical plasticity.

## Acknowledgments

YH acknowledges an insightful discussion with Prof. J. W. Hutchinson of Harvard University, and the support from NSF (grant CMS-0084980 and a supplement for the grant CMS-9896285 from the NSF International Program) and from NSFC. KCH acknowledges the support from NSFC and Ministry of Education of China.

## References

- [1] Fleck, N. A., and Hutchinson, J. W., 1997, "Strain Gradient Plasticity," *Adv. Appl. Mech.*, **33**, pp. 295–361.
- [2] De Guzman, M. S., Neubauer, G., Flinn, P., and Nix, W. D., 1993, "The Role of Indentation Depth on the Measured Hardness of Materials," *Mat. Res. Sym. Proc.*, **308**, pp. 613–618.
- [3] Stelmashenko, N. A., Walls, M. G., Brown, L. M., and Milman, Y. V., 1993, "Microindentation on W and Mo Oriented Single Crystals: An STM Study," *Acta Metall. Mater.*, **41**, pp. 2855–2865.

- [4] Fleck, N. A., Muller, G. M., Ashby, M. F., and Hutchinson, J. W., 1994, "Strain Gradient Plasticity: Theory and Experiments," *Acta Metall. Mater.*, **42**, pp. 475–487.
- [5] Lloyd, D. J., 1994, "Particle Reinforced Aluminum and Magnesium Matrix Composites," *Int. Mater. Rev.*, **39**, pp. 1–23.
- [6] Ma, Q., and Clarke, D. R., 1995, "Size Dependent Hardness of Silver Single Crystals," *J. Mater. Res.*, **10**, pp. 853–863.
- [7] Poole, W. J., Ashby, M. F., and Fleck, N. A., 1996, "Micro-hardness of Annealed and Work-Hardened Copper Polycrystals," *Scr. Metall. Mater.*, **34**, pp. 559–564.
- [8] McElhane, K. W., Vlassak, J. J., and Nix, W. D., 1998, "Determination of Indenter Tip Geometry and Indentation Contact Area for Depth-Sensing Indentation Experiments," *J. Mater. Res.*, **13**, pp. 1300–1306.
- [9] Stolken, J. S., and Evans, A. G., 1998, "A Microbend Test Method for Measuring the Plasticity Length Scale," *Acta Mater.*, **46**, pp. 5109–5115.
- [10] Smyshlyaev, V. P., and Fleck, N. A., 1996, "Role of Strain Gradients in the Grain Size Effect for Polycrystals," *J. Mech. Phys. Solids*, **44**, pp. 465–495.
- [11] Gao, H., Huang, Y., Nix, W. D., and Hutchinson, J. W., 1999, "Mechanism-Based Strain Gradient Plasticity—I. Theory," *J. Mech. Phys. Solids*, **47**, pp. 1239–1263.
- [12] Huang, Y., Gao, H., Nix, W. D., and Hutchinson, J. W., 2000, "Mechanism-Based Strain Gradient Plasticity—II. Analysis," *J. Mech. Phys. Solids*, **48**, pp. 99–128.
- [13] Huang, Y., Xue, Z., Gao, H., Nix, W. D., and Xia, Z. C., 2000, "A Study of Micro-Indentation Hardness Tests by Mechanism-Based Strain Gradient Plasticity," *J. Mater. Res.*, **15**, pp. 1786–1796.
- [14] Gao, H., Huang, Y., and Nix, W. D., 1999, "Modeling Plasticity at the Micrometer Scale," *Naturwissenschaften*, **86**, pp. 507–515.
- [15] Hwang, K. C., and Inoue, T., 1998, "Recent Advances in Strain Gradient Plasticity," *Mat. Sci. Res. Int.*, **4**, pp. 227–238.
- [16] Acharya, A., and Bassani, J. L., 2000, "Lattice Incompatibility and a Gradient Theory of Crystal Plasticity," *J. Mech. Phys. Solids*, **48**, pp. 1565–1595.
- [17] Acharya, A., and Beaudoin, A. J., 2000, "Grain-Size Effect in Viscoplastic Polycrystals at Moderate Strains," *J. Mech. Phys. Solids*, **48**, pp. 2213–2230.
- [18] Dai, H., and Parks, D. M., 2001, "Geometrically Necessary Dislocation Density in Continuum Crystal Plasticity Theory and FEM Implementation," unpublished manuscript.
- [19] Qiu, X., Huang, Y., Wei, Y., Gao, H., and Hwang, K. C., 2001, "The Flow Theory of Mechanism-Based Strain Gradient Plasticity," submitted for publication.
- [20] Hutchinson, J. W., 1968, "Singular Behavior at the End of a Tensile Crack in a Hardening Material," *J. Mech. Phys. Solids*, **16**, pp. 13–31.
- [21] Rice, J. R., and Rosengren, G. F., 1968, "Plane Strain Deformation Near a Crack Tip in a Power Law Hardening Material," *J. Mech. Phys. Solids*, **16**, pp. 1–12.

# Normal Indentation of Elastic Half-Space With a Rigid Frictionless Axisymmetric Punch

G. Fu

Ph.D. Candidate

A. Chandra

Engel Professor Fellow ASME

e-mail: achandra@iastate.edu

Department of Mechanical Engineering,  
Iowa State University,  
Ames, IA 50011

*The contact of a simply connected axisymmetric punch with an elastic half-space is examined. The problem is mathematically formulated by using potential theory and complex variable analysis. The final solution of these equations is obtained by assuming a polynomial punch profile. The conditions for complete contact and incomplete contact are also derived. The solutions give the pressure profile at the punch-elastic half-space interface for any polynomial punch profile, even for noninteger power polynomials, as long as the contact region is simply connected. The results show that some classic solutions in linear elasticity are special cases of the derived solution and determine the range of validity for those solutions. [DOI: 10.1115/1.1445145]*

## 1 Introduction

Contact pressure distribution between two surfaces has always been of great interest to engineers. Perhaps the most widely used equation for bearing application is Hertz's solution. Boussinesq solution for flat-ended punch finds its application in the safety evaluation of foundations in civil engineering. Recently, researchers used Love and Sneddon solution for conical punch to explain nanoindentation experimental data (e.g., Hay et al. [1]). In elastic emission machining (EEM), the material is removed through the atomic scale elastic fracture without plastic deformation (see Komanduri [2]). Indentation model for different particle shape is needed to investigate this process. The material removal rate in chemical mechanical planarization (CMP) of silicon wafer largely depends on the pressure distribution on the wafer surface (Fu and Chandra [3]). Shield and Bogy [4] investigated the indentation of a flat-ended punch into layered elastic half-space. Their solution may be used in the evaluation of protective coating to prevent the substrate from wear under sliding contact.

When a rigid axisymmetric punch indents normally into an elastic half-space, there are two possibilities: one is that the whole punch surface contacts with the half-space; the other is that only part of the punch contacts with the half-space. Following the terminology by Gladwell [5], the first contact is called complete or bonded, and the second one is termed incomplete or unbonded. In the second case, the contact pressure will drop to zero at the boundary of the contact region. Complete contact can be classified further into critical complete contact and general complete contact. In general complete contact, pressure at the punch edge goes to infinity; in critical complete contact, pressure drops to zero at the punch edge and the pressure profile is similar to that of incomplete contact.

The axisymmetric solutions for a punch whose shape is flat-ended, conical, or parabolic have been known for years. Hertz found the solution for the parabolic punch in 1882 when he investigated the pattern of interference fringes between glass lenses (see Johnson [6]). His solution is only valid when the contact is incomplete. Boussinesq obtained the pressure distribution for a flat-ended punch in 1885 and found the square root singularity at

the punch edge (see Johnson [6]). To solve conical punch problem, Love [7] used potential theory and Sneddon [8] used integral transform method to get the same result. They found that there exists a logarithmic singularity at the conical tip, and their solutions are also for incomplete contact. For circular annular punch problem, Collins [9] used potential theory and superposition method to obtain the solution.

Popov [10] shows: If a normal pressure distribution on the plane  $z=0$  over a circular area with radius  $a$  has a square-root singularity at the edge and is in the form  $P_{2n}[(1-r^2/a^2)^{1/2}]/(1-r^2/a^2)^{1/2}$  where  $P_n(x)$  is the Legendre polynomial, then the vertical displacement on the plane  $z=0$  over the circular area will be proportional to  $P_{2n}[(1-r^2/a^2)^{1/2}]$ , which is an even polynomial.

In this paper, we consider a rigid frictionless axisymmetric punch with a polynomial profile and axis of revolution as the  $z$ -axis, indenting normally into the plane  $z=0$  of an elastic half-space  $z \geq 0$ . The problem is considered in linear theory of elasticity and the elastic half-space is assumed to be isotropic and homogeneous. The punch is assumed to be rigid with sharp corners, which may lead to singularities in the contact pressure at those corners. The problem is solved by using potential theory and complex variable analysis. Green's solution [11] is utilized and with the aid of mathematical software *MATHEMATICA* (Wolfram [12]), the final solution is obtained. Also, the conditions for the complete and incomplete contacts are derived. The solutions give the pressure profile at the punch-elastic half-space interface for any polynomial punch profile, even for noninteger power polynomials so long as the contact region remains simply connected. As special cases of the obtained solution, we show the results for five kinds of punches: flat-ended punch, square-root punch, conical punch, three half-power punch, and parabolic punch.

## 2 The Problem Formulation in the Theory of Linear Elasticity

The following equations give the relevant displacement and stresses. The vertical component of the displacement is denoted by  $u_z$ , and the stress components have two subscripts corresponding to the appropriate coordinates.  $E$  and  $\nu$  are Young's modulus and Poisson's ratio for the elastic half-space.

As Fig. 1 shows, the boundary conditions for the indentation problem are

$$\tau_{zr} = \tau_{z\theta} = 0, \quad (0 \leq r < \infty) \quad (1)$$

$$\sigma_{zz} = 0, \quad (r > a) \quad (2)$$

Contributed by the Applied Mechanics Division of THE AMERICAN SOCIETY OF MECHANICAL ENGINEERS for publication in the ASME JOURNAL OF APPLIED MECHANICS. Manuscript received by the ASME Applied Mechanics Division, June 5, 2001; final revision, Sept. 21, 2001. Associate Editor: J. R. Barber. Discussion on the paper should be addressed to the Editor, Prof. Lewis T. Wheeler, Department of Mechanical Engineering, University of Houston, Houston, TX 77204-4792, and will be accepted until four months after final publication of the paper itself in the ASME JOURNAL OF APPLIED MECHANICS.

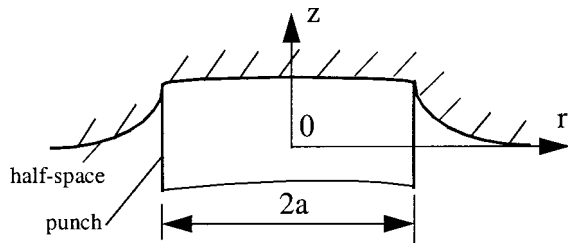


Fig. 1 Normal indentation of an elastic half-space

and,

$$u_z = f(r), \quad (0 \leq r \leq a) \quad (3)$$

where  $f(r)$  is the final position of the punch.

This boundary value problem can be changed into the following equivalent potential theory problem (see Green and Zerna [11]):

$$\frac{\partial \omega}{\partial z} = 0, \quad (r > a) \quad (4)$$

$$\omega = f(r), \quad (0 \leq r \leq a) \quad (5)$$

$$\nabla^2 \omega = 0. \quad (6)$$

Green [11] considers the following potential function for  $\omega$ , which can be obtained through Fourier cosine transform (see Gladwell [5]):

$$\omega(r, z) = \frac{1}{2} \int_0^a \frac{g(t) dt}{\sqrt{r^2 + (z + it)^2}} + \frac{1}{2} \int_0^a \frac{g(t) dt}{\sqrt{r^2 + (z - it)^2}}. \quad (7)$$

Green [11] finds that if  $f(r)$  is continuously differentiable in  $0 \leq r \leq a$ , then

$$g(t) = \frac{2}{\pi} \frac{d}{dt} \int_0^t \frac{r f(r)}{\sqrt{t^2 - r^2}} dr. \quad (8)$$

His further derivation leads to

$$\sigma_{zz}|_{z=0} = \frac{1}{2} \cdot \frac{E}{1-\nu^2} \cdot \frac{1}{r} \cdot \frac{\partial}{\partial r} \int_r^a \frac{t g(t)}{\sqrt{t^2 - r^2}} dt, \quad (0 \leq r \leq a). \quad (9)$$

Green and Zerna [11] have used Eq. (9) to solve the Boussinesq problem for a flat-ended punch. This paper will derive the solution for punches with general polynomial profiles and the conditions for this solution to be valid in different contact situations; the load-displacement relationship is also given.

### 3 Analytical Solutions

We express the displacement field under the punch as a polynomial:

$$f(r) = \sum_{\alpha=0}^{\alpha_n} a_\alpha r^\alpha, \quad (\alpha=0, \alpha_1, \alpha_2, \dots, \alpha_n \quad \text{and} \quad \alpha \geq 0) \quad (10)$$

where the function  $\sum_{\alpha=\alpha_1}^{\alpha_n} a_\alpha r^\alpha$  describes the shape of the punch,  $a_0$  describes the depth of indentation and is non-negative, and  $\alpha$  is not necessarily an integer.

**3.1 The Solution When  $\alpha$  is Not an Integer but is a Positive Real Number.** Substituting Eq. (10) into Eq. (8) and Eq. (9), with the aid of the symbolic manipulation program *MATHEMATICA* (Wolfram [12]) we have

$$\sigma_{zz}|_{z=0} = \frac{1}{2\sqrt{\pi}} \cdot \frac{E}{1-\nu^2} \sum_{\alpha=0}^{\alpha_n} a_\alpha (1+\alpha) \cdot \frac{\Gamma\left(\frac{2+\alpha}{2}\right)}{\Gamma\left(\frac{3+\alpha}{2}\right)} \Phi(r, \alpha) \quad (11)$$

where

$$\Phi(r, \alpha) = \frac{\sqrt{\pi}}{2} \cdot (1+\alpha) \cdot \frac{\Gamma\left(-\frac{1+\alpha}{2}\right)}{\Gamma\left(-\frac{\alpha}{2}\right)} r^{-1+\alpha} - \frac{a^{1+\alpha}}{r^2} \left[ \frac{1}{\sqrt{1-\frac{r^2}{a^2}}} {}_2F_1\left(\frac{1}{2}, -\frac{1+\alpha}{2}; \frac{1-\alpha}{2}; \frac{r^2}{a^2}\right) \right] \quad (12)$$

and  ${}_2F_1(a, b; c; z)$  is hypergeometric function.

Equation (11) and Eq. (12) are general formats; however, one cannot use them directly when  $\alpha$  a non-negative integer. The following two sections will give the explanations and the specific formats when this happens.

**3.2 The Solution When  $\alpha$  is Zero or a Positive Even Integer.** If we utilize Eq. (12) and note  $\Gamma(-\alpha/2) = \infty$ , the function  $\Phi(r, \alpha)$  can be simplified as

$$\Phi(r, \alpha) = -\frac{a^{1+\alpha}}{r^2} \left[ \frac{1}{\sqrt{1-\frac{r^2}{a^2}}} {}_2F_1\left(\frac{1}{2}, -\frac{1+\alpha}{2}; \frac{1-\alpha}{2}; \frac{r^2}{a^2}\right) \right]. \quad (13)$$

To use elementary functions to express  $\Phi(r, \alpha)$ , we can derive by hand by letting  $t = r \sec \theta$  and obtain the following alternative expression:

$$\Phi(r, \alpha) = (1+\alpha) r^{\alpha-1} \left[ \sum_{i=0}^{\alpha/2} \frac{\Gamma\left(\frac{\alpha}{2} + 1\right)}{\Gamma\left(\frac{\alpha}{2} + 1 - i\right) \Gamma(i+1)} \cdot \left(\frac{\sqrt{a^2 - r^2}}{r}\right)^{2i+1} \right] - \frac{a^{1+\alpha}}{r^2} \frac{1}{\sqrt{1-\frac{r^2}{a^2}}}. \quad (14)$$

**3.3 The Solution When  $\alpha$  is a Positive Odd Integer.** If we use Eq. (12), we will have  $\Phi(r, \alpha) = \infty - \infty$  and it is difficult to decide its limit. To avoid this problem, we let  $t = r \sec \theta$  and derive by hand the following solution:

$$\Phi(r, \alpha) = (1+\alpha) \cdot r^{\alpha-1} \sum_{i=0}^{\alpha+1/2} \frac{\Gamma\left(\frac{\alpha+3}{2}\right)}{\Gamma\left(\frac{\alpha+3}{2} - i\right) \Gamma(i+1)} I_i(r) - \frac{a^{1+\alpha}}{r^2} \frac{1}{\sqrt{1-\frac{r^2}{a^2}}} \quad (15)$$

where

$$I_i = \frac{1}{2i} \cdot \frac{a}{r} \cdot \left( \frac{\sqrt{a^2 - r^2}}{r} \right)^{2i-1} - \frac{2i-1}{2i} I_{i-1} \text{ with } I_0(r) = \frac{1}{2} \ln \left( \frac{a + \sqrt{a^2 - r^2}}{a - \sqrt{a^2 - r^2}} \right). \quad (16)$$

**3.4 Total Load.** The total vertical force needed to cause the displacement  $a_0$  is

$$F_z = - \int_0^a \sigma_{zz}|_{z=0} \cdot 2\pi r dr = \sqrt{\pi} \frac{E}{1-\nu^2} \sum_{\alpha=0}^{\alpha_n} a_\alpha \cdot \frac{\Gamma\left(\frac{2+\alpha}{2}\right)}{\Gamma\left(\frac{3+\alpha}{2}\right)} a^{1+\alpha}. \quad (17)$$

**3.5 Condition for Using the Solution.** If the whole punch contacts with the half-space, i.e., the contact region is simply connected, we need to have

$$\sigma_{zz}|_{z=0} \leq 0 \quad (0 \leq r \leq a) \quad \text{or} \quad \lim_{r \rightarrow a^-} \sigma_{zz}|_{z=0} \leq 0. \quad (18)$$

At the punch edge we need to have  $\sigma_{zz}|_{z=0, r=a} \leq 0$ . From Eq. (12) and noting

$${}_2F_1\left(\frac{1}{2}, -\frac{1+\alpha}{2}; \frac{1-\alpha}{2}; 1\right) = -\frac{\sqrt{\pi}}{2} \cdot (1+\alpha) \cdot \frac{\Gamma\left(-\frac{1+\alpha}{2}\right)}{\Gamma\left(-\frac{\alpha}{2}\right)},$$

we have

$$\sum_{\alpha=0}^{\alpha_n} (1+\alpha) \cdot a_\alpha \cdot \frac{\Gamma\left(\frac{2+\alpha}{2}\right)}{\Gamma\left(\frac{3+\alpha}{2}\right)} a^\alpha \geq 0. \quad (19)$$

If the contact is complete and the pressure at the punch edge is zero which is the condition for critical complete contact, the following condition has to be satisfied:

$$\sum_{\alpha=0}^{\alpha_n} (1+\alpha) \cdot a_\alpha \cdot \frac{\Gamma\left(\frac{2+\alpha}{2}\right)}{\Gamma\left(\frac{3+\alpha}{2}\right)} a^\alpha = 0. \quad (20)$$

## 4 Solutions for Some Special Cases

**4.1 Flat-Ended Punch.** When  $f(r) = a_0$  ( $0 \leq r \leq a$ ), we have

$$\sigma_{zz}|_{z=0} = -\frac{a_0}{\pi} \cdot \frac{E}{1-\nu^2} \cdot \frac{1}{\sqrt{a^2 - r^2}}, \quad (21)$$

which is the same as Boussinesq's solution and there is a square-root singularity at the punch edge.

**4.2 One-Half Power Punch.** In this case, punch vertical displacement field is defined as  $f(r) = a_0 + a_{1/2} r^{1/2}$  ( $0 \leq r \leq a$ ). When

$$a_0 \frac{\Gamma(1)}{\Gamma\left(\frac{3}{2}\right)} + \frac{3}{2} \cdot a_{1/2} \cdot \frac{\Gamma\left(\frac{5}{4}\right)}{\Gamma\left(\frac{7}{4}\right)} \cdot a^{1/2} \geq 0, \quad (22)$$

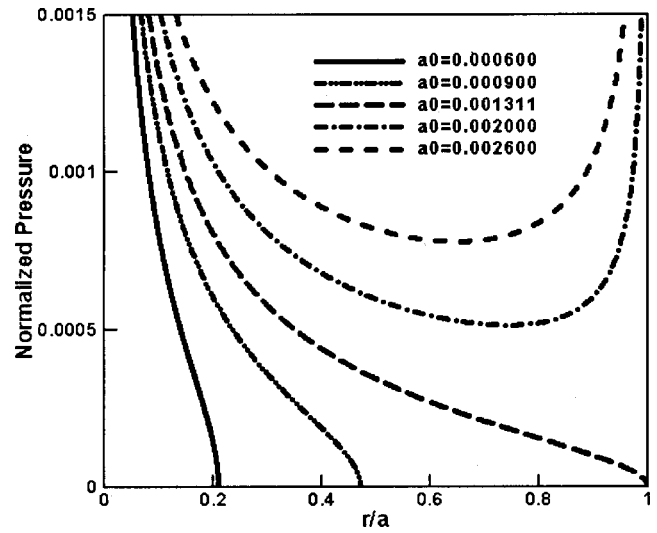


**Fig. 2 One-half power punch.** The pressure is normalized with respect to  $-E/(1-\nu^2)$ .

$$\sigma_{zz}|_{z=0} = -\frac{a_0}{\pi} \cdot \frac{E}{1-\nu^2} \cdot \frac{1}{\sqrt{a^2 - r^2}} + \frac{3}{4\sqrt{\pi}} \cdot \frac{E}{1-\nu^2} \cdot a_{1/2} \cdot \frac{\Gamma\left(\frac{5}{4}\right)}{\Gamma\left(\frac{7}{4}\right)} \cdot \Phi\left(r, \frac{1}{2}\right) \quad (23)$$

where

$$\Phi\left(r, \frac{1}{2}\right) = \frac{3\sqrt{\pi}}{4} \cdot \frac{\Gamma\left(-\frac{3}{4}\right)}{\Gamma\left(-\frac{1}{4}\right)} r^{-1/2} - \frac{a^{3/2}}{r^2} \left[ \frac{1}{\sqrt{1 - \frac{r^2}{a^2}}} {}_2F_1\left(\frac{1}{2}, -\frac{3}{4}; \frac{1}{4}; \frac{r^2}{a^2}\right) \right]. \quad (24)$$

Figure 2 shows the pressure distributions for a punch with radius 1 and profile  $f(r) = a_0 - 0.001 r^{1/2}$  under different depth of indentation  $a_0$ . When  $a_0 = 0.001311$ , it is critical complete contact. There is a singularity at the tip when the indentation depth is no more than the one for critical complete contact. There will be singularities both at the tip and at the edge (square-root singularity) when the indentation depth is greater than the one for critical complete contact.

**4.3 Conical Punch.** In this case, punch vertical displacement field is defined as  $f(r) = a_0 + a_1 r$  ( $0 \leq r \leq a$ ). When

$$a_0 \frac{\Gamma(1)}{\Gamma\left(\frac{3}{2}\right)} + 2a_1 \frac{\Gamma\left(\frac{3}{2}\right)}{\Gamma(2)} a > 0, \quad (25)$$

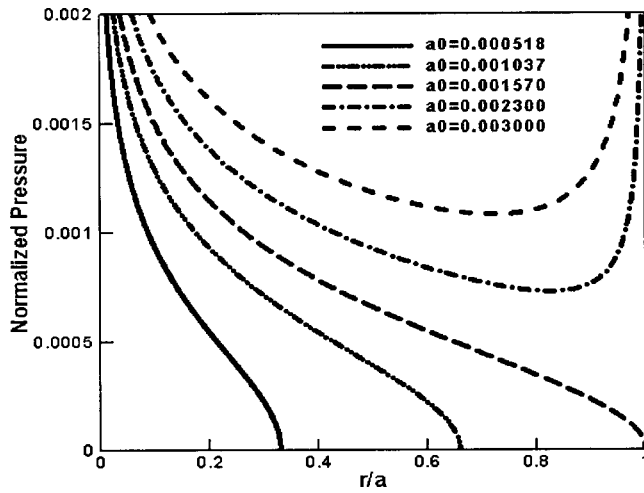


Fig. 3 Conical punch. The pressure is normalized with respect to  $-E/(1-\nu^2)$ .

$$\sigma_{zz}|_{z=0} = \frac{1}{2\sqrt{\pi}} \cdot \frac{E}{1-\nu^2} \cdot a_1 \cdot 2 \cdot \frac{\Gamma\left(\frac{3}{2}\right)}{\Gamma(2)} \cdot \left[ \frac{1}{2} \ln \left( \frac{a + \sqrt{a^2 - r^2}}{a - \sqrt{a^2 - r^2}} \right) \right] + \frac{1}{2\sqrt{\pi}} \cdot \frac{E}{1-\nu^2} \cdot \left[ \frac{a_0}{a} \frac{\Gamma(1)}{\Gamma\left(\frac{3}{2}\right)} + 2a_1 \frac{\Gamma\left(\frac{3}{2}\right)}{\Gamma(2)} \right] \cdot \left[ \frac{a^2}{r^2} \left( \sqrt{1 - \frac{r^2}{a^2}} - \frac{1}{\sqrt{1 - \frac{r^2}{a^2}}} \right) \right]. \quad (26)$$

There is a square-root singularity at the punch edge and a logarithmic singularity at the punch tip.

For critical complete contact,  $a_0\Gamma(1)/\Gamma(3/2) + 2a_1\Gamma(3/2)/\Gamma(2)a = 0$  and  $\sigma_{zz}|_{z=0} = a_1/4 \cdot E/(1-\nu^2) \cdot \ln(a + \sqrt{a^2 - r^2}/a - \sqrt{a^2 - r^2})$ . It leads to the same solutions as those of Love [7] and Sneddon [8]. At the punch edge, pressure drops to zero and there is a logarithmic singularity at the punch tip.

Fig. 3 shows the pressure distributions for a conical punch with radius 1 and profile  $f(r) = a_0 - 0.001r$  under different depth of indentation  $a_0$ . When  $a_0 = 0.001570$ , it is critical complete contact. There is a logarithmic singularity at the tip when the indentation depth is no more than the one for critical complete contact. There will be singularities at both the tip (logarithmic singularity) and the edge (square-root singularity) when the indentation depth is greater than the one for critical complete contact.

**4.4 Three-Half Power Punch.** In this case, punch vertical displacement field is defined as  $f(r) = a_0 + a_{3/2}r^{3/2}$  ( $0 \leq r \leq a$ ).

When

$$a_0 \frac{\Gamma(1)}{\Gamma\left(\frac{3}{2}\right)} + \frac{5}{2} \cdot a_{3/2} \cdot \frac{\Gamma\left(\frac{7}{4}\right)}{\Gamma\left(\frac{9}{4}\right)} \cdot a^{3/2} \geq 0, \quad (27)$$

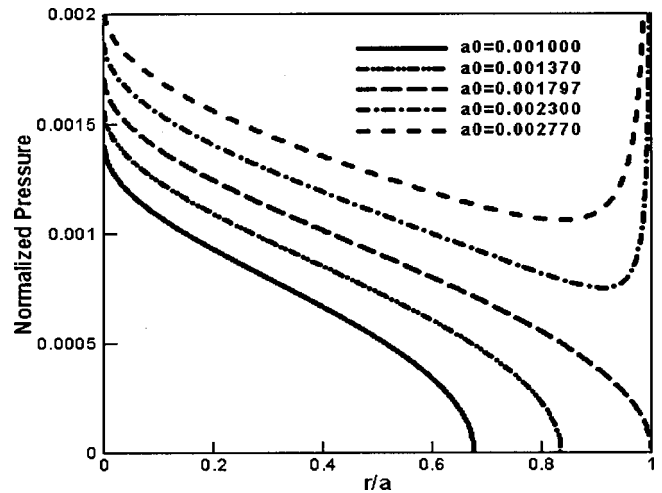


Fig. 4 Three-half power punch. The pressure is normalized with respect to  $-E/(1-\nu^2)$ .

$$\sigma_{zz}|_{z=0} = -\frac{a_0}{\pi} \cdot \frac{E}{1-\nu^2} \cdot \frac{1}{\sqrt{a^2 - r^2}} + \frac{5}{4\sqrt{\pi}} \cdot \frac{E}{1-\nu^2} \cdot a_{3/2} \cdot \frac{\Gamma\left(\frac{7}{4}\right)}{\Gamma\left(\frac{9}{4}\right)} \cdot \Phi\left(r, \frac{3}{2}\right) \quad (28)$$

where

$$\Phi\left(r, \frac{3}{2}\right) = \frac{5\sqrt{\pi}}{4} \cdot \frac{\Gamma\left(-\frac{5}{4}\right)}{\Gamma\left(-\frac{3}{4}\right)} r^{1/2} - \frac{a^{5/2}}{r^2} \left[ \frac{1}{\sqrt{1 - \frac{r^2}{a^2}}} {}_2F_1\left(\frac{1}{2}, -\frac{5}{4}; -\frac{1}{4}; \frac{r^2}{a^2}\right) \right]. \quad (29)$$

Fig. 4 shows the pressure distributions for a punch with radius 1 and profile  $f(r) = a_0 - 0.001r^{3/2}$  under different depth of indentation  $a_0$ . When  $a_0 = 0.001797$ , it is critical complete contact. There is no singularity when the indentation depth is no more than the one for critical complete contact; but there will be a square-root singularity at the edge when the indentation depth is greater than the one for critical complete contact.

**4.5 Parabolic Punch.** In this case, punch vertical displacement field is defined as  $f(r) = a_0 + a_2r^2$  ( $0 \leq r \leq a$ ).

When

$$a_0 \cdot \frac{\Gamma(1)}{\Gamma\left(\frac{3}{2}\right)} + 3a_2 \cdot \frac{\Gamma(2)}{\Gamma\left(\frac{5}{2}\right)} \cdot a^2 > 0, \quad \sigma_{zz}|_{z=0} = -\frac{1}{2\sqrt{\pi}} \cdot \frac{E}{1-\nu^2} \cdot \left[ \frac{\Gamma(1)}{\Gamma\left(\frac{3}{2}\right)} a_0 \frac{1}{\sqrt{a^2 - r^2}} + 3 \frac{\Gamma(2)}{\Gamma\left(\frac{5}{2}\right)} a_2 \frac{2r^2 - a^2}{\sqrt{a^2 - r^2}} \right] \quad (30)$$



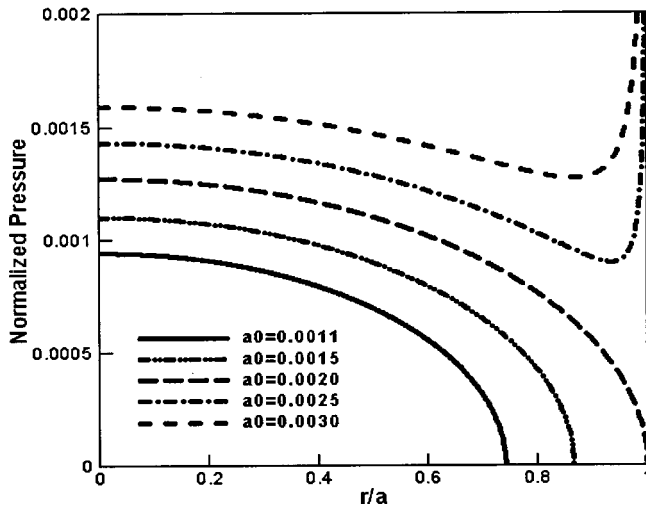


Fig. 5 Parabolic punch. The pressure is normalized with respect to  $-E/(1-\nu^2)$ .

there is a square-root singularity at the punch edge. When

$$a_0 \cdot \frac{\Gamma(1)}{\Gamma\left(\frac{3}{2}\right)} + 3a_2 \cdot \frac{\Gamma(2)}{\Gamma\left(\frac{5}{2}\right)} \cdot a^2 = 0,$$

we have

$$\sigma_{zz}|_{z=0} = \frac{4}{\pi} \cdot \frac{E}{1-\nu^2} \cdot a_2 \cdot \sqrt{a^2 - r^2}. \quad (31)$$

The pressure drops to zero at the punch edge and the solution is the same as Hertz's.

Figure 5 shows the pressure distributions for a parabolic punch with radius 1 and profile  $f(r) = a_0 - 0.001r^2$  under different depth of indentation  $a_0$ . When  $a_0 = 0.0020$ , it is critical complete contact. There is no singularity when the indentation depth is no more than the one for critical complete contact. There will be a square-root singularity at the edge when the indentation depth is greater than the one for critical complete contact.

## 5 Discussions

The solutions obtained in this paper can be the basis for finding contact pressure between two smooth surfaces with arbitrary shape profile.

For the nanoindentation using an axisymmetric indenter, these solutions will provide a good theoretical basis for interpreting the load-displacement curve and evaluating Young's modulus and Poisson's ratio.

For punch displacement profile in the formula of  $f(r) = a_0 + a_{2m}r^{2m}$  ( $m$  is positive integer), the pressure distribution will not have singularities when the indentation depth is not more than the one for critical complete contact and will have a square-root singularity at the punch edge when the indentation depth is greater than the one for critical complete contact.

For punch displacement profile in the formula of  $f(r) = a_0 + a_{2m-1}r^{2m-1}$  ( $m$  is positive integer), the pressure distribution will always have a logarithmic singularity at the punch tip and will have a square-root singularity at the punch edge when the indentation depth is greater than the one for critical complete contact.

It should be emphasized that the solution is only valid when the contact region is a simply connected domain. When a general

punch profile is considered such as  $f(r) = \sum_{\alpha=0}^{\infty} a_{\alpha}r^{\alpha}$ , one should first investigate if the contact area is simply connected before using the presented solution.

The derived solution can be the basis for further investigation of the indentation of elastic half-space when the interface friction is considered.

## Acknowledgment

This material is based upon work supported by the U.S. National Science Foundation under Grant No. DMI-0084736. The authors gratefully acknowledge this financial support. Any opinions, findings, and conclusions or recommendations expressed in this material are those of the authors and do not necessarily reflect the views of the National Science Foundation.

## Appendix

Listed here are the identities used in the derivation which can be obtained by using the symbolic manipulation program *MATH-EMATICA*:

$$\begin{aligned} 1. \quad & \int_0^t \frac{r^{1+k}}{\sqrt{t^2-r^2}} dr = \frac{\sqrt{\pi}}{2} \cdot \frac{\Gamma\left(\frac{2+k}{2}\right)}{\Gamma\left(\frac{3+k}{2}\right)} t^{1+k} \\ 2. \quad & \int_r^a \frac{t^{1+k}}{\sqrt{t^2-r^2}} dt = \frac{\sqrt{\pi}}{2} \cdot \frac{\Gamma\left(-\frac{1+k}{2}\right)}{\Gamma\left(-\frac{k}{2}\right)} r^{1+k} \\ & + \frac{a^{1+k}}{1+k} \cdot {}_2F_1\left(\frac{1}{2}, -\frac{1+k}{2}; \frac{1-k}{2}; \frac{r^2}{a^2}\right) \\ 3. \quad & \frac{\partial}{\partial r} \left[ {}_2F_1\left(\frac{1}{2}, -\frac{1+k}{2}; \frac{1-k}{2}; \frac{r^2}{a^2}\right) \right] \\ & = -\frac{1+k}{r} \left[ \frac{1}{\sqrt{1-\frac{r^2}{a^2}}} - {}_2F_1\left(\frac{1}{2}, -\frac{1+k}{2}; \frac{1-k}{2}; \frac{r^2}{a^2}\right) \right] \\ 4. \quad & \int_0^a \left[ \frac{1}{\sqrt{1-\frac{r^2}{a^2}}} - {}_2F_1\left(\frac{1}{2}, -\frac{1+k}{2}; \frac{1-k}{2}; \frac{r^2}{a^2}\right) \right] \frac{dr}{r} \\ & = \frac{1}{1+k} + \frac{\sqrt{\pi}}{2} \cdot \frac{\Gamma\left(-\frac{1+k}{2}\right)}{\Gamma\left(-\frac{k}{2}\right)}. \end{aligned}$$

## References

- [1] Hay, J. C., Bolshakov, A., and Pharr, G. M., 1999, "Critical Examination of the Fundamental Relations Used in the Analysis of Nanoindentation Data," *J. Mater. Res.*, **14**, pp. 2296–2305.
- [2] Komanduri, R., Lucca, D. A., and Tani, Y., 1997, "Technological Advances in Fine Abrasive Processes," *Ann. CIRP*, **46**, No. 2, pp. 545–596.
- [3] Fu, G., and Chandra, A., 2001, "A Model for Wafer Scale Variation of Material Removal Rate in Chemical Mechanical Polishing Based on Elastic Pad Deformation," *J. Electron. Mater.*, **30**, pp. 400–408.
- [4] Shield, T. W., and Bogy, D. B., 1989, "Some Axisymmetric Problem for Layered Elastic Media: Part I—Multiple Region Contact Solutions for Simple-Connected Indenters," *ASME J. Appl. Mech.*, **56**, pp. 798–806.
- [5] Gladwell, G. M. L., 1980, *Contact Problems in the Classical Theory of Elasticity*, Sijthoff & Noordhoff, Alphen aan den Rijn, The Netherlands.

- [6] Johnson, K. L., 1985, *Contact Mechanics*, Cambridge University Press, Cambridge, UK.
- [7] Love, A. E. H., 1939, "Boussinesq's Problem for a Rigid Cone," *Quarterly J. Math.* **10**, pp. 161–175.
- [8] Sneddon, I. N., 1948, "Boussinesq's Problem for a Rigid Cone," *Proc. Cambridge Philos. Soc.* **44**, pp. 492–507.
- [9] Collins, W. D., 1963, "Potential Problems for a Circular Annulus," *Proc. Edinburgh Math. Soc.*, **13**, pp. 235–246.
- [10] Popov, G. Ia., 1962, "The Contact Problem of the Theory of Elasticity for the Case of a Circular Area of Contact," *J. Appl. Math. Mech.*, (English translation of PMM), **26**, pp. 207–225.
- [11] Green, A. E., and Zerna, W., 1954, *Theoretical Elasticity*, Oxford University Press, London.
- [12] Wolfram, S., 1991, *Mathematica—A System for Doing Mathematics by Computer*, Addison-Wesley, Reading, MA.

**K. V. Spiliopoulos**

Associate Professor,  
Institute of Structural Analysis and  
Seismic Research,  
Department of Civil Engineering,  
National Technical University of Athens,  
Zografou Campus,  
GR-157 73, Athens, Greece

# A Simplified Method to Predict the Steady Cyclic Stress State of Creeping Structures

*Simplified methods have been developed to find the long-term cyclic state of stress for structures that exhibit inelastic creep and are subjected to a short period cyclic loading. In the present work a new simplified method is presented which may be applied to cyclic loads having any period. The method is based on decomposing the residual stress in Fourier series. The various Fourier coefficients are computed, in an iterative way, by satisfying equilibrium and compatibility at a few time points inside the cycle. The whole numerical procedure is formulated within the finite element method and examples of various structures are presented. [DOI: 10.1115/1.1430234]*

## 1 Introduction

Structures such as nuclear reactors, aircraft gas turbine propulsion engines, etc., operate in high levels of loads and temperature. It is essential, therefore, for the design of these structures, to predict the inevitable accumulation of inelastic strains throughout their life.

The complete response of a structure, which is subjected to a given mechanical loading and exhibits inelastic time independent (plastic) and inelastic time-dependent (creep) behavior, is quite complex. The reasons of the complexity are the laborious and often numerically unstable time-stepping calculations that have to be performed following the exact loading history.

When the loading is highly regular, i.e., it is either constant or cyclic, much of the complexity of the inelastic response is confined to an initial transient stage. It is very frequently true that the stresses and the strain rates tend towards a steady or a cyclic pattern. If this pattern develops early enough, then it may well suffice to assess the complete behavior with perhaps a very limited time-stepping analysis at the early stages of the application of the loading.

The methods that seek to find this stress pattern right from the start of the calculations are called simplified methods. These methods, not only arrive at the steady-state stress pattern much quicker than full time-stepping analyses, but also provide a much better insight into the inelastic response of a structure. Well-known examples of such methods, with plastic behavior only present, are the limit and shakedown analyses of structures.

For elevated temperature conditions the effects of creep must be taken into account. Leckie and Ponter [1] proved theoretically and verified experimentally ([2]) that, when the level of cyclic loading is below  $n/(n+1)$  of the elastic shakedown loading, where  $n$  is the creep index in the power creep law, creep effects are the dominant ones and plasticity may be neglected.

When only creep effects are present, Ponter [3] developed a simplified method that may be applied to loads having a very short period cycle. It is natural, then, to assume, that there is no time for any stress redistribution to take place inside a cycle. Keeping, therefore, the residual stress constant inside the cycle, an iterative procedure was then set up, which updates the residual

stress by satisfying equilibrium and compatibility at the end of the cycle. The process stops when there is no more change in the values of the residual stresses. Examples of applications to various structures have been presented by Ponter and Brown [4]. Spiliopoulos [5] proved that a fictitious cycle period may be used so that the rate of convergence improves substantially.

When an engineer, though, faces the problem of the long-term structural response of a cyclically loaded structure, he cannot know, in advance, whether the cycle is short or not. There is a need, therefore, to estimate this response in a simple way, regardless the cyclic duration, without having to resort to time-stepping calculations.

In this work a new simplified method, originally proposed for application to a simple structure ([6]), is developed. This method may be applied to any structure which is subjected to a cyclic loading of any period. The main ingredient of the method is the time decomposition of the unknown residual stress distribution into Fourier series. Thus the problem is converted to a problem of evaluating the Fourier coefficients of the various terms of the series. These coefficients may be calculated in an iterative way, using the time derivatives of the residual stresses to which these coefficients are shown to be directly connected. By satisfying equilibrium and compatibility, these derivatives may be calculated at discrete time points inside the cycle. An update of the Fourier coefficients then takes place by numerically integrating over the cycle. The iterations stop when no more significant change in their values, within a specified tolerance, takes place. In order for the sequence of iterations to be convergent, a special acceleration numerical scheme is used. The whole procedure is formulated within the framework of the finite element method and examples of application to one and two-dimensional structures are included in the paper.

## 2 The Steady Cyclic Stress State

Let us assume that a structure is subjected to a cyclic mechanical loading of period  $T$ :

$$P(t+T) = P(t). \quad (1)$$

In response to this loading, the structure develops a stress system  $\sigma_{ij}(t)$ , which may be decomposed into two parts: Assuming a completely linear elastic material behavior, the first part is a cyclic elastic stress  $\sigma_{ij}^e(t)$  that equilibrates the cyclic loading that is applied, and the second part is a self-equilibrating stress system  $\rho_{ij}(t)$  due to the inelasticity that creep induces in the structure. Thus one can write

$$\sigma_{ij}(t) = \sigma_{ij}^e(t) + \rho_{ij}(t). \quad (2)$$

Contributed by the Applied Mechanics Division of THE AMERICAN SOCIETY OF MECHANICAL ENGINEERS for publication in the ASME JOURNAL OF APPLIED MECHANICS. Manuscript received by the ASME Applied Mechanics Division, Jan 13, 2001; final revision, Aug. 6, 2001. Associate Editor: M.-J. Pindera.

Discussion on the paper should be addressed to the Editor, Professor Lewis T. Wheeler, Department of Mechanical Engineering, University of Houston, Houston, TX 77204-4792, and will be accepted until four months after final publication of the paper itself in the ASME JOURNAL OF APPLIED MECHANICS.

The strain rates, in the same way, may also be decomposed into two terms  $\dot{\epsilon}_{ij}^{el}$  and  $\dot{\epsilon}_{ijr}$ :

$$\dot{\epsilon}_{ij} = \dot{\epsilon}_{ij}^{el} + \dot{\epsilon}_{ijr} = \dot{\epsilon}_{ij}^{el} + \dot{\epsilon}_{ijr}^{el} + \dot{\epsilon}_{ijr}^{cr} \quad (3)$$

In the above equation the residual strain rate term has been itself decomposed into elastic and creep parts.

The elastic strain rates are related to their corresponding stress rates by

$$\begin{aligned} \dot{\epsilon}_{ij}^{el} &= C_{ijkl} \dot{\sigma}_{kl}^{el} \\ \dot{\epsilon}_{ijr}^{el} &= C_{ijkl} \dot{\rho}_{kl} \end{aligned} \quad (4)$$

with  $C_{ijkl}$  being the tensor of the elastic constants.

For the creep component, Norton's viscous power law is assumed to hold

$$\dot{\epsilon}_{ijr}^{cr} = \frac{l}{n+1} \frac{\partial \phi}{\partial \sigma_{ij}} \quad (5)$$

where  $\phi$  is a strictly convex creep surface.

For two different states of stress  $\sigma_{ij}$  and  $\sigma_{ij}^*$ , the corresponding creep strain rates satisfy the Drucker's postulate of stability ([7]):

$$(\sigma_{ij} - \sigma_{ij}^*)(\dot{\epsilon}_{ijr}^{cr} - \dot{\epsilon}_{ijr}^{cr*}) \geq 0. \quad (6)$$

The above postulate has been used by Frederick and Armstrong [8] to prove the existence of a steady cyclic stress state, which can be stated as follows (Gokhfeld and Cherniavsky [9]):

"At cyclic loading of a structure made of Drucker's material the stresses and the strain rates gradually stabilize to remain unaltered on passing to the next cycle."

The above theorem states that after many applications of the load cycles  $\sigma_{ij}(t+T) \rightarrow \sigma_{ij}(t)$  and since the elastic stress is itself cyclic:  $\rho_{ij}(t+T) \rightarrow \rho_{ij}(t)$ .

It can also be proved ([9]) that the stress distribution in the steady cycle is unique and does not depend on any initial state of the structure.

### 3 Fourier Decomposition of Residual Stresses

In order to calculate, therefore, this cyclic stress distribution, it is sufficient to compute the residual stress distribution of the cyclic stress state  $\rho_{ij}(t)$ . Since this stress also becomes periodic, it may be decomposed in its Fourier series over the period of loading, as this can be done for any periodic function (see, for example, Tolstov [10]):

$$\rho_{ij}(t) = \frac{a_0}{2} + \sum_{k=1}^{\infty} \left( a_k \cos \frac{2k\pi t}{T} + b_k \sin \frac{2k\pi t}{T} \right) \quad (7)$$

where the coefficients  $a_0$ ,  $a_k$  and  $b_k$ ,  $k=1,2,\dots$  are called the Fourier coefficients of the Fourier series. The problem therefore is now transformed to evaluate these coefficients. In a classical Fourier analysis problem these coefficients can be evaluated if the function is known. In our case, though, it is the function  $\rho_{ij}(t)$  we seek to find. Nevertheless, let us differentiate Eq. (7) with respect to time. Then we get

$$\dot{\rho}_{ij}(t) = \frac{2\pi}{T} \sum_{k=1}^{\infty} \left\{ (-ka_k) \sin \frac{2k\pi t}{T} + kb_k \cos \frac{2k\pi t}{T} \right\}. \quad (8)$$

From the above equation we observe that the Fourier coefficients  $a_k$  and  $b_k$ ,  $k=1,2,\dots$  appear also in the expansion of the time derivative of the residual stresses. Making use of the orthogonality properties of the trigonometric functions we can get expressions that may be used to evaluate these coefficients in terms of the time derivative  $\dot{\rho}_{ij}(t)$ :

$$a_k = -\frac{1}{k\pi} \int_0^T \dot{\rho}_{ij}(t) \sin \frac{2k\pi t}{T} dt \quad (9)$$

$$b_k = \frac{1}{k\pi} \int_0^T \dot{\rho}_{ij}(t) \cos \frac{2k\pi t}{T} dt. \quad (10)$$

On the other hand, if we integrate  $\dot{\rho}_{ij}(t)$  over the period  $T$ , we get

$$\begin{aligned} \int_0^T \dot{\rho}_{ij}(t) dt &= \rho_{ij}(T) - \rho_{ij}(0) \\ &= \left( \frac{a_0(T)}{2} + \sum_{k=1}^{\infty} a_k(T) \right) - \left( \frac{a_0(0)}{2} + \sum_{k=1}^{\infty} a_k(0) \right) \end{aligned} \quad (11)$$

where use of the expression (7) was made at the beginning and at the end of the cycle period. Equation (11) may be used to evaluate the coefficient  $a_0$ .

If one satisfies equilibrium and compatibility at some discrete time points inside the cycle, the time derivatives of the residual stresses themselves may be expressed in terms of the Fourier coefficients we seek to find. Thus Eqs. (9), (10), and (11) may be used in an iterative manner which, in case of convergence, may lead to the values of the Fourier coefficients within a specified tolerance.

### 4 Formulation Using Finite Elements

The way to evaluate the time derivatives of the residual stresses may be done, for any structure, using the finite element method. To this end our structure is discretized into a finite number of elements which are assumed to be interconnected at a discrete number of nodal points situated on their boundaries.

In the sequel, we denote vectors and matrices by bold letters.

Let us denote, by  $\dot{\mathbf{r}}$ , the vector of the time rates of the displacements of the nodal points of the discretized structure at some time  $t$ . The strain rates  $\dot{\epsilon}$  at the Gauss integration points are given in terms of  $\dot{\mathbf{r}}$  by

$$\dot{\epsilon} = \mathbf{B}\dot{\mathbf{r}}. \quad (12)$$

Using the discretized form of Eqs. (2)–(5) one may write solving in terms of the residual stress rates, also at the Gauss points

$$\dot{\rho} = \mathbf{D}(\dot{\epsilon} - \dot{\epsilon}^{el} - \dot{\epsilon}^{cr}) \quad (13)$$

where  $\mathbf{D}$  is the elasticity matrix and consists of the inverse terms of  $C_{ijkl}$ .

Since the strain rates are compatible and the residual stress rates are self-equilibrated, from the principle of virtual work (P.V.W), we may obtain

$$\int_V \dot{\epsilon}' \dot{\rho} dV = 0 \quad (14)$$

where "prime" denotes the transpose of a vector or matrix.

After the substitution of (12) and (13), in (14), we may write

$$\dot{\mathbf{r}}' \int_V \mathbf{B}' \mathbf{D} (\mathbf{B}\dot{\mathbf{r}} - \dot{\epsilon}^{el} - \dot{\epsilon}^{cr}) dV = 0 \quad (15)$$

and since this equation must hold for any  $\dot{\mathbf{r}}$ ,

$$\left( \int_V \mathbf{B}' \mathbf{D} \mathbf{B} dV \right) \dot{\mathbf{r}} = \int_V \mathbf{B}' \dot{\epsilon}^{el} dV + \int_V \mathbf{B}' \mathbf{D} \dot{\epsilon}^{cr} dV \quad (16)$$

or

$$\mathbf{K}\dot{\mathbf{r}} = \dot{\mathbf{R}} + \int_V \mathbf{B}' \mathbf{D} \dot{\epsilon}^{cr} dV \quad (17)$$

where  $\mathbf{K}$  is the stiffness matrix of the structure and  $\dot{\mathbf{R}}$  is the nodal vector of the time rate of the given loading.

## 5 Numerical Procedure

The form of the expressions (9), (10), and (11) allow us to evaluate the Fourier coefficients of the various terms of the Fourier series (7) in an iterative manner, since an update of these terms may be provided at the end of the cycle, after integrating over its period  $T$ .

The elastic problem is solved first and the elastic stresses, due to the applied loading, at the Gauss points  $\sigma^e(t)$  are determined at discrete time points inside the cycle.

Initial values for  $\mathbf{a}_0^{(0)}$ ,  $\mathbf{a}_k^{(0)}$ ,  $\mathbf{b}_k^{(0)}$ ,  $k=1,2,\dots$ , which are also assigned at the same Gauss points, are given (normally zero). Using the discretized form of (7), the residual stresses  $\rho^{(0)}(t)$  at the Gauss points may be evaluated for any of the discrete time points inside the cycle. Creep strain rates at the Gauss points and at the same time points may then be determined with the aid of the discretized form of (5). After solving the system of Eqs. (17), using (12) and (13) the residual stress rates  $\dot{\rho}^{(0)}(t)$  may be determined at the Gauss points and at the same time points. It should be noted here that the initial decomposition of the stiffness matrix that was performed for the solution of the elastic problem, is used throughout the whole computation. An update of the Fourier coefficients may then take place using the discretized form of (9), (10), and (11), by numerically integrating over the time period  $T$ .

More specifically, if we denote by  $(\mu)$  the current iteration we can write the following expressions:

$$\begin{aligned} \mathbf{g}_k^{(\mu)} &= -\frac{1}{k\pi} \int_0^T [\dot{\rho}^{(\mu)}(t)] \sin \frac{2k\pi t}{T} dt \\ \mathbf{u}_k^{(\mu)} &= \frac{1}{k\pi} \int_0^T [\dot{\rho}^{(\mu)}(t)] \cos \frac{2k\pi t}{T} dt \\ \mathbf{s}_0^{(\mu)} &= \frac{1}{2} \mathbf{a}_0^{(\mu)} - \sum_{k=1}^{\infty} \mathbf{g}_k^{(\mu)} + \sum_{k=1}^{\infty} \mathbf{a}_k^{(\mu)} + \int_0^T [\dot{\rho}^{(\mu)}(t)] dt. \end{aligned} \quad (18)$$

In order for convergence to take place, an indirect update, based on a special acceleration procedure for nonlinear systems of equations (Isaacson and Keller [11]), is used:

$$\begin{aligned} \mathbf{a}_k^{(\mu+1)} &= \varphi \mathbf{g}_k^{(\mu)} + (1-\varphi) \mathbf{a}_k^{(\mu)} \\ \mathbf{b}_k^{(\mu+1)} &= \varphi \mathbf{u}_k^{(\mu)} + (1-\varphi) \mathbf{b}_k^{(\mu)} \\ \frac{\mathbf{a}_0^{(\mu+1)}}{2} &= \varphi \mathbf{s}_0^{(\mu)} + (1-\varphi) \frac{\mathbf{a}_0^{(\mu)}}{2} \end{aligned} \quad (19)$$

where  $\varphi$  is an acceleration and convergence parameter.

The discretized form of the sum inside the brackets, of the first term of the right-hand side of Eq. (11), is an expression for the residual stress at the end of the cycle. The Euclidean norm of this residual stress vector may serve as a means to stop the iterative procedure, i.e., the iterations may stop when

$$\frac{\|\rho^{(\mu+1)}(T)\|_2 - \|\rho^{(\mu)}(T)\|_2}{\|\rho^{(\mu+1)}(T)\|_2} \leq \epsilon_s \quad (20)$$

where  $\epsilon_s$  is a pre-specified error tolerance.

The proposed numerical scheme has a linear rate of convergence. The value of  $\varphi$  may be chosen, in a trial and error fashion, so as to produce a fast and uniform convergence of the whole procedure something which is easily detected in the very few first iterations. Then this value is kept constant throughout the whole history of the iterations. If one performs an error analysis ([11]), the "best" value of the parameter  $\varphi$  at each iteration may be found by evaluating the derivatives, with respect to the Fourier coefficients, of the various functions involved. These derivatives, however, cannot be found explicitly and an implicit evaluation of them is time-consuming because of the amount of the Fourier coefficients which may increase considerably depending on the number of terms of the Fourier series considered. Due to this fact the

evaluation of the Jacobian of the system of Eq. (18) becomes quite a cumbersome task and thus the conversion of the scheme to one which has almost a quadratic convergence does not seem to reduce the computational effort.

## 6 Examples of Application

The numerical procedure that was described above is applied to three examples, the first one being a one-dimensional, the second one a two-dimensional axisymmetric, and the third a pure two-dimensional one. All the structures were subjected to a loading whose variation with time has the form

$$P(t) = P_0 \sin^2 \left( \frac{\pi t}{T} \right). \quad (21)$$

The time variation of the load over four cycles can be seen in Fig. 1.

The equivalent to (5) uniaxial creep law is given by

$$\dot{\epsilon}^{cr} = K \sigma^n. \quad (22)$$

The structures were assumed to be made of steel with its parameters listed in Table 1.

The maximum values of the applied loading  $P_0$  were chosen so that the maximum elastic stress does not exceed the steel yield stress of 300 Mpa.

**6.1 Pin-jointed Framework.** The pin-jointed framework shown in Fig. 2 was chosen to serve as a first example of application of the proposed method ([12]). All the elements of the truss have an equal cross-sectional area of  $A = 1 \text{ cm}^2$ .

A period  $T = 100 \text{ hrs}$  was considered whereas the maximum value of the concentrated loading, that was applied at node 3 downwards, was taken as  $P_0 = 30 \text{ kN}$ .

The variation of the cyclic residual stress distribution with time over a cycle for the various truss elements can be seen in Fig. 3. Due to the structure's symmetry results for elements 2-4 and 3-2 are identical to the ones of elements 1-3 and 1-4, respectively.

**6.2 Thick Cylinder.** A thick cylinder of an internal radius of 10 cm and an external one of 20 cm is considered next. The cylinder is subjected to an internal pressure that is not varying spatially. Since both structure and loading is axisymmetric, five axisymmetric finite elements were used to discretize a vertical section of the cylinder (Fig. 4). In the same figure the boundary conditions are also shown. The material was assumed incompressible and, for this reason, Poisson's ratio was taken equal to  $\nu = 0.4999$ . Eight-noded isoparametric elements with  $2 \times 2$  Gauss

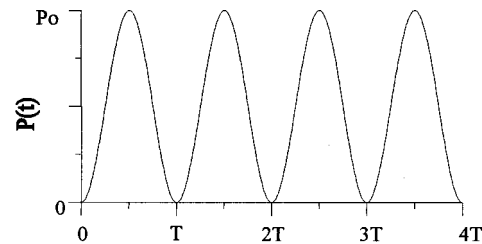


Fig. 1 Load variation with time over four periods used in the examples

Table 1 Material constants

Young's modulus:	$E = .21 \times 10^5 \text{ kN/cm}^2$
Poisson's ratio:	$\nu = 0.4999$
Constant in Norton's law:	$K = .68 \times 10^{-8} \text{ (SI units)}$
Index in Norton's power law:	$n = 3.0$



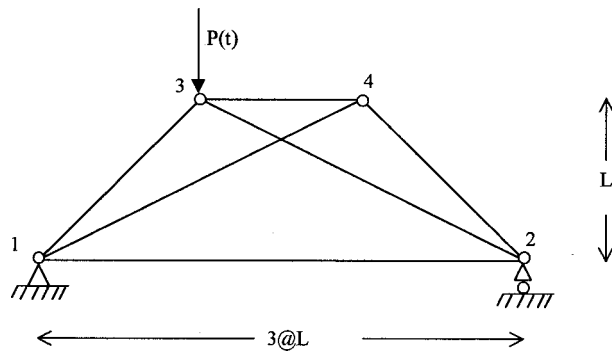


Fig. 2 Pin-jointed framework

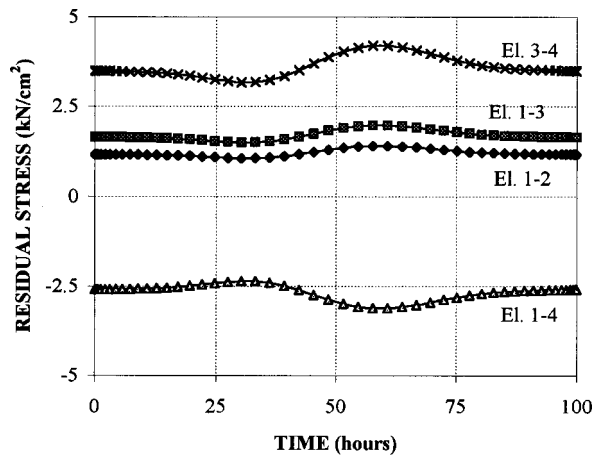


Fig. 3 Cyclic steady-state residual stress distribution in the truss elements of the six-bar structure inside a cycle

integration points were used, which showed no “locking” phenomenon due to the assumed incompressibility of the material.

To check the correctness of the computer program that was written following the numerical procedure that was described in the previous sections, a constant in-time load was considered first and the results were found in complete agreement with the analytical results (Kraus [13]).

The cyclic loading case was considered next. The cycle period was taken to be  $T=100$  hrs., whereas the maximum value of loading was taken as  $P_0=20$  kN/cm<sup>2</sup>. Results are reported at the nearest to the load Gauss integration points 1 and 2 (shown in Fig. 4). In Fig. 5 one can see the variation inside a cycle of the radial stress assuming a completely elastic behavior and the variation of the same stress in its cyclic steady-state. It is easily realized that inelastic creep has a small effect on the radial stress. This is not the case with the hoop stress at the same points (Fig. 6). In Fig.

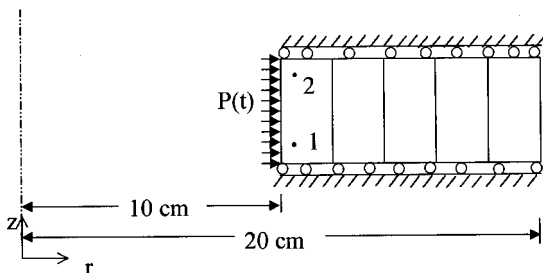


Fig. 4 Finite element discretization of thick cylinder

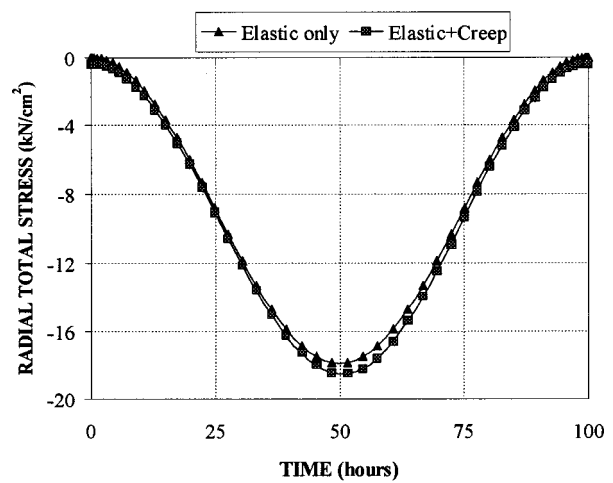
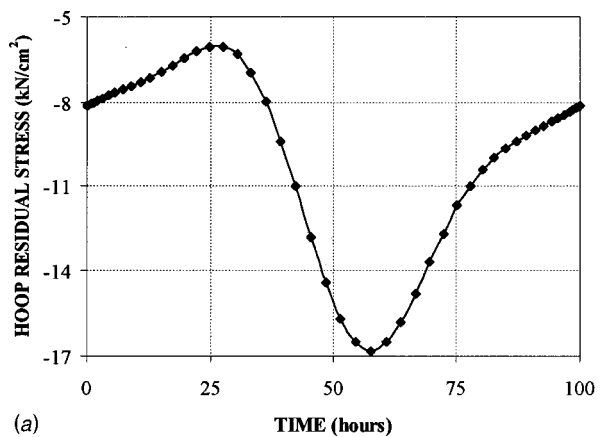
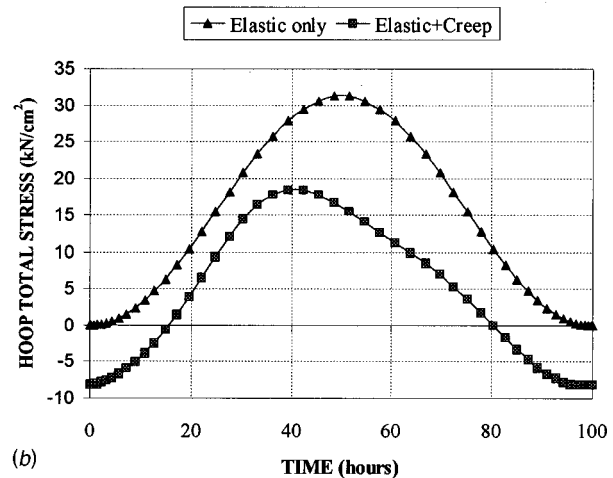


Fig. 5 Distribution of the cyclic steady-state radial stress inside a cycle for elastic and inelastic behavior at Gauss points 1 and 2



(a)



(b)

Fig. 6 Distribution of the cyclic steady-state hoop stress inside a cycle at Gauss points 1 and 2; (a) residual stress, (b) total stress for elastic and inelastic behavior

6(a) one can see the variation of the cyclic steady-state hoop residual stress inside a cycle. This residual stress, induced by creep, causes a significant effect on the elastic stress resulting to a downward shift when the cyclic steady-state condition is reached while, at the point of the occurrence of the maximum stress moves towards the left (Fig. 6(b)).

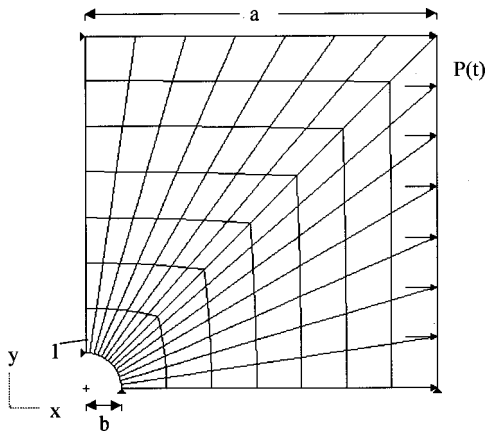


Fig. 7 Finite element discretization of a quarter of a plate

**6.3 Square Plate with a Hole.** The last example of application is a plane stress concentration example of a square plate with dimensions  $20 \times 20$  cm and having a circular hole in its middle of a diameter of 2 cm. The loading is applied in equal pairs right at the two vertical edges of the plate. Due to the symmetry of the structure and the loading one quarter of the structure is only analyzed with  $a=10$  cm and  $b=1$  cm. Ninety-eight eight-noded isoparametric elements with  $3 \times 3$  Gauss integration points were used for the finite element discretization (Fig. 7).

Because of the dimensions of the plate and the hole this problem approaches the infinite plate solution and the elastic  $xx$ -stress

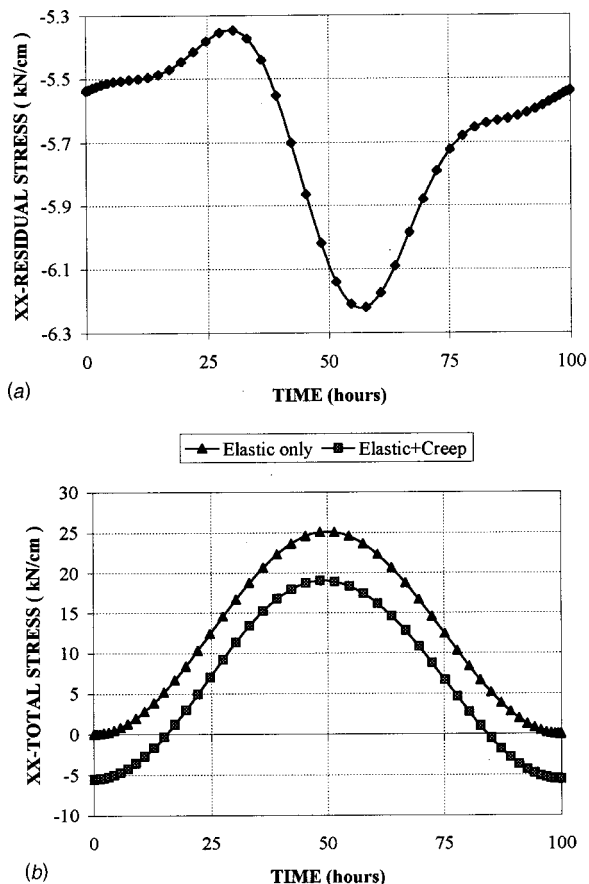


Fig. 8 Distribution of the cyclic steady-state  $xx$ -stress inside a cycle at Gauss point 1; (a) residual stress (b) total stress for elastic and inelastic behavior

at the Gauss integration point 1 shown in Fig. 7 turns out to be  $2.54 P$ . This point is the nearest integration point to the corner where the maximum longitudinal elastic stress should be approximately equal to  $3P$ .

The maximum value of the cyclic loading was taken as  $P_0 = 10$  kN/cm. The cyclic steady-state residual stress distribution inside a cycle at the same integration point can be seen in Fig. 8(a), whereas the corresponding total stress distribution can be seen in Fig. 8(b), for elastic and inelastic behavior. As it may be observed, inelasticity causes a total translation of the elastic stress distribution downwards without changing the time point where the maximum stress occurs.

The numerical procedure was then applied using the same loading but for a cycle period of  $T=1$  hr. This period turned out to be a "short cycle" period since the residual stresses in the steady-state were found to be constant inside the cycle with the value of the  $xx$ -residual stress at the Gauss integration point 1 being approximately  $\rho_{xx} = -5.77$  kN/cm.

The results of the two last examples were found in good agreement with the ones obtained by a time-stepping general purpose finite element program (ABAQUS [14]). An explicit time integration scheme was adopted and in order to get higher accuracy this time-stepping program had to go through many time increments to get near the steady-state solution especially for the stress concentration problem.

For all the examples that were presented above, based on a good choice of the parameter  $\varphi$ , the cyclic steady-state was reached in a few iterations, presenting no numerical instability. A very few number of terms of the Fourier series generally proved sufficient. A limited number of time points inside the cycle are needed, mainly to properly describe the time variation of the load. The stiffness matrix that is used for the time derivative evaluation of the residual stresses at these points needs to be formulated and decomposed only once; thus the whole procedure turns out to be quite an efficient one.

## 7 Concluding Remarks

A new simplified method that may be used to estimate the long-term nonlinear creep behavior of structures under cyclic loads is presented. The method removes the short cycle assumption of existing simplified methods and can be applied to cyclic loads of any period. It is based on decomposing the sought residual stresses in the steady-state in Fourier series. The various terms of the Fourier series are evaluated in an efficient way through an iterative process. The whole procedure not only avoids the very laborious time stepping computations and leads quickly to the final cyclic state, but also provides a good insight on the effect that inelasticity has on the structure.

## References

- [1] Leckie, F. A., and Ponter, A. R. S., 1970, "Deformation Bounds for Bodies Which Creep in the Plastic Range," *ASME J. Appl. Mech.* **37**, pp. 426–430.
- [2] Leckie, F. A., and Ponter, A. R. S., 1972, "Theoretical and Experimental Investigation of the Relationship Between Plastic and Creep Deformation of Structures," *Archives of Mechanics* **24**, pp. 419–437.
- [3] Ponter, A. R. S., 1976, "The Analysis of Cyclically Loaded Creeping Structures for Short Cycle Times," *Int. J. Solids Struct.* **12**, pp. 809–825.
- [4] Ponter, A. R. S., and Brown, P. R., 1978, "The Finite Element Solution of Rapid Cycling Creep Problems," *Int. J. Numer. Methods Eng.* **12**, pp. 1001–1024.
- [5] Spiliopoulos, K. V., 1984, "Estimation of Accumulated Creep Deformation for Structures Subjected to Cyclic Change of Loading in the Plastic Range," Ph.D. thesis, Imperial College, University of London.
- [6] Spiliopoulos, K. V., 2000, "Simplified Methods for the Steady State Inelastic Analysis of Cyclically Loaded Structures," *Inelastic Analysis of Structures Under Variable Loads: Theory & Engineering Applications*, D. Weichert and G. Maier, eds., Kluwer Academic Publishers, Dordrecht, pp. 213–232.
- [7] Drucker, D. C., 1959, "A Definition of Stable Inelastic Material," *ASME J. Appl. Mech.* **26**, pp. 101–106.
- [8] Frederick, C. O., and Armstrong, P. J., 1966, "Convergent Internal Stresses and Steady Cyclic States of Stress," *J. Strain Anal.* **1**, pp. 154–169.

- [9] Gokhfeld, D. A., and Cherniavsky, O. F., 1980, *Limit Analysis of Structures at Thermal Cycling*, Sijthoff & Noordhoff, Alpen aan dan Rijn, The Netherlands.
- [10] Tolstov, G. P., 1962, *Fourier Series*, Dover, New York.
- [11] Isaacson, E., and Keller, H. B., 1966, *Analysis of Numerical Methods*, John Wiley and Sons, New York.
- [12] Spiliopoulos, K. V., 2000, "Numerical Implementation of Simplified Methods of Analysis for Structures That Creep Under Large Period Cyclic Loads, *CD-Rom Proc. ECCOMAS 2000*, CIMNE Publication, Barcelona.
- [13] Kraus, H., 1980, *Creep Analysis*, John Wiley and Sons, New York.
- [14] ABAQUS, 1998, *Finite Element Code*, Hibbit, Karlsson and Sorensen, Warrington, UK.

# A Boundary Element Method Without Internal Cells for Two-Dimensional and Three-Dimensional Elastoplastic Problems

**X.-W. Gao**

Faculty Research Associate,  
Department of Mechanical  
and Aerospace Engineering,  
Arizona State University,  
Tempe, AZ 85287-6106  
e-mail: gao@zonatech.com

*In this paper, a new and simple boundary element method without internal cells is presented for the analysis of elastoplastic problems, based on an effective transformation technique from domain integrals to boundary integrals. The strong singularities appearing in internal stress integral equations are removed by transforming the domain integrals to the boundary. Other weakly singular domain integrals are transformed to the boundary by approximating the initial stresses with radial basis functions combined with polynomials in global coordinates. Three numerical examples are presented to demonstrate the validity and effectiveness of the proposed method. [DOI: 10.1115/1.1433478]*

## 1 Introduction

The conventional boundary integral equations dealing with inelastic problems include domain integrals associated with initial stresses (strains) (Swedlow and Cruse [1], Mukherjee [2], Telles and Brebbia [3], and Banerjee and Raveendra [4]). To evaluate the domain integrals, the yield region (nonlinear region) requires that it be discretized into internal cells and that the initial stresses at cells' nodes be determined. Therefore, integral equations for internal stresses are introduced. Since domain integrals involved in the internal stress integral equations are strongly singular when the source point is one of the cell's nodes, particular treatment is required. One of the challenging tasks in the inelastic boundary element method is to remove the strong singularities appearing in the stress domain integrals. Towards this end, substantial effort has been expended in this area, such as the works of Ricardella [5], Mendelson and Albers [6], Telles [7], Lee and Fenner [8], Chandra and Saigal [9], Guiggiani et al. [10], Dallner and Kuhn [11], Okada and Atluri [12], Huber et al. [13], and Aliabadi and Martin [14]. A detailed review can be found in the article by Gao and Davies [15]. However, until recently the first boundary element method computer code (BEMECH) dealing with two-dimensional and three-dimensional elastoplastic problems has been released by Gao and Davies [16] based on an effective removal of the strong singularities ([15]). In this code, as in the literatures listed above, the yield region of a problem is discretized into internal cells for evaluation of the domain integrals associated with the initial stresses. Although the cell integration scheme can give accurate results, the discretization of the internal region eliminates, to a certain extent, the advantage of the boundary element method in that only the boundary of the problem needs to be discretized into elements.

During the past two decades, various techniques have been developed to overcome the deficiency of the domain integrals appearing in problems with body forces and time-dependent terms.

The most popular technique is the so-called *dual reciprocity method* (DRM) proposed by Nardini and Brebbia in 1982 [17] for solid dynamics. This method, approximating the body force effect quantities using a series of prescribed basis functions, transforms the domain integrals to the boundary by employing particular solutions that are derived from the differential operator for these basis functions. Since the publication of the first book on the DRM by Partridge et al. in 1992, [18] the method has been extensively used by means of using the *radial basis functions* (RBF) (e.g., Zhu and Zhang [19], Golberg et al. [20], Power and Mingo [21], Cheng et al. [22]). More recently, Sensale et al. [23] successfully applied the DRM to solve viscoelastic problems using the *pseudo-surface traction* and *pseudo-body force* approach.

In order to avoid the need for domain discretization in the inelastic boundary element method, a method called the *particular-integral approach* was proposed by Henry and Banerjee [24]. In this approach, the solutions are decomposed into two parts—the complementary and particular solutions (see also Kane [25]). The complementary solutions satisfy the elastic boundary element method equations, while the particular solutions are related to the initial stresses by using a Galerkin vector which is approximated with specified global interpolation functions. The equations established using this method do not include any domain integral, so no internal cells are needed. However, to date, there are no strong benchmark tests and engineering applications to demonstrate its potential.

Recently, Ochiai and Kobayashi [26] presented an improved multiple-reciprocity boundary element method to transform the domain integrals to the boundary. Since both the initial stresses and the kernel functions are operated using Laplace equations, the resulting boundary integral equations are very complicated.

In this paper, an effective transformation method, called the *radial integration method*, from domain integrals to boundary integrals is presented without using any particular solution and Galerkin vector. Based on this method, a strongly singular domain integral used to isolate the strong singularities in the internal stress integral equations is analytically transformed to the boundary. All remaining weakly singular domain integrals that involve the unknown initial stresses are transformed to the boundary by approximating the initial stresses with the RBF combined with polynomials in global coordinates as commonly used in the DRM. Finally, one numerical example is presented to verify the proposed trans-

Contributed by the Applied Mechanics Division of THE AMERICAN SOCIETY OF MECHANICAL ENGINEERS for publication in the ASME JOURNAL OF APPLIED MECHANICS. Manuscript received by the ASME Applied Mechanics Division, February 12, 2001; final revision, October 25, 2001. Editor: M. Ortiz. Discussion on the paper should be addressed to the Editor, Prof. Lewis T. Wheeler, Department of Mechanical Engineering, University of Houston, Houston, TX 77204-4792, and will be accepted until four months after final publication of the paper itself in the ASME JOURNAL OF APPLIED MECHANICS.



formation technique, while other two are provided to demonstrate the effectiveness of the elastoplastic boundary element method described in this paper.

## 2 The Radial Integration Method for Transforming Domain Integrals to the Boundary

For a two-dimension domain  $\Omega$  bounded by a boundary  $\Gamma$ , define a Cartesian coordinate system  $(x_1, x_2)$  and a polar coordinate system  $(r, \theta)$  with the origin at the source point  $p$ . The relationships between the Cartesian and polar coordinate systems are

$$\begin{cases} r_1 = x_1 - x_1^p = r \cos \theta \\ r_2 = x_2 - x_2^p = r \sin \theta \end{cases} \quad 0 \leq \theta \leq 2\pi \quad (1)$$

where  $x_i^p$  represents the Cartesian coordinates at the source point  $p$  and  $r$  is the distance between the source point and a field point. A differential domain  $d\Omega$  in the polar coordinate system can be expressed as

$$d\Omega = r dr d\theta. \quad (2)$$

Referring to Fig. 1, when the field point is located on the boundary, the following relationship can be obtained:

$$r d\theta = d\Gamma \cos \varphi = d\Gamma \frac{r_i n_i}{r} \quad (3)$$

where  $\varphi$  is the angle between the normals of the differential arc  $rd\theta$  with radius  $r$  and the differential boundary  $d\Gamma$  with outward normal  $n_i$ . The summation convention is adopted for the repeated subscript  $i$ .

Using Eq. (3), Eq. (2) can be written for boundary field points as

$$d\Omega = r dr dS_I \quad (4)$$

where

$$dS_I = \frac{1}{r} \frac{\partial r}{\partial n} d\Gamma \quad (5)$$

in which, the following equations are used:

$$\frac{\partial r}{\partial n} = r_{,i} n_i \quad (6)$$

$$r_{,i} = \frac{\partial r}{\partial x_i} = \frac{r_i}{r}. \quad (7)$$

For three-dimensional problems, through defining a spherical coordinate system, a similar equation can be obtained ([15]) as

$$d\Omega = r^2 dr dS_I \quad (8)$$

where

$$dS_I = \frac{1}{r^2} \frac{\partial r}{\partial n} d\Gamma. \quad (9)$$

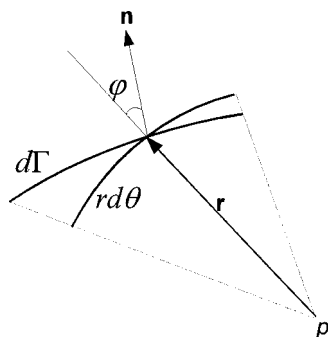


Fig. 1 Relationship between differential elements  $rd\theta$  and  $d\Gamma$

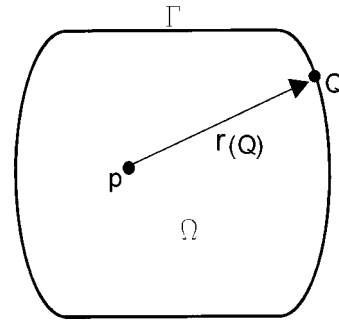


Fig. 2 Integration pattern along radial direction  $r$

Equations (6) and (7) are still valid for the three-dimensional problems with the understanding that the subscript  $i$  takes values from 1 to 3.

Equations (4) and (8) have been used to remove the strong singularities appearing in the inelastic boundary element method (e.g., [16]). In this paper, they are used to transform a domain integral to the boundary. Considering a general function  $f(x)$  with  $x$  representing  $(x_1, x_2, x_3)$ , its domain integral can be performed using Eqs. (4) and (8) as follows:

$$\int_{\Omega} f(x) d\Omega = \int_s \left\{ \int_0^{r(Q)} f r^{\beta-1} dr \right\} dS_I(Q) = \int_s F(Q) dS_I(Q) \quad (10)$$

where

$$F(Q) = \int_0^{r(Q)} f r^{\beta-1} dr. \quad (11)$$

In the above equations,  $\beta=2$  for two-dimensions and  $\beta=3$  for three-dimensions, and the symbol  $Q$  implies that the corresponding variables take values on the boundary  $\Gamma$  (see Fig. 2).

Substituting Eqs. (5) and (9) into Eq. (10) leads to

$$\int_{\Omega} f(x) d\Omega = \int_{\Gamma} \frac{1}{r^{\beta-1}} \frac{\partial r}{\partial n} F(Q) d\Gamma(Q). \quad (12)$$

Now the domain integral has been transformed into a boundary integral based on the radial integral (11). It is noted that the boundary integral in Eq. (12) is performed in the Cartesian coordinate system and the source point can be either a boundary node or an internal point.

For most cases, Eq. (11) can be analytically integrated. To do this, the coordinates  $x$  appearing in the function  $f(x)$  should be expressed in terms of  $r$  using the following equations:

$$x_i = x_i^p + r_{,i} r \quad (13)$$

$$r_{,i} r_{,i} = 1. \quad (14)$$

It is important to note that the quantity  $r_{,i}$  is constant for the radial integral (11). For some complicated functions  $f(x)$ , Gaussian quadrature formulas may be used for evaluation of the radial integral Eq. (11). Experience shows that four Gauss points are sufficient. To use the Gaussian quadrature formulas, the following variable transformation is required:

$$r = \frac{r(Q)}{2} \xi + \frac{r(Q)}{2} \quad (-1 \leq \xi \leq 1) \quad (15)$$

where  $\xi$  is the Gauss coordinate. Any domain integral can be transformed to the boundary by Eq. (12) with the use of the Gauss quadrature to evaluate the radial integral (11).

### 3 Boundary Integral Equations and Regularization for Elastoplastic Problems

The direct boundary integral equations for elastoplasticity can be expressed in the incremental form ([15]) as

$$\begin{aligned} c_{ij}(P)\dot{u}_j(P) + \int_{\Gamma} T_{ij}(P, Q)\dot{u}_j(Q)d\Gamma(Q) \\ = \int_{\Gamma} U_{ij}(P, Q)\dot{t}_j(Q)d\Gamma(Q) + \int_{\Omega} E_{ijk}(P, q)\dot{\sigma}_{jk}^p(q)d\Omega(q) \end{aligned} \quad (16)$$

where  $T_{ij}(P, Q)$  and  $U_{ij}(P, Q)$  are the Kelvin fundamental solutions for tractions and displacements at a point  $Q$  in the  $j$ th direction due to a unit load at point  $P$  and  $E_{ijk}(P, q)$  is the corresponding strain kernel

$$E_{ijk} = \frac{1}{r^{\beta-1}} \Psi_{ijk} \quad (17)$$

where

$$\begin{aligned} \Psi_{ijk} = \frac{-1}{8\pi(\beta-1)(1-\nu)G} \{ (1-2\nu)(r_{,k}\delta_{ij} + r_{,j}\delta_{ik}) \\ - r_{,i}\delta_{jk} + \beta r_{,i}r_{,j}r_{,k} \} \end{aligned} \quad (18)$$

In Eq. (16),  $c_{ij} = 1/2\delta_{ij}$  for smooth boundary points and  $c_{ij} = \delta_{ij}$  for internal points. The strongly singular terms arising from the integration of the traction kernel are determined indirectly using the rigid-body (translation) condition. The stress increments  $\dot{\sigma}_{ij}$  at an internal point  $p$  can be computed using

$$\begin{aligned} \dot{\sigma}_{ij}(p) = \int_{\Gamma} U_{ijk}(p, Q)t_k(Q)d\Gamma(Q) - \int_{\Gamma} T_{ijk}(p, Q)\dot{u}_k(Q)d\Gamma(Q) \\ + \int_{\Omega} E_{ijkl}(p, q)\dot{\sigma}_{kl}^p(q)d\Omega(q) + F_{ij}^{\sigma}(\dot{\sigma}_{kl}^p) \end{aligned} \quad (19)$$

where  $F_{ij}^{\sigma}(\dot{\sigma}_{kl}^p)$  are the free terms (e.g., Telles [7], and Banerjee and Davies [27]), and

$$E_{ijkl} = \frac{1}{r^{\beta}} \Psi_{ijkl} \quad (20)$$

in which

$$\begin{aligned} \Psi_{ijkl} = \frac{1}{4\pi(\beta-1)(1-\nu)} \{ (1-2\nu)(\delta_{ik}\delta_{lj} + \delta_{jk}\delta_{li} - \delta_{ij}\delta_{kl}) \\ + \beta\delta_{ij}r_{,k}r_{,l} + \beta\nu(\delta_{li}r_{,j}r_{,k} + \delta_{jk}r_{,l}r_{,i} + \delta_{ik}r_{,l}r_{,j} + \delta_{jl}r_{,i}r_{,k}) \\ + \beta\delta_{kl}r_{,i}r_{,j} - \beta(\beta+2)r_{,i}r_{,j}r_{,k}r_{,l} \} \end{aligned} \quad (21)$$

The integrals in Eqs. (16) and (19) should be interpreted in the Cauchy principal value sense. After use of the cell subdivision technique ([16]), the weakly singular domain integral in Eq. (16) involving the kernel  $E_{ijk}$  is bounded, while the strongly singular domain integral in Eq. (19) involving the kernel  $E_{ijkl}$  is still singular, with order  $1/r$ . Special integration techniques must therefore be adopted in order to make the integral bounded. To do this, the domain integral in Eq. (19) can be written as

$$\begin{aligned} \int_{\Omega} E_{ijkl}(p, q)\dot{\sigma}_{kl}^p(q)d\Omega(q) \\ = \int_{\Omega} E_{ijkl}(p, q)\{\dot{\sigma}_{kl}^p(q) - \dot{\sigma}_{kl}^p(p)\}d\Omega(q) \\ + \dot{\sigma}_{kl}^p(p) \left( \int_{\Omega} E_{ijkl}(p, q)d\Omega(q) \right) \end{aligned} \quad (22)$$

where  $\dot{\sigma}_{kl}^p(p)$  is the initial stress at the source point  $p$ . Now the first integral on the right-hand side of Eq. (22) is weakly singular and can be evaluated by the cell subdivision technique, while the strong singularity is shifted to the second integral of the right-hand side. Since the integration is carried out in the Cauchy principal value sense, a small sphere (or circle for two-dimensional)  $\Omega_{\varepsilon}$  with radius  $\varepsilon$  around the singular point  $p$  and bounded by a boundary  $\Gamma_{\varepsilon}$  can be cut off. Thus, in terms of Eq. (20), the radial integral (11) for the last integral in Eq. (22) becomes

$$\begin{aligned} F(Q) = \lim_{\varepsilon \rightarrow 0} \int_{\varepsilon}^{r(Q)} \frac{1}{r^{\beta}} \Psi_{ijkl} r^{\beta-1} dr \\ = \ln r(Q) \Psi_{ijkl} - \lim_{\varepsilon \rightarrow 0} \{ \ln \varepsilon \Psi_{ijkl} \} \end{aligned} \quad (23)$$

And according to Eq. (12), it follows that

$$\begin{aligned} \int_{\Omega} E_{ijkl}(p, q)d\Omega(q) = \int_{\Gamma} \frac{1}{r^{\beta-1}} \frac{\partial r}{\partial n} \ln r \Psi_{ijkl} d\Gamma \\ - \lim_{\varepsilon \rightarrow 0} \int_{\Gamma_{\varepsilon}} \frac{1}{r^{\beta-1}} \frac{\partial r}{\partial n} \ln \varepsilon \Psi_{ijkl} d\Gamma \\ = \int_{\Gamma} r \frac{\partial r}{\partial n} \ln r E_{ijkl} d\Gamma \\ + \lim_{\varepsilon \rightarrow 0} \frac{\ln \varepsilon}{\varepsilon^{\beta-1}} \int_{\Gamma_{\varepsilon}} \Psi_{ijkl} d\Gamma \end{aligned} \quad (24)$$

in which  $\partial r / \partial n = -1$  and  $r = \varepsilon$  have been used for the integral over the spherical surface (or circle)  $\Gamma_{\varepsilon}$ . It can be shown that the last integral on the right-hand side of Eq. (24) is identical to zero ([15]). Hence, Eq. (24) becomes

$$\int_{\Omega} E_{ijkl}(p, q) d\Omega(q) = \int_{\Gamma} r \frac{\partial r}{\partial n} \ln r E_{ijkl} d\Gamma. \quad (25)$$

Now the strongly singular domain integral has been transformed into a boundary integral. Since the source point  $p$  is located inside the domain, no singularity occurs and standard Gaussian quadrature formulas can be used to evaluate this integral.

### 4 Transformation of Domain Integrals to Boundary Using Approximation Functions

In the previous section, the last integral in Eq. (22) consisting of the known function  $E_{ijkl}$  has been directly transformed into a boundary integral as shown in Eq. (25). However, the first domain integral on the right-hand side of Eq. (22) and the domain integral in Eq. (16) contain the unknown initial stresses  $\dot{\sigma}_{jk}^p(q)$ . The direct transformation is infeasible. Following the idea successfully used in the DRM (Nardini and Brebbia [17], and Partridge et al. [18]), this paper approximates the initial stress increments  $\dot{\sigma}_{kl}^p(q)$  by a series of prescribed basis functions.

**4.1 Approximation of Initial Stress Increments Using Augmented Radial Basis Functions (RBFs).** It has been demonstrated that the combination of the *radial basis functions* (RBF) and *polynomials* in global coordinates can give satisfactory results (Partridge and Sensale [28], and Golberg et al. [29]). In this study, linear, quadratic, and cubic polynomials are considered. Thus, the initial stresses can be approximated by

$$\begin{aligned} \dot{\sigma}_{kl}^p(x) = \sum_{A=1}^{N_A} a_{kl}^A \phi_A(x) + c_{kl}^0 + \sum_{i=1}^{\beta} c_{kl}^i x_i + \sum_{i=1}^{\beta} \sum_{j=i}^{\beta} c_{kl}^{ij} x_i x_j \\ + \sum_{i=1}^{\beta} \sum_{j=i}^{\beta} \sum_{n=j}^{\beta} c_{kl}^{ijn} x_i x_j x_n \end{aligned} \quad (26)$$

**Table 1 Commonly used RBF  $\phi_A(x)$**

Linear	Cubic	TPS	Multiquadric
$R$	$R^3$	$R^2 \ln R$	$\sqrt{R^2 + c^2}$

$$\sum_{A=1}^{N_A} a_{kl}^A = \sum_{A=1}^{N_A} a_{kl}^A x_i^A = \sum_{A=1}^{N_A} a_{kl}^A x_i^A x_j^A = \sum_{A=1}^{N_A} a_{kl}^A x_i^A x_j^A x_n^A = 0 \quad (27)$$

where  $N_A$  is the total number of application points consisting of all boundary nodes and some selected internal points,  $a_{kl}^A$ ,  $c_{kl}^0$ ,  $c_{kl}^i$ ,  $c_{kl}^{ij}$ , and  $c_{kl}^{ijn}$  are coefficients to be determined and  $x_i^A$  denotes the Cartesian coordinates at the application point  $A$ . If quadratic polynomial is used, neglect the terms associated with  $c_{kl}^{ijn}$ ; if linear polynomial is used, neglect the terms associated with both  $c_{kl}^{ijn}$  and  $c_{kl}^i$ ; and if RBF only are used, only keep the terms associated with  $a_{kl}^A$ . Four types of commonly used RBFs  $\phi_A(x)$  (e.g., Partridge [30]) are listed in Table 1.

In Table 1,  $R$  is the distance from the application point  $A$ , i.e.,  $R = \|x - x^A\|$ . For convenience, Eq. (26) can be expressed in a simple form as

$$\sigma_{kl}^p(x) = \sum_{s=1}^{N_s} \alpha_{kl}^s \Phi_s(x) = \{\Phi(x)\}^T \{\alpha_{kl}\} \quad (28)$$

where the vectors  $\{\Phi(x)\}$  and  $\{\alpha_{kl}\}$  are arranged as follows:

$$\{\Phi(x)\}^T = \{\phi_1(x), \phi_2(x), \dots, 1, x_1, x_2, x_3, x_1^2, x_1 x_2, \dots, x_1^3, x_1^2 x_2, \dots\} \quad (29)$$

$$\{\alpha_{kl}\}^T = \{a_{kl}^1, a_{kl}^2, \dots, c_{kl}^0, c_{kl}^1, c_{kl}^2, c_{kl}^3, c_{kl}^{11}, c_{kl}^{12}, \dots, c_{kl}^{111}, c_{kl}^{112}, \dots\}. \quad (30)$$

In Eq. (28),  $N_s = N_A + N_p$  with  $N_p$  being the total number of polynomial terms. Table 2 displays the value of  $N_p$  for different types of the polynomials.

To determine the coefficients in Eq. (30), let  $x$  in Eq. (28) take values through all the application points. This provides  $N_A$  equations. Then together with Eq. (27), a set of algebraic equations with the size  $N_s$  result in (in the matrix form)

$$\{\sigma_{kl}^p\} = [\Phi] \{\alpha_{kl}\} \quad (31)$$

where  $\{\sigma_{kl}^p\}$  is a vector consisting of the initial stress component  $\sigma_{kl}^p$  at all application points. If no any two nodes share the same coordinates, the matrix  $[\Phi]$  is invertible and thereby

$$\{\alpha_{kl}\} = [\Phi]^{-1} \{\sigma_{kl}^p\}. \quad (32)$$

It is noted that, to ensure a healthy square matrix  $[\Phi]$ , the number of application points should be more than the number of the polynomial terms, i.e.,  $N_A > N_p$ .

#### 4.2 Transformation of Domain Integrals to the Boundary.

Substituting Eq. (28) into the domain integral in Eq. (16) and in terms of Eq. (12), it follows that

$$\int_{\Omega} E_{ijk}(P, q) \sigma_{jk}^p(q) d\Omega(q) = \alpha_{jk}^s \int_{\Gamma} \frac{1}{r^{\beta-1}} \frac{\partial r}{\partial n} F_{ijk}^s(Q) d\Gamma(Q) \quad (33)$$

**Table 2 The number ( $N_p$ ) of polynomial terms**

	RBF only	Linear	Quadratic	Cubic
Two-dimensional	0	3	6	10
Three-dimensional	0	4	10	20

where the summation convention is used for the repeated superscript  $s$  and  $F_{ijk}^s$  is derived from Eqs. (11) and (17):

$$F_{ijk}^s(Q) = \int_0^{r(Q)} \Psi_{ijk} \Phi_s dr = \Psi_{ijk} \int_0^{r(Q)} \Phi_s dr = \Psi_{ijk} F^s(Q). \quad (34)$$

Substituting Eq. (34) into (33) and taking account of Eq. (17), one can obtain

$$\int_{\Omega} E_{ijk}(P, q) \sigma_{jk}^p(q) d\Omega(q) = \alpha_{jk}^s \int_{\Gamma} E_{ijk} \frac{\partial r}{\partial n} F^s(Q) d\Gamma(Q). \quad (35)$$

Referring to the vector shown in Eq. (29),  $F^s(Q)$  consists of the following radial integrals:

$$F^s(Q) = \int_0^{r(Q)} \Phi_s dr = \begin{cases} \int_0^{r(Q)} \phi_A dr & \text{for } s=1 \text{ through } N_A \\ \int_0^{r(Q)} dr = r & \text{for } s=N_A+1 \end{cases} \quad (36)$$

$$= \begin{cases} \int_0^{r(Q)} x_i dr & \text{for linear polynomial} \\ \int_0^{r(Q)} x_i x_j dr & \text{for quadratic} \\ \int_0^{r(Q)} x_i x_j x_n dr & \text{for cubic.} \end{cases} \quad (37a)$$

$$\quad (37b)$$

$$\quad (37c)$$

Using Eq. (13), integrals (37a)–(37c) can easily be integrated as

$$\int_0^{r(Q)} x_i dr = x_i^p r + \frac{1}{2} r_{,i} r^2 \quad (38a)$$

$$\int_0^{r(Q)} x_i x_j dr = x_i^p x_j^p r + \frac{1}{2} b_{ij} r^2 + \frac{1}{3} r_{,i} r_{,j} r^3 \quad (38b)$$

$$\int_0^{r(Q)} x_i x_j x_n dr = x_i^p x_j^p x_n^p r + \frac{1}{2} g_{ijn} r^2 + \frac{1}{3} h_{ijn} r^3 + \frac{1}{4} r_{,i} r_{,j} r_{,n} r^4 \quad (38c)$$

where

$$b_{ij} = x_i^p r_{,j} + x_j^p r_{,i} \quad (39)$$

$$h_{ijn} = b_{ij} r_{,n} + x_n^p r_{,i} r_{,j}.$$

As for the integral shown in Eq. (36), since  $\phi_A$  are explicit functions of distance  $R$  (see Table 1), first  $R$  needs to be expressed in terms of  $r$  which is the distance from the source point  $p$  to the field point  $Q$ . Referring to Fig. 3, one can obtain

$$R = \sqrt{r^2 + s r + \bar{R}^2} \quad (40)$$

where

$$s = 2 r_{,i} \bar{R}_i$$

$$\bar{R} = \|x^p - x^A\| = \sqrt{\bar{R}_i \bar{R}_i} \quad (41)$$

$$\bar{R}_i = x_i^p - x_i^A.$$

In a similar manner, the first domain integral on the right-hand side of Eq. (22) can easily be transformed into a boundary integral by Eqs. (11), (12), and (28) as follows:

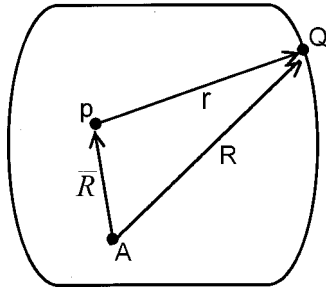


Fig. 3 Relationship between distances

$$\begin{aligned} \int_{\Omega} E_{ijkl}(p, q) \{ \dot{\sigma}_{kl}^p(q) - \dot{\sigma}_{kl}^p(p) \} d\Omega(q) \\ = \alpha_{kl}^s \int_{\Gamma} E_{ijkl} r \frac{\partial r}{\partial n} \bar{F}^s(Q) d\Gamma(Q) \end{aligned} \quad (42)$$

where

$$\begin{aligned} \bar{F}^s(Q) &= \int_0^{r(Q)} \frac{1}{r} \{ \Phi_s - \Phi_s(x^p) \} dr \\ &= \begin{cases} \int_0^{r(Q)} \frac{1}{r} \{ \phi_A - \phi_A(x^p) \} dr & \text{for } s=1 \text{ through } N_A \\ 0 & \text{for } s=N_A+1 \\ r_{,i} r & \text{for linear polynomial} \\ b_{ij} r + \frac{1}{2} r_{,i} r_{,j} r^2 & \text{for quadratic} \\ g_{ijn} r + \frac{1}{2} h_{ijn} r^2 + \frac{1}{3} r_{,i} r_{,j} r_{,n} r^3 & \text{for cubic.} \end{cases} \end{aligned} \quad (43)$$

Although the radial integrals (36) and (43) can be analytically integrated for all the functions listed in Table 1 using relationship (40), it is more convenient, as done in this study, to use Gaussian quadrature formulas to evaluate these integrals with the variable transformation (15).

After discretizing the boundary  $\Gamma$  into elements, the transformed boundary integrals (35) and (42) can be evaluated using the standard Gaussian quadrature formulas as the basic boundary integrals in Eqs. (16) and (19) are performed. The coefficients  $\alpha_{kl}^s$  in Eqs. (35) and (42) can be expressed in terms of initial stress increments by using Eq. (32). Finally a system of equations similar to that in the conventional elastoplastic boundary element method can be formed and solved with a Newton-Raphson iterative scheme (see [15]).

## 5 Numerical Examples

Three numerical examples are presented here. The first one is aimed to validate the transformation Eq. (12), while other two are used to demonstrate the effectiveness of the nonlinear boundary element method described in this paper.

**5.1 Two-Dimensional Domain Integral Over a Nonconvex Domain.** Consider the following two-dimensional domain integral over a nonconvex domain as shown in Fig. 4.

$$I(p) = \int_{\Omega} \frac{b}{r(p, q)} d\Omega \quad (44)$$

where  $r(p, q) = \sqrt{(x-x^p)^2 + (y-y^p)^2}$  and

$$b = \frac{10\bar{x}\bar{y} + 3 \sin(\bar{x}\pi/2)\cos(\bar{y}\pi/2) + 5e^{\bar{x}^2+\bar{y}^2}}{2\bar{y}^3 + \sqrt{\bar{x}^2+\bar{y}^2}\ln(2+\bar{x}+\bar{y}) + \cos(\bar{x}) + e^{\bar{y}}} \quad (45)$$

in which  $\bar{x}=x/L_1$ ,  $\bar{y}=y/L_2$ , with  $L_1=5$  and  $L_2=4$  and the origin of the coordinate system  $(x, y)$  located at the bottom-left corner of Fig. 4. It is known that the weakly singular domain integral (44) can be accurately computed using the cell-integration scheme ([16]) by discretizing the domain into internal cells. It may be quite difficult to use existing methods to transfer the domain integral (44) into a boundary integral. However, it is very easy to employ Eqs. (11) and (12) to transform this integral into an equivalent boundary integral as follows:

$$I(p) = \int_{\Gamma} \frac{1}{r(p, Q)} \frac{\partial r}{\partial n} F(Q) d\Gamma(Q) \quad (46)$$

where

$$F(Q) = \int_0^{r(Q)} b dr. \quad (47)$$

Since  $b$  is a very complicated function of  $x$  and  $y$ , it is difficult to integrate the radial integral (47) analytically. Instead, the function  $F(Q)$  is computed numerically using the variable transformation (15) and relationship (13). To compute the integral (46), the boundary of the domain is approximated using 112 linear line elements with 112 boundary nodes (see Fig. 4).

Table 3 shows the computed results at four selected boundary nodes and four internal nodes. For comparison, the results from the cell-integration scheme are also listed there.

From Table 3 we can see that the results from the *current* transformed boundary integral are in excellent agreement with the results from the traditional cell-integration technique. The small discrepancy at some points may be due to the roundoff error of computation. The computational time spent in the *current* method is 42 percent of the cell-integration technique.

## 5.2 Three-Dimensional Cube Under Uniaxial Tension.

The second example deals with a cube, with dimensions of  $10 \times 10 \times 10$ , subjected to a uniformly distributed load ( $\mathbf{p}=1$ ) on the top. The bottom is fixed in the vertical direction and free in other directions. The material satisfies the *Von Mises criterion* with the yield stress limit  $\sigma_y=0.8$  and the hardening modulus  $H'=0.1$ . The elastic properties are Young's modulus  $E=1$  and Poisson's ratio  $\nu=0.3$ . The cube was discretized into 54 linear boundary

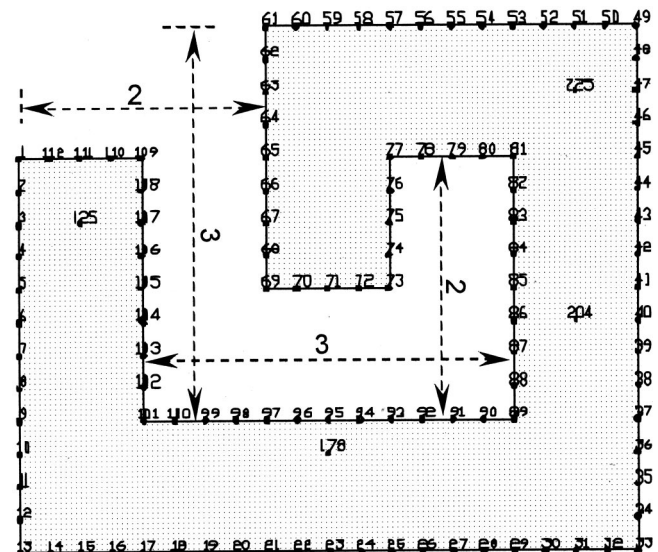


Fig. 4 Boundary elements



**Table 3 Computational results at some selected points**

Node	1	23	40	69	125	178	204	225
Current	17.5631	30.0857	37.7095	28.4012	24.6407	36.5790	46.3420	41.8402
Cell-integration	17.5631	30.0857	37.7094	28.4012	24.6407	36.5789	46.3419	41.8401

elements with 56 boundary nodes (Fig. 5). No internal points are used and all boundary nodes serve as the application points.

Table 4 shows the calculated vertical displacements at the top of the cube using the four types of the RBFs listed in Table 1 augmented with different orders of the polynomials. Usually the constant  $c$  in the multiquadric function is problem dependent ([29]). Herein the element size (3) is adopted.

From Table 4, it is observed that an RBF must be combined with polynomials to obtain a satisfactory result.

**5.3 Three-Dimensional Flexible Square Footing.** The third example pertains to the behavior of a vertically loaded square footing (with dimension  $B=1$ ), up to collapse, founded on the ground surface. This example has been analyzed by Gao and Davies [16] using the conventional cell-integration technique. Here it is used to verify the validity and demonstrate the effectiveness of the current method. The Von Mises yield criterion is employed with the yield stress limit  $\sigma_y=2C_u=2$  and perfect plasticity. The elastic material parameters are  $E=1000$  and  $\nu=0.3$ . In the boundary element method model, the far-field ground surface was simply discretized using progressively larger boundary elements and part of the near-field discretization scheme is depicted in Fig. 6 where the nine shaded elements are over the footing and subjected to a uniform vertical pressure. Due to symmetry, only a quarter of the problem is analyzed. The whole boundary element method model consists of 57 quadratic boundary elements with 200 boundary nodes. In addition, 997 nodes are placed inside the domain in the expected yield zone. Figure 7 shows the internal nodes in elevation. It is noted that these internal

nodes are consistent with the quadratic internal cells used in the cell-integration scheme ([16]). They may not be located at the optimal position.

Figure 8 is load-displacement plots for the “mean” displacement that is computed using the equation (Fox, [31]),  $u_m = \frac{1}{3}(u_{corner} + 2u_{center})$ . This equation should yield approximately the same displacement as a rigid footing. For comparison, the results from the cell-integration scheme are also plotted in Fig. 8. Although, the exact solution to this problem is not known, the normalized collapse load for a rigid circular footing under the same condition is approximately 6 ([27]), and it is probable that the collapse load for a square footing will not be much greater. The computed collapse loads are: 6.19 and 6.48 for the *Cell-integration* scheme and *Current* method, respectively. The combination of the cubic polynomials with all the RBFs listed in Table 1 gives very close results and from Fig. 8 we can see that they are in good agreement with the cell-integration results. However, as shown in Fig. 8 for the results of TPS only, none of the RBFs can give satisfactory results without combination with polynomials.

Figures 9 and 10 show the yielded nodes and deformed ground

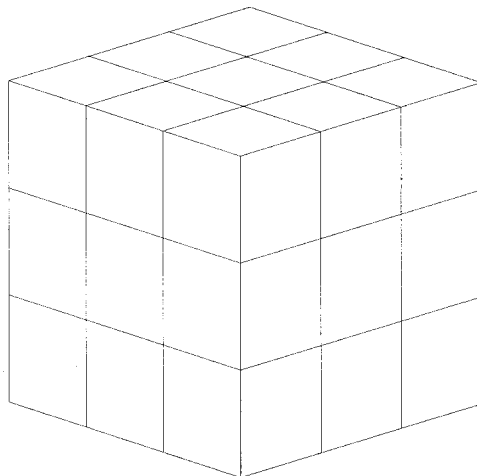


**Fig. 5 Mesh of a cube under tension**

**Table 4 Computed displacements at top of the cube (the analytical solution is 30)**

	$R$	$R^3$	$R^2 \ln R$	$\sqrt{R^2+9}$
RBF only	27.9724	29.7168	30.2716	29.4594
Linear	30.0019	29.9948	29.9975	30.0080
Quadratic	30.0007	30.0007	30.0035	29.9905
Cubic	30.0002	29.9908	30.0004	29.9903

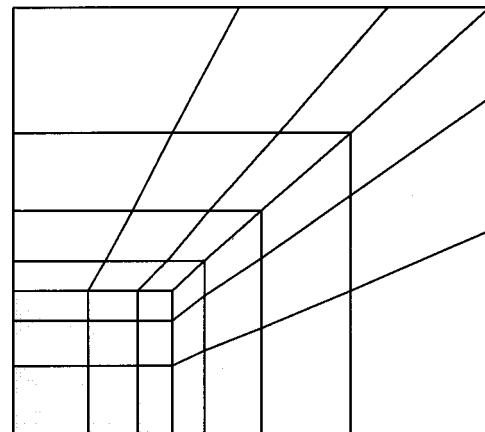


**Fig. 6 Boundary elements in plan**

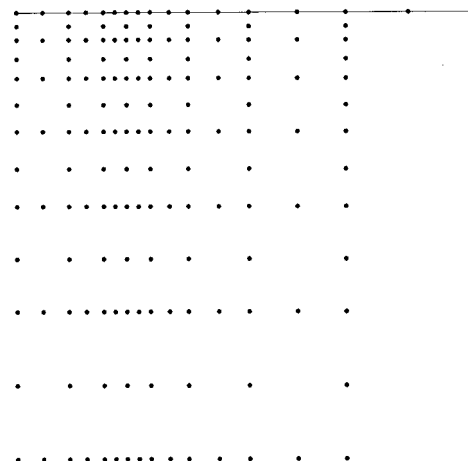


**Fig. 7 Internal nodes in elevation**

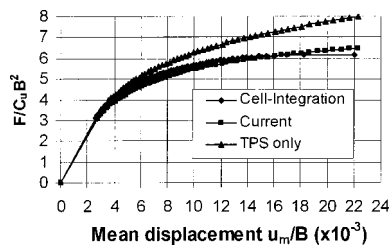


Fig. 8 Load-(mean) settlement response for a square footing

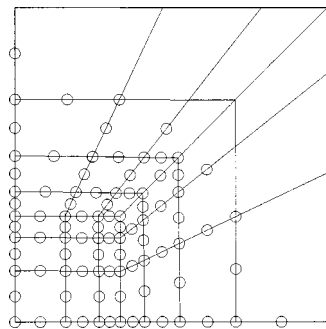


Fig. 9 Yielded nodes in plan

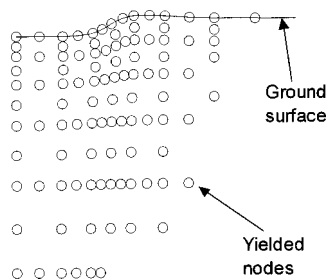


Fig. 10 Deformed ground surface and yielded nodes in elevation

surface (at a load level near to collapse) in plan and transverse sections for the *current* results. The maximum dimensions of the yielded range are  $2.68 B$  in vertical and  $2.56 B$  in horizontal directions. The computational time spent in the computation of non-linear coefficient matrices in the current method is 46 percent of the cell-integration scheme.

## 6 Conclusions

In this paper, a new elastoplastic boundary element method has been described that does not require internal cells. Experience shows that more than half of the computational time can be saved over the conventional cell-integration scheme. It has also been shown that the good accuracy stems more from the augmentation terms than the RBF employed.

## References

- [1] Swedlow, J. L., and Cruse, T. A., 1971, "Formulation of Boundary Integral Equations for Three-Dimensional Elasto-Plastic Flow," *Int. J. Solids Struct.*, **7**, pp. 1673–1683.
- [2] Mukherjee, S., 1977, "Corrected Boundary Integral Equations in Planar Thermo-Elastoplasticity," *Int. J. Solids Struct.*, **13**, pp. 331–335.
- [3] Telles, J. C. F., and Brebbia, C. A., 1979, "On the Application of the Boundary Element Method to Plasticity," *Appl. Math. Model.*, **3**, pp. 466–470.
- [4] Banerjee, P. K., and Raveendra, S. T., 1986, "Advanced Boundary Element Analysis of Two- and Three-Dimensional Problems of Elasto-Plasticity," *Int. J. Numer. Methods Eng.*, **23**, pp. 985–1002.
- [5] Riccardella, P., 1973, "An Implementation of the Boundary Integral Technique for Planar Problems of Elasticity and Elastoplasticity," Ph.D. thesis, Carnegie-Mellon University, Pittsburgh, PA.
- [6] Mendelson, A., and Albers, L. V., 1975, "An Application of the Boundary Integral Equation Method to Elastoplastic Problems," *Proc. ASME Conf. On Boundary Integral Equation Methods*, T. A. Cruse and F. J. Rizzo, eds., AMD-Vol. 11, ASME, New York.
- [7] Telles, J. C. F., 1983, *The Boundary Element Method Applied to Inelastic Problems*, Springer-Verlag, Berlin.
- [8] Lee, K. H., and Fenner, R. T., 1986, "A Quadratic Formulation for Two-Dimensional Elastoplastic Analysis Using the Boundary Integral Equation Method," *J. Strain Anal.*, **21**, pp. 159–175.
- [9] Chandra, A., and Saigal, S., 1991, "A Boundary Element Analysis of the Axisymmetric Extrusion Process," *Int. J. Non-Linear Mech.*, **26**, pp. 1–13.
- [10] Guigiani, M., Krishnasamy, G., Rudolph, T. J., and Rizzo, F. J., 1992, "General Algorithm for the Numerical Solution of Hyper-Singular Boundary Integral Equations," *ASME J. Appl. Mech.*, **59**, pp. 604–614.
- [11] Daller, R., and Kuhn, G., 1993, "Efficient Evaluation of Volume Integrals in Boundary Element Method," *Comput. Methods Appl. Mech. Eng.*, **109**, pp. 95–109.
- [12] Okada, H. O., and Atluri, S. N., 1994, "Recent Developments in the Field-Boundary Element Method for Finite/Small Strain Elastoplasticity," *Int. J. Solids Struct.*, **31**, pp. 1737–1775.
- [13] Huber, O., Dallner, R., Partheymuller, P., and Kuhn, G., 1996, "Evaluation of the Stress Tensor in 3-D Elastoplasticity Direct Solving of Hypersingular Integrals," *Int. J. Numer. Methods Eng.*, **39**, pp. 2555–2573.
- [14] Aliabadi, M. H., and Martin, D., 2000, "Boundary Element Hyper-Singular Formulation for Elastoplastic Contact Problems," *Int. J. Numer. Methods Eng.*, **48**, pp. 995–1014.
- [15] Gao, X. W., and Davies, T. G., 2000, "An Effective Boundary Element Algorithm for 2D and 3D Elastoplastic Problems," *Int. J. Solids Struct.*, **37**, pp. 4987–5008.
- [16] Gao, X. W., and Davies, T. G., 2001, *Boundary Element Programming in Mechanics*, Cambridge University Press, Cambridge, UK.
- [17] Nardini, D., and Brebbia, C. A., 1982, "A New Approach for Free Vibration Analysis Using Boundary Elements," *Boundary Element Methods in Engineering*, C. A. Brebbia, ed., Springer, Berlin, pp. 312–326.
- [18] Partridge, P. W., Brebbia, C. A., and Wrobel, L. C., 1992, *The Dual Reciprocity Boundary Element Method*, Computational Mechanics Publications, Southampton, UK.
- [19] Zhu, S., and Zhang, Y., 1994, "Improvement on Dual Reciprocity Boundary Element Method for Equations With Convective Terms," *Commun. Numer. Meth. Eng.*, **10**, pp. 361–371.
- [20] Golberg, M. A., Chen, C. S., and Bowman, H., 1999, "Some Recent Results and Proposals for the Use of Radial Basis Functions in the BEM," *Eng. Anal. Boundary Elem.*, **23**, pp. 285–296.
- [21] Power, H., and Mingo, R., 2000, "The DRM Subdomain Decomposition Approach to Solve the Two-Dimensional Navier-Stokes System of Equations," *Eng. Anal. Boundary Elem.*, **24**, pp. 107–119.
- [22] Cheng, A. H. D., Young, D. L., and Tsai, C. C., 2000, "Solution of Poisson's Equation by Iterative DRBEM Using Compactly Supported, Positive Definite Radial Basis Function," *Eng. Anal. Boundary Elem.*, **24**, pp. 549–557.
- [23] Sensale, B., Partridge, P. W., and Creus, G. J., 2001, "General Boundary Elements Solutions for Ageing Viscoelastic Structures," *Int. J. Numer. Methods Eng.*, **50**, pp. 1455–1468.
- [24] Henry, D. P., and Banerjee, P. K., 1988, "A New Boundary Element Formulation for Two- and Three-Dimensional Elastoplasticity Using Particular Integrals," *Int. J. Numer. Methods Eng.*, **26**, pp. 2079–2096.
- [25] Kane, J. H., 1994, *Boundary Element Analysis in Engineering Continuum Mechanics*, Prentice-Hall, Englewood Cliffs, NJ.
- [26] Ochiai, Y., and Kobayashi, T., 1999, "Initial Stress Formulation for Elastoplastic Analysis by Improved Multiple-Reciprocity Boundary Element Method," *Eng. Anal. Boundary Elem.*, **23**, pp. 167–173.
- [27] Banerjee, P. K., and Davies, T. G., 1984, "Advanced Implementation of the Boundary Element Methods for Three-Dimensional Problems of Elastoplasticity," *Developments in Boundary Element Methods*, Elsevier, London.
- [28] Partridge, P. W., and Sensale, B., 1997, "Hybrid Approximation Functions in the Dual Reciprocity Boundary Element Method," *Commun. Numer. Meth. Eng.*, **13**, pp. 83–94.
- [29] Golberg, M. A., Chen, C. S., and Karur, S. R., 1996, "Improved Multiquadric Approximation for Partial Differential Equations," *Eng. Anal. Boundary Elem.*, **18**, pp. 9–17.
- [30] Partridge, P. W., 2000, "Towards Criteria for Selecting Approximation Functions in the Dual Reciprocity Method," *Eng. Anal. Boundary Elem.*, **24**, pp. 519–529.
- [31] Fox, E. N., 1948, "The Mean Elastic Settlement of a Uniformly Loaded Area at a Depth Below the Ground Surface," *Proc. 2nd Int. Conf. Soil Mechanics and Foundation Engng.*, Vol. 1, FNDN, p. 129.

# Effective System Properties and Special Density in Random Vibration With Parametric Excitation

**S. Krenk**

Department of Mechanical Engineering,  
Technical University of Denmark,  
DK-2800 Lyngby, Denmark

**Y. K. Lin**

Center for Applied Stochastics Research,  
Florida Atlantic University,  
Boca Raton, FL 33431

**F. Rüdinger**

Department of Mechanical Engineering,  
Technical University of Denmark,  
DK-2800 Lyngby, Denmark

*The characteristic frequency and bandwidth of the random response to parametric excitation may be influenced by the excitation processes. It is demonstrated that the effective stiffness and damping properties can be expressed as conditional mean values for given displacement and energy levels, respectively. These properties are used to describe the response in terms of its probability density function and its spectral density function. An example demonstrates the accuracy in predicting change of frequency and damping of a parametrically excited oscillator, and another example extends the method to a self-excited oscillator with domains of negative damping. [DOI: 10.1115/1.1430665]*

## 1 Introduction

Many dynamic systems are exposed to random excitation with broad-band characteristics. Examples include structures exposed to turbulent flow from, e.g., wind, ships in random seas, and earthquake excitation of structures. For linear systems simple and fairly complete procedures exist for the evaluation of the statistical properties of the response in terms of the statistical properties of the excitation processes, when these can be represented in terms of normal processes. For nonlinear systems it is usually necessary to take recourse to approximate methods. In the case of strongly nonlinear systems the most powerful method consists in representing the excitation processes as ideal white noise processes, whereby the state space formulation attains the properties of a Markov process, and the probability density function of the state space vector satisfies the Fokker-Planck equation (see, e.g., Gardiner [1] or Lin and Cai [2]).

Much effort has been invested in exact and approximate solution techniques for the Fokker-Planck equation corresponding to the stationary state. The solution for an oscillator with additive excitation and energy-dependent damping was obtained by Caughey [3] and this solution can serve as an approximate solution to systems with a general but small damping term, by replacing the damping with an equivalent energy dependent damping (Caughey [4]). Alternatively, the dimension of the problem is reduced by stochastic averaging, whereby the Fokker-Planck equation describes the probability density of the energy (e.g., Roberts [5,6]). Exact solutions for systems with parametric excitation, in which the excitation is multiplied with the response, are in general more difficult to obtain. A particular problem is that when the physical broad band excitation process is replaced by an ideal white noise process, the system equation must be modified by including the so-called Wong-Zakai terms, accounting for the effect of small but finite correlation in the physical process (Wong and Zakai [7]). The Wong-Zakai correction terms may change the effective system properties such as damping and stiffness as discussed by Zhu and Lin [8]. In the present paper the effective

stiffness and damping properties are expressed explicitly in the form of conditional expectations for given displacement and energy, respectively. An early exact solution to a specific equation was obtained by Dimentberg [9]. Exact stationary solutions for a class of systems with both additive and multiplicative excitation were obtained by Lin and Cai [10]. This class is termed the class of generalized stationary potential. It was shown by Cai and Lin [11] and Cai et al. [12] that approximate solutions can be obtained by replacing a stochastic system by an equivalent system belonging to the class of generalized stationary potential, for which a solution exists. The method is known as dissipation energy balancing. The class of generalized stationary potential is discussed in detail by Lin and Cai [2]. It has been shown by Cai and Lin [13] that the method of dissipation energy balancing is equivalent to the quasi-conservative averaging method (Stratonovich [14]) if the Wong-Zakai correction is accounted for.

The joint probability density function of the state space vector does not contain all the statistical information of the response process. The second-order statistics of the response for given time lag, is contained in the correlation function, often represented by the spectral density obtained by Fourier transformation of the correlation function. The problem of obtaining the power spectral density for the stationary response has been given less attention than that of obtaining the stationary probability density of the response. Cai and Lin [15] have proposed a method based on an extension of the cumulant-neglect closure scheme, normally applied to obtain approximations to the higher order moments. By considering the response at two different times an approximation to the covariance function is obtained. Comparison with simulated data show good agreement. However, the method involves a substantial amount of computation and relies on the convergence of the cumulant neglect approximation. In the present paper the approximate method proposed by Krenk and Roberts [16] for obtaining the spectral density is extended to nonlinear systems with parametric excitation. The autocovariance function at a given energy level is obtained by splitting the response following after a chosen time into a fully correlated part corresponding to free decay and an uncorrelated part due to the white noise excitation occurring after the selected time. The spectral density function is then obtained by application of the Fourier transform and summation of the contributions at all energy levels. This procedure, previously applied to systems with additive excitation (Krenk and Roberts [16] and Krenk [17]), is here extended to systems with parametric excitation. The effective damping of the system controls the freely decaying response used to generate the spectral

Contributed by the Applied Mechanics Division of THE AMERICAN SOCIETY OF MECHANICAL ENGINEERS for publication in the ASME JOURNAL OF APPLIED MECHANICS. Manuscript received by the Applied Mechanics Division, Jan. 22, 2001; final revision, Aug. 13, 2001. Associate Editor: N. C. Perkins. Discussion on the paper should be addressed to the Editor, Prof. Lewis T. Wheeler, Department of Mechanical Engineering, University of Houston, Houston, TX 77204-4792, and will be accepted until four months after final publication in the paper itself in the ASME JOURNAL OF APPLIED MECHANICS.

density, and the numerical example demonstrates that the damping corresponds to that of the ideal white noise form of the equations.

## 2 Probability Density and Effective System Properties

A general equation of motion of a nonlinear oscillator exposed to random excitation by stationary correlated white noise  $W_1(t), W_2(t), \dots$  may be written in the form

$$\ddot{X} + f(X, \dot{X}) = b_j(X, \dot{X}) W_j(t) \quad (1)$$

where summation over the repeated subscript  $j$  is implied. Any of the functions  $b_j(X, \dot{X})$  that actually depends on  $X$  or  $\dot{X}$  represent a parametric excitation term, while constants correspond to an additive excitation.

**2.1 Stochastic Differential Equations.** White noise processes can only be correlated at each particular instant in time, and thus the correlation function is of the form

$$R_{ij}(\tau) = E[W_i(t)W_j(t+\tau)] = 2\pi S_{ij}\delta(\tau) \quad (2)$$

where the constants  $S_{ij}$  constitute the spectral density matrix. Since the processes are uncorrelated at different times, the spectral density matrix  $S_{ij}$  is real and symmetric. The load processes can be combined into a single normalized white noise process  $W(t)$  with amplitude  $\sigma(X, \dot{X})$  such that

$$\sigma(X, \dot{X})W(t) = b_j(X, \dot{X})W_j(t) \quad (3)$$

where the amplitude function is determined via the variance as

$$\sigma(X, \dot{X})^2 = 2\pi S_{ij}b_i(X, \dot{X})b_j(X, \dot{X}). \quad (4)$$

In the absence of parametric excitation the amplitude function  $\sigma$  is a constant.

In order to identify the effective potential and damping and obtain the probability density for systems with parametric excitation the state variable representation  $(X_1, X_2) = (X, \dot{X})$  is introduced. In terms of these state variables the equation of motion (1) takes the form

$$\frac{d}{dt} \begin{bmatrix} X_1 \\ X_2 \end{bmatrix} = \begin{bmatrix} X_2 \\ -f(X_1, X_2) \end{bmatrix} + \begin{bmatrix} 0 \\ \sigma(X_1, X_2) \end{bmatrix} W(t). \quad (5)$$

In this equation the excitation process  $W(t)$  is interpreted as smooth, but rapidly fluctuating, an interpretation often associated with Stratonovich [14].

The joint probability density function  $p_{x,\dot{x}}(x, \dot{x})$  of the stochastic variables  $(X, \dot{X})$  is determined for an equivalent Markov process, obtained by replacing the smoothed white noise process by an ideal uncorrelated white noise process. The corresponding stochastic differential equation of Itô type is obtained by writing (5) in incremental form and introducing additional drift terms to account for the change of  $\sigma(X, \dot{X})$  during the time increment (see, e.g., Wong and Zakai [7] or Gardiner [1]). In the present case, involving only one scalar amplitude function  $\sigma$ , the correction term can be written as

$$\frac{1}{4} \frac{\partial \sigma^2}{\partial x_2} = \frac{\sigma}{2} \frac{\partial \sigma}{\partial x_2} = \pi S_{ij} b_i \frac{\partial b_j}{\partial x_2}. \quad (6)$$

The Itô-type stochastic differential equation corresponding to (5) is

$$d \begin{bmatrix} X_1 \\ X_2 \end{bmatrix} = \begin{bmatrix} X_2 \\ -f(X_1, X_2) + \frac{1}{4} \frac{\partial \sigma^2(X_1, X_2)}{\partial X_2} \end{bmatrix} dt + \begin{bmatrix} 0 \\ \sigma(X_1, X_2) \end{bmatrix} dB(t) \quad (7)$$

where  $dB(t)$  is the increment of a unit Wiener process. In the stochastic differential equation  $X$  and  $\dot{X}$  correspond to time  $t$  at the beginning of the time increment  $dt$ , and the increment  $dB$  is inde-

pendent of  $X, \dot{X}$ . In the ordinary differential Eq. (5)  $\dot{X}$  and  $W$  are correlated, and the product  $\dot{X}W$  represents the rate of energy input by the excitation process.

**2.2 The Fokker-Planck Equation.** The joint probability density  $p_{x,\dot{x}}(x, \dot{x})$  of the stochastic variables  $(X, \dot{X})$  satisfy the Fokker-Planck equation. In the case of (7) the general formula specializes to

$$\frac{\partial}{\partial x_1} (-x_2 p_{x,\dot{x}}) + \frac{\partial}{\partial x_2} \left( f p_{x,\dot{x}} - \frac{1}{4} \frac{\partial \sigma^2}{\partial x_2} p_{x,\dot{x}} + \frac{1}{2} \frac{\partial}{\partial x_2} (\sigma^2 p_{x,\dot{x}}) \right) = 0. \quad (8)$$

This equation is not easily solved for nonlinear systems of practical interest (see, e.g., the discussion by Yong and Lin [18] and Lin and Cai [10,19]). However, a particular class of solutions—the class of generalized stationary potential—can be obtained by writing the joint probability density function  $p(x, \dot{x})$  in the form of an exponential function

$$p_{x,\dot{x}}(x, \dot{x}) = C \exp(-\psi(x, \dot{x})) \quad (9)$$

supplemented by the condition that the internal force function  $f(x, \dot{x})$  can be written in the form

$$f(x_1, x_2) = g(x_1) - \frac{1}{4} \frac{\partial \sigma^2}{\partial x_2} + \frac{\sigma^2}{2} \frac{\partial \psi}{\partial x_2} \quad (10)$$

where the function  $g(x_1)$  does not depend on  $x_2$ . Substitution of these representations into the Fokker-Planck Eq. (8) leads to the equation

$$-x_2 \frac{\partial p_{x,\dot{x}}}{\partial x_1} + g(x_1) \frac{\partial p_{x,\dot{x}}}{\partial x_2} = \left( x_2 \frac{\partial \psi}{\partial x_1} - g(x_1) \frac{\partial \psi}{\partial x_2} \right) p_{x,\dot{x}} = 0. \quad (11)$$

This relation is identically satisfied, if  $\psi = \psi(\lambda)$ , where the variable  $\lambda$  represents the effective energy of the system

$$\lambda = \frac{1}{2} \dot{x}^2 + G(x) \quad (12)$$

and  $G(x)$  is the effective force potential function

$$G(x) = \int_{x_0}^x g(x_1) dx_1. \quad (13)$$

In the following it is assumed that the lower integration limit  $x_0$  can be chosen such that  $g(x_0) = 0$ , and that  $x_0$  is the only root of this equation. If functions  $g(x)$  and  $\psi(\lambda)$  exist, such that (10) is satisfied, the system belongs to the class of generalized stationary potential (Lin and Cai [10]).

It is observed that the potential  $G(x)$  is the integral of the function  $g(x)$ , defined via the representation (10). Thus  $g(x)$ , and thereby the effective potential  $G(x)$ , may contain contributions from the excitation amplitude function  $\sigma(x, \dot{x})$ .

**2.3 Effective Stiffness Probability Potential.** In most cases of practical interest the internal force function cannot be represented exactly in the form (10). In these cases, an approximate probability density can be obtained by matching the given internal force function  $f(x, \dot{x})$  to a representation of the form (10). The matching procedure must identify the function  $\psi(\lambda)$  as well as the effective potential force  $g(x)$ .

The Eq. (10) is a representation of the internal force. This force may be considered as consisting of a recoverable part, represented by  $g(x)$ , and a dissipative part representing the damping in the system. In the representation it is assumed that a function  $g(x_1)$  can be determined as

$$g(x_1) = f(x_1, x_2) + \frac{1}{4} \frac{\partial \sigma^2}{\partial x_2} - \frac{\sigma^2}{2} \frac{\partial \psi}{\partial x_2} \quad (14)$$



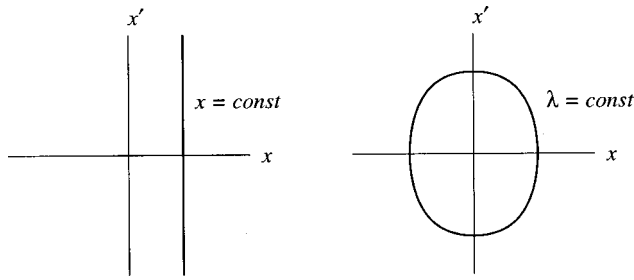


**Fig. 1 Conditional expectations: (a) potential force via  $E[*|x]$ , (b) exponent  $\psi(\lambda)$  and damping via  $E[*|\lambda]$**

in such a way that  $g(x_1)$  is independent of  $x_2$ . In general the right-hand side may depend on  $x_2$ . In these cases an approximate potential force function  $g(x)$  is determined as the conditional expectation of the representation (14) for given value of  $x_1$ ,

$$g(x_1) = E \left[ f(x_1, X_2) + \frac{1}{4} \frac{\partial \sigma^2}{\partial X_2} - \frac{\sigma^2}{2} \frac{\partial \psi}{\partial X_2} \middle| x_1 \right]. \quad (15)$$

The conditional expectation in (15) corresponds to integration with respect to  $x_2$  for constant  $x_1$  as illustrated in Fig. 1(a),

$$E[*|x_1] = \int_{-\infty}^{\infty} * p_{x|x}(x_2|x_1) dx_2. \quad (16)$$

The last term in (15) can therefore be integrated by parts to give the following conditional expectation formula for the potential force function,

$$g(x_1) = E \left[ f(x_1, X_2) - \frac{1}{4} \frac{\partial \sigma^2}{\partial X_2} \middle| x_1 \right]. \quad (17)$$

Thus, the effective potential force function  $g(x)$  is determined as the conditional expectation of the internal force, including the Wong-Zakai correction, as it appears in the stochastic differential Eq. (7). This approximation may be considered as an unbiased mean value.

When the argument of (17) does not depend on  $X_2$ , the effective force function  $g(x_1)$  can be identified directly, without knowledge of the probability density  $p_{x,\dot{x}}(x, \dot{x})$ . However, in the general case it may be necessary to let (17) determine  $g(x_1)$  in a form including parameters to be determined by an iterative procedure involving the probability density  $p_{x,\dot{x}}(x, \dot{x})$ .

The function  $\psi(\lambda)$  is determined from the requirement of equal energy dissipation of the given function  $f(x, \dot{x})$  and its representation via (10). The rate of energy dissipation is obtained from (10) via multiplication by the velocity  $\dot{x}$ , whereby

$$f(x_1, x_2) x_2 = g(x_1) x_2 - \frac{1}{4} \frac{\partial \sigma^2}{\partial x_2} x_2 + \frac{\sigma^2}{2} \frac{d\psi}{d\lambda} x_2. \quad (18)$$

While this relation cannot be satisfied identically in general, it can be satisfied in mean for any given energy level. This corresponds to taking the conditional mean of (18) for given energy level  $\lambda$ . This is illustrated in Fig. 1(b), showing a closed curve corresponding to  $\lambda = \text{const}$ . This curve represents an equivalent undamped oscillation, with the effective potential force function  $g(x)$ .

The first term on the right side in (18) is  $g(x)\dot{x} = dG/dt$  and will therefore not contribute in a stationary ergodic problem. The conditional mean of the energy dissipation representation (18) at given energy level therefore leads to the general approximation

$$\frac{d\psi}{d\lambda} = \frac{E \left[ \left( f + \frac{1}{4} \frac{\partial \sigma^2}{\partial X_2} \right) X_2 \middle| \lambda \right]}{E \left[ \frac{1}{2} \sigma^2 X_2^2 \middle| \lambda \right]}. \quad (19)$$

In the absence of the correction term the numerator becomes the conditional expectation of  $f(X, \dot{X})\dot{X}$ , traditionally used to determine the equivalent damping. In the more general case, including parametric excitation, the result (19) is equivalent to that obtained by Cai and Lin [11] in a somewhat different form, by the method of dissipation energy balancing.

**2.4 A Simple Class of Exact Solutions.** A particular class of simple solutions is obtained for systems where both damping and the excitation amplitude function  $\sigma$  only depend on the variables  $x, \dot{x}$  through the energy  $\lambda$ , defined in (12) and (13). Assume that damping is defined from a potential function  $H(\lambda)$  as  $\partial H / \partial \dot{x} = H'(\lambda) \dot{x}$ , and the stiffness is  $g(x)$ . The equation of motion then is

$$\ddot{X} + H'(\Lambda) \dot{X} + g(X) = \sigma(\Lambda) W(t) \quad (20)$$

where  $\sigma(\Lambda)W(t)$  is the conglomerated effect of additive and parametric excitation. It is seen, that when  $\sigma$  only depends on  $x, \dot{x}$  through  $\lambda$ , the conditional average (17) will identify  $g(x)$  also as the effective stiffness, and thus the potential in the energy is based on  $G(x) = \int g(x) dx$ .

The force term in the equation of motion (20) is of the form (10) permitting a simple closed form solution. Identification of the damping terms gives

$$H'(\lambda) = \frac{1}{2} \sigma(\lambda)^2 \psi'(\lambda) - \frac{1}{2} \sigma(\lambda) \sigma'(\lambda). \quad (21)$$

This identifies the function  $\psi'(\lambda)$  as

$$\psi'(\lambda) = \frac{2H'(\lambda)}{\sigma(\lambda)^2} + \frac{\sigma'(\lambda)}{\sigma(\lambda)}. \quad (22)$$

Substitution of this expression into the potential format (9) of the probability density function gives

$$p_{x,\dot{x}}(x, \dot{x}) = \frac{C}{\sigma(\lambda)} \exp \left( - \int_0^\lambda \frac{2H'(\xi)}{\sigma(\xi)^2} d\xi \right) \quad (23)$$

This class contains several of the exact solutions, extracted in Lin and Cai [2] as special cases of the approximate solutions obtained, e.g., by weighted averaging. The well-known case of additive excitation alone corresponds to  $\sigma = \text{const}$ . (Caughey [3]).

An intuitive explanation of the simplicity of this class of problems is, that for systems in which dissipation from damping is small, or the dissipation is nearly balanced by the energy input of the excitation process, the system energy changes slowly, and thus the modulation of the excitation process via  $\sigma(\lambda)$  is also slow. The solution (23) is therefore of the same form as for constant  $\sigma$ . Note, however, the factor  $\sigma(\lambda)^{-1}$  outside the exponential, which is not identified explicitly for  $\sigma = \text{const}$ .

An obvious restriction of this class of solutions is the requirement that the amplitude function of all excitation processes, determined from the instantaneous variance by (4), should be a function of  $x, \dot{x}$  only through the variable  $\lambda$ , defined by the system. This restriction prevents representation of some coupling effects, that can be captured, if stiffness and damping are determined by the conditional expectations (17) and (19).

### 3 Modified State Space Representation

Let the effective stiffness  $g(x)$  be determined from the conditional expectation (17), thereby defining the system energy  $\lambda$ . For lightly damped systems, or systems in which energy dissipation and input nearly balance, the change of the system energy is slow compared with a typical period of oscillation. For such systems fairly detailed information about the behavior within time intervals of the order of a few typical oscillation periods can be obtained by appealing to local similarity between the mean behavior under stochastic load and a similar free undamped oscillation at the same energy level. This idea goes back to Stratonovich [14]



and lies behind the so-called quasi-conservative averaging method, using local time averages corresponding to constant energy (Roberts [5,6]).

**3.1 Instantaneous Angular Frequency.** It is convenient to develop the idea of local similarity in connection with a modified phase plane in which free undamped oscillations are represented by circles (Krenk and Roberts [16]). Thus the Cartesian state variables  $z_1, z_2$  must satisfy the relation

$$2\lambda = 2G(x) + \dot{x}^2 = z_1^2 + z_2^2 \quad (24)$$

corresponding to the polar representation

$$z_1 = \sqrt{2\lambda} \cos \varphi, \quad z_2 = -\sqrt{2\lambda} \sin \varphi \quad (25)$$

in terms of radius  $\sqrt{2\lambda}$  and phase angle  $\varphi$ . There is a certain freedom in choosing the modified state variables  $z_1, z_2$ , but it appears to be most convenient to use

$$z_1 = \text{sgn}(g(x))\sqrt{2G(x)}, \quad z_2 = \dot{x}. \quad (26)$$

As already mentioned, the integration limit  $x_0$  in the definition (13) of the potential  $G(x)$  is assumed to be the only root of the equation  $g(x_0) = 0$ . This choice implies that  $G(x_0) = 0$  and continuity of the mapping of  $x$  on  $z_1$ .

The instantaneous angular frequency is defined as the derivative of the phase velocity, and use of (25) and (26) leads to

$$\omega = \frac{d\varphi}{dt} = \frac{dz_1}{dx} = \frac{|g(x)|}{\sqrt{2G(x)}}. \quad (27)$$

The instantaneous angular frequency can be considered as a function of the displacement  $x$  or the modified phase plane variable  $z_1$ . It is seen that the modification of the phase plane implied by the transformation (26) amounts to a local rescaling of the  $x$ -axis with the instantaneous angular frequency,  $dz_1 = \omega(x)dx$ .

The instantaneous angular frequency  $\omega(x)$  plays an important role in the relation between the probability density function  $p_{x,\dot{x}}(x, \dot{x})$  of the original variables  $X, \dot{X}$  and the probability density  $p_{\lambda, \varphi}(\lambda, \varphi)$  of the polar state variables  $\Lambda, \Phi$ . As demonstrated by Krenk and Roberts [16]

$$p_{\lambda, \varphi}(\lambda, \varphi) = \frac{1}{\omega(x)} p_{x, \dot{x}}(x, \dot{x}). \quad (28)$$

For the class of solutions considered here  $p_{x, \dot{x}} = p_{x, \dot{x}}(\lambda)$ , and thereby independent of the phase angle  $\varphi$ . The marginal probability density  $p_\lambda(\lambda)$  of  $\Lambda$  is obtained from (28) by integration over the phase angle  $\varphi$ ,

$$p_\lambda(\lambda) = T(\lambda) p_{x, \dot{x}}(\lambda) \quad (29)$$

where the factor

$$T(\lambda) = \int_0^{2\pi} \frac{d\varphi}{\omega(\lambda, \varphi)} \quad (30)$$

is the period of a free undamped oscillation at energy level  $\lambda$ .

**3.2 Effective Damping Properties.** The state variables  $z_1, z_2$  in the modified phase plane clearly bring out the structure of the nonlinear system, and its relation to a linear system. In the case of parametric excitation it is important to distinguish between the wide-band (Stratonovich) formulation (5), and the formulation (7) as a stochastic (Itô) differential equation. It is seen that the effect of removing the excitation term is different in the two formulations. In the following the effective damping properties of the system under random parametric excitation will be identified by assuming that the response after a selected time  $t$  can be considered as the sum of two independent contributions: one corresponding to the response in the absence of further excitation, and the other as the response generated by the excitation after the time  $t$ . This argument assumes independence of the two parts, and

therefore suggests the use of the stochastic differential form (7) in which the excitation has strictly independent increments.

The modified phase plane representation of the stochastic differential Eq. (7) is

$$d \begin{bmatrix} Z_1 \\ Z_2 \end{bmatrix} = \begin{bmatrix} 0 & \omega \\ -\omega & 0 \end{bmatrix} \begin{bmatrix} Z_1 \\ Z_2 \end{bmatrix} dt - \begin{bmatrix} 0 \\ h \end{bmatrix} dt + \begin{bmatrix} 0 \\ \sigma \end{bmatrix} dB(t) \quad (31)$$

where the force  $h$  associated with damping follows from (7) and the potential representation (10) as

$$h = \frac{1}{2} \sigma^2 \psi'(\Lambda) \dot{X} - \frac{1}{2} \partial \sigma^2 / \partial \dot{X}. \quad (32)$$

The first term describes the circular motion in the modified phase plane with nonuniform angular velocity  $\omega = \omega(X)$  corresponding to a free undamped oscillation, the second term represents damping via  $h = h(X, \dot{X})$ , and the last term is the excitation with amplitude function  $\sigma = \sigma(X, \dot{X})$ . Linear stiffness simply corresponds to  $\omega = \text{const}$ .

The change of the system energy  $\Lambda = 1/2(Z_1^2 + Z_2^2)$  follows from (31) by scalar multiplication with the vector  $(Z_1, Z_2)$ . If considering the response locally as consisting of the sum of a part due to excitation prior to some time  $t$  and another part with homogeneous initial conditions at  $t$  generated by the excitation after  $t$ , the energy of the part without excitation after time  $t$  would be governed by the differential equation

$$\frac{d\Lambda}{dt} = -\dot{X}h(X, \dot{X}) = -\dot{X} \left( \frac{1}{2} \sigma^2 \psi'(\Lambda) \dot{X} - \frac{1}{2} \partial \sigma^2 / \partial \dot{X} \right). \quad (33)$$

For linear systems and constant  $\sigma$  the split into independent additive parts is exact, while for nonlinear systems it represents only a local approximation. The rate of energy change in (33) changes over a typical period and vanishes for  $\dot{X} = 0$ . For lightly damped systems the change in energy over one period is small, and it is expedient to work with an effective rate of energy change, approximated by the expectation conditional on the energy  $\lambda$  at the initial time  $t$ . Thus the average energy change in the part of the response without current excitation is governed by the equation

$$\left\langle \frac{d\Lambda}{dt} \right\rangle_t = -E \left[ \frac{1}{2} \sigma^2 \psi'(\lambda) \dot{X}^2 - \frac{1}{2} \dot{X} \partial \sigma^2 / \partial \dot{X} | \lambda \right] \quad (34)$$

where  $\langle \rangle_t$  denotes time average. Substitution of  $\psi(\lambda)$  from (18) then gives the averaged rate of energy change in terms of the original system properties as

$$\left\langle \frac{d\Lambda}{dt} \right\rangle_t = -E \left[ f(X, \dot{X}) \dot{X} - \frac{1}{4} \dot{X} \partial \sigma^2 / \partial \dot{X} | \lambda \right]. \quad (35)$$

The damping coefficient of a freely decaying system is defined by the relation

$$\frac{d\lambda}{dt} = -\eta_\lambda \lambda. \quad (36)$$

Thus, the effective damping coefficient of the decaying part of the response at energy level  $\lambda$  follows from (35) as

$$\eta_\lambda = \frac{1}{\lambda} E \left[ \left( f - \frac{1}{4} \frac{\partial \sigma^2}{\partial X_2} \right) X_2 | \lambda \right] = \frac{1}{\lambda} \left\langle \left( f - \frac{1}{4} \frac{\partial \sigma^2}{\partial X_2} \right) X_2 | \lambda \right\rangle_t. \quad (37)$$

It is noted that in this formula the recoverable part of  $f(X, \dot{X})$  represented by  $g(X)\dot{X}$  does not contribute.

The effective damping of the system treated in Section 2.4 with damping force  $H'(\Lambda)\dot{X}$  and parametric excitation  $\sigma(\Lambda)W(t)$  takes a particularly simple form. Direct substitution into (37) gives

$$\eta_\lambda = \frac{1}{\lambda} \left( H' - \frac{1}{4} \frac{d\sigma^2}{d\lambda} \right) E[X_2^2|\lambda] = \frac{1}{\lambda} \left( H' - \frac{1}{4} \frac{d\sigma^2}{d\lambda} \right) \langle X_2^2|\lambda \rangle_t. \quad (38)$$

This formula clearly displays the effective damping as consisting of the coefficient  $H'$  from the governing differential equation, and a correction term  $-1/4 d\sigma^2/d\lambda$  arising from parametric excitation. It is seen that the effective damping is reduced by parametric excitation increasing with the energy. In the case of nonparametric excitation the latter term is absent, and the effective damping is independent of the excitation.

#### 4 Response Covariance and Spectral Density

The spectral density of the response is estimated by an approximate procedure proposed by Krenk and Roberts [16] and Krenk [17]. The idea is to estimate the covariance function of the velocity process  $\dot{X}(t)$  from the local behavior of the response in a limited time interval around  $t$  in the spirit of linear regression. If the response is assumed known at time  $t$ , the response at a later time  $t+\tau$  can be considered as consisting of two parts: a fully correlated part corresponding to freely decaying response, and a part generated by the stochastic excitation process within the interval  $t+\tau$ . For linear systems under additive white noise excitation, the two contributions are strictly uncorrelated, and thus the covariance between  $\dot{X}_t$  and  $\dot{X}_{t+\tau}$  is determined entirely by the first part. In the present case of a nonlinear system with parametric as well as additive excitation it is assumed that the local response, and thereby the covariance function, can similarly be estimated from the part of the response corresponding to freely decaying oscillations alone. A key point in this argument is that, the correlated part of the response is locally similar to a free undamped oscillation.

Following Roberts [6] the free undamped oscillation is represented by introducing a harmonic representation of the free oscillation velocity, i.e., a representation of the form

$$\sin \varphi_t = \sum_{j=1}^{\infty} s_j \sin(j\omega_\lambda \tau) \quad (39)$$

where the mean angular frequency  $\omega_\lambda = 2\pi/T(\lambda)$  at energy level  $\lambda$  has been introduced for convenience. This leads to the following approximation for the response covariance function,

$$C_x(\tau|\lambda) = \lambda \exp\left(-\frac{1}{2} \eta_\lambda \tau\right) \sum_{j=1}^{\infty} \left(\frac{s_j}{j\omega_\lambda}\right)^2 \times \left[ \cos(\Omega_j \tau) + \frac{\zeta_j}{\sqrt{1-\zeta_j^2}} \sin(\Omega_j \tau) \right], \quad (40)$$

where the damping ratio  $\zeta_j$  and the damped angular frequency  $\Omega_j$  of harmonic No.  $j$  are defined as

$$\zeta_j = \frac{\eta_\lambda}{2j\omega_\lambda}, \quad \Omega_j = j\sqrt{1-\zeta_j^2} \omega_\lambda. \quad (41)$$

The damping ratio  $\zeta_j$ , representing the *relative* bandwidth of the harmonic component No.  $j$  with angular frequency  $j\omega_\lambda$ , is inversely proportional to  $j$ , and thus the *absolute* bandwidth of all harmonics are equal at any particular energy level  $\lambda$ .

The conditional covariance function  $C_x(\tau|\lambda)$  in (40) is in the form of a weighted sum of covariance functions corresponding to a linear system. The one-sided spectral density is here introduced via the definition

$$S_x(\omega) = \frac{1}{\pi} \int_{-\infty}^{\infty} C_x(\tau) \cos(\omega \tau) d\tau. \quad (42)$$

The conditional spectral density then follows from (40) as

$$S_x(\omega|\lambda) = \frac{\eta_\lambda \lambda}{\pi} \sum_{j=1}^{\infty} \frac{2s_j^2}{(j^2 \omega_\lambda^2 - \omega^2)^2 + \eta_\lambda^2 \omega^2}. \quad (43)$$

Finally, the unconditional spectral density is found by integration over the energy levels, using the energy probability density  $p_\lambda(\lambda)$  from (29).

$$S_x(\omega) = \int_0^\infty S_x(\omega|\lambda) p_\lambda(\lambda) d\lambda \quad (44)$$

Fogli et al. [20] have proposed a method where  $S_x(\omega|\lambda)$  is given by a single term of the form (43). This approach does not seem to capture the presence of higher harmonics for systems with nonlinear stiffness.

It is seen that nonlinear effects can enter the spectrum via nonlinear damping  $\eta_\lambda$  and nonlinear stiffness  $\omega_\lambda$ , and both effects are then averaged via the energy probability density  $p_\lambda(\lambda)$ . The higher harmonics in the spectral density (43) vanish for linear stiffness, which implies  $\omega_\lambda = \text{const}$ , and  $s_1 = 1, s_3 = s_5 = \dots = 0$ .

#### 5 Examples

The following examples illustrate determination of response properties of systems with parametric excitation, and compare the theoretical results with simulations carried out by use of a fourth-order Runge-Kutta integration scheme.

**Example 1.** It follows from the definition (17) of the stiffness function  $g(x)$  that the stiffness and thereby the characteristic frequency of the system may be changed by the parametric excitation. This effect is illustrated by the following system, also investigated by Zhu and Lin [8] combining parametric and nonparametric excitation,

$$\ddot{X} + \omega_0(2\zeta + W_2(t))\dot{X} + \omega_0^2(1 + W_1(t))X = W_0(t). \quad (45)$$

Here  $W_0(t)$ ,  $W_1(t)$ , and  $W_2(t)$  are white noise processes with spectral density matrix  $S_{ij}$ . It is assumed that  $S_{01} = S_{02} = 0$ , whereby the nonparametric excitation term is uncorrelated with the two parametric excitation terms. The amplitude follows from (4),

$$\sigma(X, \dot{X})^2 = 2\pi(S_{00} + \omega_0^4 X^2 S_{11} + 2\omega_0^3 X \dot{X} S_{12} + \omega_0^2 \dot{X}^2 S_{22}) \quad (46)$$

The effective stiffness is evaluated from (17) as

$$g(x) = E\left[f(x, \dot{X}) - \frac{1}{4} \frac{\partial \sigma(x, \dot{X})^2}{\partial \dot{X}} \middle| x\right] = (\xi \omega_0)^2 x \quad (47)$$

where  $\xi^2$  is the ratio between the effective stiffness and the apparent stiffness of the system

$$\xi^2 = 1 - \pi \omega_0 S_{12}. \quad (48)$$

It is seen that correlation between the two parametric excitation processes  $W_1(t)$  and  $W_2(t)$  leads to a change of effective stiffness. The elastic potential is obtained by integration of the stiffness and the energy follows as

$$\lambda = \frac{1}{2} \dot{x}^2 + \frac{1}{2} (\xi \omega_0)^2 x^2. \quad (49)$$

The phase plane representation (25) reduces to

$$(\xi \omega_0)x = \sqrt{2\lambda} \cos \varphi, \quad \dot{x} = -\sqrt{2\lambda} \sin \varphi \quad (50)$$

by which the state vector  $(x, \dot{x})$  is represented by the energy and phase  $(\lambda, \varphi)$ . The undamped free response is harmonic, and the expectation for given energy level therefore reduces to an average over the phase angle  $\varphi$ . The Eq. (19) for the gradient of the potential  $\psi(\lambda)$  then takes the form

$$\frac{d\psi}{d\lambda} = \frac{\frac{1}{2\pi} \int_0^{2\pi} \left( f(x, \dot{x}) \dot{x} + \frac{1}{4} \frac{\partial \sigma(x, \dot{x})^2}{\partial \dot{x}} \dot{x} \right) d\varphi}{\frac{1}{2\pi} \int_0^{2\pi} \frac{1}{2} \sigma(x, \dot{x})^2 \dot{x}^2 d\varphi} \quad (51)$$

with  $x$  and  $\dot{x}$  given by (50). Evaluation of the integrals gives

$$\frac{d\psi}{d\lambda} = \frac{4\zeta\omega_0 + 2\pi\omega_0^2 S_{22}}{2\pi S_{00} + (\pi\omega_0^2 \xi^{-2} S_{11} + 3\pi\omega_0^2 S_{22})\lambda}. \quad (52)$$

This expression is rewritten by introducing a reference energy level  $\lambda_0$  and a nondimensional parameter  $\nu$ ,

$$\lambda_0 = \frac{2S_{00}}{\omega_0^2 \xi^{-2} S_{11} + 3\pi\omega_0^2 S_{22}}, \quad \nu = \frac{4\zeta - \pi\omega_0 \xi^{-2} S_{11} - \pi\omega_0 S_{22}}{\pi\omega_0 \xi^{-2} S_{11} + 3\pi\omega_0 S_{22}} \quad (53)$$

whereby it takes the simple form

$$\frac{d\psi}{d\lambda} = \frac{\nu + 1}{\lambda_0 + \lambda}. \quad (54)$$

After introducing the nondimensional energy  $\tilde{\lambda} = \lambda/\lambda_0$  integration of (54) leads to the probability density function

$$p_{\tilde{\lambda}}(\tilde{\lambda}) = \frac{\nu}{(1 + \tilde{\lambda})^{\nu+1}}, \quad \nu > 0. \quad (55)$$

The distribution of  $\tilde{\lambda}$  is seen to depend on only one variable  $\nu$ . The probability density is defined for  $\nu > 0$ . However, the mean value is given by

$$E[\tilde{\lambda}] = \mu_{\tilde{\lambda}} = \frac{1}{\nu - 1}, \quad \nu > 1 \quad (56)$$

so for  $0 < \nu \leq 1$  the distribution does not have a mean value, which implies that the variance of the displacement is infinite and the idea of a stationary process meaningless. The following investigation therefore concentrates on systems fulfilling the requirement  $\nu > 1$ .

The correlation between the two parametric excitation processes is quantified via the correlation coefficient

$$\rho = \frac{S_{12}}{\sqrt{S_{11}S_{22}}}, \quad -1 \leq \rho \leq 1. \quad (57)$$

The effective damping is evaluated by (37) as

$$\eta_{\lambda} = \frac{1}{\lambda} E \left[ f\dot{X} - \frac{1}{4} \frac{\partial \sigma^2}{\partial \dot{X}} \dot{X} | \lambda \right] = 2\zeta_e \omega_0, \quad \zeta_e = \zeta - \frac{1}{2} \pi \omega_0 S_{22}. \quad (58)$$

**Table 1 System parameters with  $S_{11} = S_{22}$**

$\zeta$	0.0500	0.1000
$\omega_0 S_{jj}$	0.0064	0.0120
$\rho$	0	1
$\zeta_e$	0.040	0.081
$\xi$	1.000	0.990
$\nu$	2.000	1.985

$\zeta_e$  is the effective damping ratio, which reduces to the parameter  $\zeta$  for  $W_2(t) \equiv 0$ . For  $W_2(t) \neq 0$  the energy input of the excitation is biased, which leads to a reduction in the effective damping.

The energy conditional spectral density reduces to

$$S_X(\omega | \lambda) = \frac{\eta_{\lambda} \lambda}{\pi} \frac{2}{((\xi\omega_0)^2 - \omega^2)^2 + \eta_{\lambda}^2 \omega^2} \quad (59)$$

where the effective eigenfrequency  $\xi\omega_0$  enters. The integration (44) for the unconditional spectral density can be carried out explicitly, whereby

$$\frac{S_X(r)\omega_0}{\sigma_x^2} = \frac{2\zeta_e/\xi}{\pi} \frac{1}{(1-r^2)^2 + (2\zeta_e/\xi)^2 r^2}, \quad r = \frac{\omega}{\xi\omega_0}. \quad (60)$$

The right-hand side in this representation integrates to one. The variance of the position is given by

$$\sigma_x^2 = \frac{E[\lambda]}{(\xi\omega_0)^2} = \frac{\lambda_0}{(\xi\omega_0)^2(\nu - 1)}. \quad (61)$$

Table 1 gives the parameters of two different systems under two different loading situations. The systems have damping ratio  $\zeta = 0.05$  and  $0.1$ , respectively, and the excitation processes  $W_1(t)$  and  $W_2(t)$  have identical intensity, but are either uncorrelated or fully correlated.

In each case the effective damping ratio  $\zeta_e$  given by (58b) is reduced by about 20 percent, independent of the correlation. The relative natural frequency  $\xi$  from (48), on the other hand, is equal to unity for uncorrelated excitation, but reduced for the correlated excitation. The shape parameter  $\nu$  from (53b) is also reduced by correlation of the excitation processes. The probability densities corresponding to the parameter combinations given in Table 1 are shown in Fig. 2. The solid curves represent the theoretical densities given by (55). Since the nondimensional form of the probability density only depends on the shape parameter  $\nu$ , and  $\nu \approx 2$  for all four cases, the four probability density functions are very similar.

The theoretical results are compared to results obtained by numerical simulation of 20,000 periods using a fourth-order Runge-Kutta integration scheme. The white noise excitation is repre-

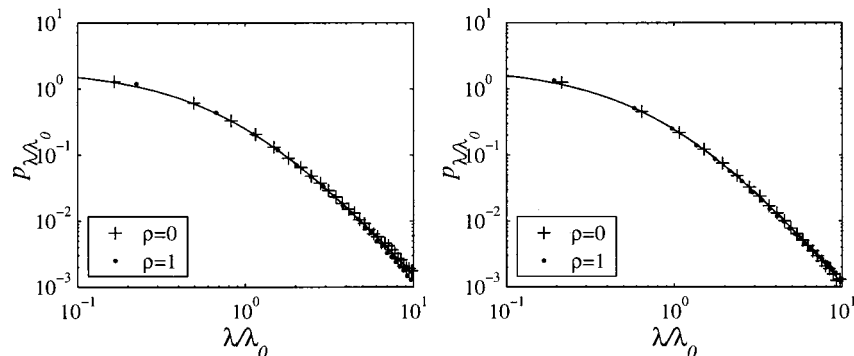


**Fig. 2 Probability density  $p_{\tilde{\lambda}}(\tilde{\lambda})$ ; (a)  $\zeta = 0.05$ ,  $\omega_0 S_{11} = \omega_0 S_{22} = 0.0064$ , (b)  $\zeta = 0.1$ ,  $\omega_0 S_{11} = \omega_0 S_{22} = 0.012$**

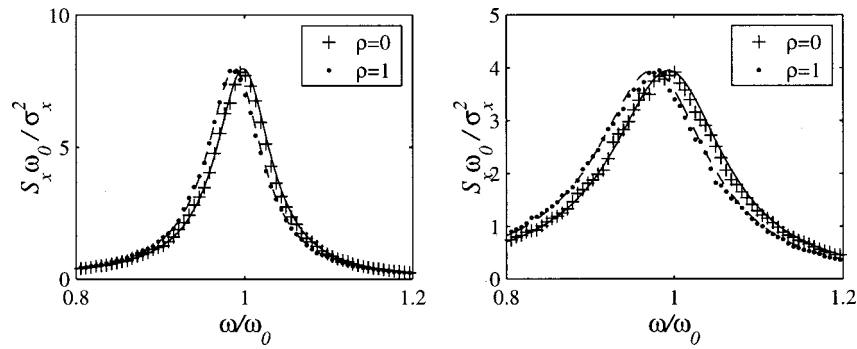


**Fig. 3 Auto-spectral density  $S_x(\omega)\omega_0/\sigma_x^2$ ; (a)  $\zeta=0.05$ ,  $\omega_0 S_{11}=\omega_0 S_{22}=0.0064$ , (b)  $\zeta=0.1$ ,  $\omega_0 S_{11}=\omega_0 S_{22}=0.012$**

sented by linear interpolation of independent Gaussian stochastic variables. At a sampling rate of  $2\pi\Delta t/\omega_0=0.02$  such a process is very broad-banded with respect to the system. The probability density of the simulated records are shown by crosses and dots in Fig. 2. The theoretical results are seen to agree very well with the results obtained by stochastic simulation.

The spectral densities for the parameter combinations given in Table 1 are shown in Fig. 3. The solid curves correspond to the theoretical expression (60). The reduction of the natural frequency for positively correlated excitation processes ( $\xi=0.990$  and  $\xi=0.981$ ) is clearly illustrated in the figure. The spectra are compared to results obtained by numerical simulation of 400,000 periods. The simulated spectra are given by the crosses and dots in Fig. 3. The theoretical results agree very well with the results obtained from stochastic simulation, thus confirming the theoretical prediction of the reduction of natural frequency.

Figure 4 shows the same simulated spectra as in Fig. 3, but here compared to the theoretical predictions that would result from neglecting the parametric correction term in the definition (37) of the effective damping coefficient, leading to  $\zeta_e=\zeta$ , irrespective of the parametric excitation. Comparison of Figs. 3 and 4 clearly illustrates the effect of the parametric correction term on the shape of the spectral density, and the accuracy of the definition of the effective damping coefficient  $\eta_\lambda$  by (37).

Finally, a few words concerning the stability of the system should be added. The additive excitation term will not influence the stability of the system. In the case where  $W_1(t)\equiv 0$  an exact stability limit can be obtained following a procedure described by, e.g., Lin and Cai [2] Section 6.3. An equation governing the logarithm of the Euclidean norm of the state-space vector can be established. This equation is integrated from 0 to  $t$ . Letting  $t$  tend to infinity, the following stability criterion is obtained:

$$\frac{\pi\omega_0 S_{22}}{\zeta} < 2 \quad \text{for } S_{11}=0. \quad (62)$$

From (58b) it is seen that this corresponds to requiring positive effective damping. The stability of this system has been discussed by Dimentberg [9] for the special case  $S_{11}=S_{22}$ .

**Example 2.** This example explores the response properties of a parametrically excited oscillator with nonlinear damping with a stable limit cycle (Lin and Cai [2]). The oscillator is described by the equation

$$\ddot{X} - \omega_0 \left[ \beta - \frac{2\alpha\omega_0^2}{\dot{X}^2 + \omega_0^2 X^2} \right] X \dot{X} + \omega_0^2 [1 + W(t)] X = 0. \quad (63)$$

The amplitude function  $\sigma(x, \dot{x})$  for the excitation follows from (4) as

$$\sigma^2 = 2\pi S_w \omega_0^4 x^2 \quad (64)$$

where  $S_w$  is the spectral density of the white noise process  $W(t)$ . The system has linear stiffness and energy function  $\lambda$  given by

$$g(x) = \omega_0^2 x, \quad \lambda = \frac{1}{2}(\dot{x}^2 + \omega_0^2 x^2). \quad (65)$$

For  $\alpha > 0$  the damping is negative at small energy levels, and changes to positive damping, when the energy exceeds the neutrally damped energy level

$$\lambda_0 = \frac{\alpha\omega_0^2}{\beta}. \quad (66)$$

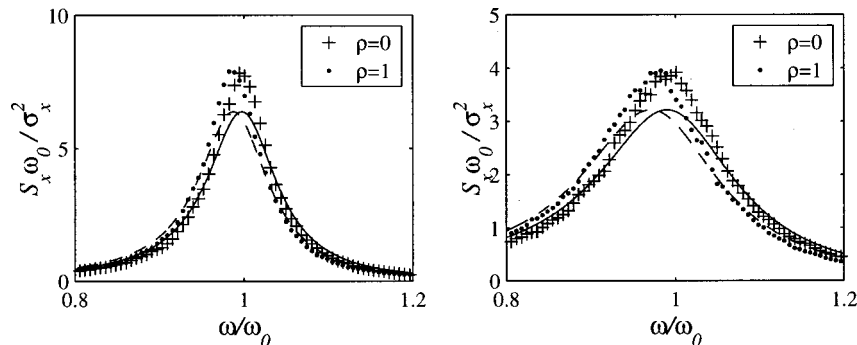


**Fig. 4 Auto-spectral density  $S_x(\omega)\omega_0/\sigma_x^2$ ; (a)  $\zeta=0.05$ ,  $\omega_0 S_{11}=\omega_0 S_{22}=0.0064$ , (b)  $\zeta=0.1$ ,  $\omega_0 S_{11}=\omega_0 S_{22}=0.012$**

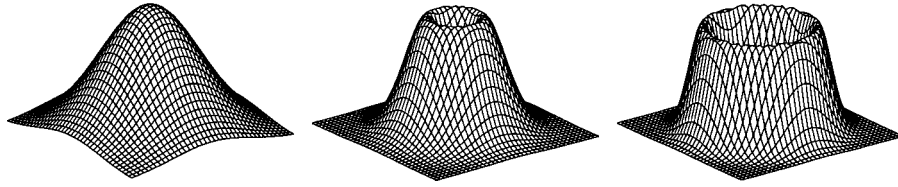


Fig. 5 Probability density  $p_{x,\dot{x}}(x,\dot{x})$  for (a)  $\tilde{\alpha}=0$ , (b)  $\tilde{\alpha}=0.5$ , (c)  $\tilde{\alpha}=5$

Systems with this particular limit circle-type behavior have been used to represent vortex-induced structural vibrations (Rüdinger and Krenk [21]).

In the present example the excitation amplitude  $\sigma$  is independent of  $\dot{x}$ , and thus it follows from (10) and (64) that

$$\frac{d\psi}{d\lambda} = \frac{1}{\pi S_w \omega_0^3} \left[ \beta - \frac{\alpha \omega_0^2}{\lambda} \right]. \quad (67)$$

By introduction of the nondimensional variables

$$\tilde{\alpha} = \frac{\alpha}{\pi S_w \omega_0}, \quad \tilde{\lambda} = \frac{\lambda}{\lambda_0} = \frac{\lambda \beta}{\alpha \omega_0^2} \quad (68)$$

Eq. (67) takes the simple form

$$\frac{d\psi}{d\tilde{\lambda}} = \tilde{\alpha} \left[ 1 - \frac{1}{\tilde{\lambda}} \right]. \quad (69)$$

After integration the joint probability density of  $(X, \dot{X})$  follows from (9) as

$$p_{x,\dot{x}}(x,\dot{x}) = C \tilde{\lambda}^{\tilde{\alpha}} \exp(-\tilde{\alpha} \tilde{\lambda}). \quad (70)$$

Finally, the probability density function of the nondimensional energy  $\tilde{\lambda}$  is determined from (29) with  $T=2\pi/\omega_0$  as

$$p_{\tilde{\lambda}}(\tilde{\lambda}) = \lambda_0 p_{\lambda}(\lambda) = \lambda_0 T p_{x,\dot{x}}(x,\dot{x}) = \frac{(\tilde{\alpha} \tilde{\lambda})^{\tilde{\alpha}}}{\Gamma(\tilde{\alpha})} \exp(-\tilde{\alpha} \tilde{\lambda}). \quad (71)$$

The factor  $\Gamma(\tilde{\alpha})$  follows from normalization of the probability density integral and implies that the parameter  $C$  in the previous formula is given by  $C = (\omega_0/2\pi\lambda_0) \tilde{\alpha}^{\tilde{\alpha}}/\Gamma(\tilde{\alpha})$ .

It is seen that the nondimensional energy  $\tilde{\lambda}$  is gamma distributed with parameter  $\tilde{\alpha}$ . Integrability of the probability density  $p_{\tilde{\lambda}}(\tilde{\lambda})$  requires that  $\tilde{\alpha} > -1$ , and for  $-1 < \tilde{\alpha} < 0$  the probability density has a singularity at  $\tilde{\lambda}=0$ . For  $\tilde{\alpha}=0$  the stochastic variables  $(X, \dot{X})$  are joint normal, and for  $\tilde{\alpha}>0$  the probability density function  $p_{x,\dot{x}}(x,\dot{x})$  develops an increasingly sharper maximum around the circle  $\dot{x}^2 + (\omega_0 x)^2 = 2\lambda_0$  as illustrated in Fig. 5. Figure 6 shows the probability density  $p_{\tilde{\lambda}}(\tilde{\lambda})$  of the nondimensional energy for  $\tilde{\alpha}=0$ ,  $\tilde{\alpha}=0.5$ , and  $\tilde{\alpha}=5.0$ , respectively. The solid curve

corresponds to the expression (71) and the points are obtained by simulation of response records by fourth-order Runge-Kutta integration. The agreement is seen to be excellent.

In the present case of linear stiffness the undamped free response at energy level  $\lambda$  is harmonic,

$$x_t = \frac{\sqrt{2\lambda}}{\omega_0} \cos(\omega_0 t), \quad \dot{x}_t = -\sqrt{2\lambda} \sin(\omega_0 t), \quad (72)$$

corresponding to  $s_j=1,0,\dots$  in (39). The effective damping at energy level  $\lambda$  is determined from (37) by averaging over the undamped period,

$$\eta_{\lambda} = \frac{\omega_0}{\lambda} \left[ \beta - \frac{\alpha \omega_0^2}{\lambda} \right] \langle X^2 \dot{X}^2 | \lambda \rangle_t = \frac{1}{2} \alpha \omega_0 (\tilde{\lambda} - 1), \quad (73)$$

where  $\tilde{\lambda}$  is the nondimensional energy introduced in (68b).

The effective damping can be either positive or negative, but in either case its absolute value determines the rate of any transient, and thus the spectral density (43) in this case takes the form

$$S_x(\omega|\lambda) = \frac{|\eta_{\lambda}| \lambda}{\pi} \frac{2}{(\omega_0^2 - \omega^2)^2 + \eta_{\lambda}^2 \omega^2}. \quad (74)$$

The unconditional auto spectral density is found by weighted integration according to (44). When the frequency ratio  $r = \omega/\omega_0$  is introduced, the resulting integral is

$$S_x(r) = \frac{4\lambda_0 \alpha}{\omega_0^3 \pi \Gamma(\tilde{\alpha})} \int_0^{\infty} (\tilde{\alpha} \tilde{\lambda})^{\tilde{\alpha}} \exp(-\tilde{\alpha} \tilde{\lambda}) \times \frac{\tilde{\lambda} |\tilde{\lambda} - 1|}{4(1-r^2)^2 + \alpha^2 r^2 (\tilde{\lambda} - 1)^2} d\tilde{\lambda}. \quad (75)$$

The integration is carried out numerically and Fig. 7 shows the theoretical results as solid curves for four parameter combinations. Results obtained by application of the fast Fourier transform to the simulated records are indicated by dots. The agreement between the theory and the simulated results is very good, although a small but systematic deviation appears in the two lower figures with  $\tilde{\alpha}=5$ . As seen from (68a) a "large" value of  $\tilde{\alpha}$  cor-

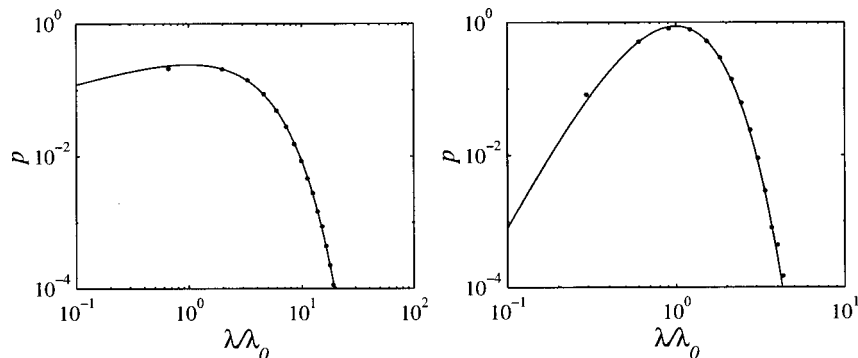
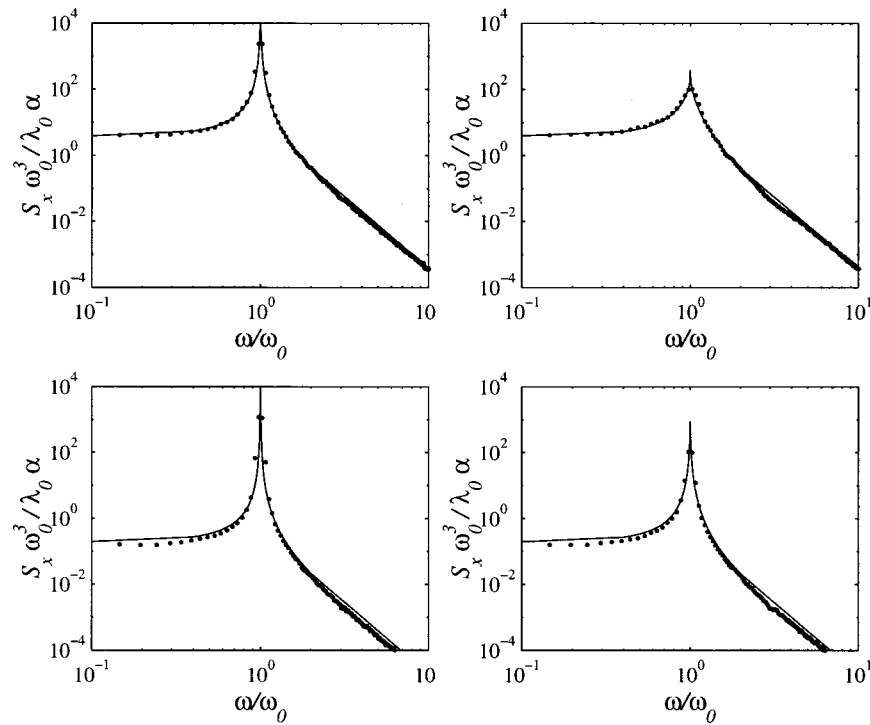


Fig. 6 Probability density of nondimensional energy; (a)  $\tilde{\alpha}=0.5$ , (b)  $\tilde{\alpha}=5$





**Fig. 7 Auto-spectral density of position; (a)  $\tilde{\alpha}=0.5$ ,  $\alpha=0.01$ , (b)  $\tilde{\alpha}=0.5$ ,  $\alpha=0.1$ , (c)  $\tilde{\alpha}=5$ ,  $\alpha=0.01$ , (d)  $\tilde{\alpha}=5$ ,  $\alpha=0.1$**

responds to a “small” excitation intensity  $S_w$ , and thus these figures corresponds to a smaller stochastic contribution to motion in the stable limit cycle.

It follows from (75) that like the probability density function  $p_{\tilde{\lambda}}(\tilde{\lambda})$  the asymptotic behavior of the normalized spectral density  $S_x(r)\omega_0^3/\lambda_0\alpha$  depends only on the parameter  $\tilde{\alpha}$ . On the other hand, it is seen from Fig. 7 that for identical value of  $\tilde{\alpha}$  the peak value of the normalized spectral density  $S_x(r)\omega_0^3/\lambda_0\alpha$  decreases with increasing  $\alpha$ . In fact it follows from (75) with  $r=1$  that the peak value is proportional to  $\alpha^{-2}$ . The decrease of the peak value and the corresponding spreading of the spectral density is a consequence of the increased intensity of the parametric excitation process. Thus, increase of the intensity of the parametric excitation leads to decreasing narrow-band characteristics of the response.

## 6 Conclusions

A random excitation of parametric type may fundamentally change the random response properties. The transformation of the original differential equations for rapidly fluctuating excitation with very small correlation length to a stochastic differential equation for ideal white noise excitation introduces a correction term—the so-called Wong-Zakai term—in the formulation. This term appears in three different contexts: in the definition of the probability density potential  $\psi(x, \dot{x})$ , in the effective stiffness function  $g(x)$ , and in the effective damping coefficient  $\eta_{\tilde{\lambda}}(\tilde{\lambda})$ . In the present paper each of these functions have been expressed in the form of a conditional expectation including an appropriate correction of Wong-Zakai type. The definition of probability density potential and the effective stiffness relies on the decomposition (10), which has been obtained previously (see, e.g., Lin and Cai [2]). The definition of the damping coefficient is based on a new argument involving a local split of the response into a fully correlated and a completely uncorrelated part. This generalizes a previous argument by Krenk and Roberts [16] for additive excitation by observing that for parametric excitation the system prop-

erties should be taken from the corresponding stochastic differential equation in order to obtain the appropriate split into correlated and uncorrelated parts.

The influence of the parametric excitation on the stiffness and damping properties has been illustrated via the spectral density of a linear system. The theory and numerically simulated records clearly identify a change in natural frequency and a change in the response bandwidth, indicating a change in effective damping. The theory has also been used to obtain the probability density and spectral density of a self-excited oscillator, which has been used to represent vortex-induced vibrations. In this case the absolute value of the damping coefficient is used to represent the time scale of energy changes. In both examples the numerical simulations show excellent agreement with the theoretical results.

## Acknowledgment

Part of this work was carried out while the first author was Charles E. Schmidt Visiting Professor at Florida Atlantic University, Boca Raton. The project has also been supported by the Danish Technical Research Council.

## References

- [1] Gardiner, C. W., 1985, *Handbook of Stochastic Methods*, Springer-Verlag, Berlin.
- [2] Lin, Y. K., and Cai, G. Q., 1995, *Probabilistic Structural Dynamics*, McGraw-Hill, New York.
- [3] Caughey, T. K., 1971, “Nonlinear Theory of Random Vibrations,” *Advances in Applied Mechanics*, Vol. 11, C. S. Yih, ed., Academic Press, New York, pp. 209–253.
- [4] Caughey, T. K., 1986, “On the Response of Non-linear Oscillators to Stochastic Excitation,” *Probab. Eng. Mech.*, **1**, pp. 2–4.
- [5] Roberts, J. B., 1978, “The Energy Envelope of a Randomly Excited Non-linear Oscillator,” *J. Sound Vib.*, **60**, pp. 177–185.
- [6] Roberts, J. B., 1983, “Energy Methods for Non-linear Systems With Non-white Excitation,” *IUTAM Symposium on Random Vibrations and Reliability*, K. Hennig, ed., Akademie-Verlag, Berlin, pp. 285–294.
- [7] Wong, E., and Zakai, M., 1965, “On the Relation Between Ordinary and Stochastic Differential Equations,” *Int. J. Eng. Sci.*, **3**, pp. 213–229.

- [8] Zhu, W., and Lin, Y. K., 1991, "Stochastic Averaging of Energy Envelope," *J. Eng. Mech.*, **117**, pp. 1890–1905.
- [9] Dimmentberg, M. F., 1982, "An Exact Solution to a Certain Non-linear Random Vibration Problem," *Int. J. Non-Linear Mech.*, **17**, pp. 231–236.
- [10] Lin, Y. K., and Cai, G. Q., 1988, "Exact Stationary-Response Solution for Second-Order Nonlinear Systems Under Parametric and External White-Noise Excitations: Part II," *ASME J. Appl. Mech.*, **55**, pp. 702–705.
- [11] Cai, G. Q., and Lin, Y. K., 1988, "A New Approximate Solution Technique for Randomly Excited Non-linear Oscillators," *Int. J. Non-Linear Mech.*, **23**, pp. 409–420.
- [12] Cai, G. Q., Lin, Y. K., and Elishakoff, I., 1992, "A New Approximate Solution Technique for Randomly Excited Non-linear Oscillators—II," *Int. J. Non-Linear Mech.*, **27**, pp. 969–979.
- [13] Cai, G. Q., and Lin, Y. K., 1997, "Comparing Quasi-Conservative Averaging and Dissipation Energy Balancing Methods in Non-linear Random Vibration," *Int. J. Non-Linear Mech.*, **32**, pp. 121–126.
- [14] Stratonovich, R. L., 1963, *Topics in the Theory of Random Noise*, Vols. 1 and 2, Gordon and Breach, New York.
- [15] Cai, G. Q., and Lin, Y. K., 1997, "Response Spectral Densities of Strongly Nonlinear Systems Under Random Excitation," *Probabilistic Engineering Mechanics*, **12**, pp. 41–47.
- [16] Krenk, S., and Roberts, J. B., 1999, "Local Similarity in Non-linear Random Vibration," *ASME J. Appl. Mech.*, **66**, pp. 225–235.
- [17] Krenk, S., 1999, "Energy and Spectral Density in Non-linear Random Response," *Stochastic Structural Dynamics*, B. F. Spencer and E. A. Johnson, eds., Balkema, Rotterdam, pp. 43–51.
- [18] Yong, Y., and Lin, Y. K., 1987, "Exact Stationary-Response Solution for Second-Order Nonlinear Systems Under Parametric and External White-Noise Excitations," *ASME J. Appl. Mech.*, **54**, pp. 414–418.
- [19] Lin, Y. K., and Cai, G. Q., 1988, "Equivalent Stochastic Systems," *ASME J. Appl. Mech.*, **55**, pp. 918–922.
- [20] Fogli, M., Bresollette, P., and Bernard, P., 1996, "The Dynamics of a Stochastic Oscillator With Impacts," *Eur. J. Mech. A/Solids*, **15**, pp. 213–241.
- [21] Rüdinger, F., and Krenk, S., 2001, "Stochastic Analysis of Self-Induced Vibrations," submitted to *Meccanica*, for publication.

# Random Response Analysis of Preisach Hysteretic Systems With Symmetric Weight Distribution

**Y. Q. Ni**

Assistant Professor,  
Department of Civil and Structural Engineering,  
The Hong Kong Polytechnic University,  
Kowloon, Hong Kong

**Z. G. Ying**

Associate Professor,  
Department of Mechanics,  
Zhejiang University,  
Hangzhou 310027, P. R. China

**J. M. Ko**

Chair Professor and Dean,  
Faculty of Construction and Land Use,  
The Hong Kong Polytechnic University,  
Kowloon, Hong Kong

*The present study is intended to develop a new method for analyzing nonlinear stochastic dynamic response of the Preisach hysteretic systems based on covariance and switching probability analysis of a nonlocal memory hysteretic constitutive model. A nonlinear algebraic covariance equation is formulated for the single-degree-of-freedom Preisach hysteretic system subjected to stationary Gaussian white noise excitation, from which the stationary mean square response of the system is obtained. The correlation coefficients of hysteretic restoring force with response in the covariance equation are evaluated by using the second moments and switching probabilities that are derived from the disjoint event probability and the mathematical machinery of an exit problem. In recognizing the symmetry of the classical Preisach weighting function, an approximation of equal "up" and "down" switching probabilities is introduced, which greatly simplifies the evaluation of the correlation coefficients. An example of the Preisach hysteretic system with Gaussian distribution weighting function is presented and the analytical results are compared with the digital simulation findings to verify the accuracy of the derived formulas. Computation results show that there exists a sharp drop in the mean square responses with the increase of a hysteresis parameter, and the mean square responses are affected only in a certain range of the Preisach weighting function. [DOI: 10.1115/1.1428333]*

## 1 Introduction

Nonlinear hysteretic dampers and isolators have been widely used in the past decade. In addition, there has been an increasing interest recently in using smart materials such as piezoceramics, shape memory alloys, and electro or magneto-rheological fluids for vibration control. Actuators, sensors, and dampers based on these materials also exhibit significant hysteresis. Nonlinear hysteresis effects allow multiple output states for a given input state, and may cause inaccuracy in open-loop control and instability in closed-loop control. From the control perspective, it is desirable to develop hysteresis models that not only accurately capture the constitutive response but also suit themselves to control design and stability analysis. The recently popularized Preisach model ([1–4]), which is really capable of describing hysteresis nonlinearity with nonlocal memory, has many well-defined properties that make it suitable for control applications ([5]). For instance, the widely used differential-type models in mechanical and structural disciplines, can only represent hysteresis with local memory ([6]), and therefore do not allow the crossing of minor loops which can arise in real materials. As a result, models of this kind may cause inaccuracy in transient dynamic response prediction and in closed-loop control; whereas the Preisach model, due to its nonlocal memory heredity, can accurately represent crossing minor loops. The Preisach model can also be extended to describe rate-dependent hysteresis ([3]) and degrading hysteresis ([7]).

The Preisach model has enjoyed extensive applications in describing various hysteresis phenomena, such as ferromagnetic materials ([3,8]), piezoceramic actuators ([9,10]), shape memory alloy materials ([11,12]), magnetostrictive actuators ([13,14]), plasticity ([15,16]), vibration dampers ([17]), and semi-rigid struc-

tural joints ([18]). Introduction of the Preisach model supplies the lack of a suitable hysteresis model in mechanical and structural areas, which is both capable of capturing nonlocal hysteresis and mathematically tractable. Experiments revealed that the restoring force of hysteretic devices related mainly to the peak displacements incurred by them in the past deformation ([19]). The Preisach model is especially effective in representing such nonlocal but selective-memory hysteresis, in which only past input extrema rather than entire input variations leave their marks upon future states of hysteresis nonlinearities. In mechanical and structural engineering fields, the dynamic loading to which hysteretic systems are subjected is usually random in nature. To date only the mean output of the Preisach model under stochastic input for viscosity or after-effect has been studied by Mayergoyz and Korman ([20–22]). They addressed this issue by means of stochastic perturbation as a discrete-time random process and a continue-time diffusion process, respectively.

In this paper, we study the stochastic dynamics of a nonlinear hysteretic system in terms of the Preisach model. A new method for predicting the stationary mean square response and correlation coefficients of the Preisach hysteretic system (not merely Preisach model) under stationary Gaussian white noise excitation is developed. The proposed method is based on covariance and switching probability analysis through the use of integral expression of the Preisach restoring force. In particular, approximate expressions of the correlation coefficients are formulated for the case of symmetric Preisach weighting function, which greatly facilitate the response analysis. An example of the Preisach hysteretic system with weighting function in the Gaussian distribution form is presented and the analytical results are compared with the digital simulation to verify the accuracy of the derived formulas. The mean square responses against the hysteresis parameters, system parameters and excitation intensity are also studied which are significant for control application.

## 2 Preisach Model

The Preisach model was first presented by physicist F. Preisach in 1935 as a physical model of ferromagnetic hysteresis ([1]). In the 1970s and 1980s, the mathematical properties of the Preisach

Contributed by the Applied Mechanics Division of THE AMERICAN SOCIETY OF MECHANICAL ENGINEERS for publication in the ASME JOURNAL OF APPLIED MECHANICS. Manuscript received and accepted by the ASME Applied Mechanics Division, April 18, 2000. Associate Editor: L. T. Wheeler. Discussion on the paper should be addressed to the Editor, Professor Lewis T. Wheeler, Department of Mechanical Engineering, University of Houston, Houston, TX 77204-4792, and will be accepted until four months after final publication of the paper itself in the ASME JOURNAL OF APPLIED MECHANICS.

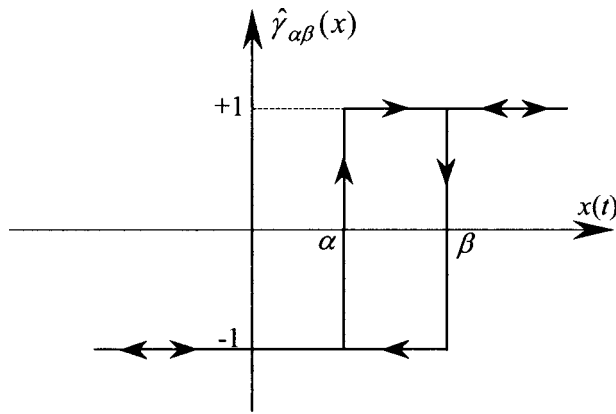


Fig. 1 Relay hysteresis operator

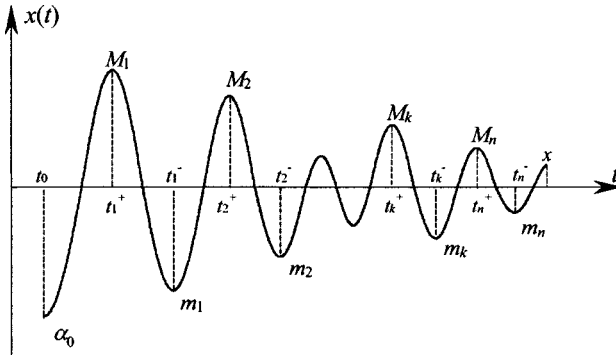


Fig. 2 Time sequence of input  $x(t)$

model were examined and explored by Russian mathematicians ([2]), who separated this model from its physical meaning and formulated it in a purely mathematical form. In this way, the basic Preisach model can be represented as a superposition of a continuous family of elementary rectangular loops, called *relay hysteresis operators* as shown in Fig. 1, in the following mathematical form ([3,4])

$$z = \int \int_{\alpha \leq \beta} \mu(\alpha, \beta) \hat{\gamma}_{\alpha\beta}(x) d\alpha d\beta, \quad (1)$$

where  $x(t)$  and  $z(t)$  denote the displacement and hysteretic restoring force variables, respectively, in the present study.  $\mu(\alpha, \beta)$  is a weighting function, called Preisach function, with support on a limiting triangle  $S$  of the  $(\alpha, \beta)$ -plane with line  $\alpha = \beta$  being the hypotenuse and point  $(\alpha_0, \beta_0) = -\alpha_0$  being the vertex. The triangle  $S$  in the half-plane  $\alpha \leq \beta$  is named Preisach plane.  $\mu(\alpha, \beta)$  is equal to zero outside  $S$ .  $\hat{\gamma}_{\alpha\beta}(x)$  is the relay hysteresis operator (Fig. 1) with thresholds  $\alpha < \beta$ . It is a two-position relay with only two values  $+1$  and  $-1$  corresponding to “up” and “down” positions, respectively, i.e.,

$$\hat{\gamma}_{\alpha\beta}(x) = \begin{cases} +1 & \text{ascending } x > \alpha \text{ or descending } x > \beta \\ -1 & \text{ascending } x < \alpha \text{ or descending } x < \beta \end{cases} \quad (2)$$

The Preisach model can be interpreted as a spectral decomposition of a complicated hysteretic constitutive law that has nonlocal memory, into the simplest relay hysteresis operators  $\hat{\gamma}_{\alpha\beta}(x)$  with local memory. Given an arbitrary input sequence  $x(t)$  as shown in Fig. 2, the Preisach plane  $S$  can be divided into two sets at any time instant  $t$ :  $S^+(t)$  consisting of points  $(\alpha, \beta)$  for which the corresponding  $\hat{\gamma}_{\alpha\beta}(x)$ -operators are in the “up” position; and  $S^-(t)$  consisting of points  $(\alpha, \beta)$  for which the corresponding

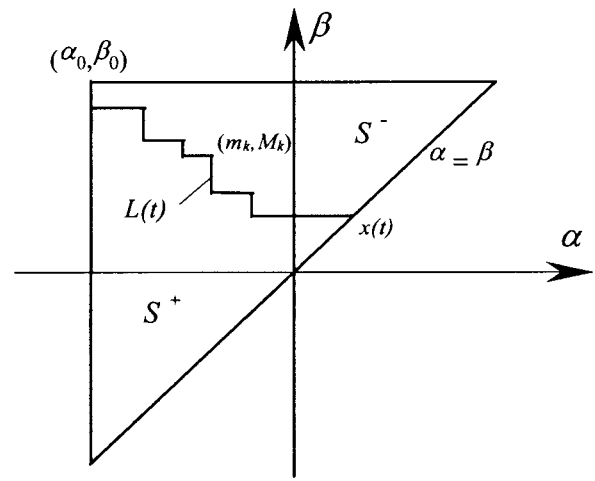


Fig. 3 Preisach plane with interface  $L(t)$

$\hat{\gamma}_{\alpha\beta}(x)$ -operators are in the “down” position. The interface  $L(t)$  between  $S^+(t)$  and  $S^-(t)$ , as shown in Fig. 3, is a staircase line whose vertices have  $\alpha$  and  $\beta$  coordinates coinciding, respectively, with local minima  $m_k$  ( $k=1, 2, \dots$ ) and maxima  $M_k$  ( $k=1, 2, \dots$ ) of the input sequence at previous instants of time. The nonlocal selective-memory is stored in this way. Thus, the output  $z(t)$  at any instant  $t$  can be equivalently expressed as

$$z(t) = \int \int_{S^+(t)} \mu(\alpha, \beta) d\alpha d\beta - \int \int_{S^-(t)} \mu(\alpha, \beta) d\alpha d\beta. \quad (3)$$

It should be noted that the interface  $L(t)$  is varying with the time evolution. Therefore, the integration domains  $S^+(t)$  and  $S^-(t)$  in Eq. (3) are the instantaneous functions of time. The basic Preisach model is characterized by two properties: the wiping-out property and the minor-loop congruence property ([3,4]). The wiping-out property refers to the constraint that the output be affected only by the current input and the alternating series of previous dominant input extrema, the effect of all other previous input values being wiped out. Following the wiping-out property, each local input minimum wipes out the vertices whose  $\alpha$ -coordinates are above this minimum, while each local maximum wipes out the vertices of  $L(t)$  whose  $\beta$ -coordinates are below this maximum. In Fig. 2,  $\mathbf{M} = \{M_i\}$  and  $\mathbf{m} = \{m_i\}$  represent the set of dominant maxima and the set of dominant minima, respectively. It follows that  $M_i > M_j$  for  $j > i$  and  $m_k < m_p$  for  $p > k$ . The contents of  $\mathbf{M}$  and  $\mathbf{m}$  vary over time. The Preisach model output  $z(t)$  is uniquely determined by the set  $\{\mathbf{M}, \mathbf{m}, x(t)\}$  for  $t \geq 0$ . The minor-loop congruence property requires that all equivalent minor hysteresis loops be congruent. Two minor loops are said to be equivalent if they are generated by an input varying monotonically between the same two extrema. Congruency between two minor loops means that one will exactly overlap the other if shifted by an appropriate vertical translation.

It is evident from Eq. (3) that the hysteresis behavior represented by the Preisach model is completely characterized by the weighting function  $\mu(\alpha, \beta)$ . The Preisach function of a specific hysteretic system is usually determined by identification from experimental data. Both the parametric and nonparametric methods have been developed for the identification of the function  $\mu(\alpha, \beta)$  ([23,24]). The weighting function  $\mu(\alpha, \beta)$  also can be determined after experimentally obtaining the set of first-order reversal (transition) curves ([3]). In the experiment, the input  $x(t)$  is first decreased to a value which is less than  $\alpha_0$ . Then the input value is gradually increased to obtain the limiting ascending branch and record its output  $z_\beta$ . At each  $\beta$  value on this branch, a subsequent

monotone decrease is imposed to obtain the first-order reversal curve with its output  $z_{\alpha\beta}$ . By defining the function

$$Z(\alpha, \beta) = z_{\beta} - z_{\alpha\beta}, \quad (4)$$

the weighting function is determined by

$$\mu(\alpha, \beta) = -\frac{1}{2} \frac{\partial^2 Z(\alpha, \beta)}{\partial \alpha \partial \beta}. \quad (5)$$

### 3 Stochastic Dynamics

**3.1 Mean Square Response.** Consider a single-degree-of-freedom nonlinear hysteretic system as shown in Fig. 4. The equation of motion of the system is written as

$$\ddot{x} + 2\zeta\dot{x} + kx + z(x, \dot{x}) = f(t) \quad (6)$$

where  $x$  denotes the nondimensional displacement;  $f(t)$  represents an external random excitation;  $\zeta$  is the viscous damping coefficient;  $k$  is the linear stiffness; and  $z$  denotes the nonlinear hysteretic restoring force governed by the Preisach model Eq. (1).

When the external excitation  $f(t)$  is a stationary Gaussian white noise with zero mean, the stationary mean response of the Preisach hysteretic system Eq. (6) is zero since the restoring force output  $z$  in Eq. (1) approaches zero for a zero-mean stationary Gaussian input process ([22]).

After rewriting the second-order governing differential Eq. (6) in a first-order differential form of state vector, the covariance matrix equation of the system response to the stationary Gaussian excitation can be derived using the state equation as

$$\begin{aligned} \dot{W}(t) &= E[\dot{Y}(t)Y^T(t)] + E[Y(t)\dot{Y}^T(t)] \\ &= AW(t) + W(t)A^T + V(t) + V^T(t) + D_F \end{aligned} \quad (7)$$

where  $E[\cdot]$  denotes the expectation operator.  $Y$ ,  $W$ ,  $A$ , and  $V$  are the state vector, the covariance matrix, the parameter matrix, and the correlation matrix of hysteretic restoring force with response, respectively. They are expressed as

$$Y = \begin{Bmatrix} x \\ \dot{x} \end{Bmatrix}, \quad (8a)$$

$$W = E[YY^T] = \begin{bmatrix} E[x^2] & E[x\dot{x}] \\ E[\dot{x}x] & E[\dot{x}^2] \end{bmatrix}, \quad (8b)$$

$$A = \begin{bmatrix} 0 & 1 \\ -k & -2\zeta \end{bmatrix}, \quad (8c)$$

$$V = \begin{bmatrix} 0 & 0 \\ -E[z\dot{x}] & -E[\dot{z}x] \end{bmatrix}. \quad (8d)$$

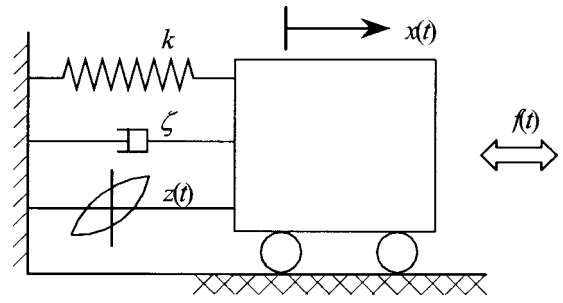


Fig. 4 Single-degree-of-freedom nonlinear hysteretic system

When the response process  $x$  becomes stationary, the covariance  $E[x\dot{x}] = E[\dot{x}x] = 0$  so that the covariance  $W$  is a diagonal matrix of the mean square response. For a stationary Gaussian white noise excitation  $f(t)$  with intensity  $D/2$ , the correlation coefficient of response to excitation is determined mainly by their initial relation and the correlation matrix  $D_F$  is given by

$$D_F = \begin{bmatrix} 0 & 0 \\ 0 & D/2 \end{bmatrix}. \quad (8e)$$

For stationary response of the system under stationary excitation, the covariance matrix  $W$  is constant and thus, Eq. (7) becomes

$$AW + WA^T + V + V^T + D_F = 0. \quad (9)$$

Equation (9) is a nonlinear algebraic equation and differs from the usual Lyapunov equation. In order to obtain the mean square response from Eq. (9), we re-express here the correlation matrix  $V$ , or  $E[z\dot{x}]$  and  $E[\dot{z}x]$ , in terms of the mean square response. Since the Preisach weighting function  $\mu(\alpha, \beta)$  in Eq. (1) is deterministic, the correlation coefficients  $E[z\dot{x}]$  and  $E[\dot{z}x]$  can be expressed in the following form ([21]):

$$E[z\dot{x}] = \int \int_{\alpha \leq \beta} \mu(\alpha, \beta) E[\hat{\gamma}_{\alpha\beta}(x)\dot{x}] d\alpha d\beta \quad (10)$$

$$E[\dot{z}x] = \int \int_{\alpha \leq \beta} \mu(\alpha, \beta) E[\hat{\gamma}_{\alpha\beta}(x)\dot{x}] d\alpha d\beta. \quad (11)$$

By keeping in mind that the elementary hysteresis operator  $\hat{\gamma}_{\alpha\beta}(x)$  is a two-position relay with either  $+1$  or  $-1$ , the correlation coefficient  $E[\hat{\gamma}_{\alpha\beta}(x)\dot{x}]$  can be expressed as

$$\begin{aligned} E[\hat{\gamma}_{\alpha\beta}(x)\dot{x}] &= E[+x]P\{\hat{\gamma}_{\alpha\beta}(x) = +1\} + E[-x]P\{\hat{\gamma}_{\alpha\beta}(x) = -1\} \\ &= (E[x|_{x \geq \alpha}]P\{\hat{\gamma}_{\alpha\beta} \text{ switching at } \alpha\} + E[x|_{x \geq \beta}]P\{\hat{\gamma}_{\alpha\beta} \text{ switching at } \beta\})P\{\hat{\gamma}_{\alpha\beta}(x) = +1\} \\ &\quad + (E[-x|_{x \leq \alpha}]P\{\hat{\gamma}_{\alpha\beta} \text{ switching at } \alpha\} + E[-x|_{x \leq \beta}]P\{\hat{\gamma}_{\alpha\beta} \text{ switching at } \beta\})P\{\hat{\gamma}_{\alpha\beta}(x) = -1\} \\ &= (E[x|_{x \geq 0} - |x|_{x \in (0, \alpha)}]q_\alpha + E[x|_{x \geq 0} - |x|_{x \in (0, \beta)}]q_\beta)P\{\hat{\gamma}_{\alpha\beta}(x) = +1\} \\ &\quad + (E[-x|_{x \leq 0} - |x|_{x \in (0, \alpha)}]q_\alpha + E[-x|_{x \leq 0} - |x|_{x \in (0, \beta)}]q_\beta)P\{\hat{\gamma}_{\alpha\beta}(x) = -1\} \\ &= (E[x|_{x \geq 0}] - E[|x|_{x \in (0, \alpha)}])q_\alpha + (E[x|_{x \geq 0}] - E[|x|_{x \in (0, \beta)}])q_\beta \\ &= \frac{1}{2} E[|x|] - E[|x|_{x \in (0, \alpha)}]q_\alpha - E[|x|_{x \in (0, \beta)}]q_\beta \end{aligned} \quad (12)$$

where  $P\{\cdot\}$  denotes the probability operator. The notations  $q_\alpha = P\{\hat{\gamma}_{\alpha\beta} \text{ switching at } \alpha\}$  and  $q_\beta = P\{\hat{\gamma}_{\alpha\beta} \text{ switching at } \beta\}$ , in which  $\hat{\gamma}_{\alpha\beta}(x)$  switching at  $x = \alpha$  (or  $\beta$ ) means its value jumping from  $-1$  (or  $+1$ ) to  $+1$  (or  $-1$ ). Obviously, there hold the probability relations  $P\{\hat{\gamma}_{\alpha\beta}(x) = +1\} + P\{\hat{\gamma}_{\alpha\beta}(x) = -1\} = 1$  and  $q_\alpha + q_\beta = 1$ .

Similarly, the correlation coefficient  $E[\hat{\gamma}_{\alpha\beta}(x)\dot{x}]$  can be expressed as



$$\begin{aligned}
E[\hat{\gamma}_{\alpha\beta}(x)\dot{x}] &= E[+\dot{x}]P\{\hat{\gamma}_{\alpha\beta}(x)=+1\} + E[-\dot{x}]P\{\hat{\gamma}_{\alpha\beta}(x)=-1\} \\
&= (E[\dot{x}|_{x\geq\alpha, \dot{x}\geq 0}]P\{\hat{\gamma}_{\alpha\beta} \text{ switching at } \alpha\} + E[\dot{x}|_{x\geq\beta, \dot{x}\leq 0}]P\{\hat{\gamma}_{\alpha\beta} \text{ switching at } \beta\})P\{\hat{\gamma}_{\alpha\beta}(x)=+1\} \\
&\quad + (E[-\dot{x}|_{x\leq\alpha, \dot{x}\geq 0}]P\{\hat{\gamma}_{\alpha\beta} \text{ switching at } \alpha\} + E[-\dot{x}|_{x\leq\beta, \dot{x}\leq 0}]P\{\hat{\gamma}_{\alpha\beta} \text{ switching at } \beta\})P\{\hat{\gamma}_{\alpha\beta}(x)=-1\} \\
&= (E[\dot{x}|_{x\geq 0, \dot{x}\geq 0} - \text{sgn}(\alpha)|\dot{x}|_{x\in(0,\alpha), \dot{x}\geq 0}]q_\alpha + E[-\dot{x}|_{x\geq 0, \dot{x}\leq 0} + \text{sgn}(\beta)|\dot{x}|_{x\in(0,\beta), \dot{x}\leq 0}]q_\beta)P\{\hat{\gamma}_{\alpha\beta}(x)=+1\} \\
&\quad + (E[-\dot{x}|_{x\leq 0, \dot{x}\geq 0} - \text{sgn}(\alpha)|\dot{x}|_{x\in(0,\alpha), \dot{x}\geq 0}]q_\alpha + E[\dot{x}|_{x\leq 0, \dot{x}\leq 0} + \text{sgn}(\beta)|\dot{x}|_{x\in(0,\beta), \dot{x}\leq 0}]q_\beta)P\{\hat{\gamma}_{\alpha\beta}(x)=-1\} \\
&= \text{sgn}(-\alpha)E[\dot{x}|_{x\in(0,\alpha), \dot{x}\geq 0}]q_\alpha + \text{sgn}(\beta)E[\dot{x}|_{x\in(0,\beta), \dot{x}\leq 0}]q_\beta \\
&= \frac{1}{2}\text{sgn}(-\alpha)E[\dot{x}|_{x\in(0,\alpha)}]q_\alpha + \frac{1}{2}\text{sgn}(\beta)E[\dot{x}|_{x\in(0,\beta)}]q_\beta.
\end{aligned} \tag{13}$$

If the random excitation is a stationary Gaussian process, the response of the equivalent linearization system of Eq. (6) is Gaussian ([25]). With the assumption of Gaussian process, the mean values of absolute displacement  $x$  and velocity  $\dot{x}$  in Eqs. (12) and (13) can be evaluated in terms of the mean square responses as follows:

$$E[|x|] = \sqrt{\frac{2E[x^2]}{\pi}} \tag{14a}$$

$$E[|x|_{x\in(0,\alpha)}] = \sqrt{\frac{E[x^2]}{2\pi}} \left( 1 - \exp\left\{-\frac{\alpha^2}{2E[x^2]}\right\} \right) \tag{14b}$$

$$E[|x|_{x\in(0,\beta)}] = \sqrt{\frac{E[x^2]}{2\pi}} \left( 1 - \exp\left\{-\frac{\beta^2}{2E[x^2]}\right\} \right) \tag{14c}$$

$$E[\dot{x}|_{x\in(0,\alpha)}] = \sqrt{\frac{E[\dot{x}^2]}{2\pi}} \text{erf}\left(\frac{\alpha}{\sqrt{2E[\dot{x}^2]}}\right) \text{sgn}(\alpha) \tag{14d}$$

$$E[\dot{x}|_{x\in(0,\beta)}] = \sqrt{\frac{E[\dot{x}^2]}{2\pi}} \text{erf}\left(\frac{\beta}{\sqrt{2E[\dot{x}^2]}}\right) \text{sgn}(\beta) \tag{14e}$$

where the error function  $\text{erf}(\cdot)$  is defined as

$$\text{erf}(x) = \frac{2}{\sqrt{\pi}} \int_0^x e^{-u^2} du. \tag{15}$$

It is known from Eq. (15) that  $\text{erf}(x)$  is an odd function, i.e.,  $\text{erf}(-x) = -\text{erf}(x)$ . This function also has the properties  $\text{erf}(0)=0$  and  $\text{erf}(\pm\infty)=\pm 1$ .

**3.2 Evaluation of Switching Probabilities.** The switching probabilities  $q_\alpha$  and  $q_\beta$  can be calculated by using the mathematical machinery of an exit problem ([26]). Since there exists the probability relation  $q_\alpha + q_\beta = 1$ , only one switching probability, for example,  $q_\alpha$  needs to be calculated alternatively. Consider the time evolution of the response process. The switching probability  $q_\alpha$  is the sum of disjoint event probabilities of even and odd numbers of switching and thus, can be expressed for different initial states as follows:

$$q_\alpha(t) = \begin{cases} \frac{1}{2}P_0^+(t) + \sum_{i=1}^{\infty} P_{2i}^+(t) & \hat{\gamma}_{\alpha\beta}(x_0) = +1 \\ \frac{1}{2}P_0^-(t) + \sum_{i=1}^{\infty} P_{2i+1}^-(t) & \hat{\gamma}_{\alpha\beta}(x_0) = -1 \end{cases} \tag{16}$$

where the switching probabilities of even and odd numbers are

$$P_j^\pm(t) = P\left\{ \begin{array}{l} j \text{ numbers of } \hat{\gamma}_{\alpha\beta} \text{ switching during} \\ \text{time interval } (0,t) | \hat{\gamma}_{\alpha\beta}(x_0) = \pm 1 \end{array} \right\} \tag{17}$$

( $j=0,1,2,\dots$ ).

The  $\hat{\gamma}_{\alpha\beta}(x)$  switching at  $\alpha$  (or  $\beta$ ) takes place at the moment when the response process  $x$  starting from the point  $x_0$  or  $\beta$  (or  $\alpha$ ) exits the semi-infinite interval  $(-\infty, \beta)$  [or  $(\alpha, +\infty)$ ] ([21]). Based on the mathematical machinery of this exit problem, the switching probabilities  $P_j^\pm$  can be expressed as a convolution form of a series of probability density functions with only one  $\hat{\gamma}_{\alpha\beta}(x)$  switching. The probability density functions are further represented by the corresponding probability functions with no  $\hat{\gamma}_{\alpha\beta}(x)$  switching and can be determined by solving the backward Kolmogorov equation. It is difficult to analytically solve the Kolmogorov equation and numerical solution is usually necessary. A Laplace transform method has been introduced to solve the equation and obtain the solution of switching probabilities ([27]). Eventually, the stationary mean-square response is calculated from Eq. (9) upon the substitution of  $q_\alpha$  in Eqs. (10) to (13). Since the correlation matrix  $V$  depends on the second moments of response, Eq. (9) is a nonlinear algebraic equation as pointed above. An iteration solution procedure is used to solve this equation.

**3.3 Case of Symmetric Weighting Function.** For the hysteresis nonlinearity with wiping-out and congruency properties, the Preisach weighting function  $\mu(\alpha, \beta)$  possesses a mirror symmetry with respect to line  $\alpha + \beta = 0$  on the Preisach plane, i.e.,  $\mu(-\beta, -\alpha) = \mu(\alpha, \beta)$  ([3]). The symmetric weighting function means that the possible  $\hat{\gamma}_{\alpha\beta}(x)$  switching events appear in couples, and the two switching probabilities of each couple are almost equal since the mean response is zero. Under this assumption and using the relation  $q_\alpha + q_\beta = 1$ , we have  $q_\alpha \cong q_\beta \cong 1/2$ .

With the assumption  $q_\alpha \cong q_\beta \cong 1/2$ , the correlation coefficients  $E[\hat{\gamma}_{\alpha\beta}(x)x]$  and  $E[\hat{\gamma}_{\alpha\beta}(x)\dot{x}]$  in Eqs. (12) and (13) become

$$\begin{aligned}
E[\hat{\gamma}_{\alpha\beta}(x)x] &= \frac{1}{2}(E[|x|] - E[|x|_{x\in(0,\alpha)}] - E[|x|_{x\in(0,\beta)}]) \\
&= \sqrt{\frac{E[x^2]}{8\pi}} (e^{-\alpha^2/2E[x^2]} + e^{-\beta^2/2E[x^2]})
\end{aligned} \tag{18}$$

$$E[\hat{\gamma}_{\alpha\beta}(x)\dot{x}] = \frac{1}{4} E[\dot{x}|_{x\in(\alpha,\beta)}] \tag{19}$$

$$= \sqrt{\frac{E[\dot{x}^2]}{32\pi}} \left[ \text{erf}\left(\frac{\beta}{\sqrt{2E[\dot{x}^2]}}\right) - \text{erf}\left(\frac{\alpha}{\sqrt{2E[\dot{x}^2]}}\right) \right].$$

The Gaussian distribution function has been widely adopted as a parameterized expression of the weighting function in the hysteresis modeling ([28,29]). In the Gaussian distribution form, the symmetric Preisach weighting function can be expressed as

$$\mu(\alpha, \beta) = \begin{cases} \frac{1}{2\pi\sigma^2} \exp\left\{-\frac{(\alpha+\nu)^2 + (\beta-\nu)^2}{2\sigma^2}\right\} & \alpha_0 \leq \alpha \leq 0 \\ & 0 \leq \beta \leq \beta_0 \\ 0 & \text{elsewhere} \end{cases} \tag{20}$$

where  $\sigma$  and  $\nu$  are the model parameters governing the width and area of hysteresis loops;  $\alpha_0 = -\beta_0$ .

By substituting Eqs. (18) to (20) into Eqs. (10) and (11), the correlation coefficients of hysteretic restoring force with response,  $E[zx]$  and  $E[z\dot{x}]$ , can be obtained as follows:

$$E[zx] = \frac{E[x^2]}{\sqrt{32\pi(\sigma^2 + E[x^2])}} e^{-(\nu^2/2(\sigma^2 + E[x^2]))} \left\{ \left[ \operatorname{erf}\left(\frac{\nu}{\sqrt{2}\sigma}\right) + \operatorname{erf}\left(\frac{\beta_0 - \nu}{\sqrt{2}\sigma}\right) \right] \cdot \left[ \operatorname{erf}\left(\frac{\nu}{\sqrt{2}\sigma} \sqrt{\frac{E[x^2]}{\sigma^2 + E[x^2]}}\right) - \operatorname{erf}\left(\frac{\alpha_0}{\sqrt{2}\sigma} \sqrt{\frac{\sigma^2 + E[x^2]}{E[x^2]}} + \frac{\nu}{\sqrt{2}\sigma} \sqrt{\frac{E[x^2]}{\sigma^2 + E[x^2]}}\right) \right] \right. \\ \left. + \left[ \operatorname{erf}\left(\frac{\nu}{\sqrt{2}\sigma}\right) - \operatorname{erf}\left(\frac{\alpha_0 + \nu}{\sqrt{2}\sigma}\right) \right] \cdot \left[ \operatorname{erf}\left(\frac{\nu}{\sqrt{2}\sigma} \sqrt{\frac{E[x^2]}{\sigma^2 + E[x^2]}}\right) + \operatorname{erf}\left(\frac{\beta_0}{\sqrt{2}\sigma} \sqrt{\frac{\sigma^2 + E[x^2]}{E[x^2]}} - \frac{\nu}{\sqrt{2}\sigma} \sqrt{\frac{E[x^2]}{\sigma^2 + E[x^2]}}\right) \right] \right\} \quad (21)$$

$$E[z\dot{x}] = \sqrt{\frac{E[\dot{x}^2]}{32\pi}} \left\{ \left[ \operatorname{erf}\left(\frac{\nu}{\sqrt{2}\sigma}\right) - \operatorname{erf}\left(\frac{\alpha_0 + \nu}{\sqrt{2}\sigma}\right) \right] \cdot \left[ \operatorname{erf}\left(\frac{\beta_0 - \nu}{\sqrt{2}\sigma}, v(u) = \frac{\sqrt{2}\sigma u + \nu}{\sqrt{2E[x^2]}}\right) - \operatorname{erf}\left(\frac{-\nu}{\sqrt{2}\sigma}, v(u) = \frac{\sqrt{2}\sigma u + \nu}{\sqrt{2E[x^2]}}\right) \right] \right. \\ \left. - \left[ \operatorname{erf}\left(\frac{\beta_0 - \nu}{\sqrt{2}\sigma}\right) + \operatorname{erf}\left(\frac{\nu}{\sqrt{2}\sigma}\right) \right] \cdot \left[ \operatorname{erf}\left(\frac{\nu}{\sqrt{2}\sigma}, v(u) = \frac{\sqrt{2}\sigma u - \nu}{\sqrt{2E[x^2]}}\right) - \operatorname{erf}\left(\frac{\alpha_0 + \nu}{\sqrt{2}\sigma}, v(u) = \frac{\sqrt{2}\sigma u - \nu}{\sqrt{2E[x^2]}}\right) \right] \right\} \quad (22)$$

where the function  $\operatorname{erf}(\cdot, \cdot)$  is defined by

$$\operatorname{erf}[x, y(u)] = \frac{2}{\sqrt{\pi}} \int_0^x e^{-u^2} \operatorname{erf}[y(u)] du. \quad (23)$$

In the degenerated case with the weighting parameter  $\nu = 0$ , the correlation coefficients (21) and (22) become

$$E[zx] = \frac{-E[x^2]}{\sqrt{32\pi(\sigma^2 + E[x^2])}} \left[ \operatorname{erf}\left(\frac{\beta_0}{\sqrt{2}\sigma}\right) \operatorname{erf}\left(\frac{\alpha_0}{\sqrt{2}\sigma} \sqrt{\frac{\sigma^2 + E[x^2]}{E[x^2]}}\right) + \operatorname{erf}\left(\frac{\alpha_0}{\sqrt{2}\sigma}\right) \operatorname{erf}\left(\frac{\beta_0}{\sqrt{2}\sigma} \sqrt{\frac{\sigma^2 + E[x^2]}{E[x^2]}}\right) \right] \quad (24)$$

$$E[z\dot{x}] = \sqrt{\frac{E[\dot{x}^2]}{32\pi}} \left[ \operatorname{erf}\left(\frac{\beta_0}{\sqrt{2}\sigma}\right) \operatorname{erf}\left(\frac{\alpha_0}{\sqrt{2}\sigma}, v(u) = \frac{\sigma u}{\sqrt{E[x^2]}}\right) - \operatorname{erf}\left(\frac{\alpha_0}{\sqrt{2}\sigma}\right) \operatorname{erf}\left(\frac{\beta_0}{\sqrt{2}\sigma}, v(u) = \frac{\sigma u}{\sqrt{E[x^2]}}\right) \right] \quad (25)$$

#### 4 Numerical Example

A numerical example is presented to verify the validity of the derived formulas for the correlation coefficients in the case of symmetric Preisach weighting function and to evaluate the mean square response of the Preisach hysteretic system. In this example, the Preisach weighting function  $\mu(\alpha, \beta)$  is taken as Eq. (20) with the parameters  $\alpha_0 = -4.0$  and  $\beta_0 = 4.0$ . Different values of the weighting parameters  $\sigma$  and  $\nu$  are used in numerical computation. Figure 5 shows the hysteresis loops corresponding to the Preisach weighting function with the parameters  $\sigma = 0.1$  and  $\nu = 2.0$  under a decayed sinusoidal input.

Tables 1, 2, and 3 show a comparison of the predicted values of the correlation coefficient  $E[zx]$  computed by using Eq. (21) and obtained from the digital simulation. The results are obtained under different values of the parameters  $\sigma$  and  $\nu$ . A good agreement between the two sets of results is observed, even in the degenerated case of the weighting parameter  $\nu = 0$ . It should be noted that the error between the two approaches might be also due to the approximation in generating pseudo-random numbers in the digital simulation. It is therefore concluded that the assumption of the equal switching probabilities  $q_\alpha$  and  $q_\beta$  in the case of symmetric Preisach weighting function holds to a significant extent. Equations (21) and (22) are good approximation for the correlation coefficients in the case of symmetric Gaussian distribution weighting function, which greatly facilitate the evaluation of mean square response of Preisach hysteretic systems.

Then the mean square responses of a Preisach hysteretic system subjected to a stationary Gaussian white noise excitation are analyzed by means of the proposed method. The system parameters, hysteresis parameters and excitation intensity are taken as  $k = 1.0$ ,  $\zeta = 0.1$ ,  $\sigma = 0.1$ ,  $\nu = 1.0$ ,  $\beta_0 = -\alpha_0 = 4.0$  and  $D = 4.0$  except additional specification. The Preisach weighting function is same

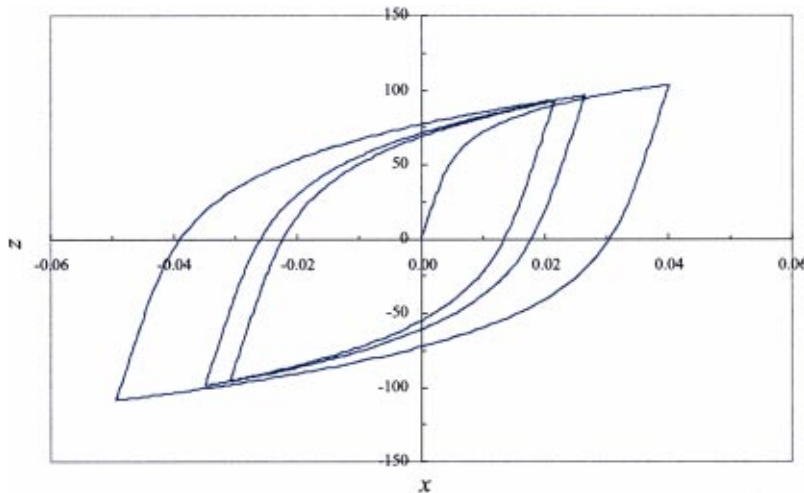


Fig. 5 Hysteresis loops

**Table 1 Predicted results of correlation coefficient for weighting parameter  $\nu=1.0$  ( $E=[zx]$ -analytical evaluation;  $E[zx]_s$ -digital simulation)**

$\sigma$	$E[zx]$	$E[zx]_s$	Error (%)
0.20	0.48376	0.48279	0.20
0.15	0.48388	0.49742	0.73
0.10	0.48393	0.49137	1.51
0.05	0.48394	0.49374	1.98
0.01	0.48394	0.49512	2.26

**Table 2 Predicted results of correlation coefficient for weighting parameter  $\sigma=0.1$  ( $E=[zx]$ -analytical evaluation;  $E[zx]_s$ -digital simulation)**

$\nu$	$E[zx]$	$E[zx]_s$	Error (%)
0.5	0.70150	0.71298	1.61
0.6	0.66433	0.67453	1.51
0.7	0.62292	0.63101	1.28
0.8	0.57834	0.58320	0.83
0.9	0.53166	0.53586	0.78
1.0	0.48393	0.49137	1.51
1.1	0.43615	0.44762	2.56
1.2	0.38921	0.40326	3.48
1.3	0.34390	0.35809	3.96
1.4	0.30087	0.31345	4.01

**Table 3 Predicted results of correlation coefficient for weighting parameter  $\nu=0$  ( $E=[zx]$ -analytical evaluation;  $E[zx]_s$ -digital simulation)**

$\sigma$	$E[zx]$	$E[zx]_s$	Error (%)
0.20	0.19560	0.19579	0.10
0.15	0.19726	0.19764	0.19
0.10	0.19848	0.19888	0.20
0.05	0.19922	0.19936	0.07
0.01	0.19946	0.19815	0.66

as the above. Figure 6 shows the mean square responses against the excitation intensity  $D$ , and Figs. 7 and 8 show the mean square responses against the linear stiffness  $k$  under different viscous damping  $\zeta$ . In these figures, direct digital simulation results are also given for comparison. A good coincidence between the results obtained by the digital simulation and by the present method is observed. Figures 9 and 10 show the mean square responses versus the weighting parameter  $\sigma$  under different excitation intensity  $D$ . It is seen that with the increase of the parameter  $\sigma$ , the mean square responses decrease at the outset, and then increase

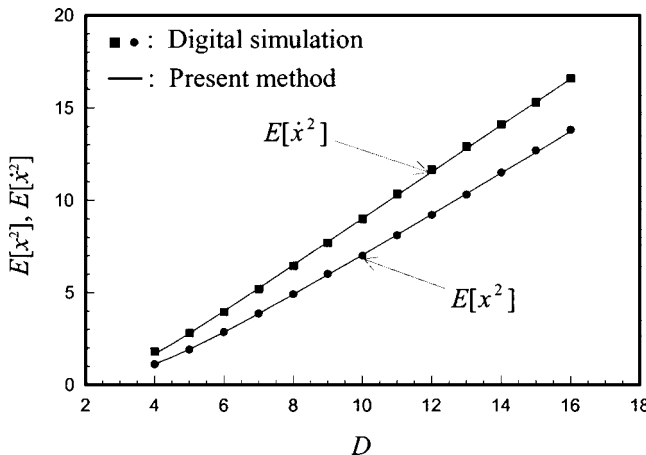


**Fig. 6 Mean square response versus excitation intensity  $D$**

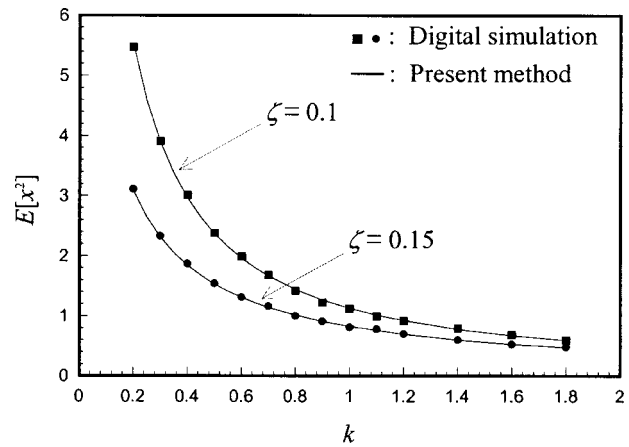


**Fig. 7 Mean square displacement versus linear stiffness  $k$**

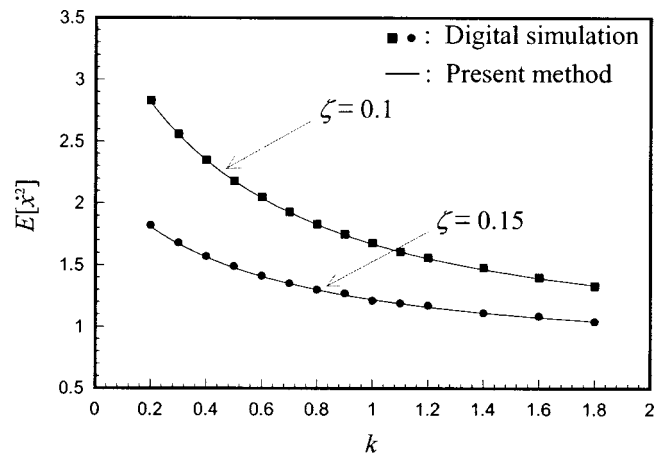


**Fig. 8 Mean square velocity versus stiffness  $k$**

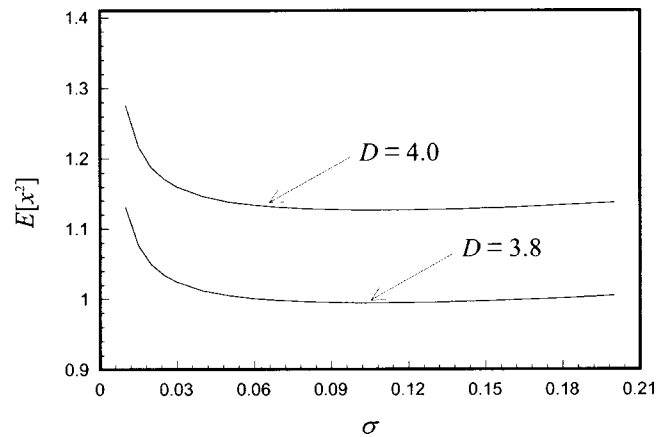


**Fig. 9 Mean square displacement versus weighting parameter  $\sigma$**

smoothly. When  $\sigma$  is less than 0.03, the mean square responses sharply drop with the increase of  $\sigma$ . In the range of  $\sigma$  from 0.03 to 0.20, the mean square responses almost do not vary with  $\sigma$ . Figures 11 and 12 show the mean square responses versus the weighting parameter  $\nu$  under different excitation intensity  $D$ . It is observed that the mean square responses decrease with the increase of the parameter  $\nu$ , but tend to be steady when  $\nu$  is greater than 1.4 for the mean square displacement and 1.8 for the mean square

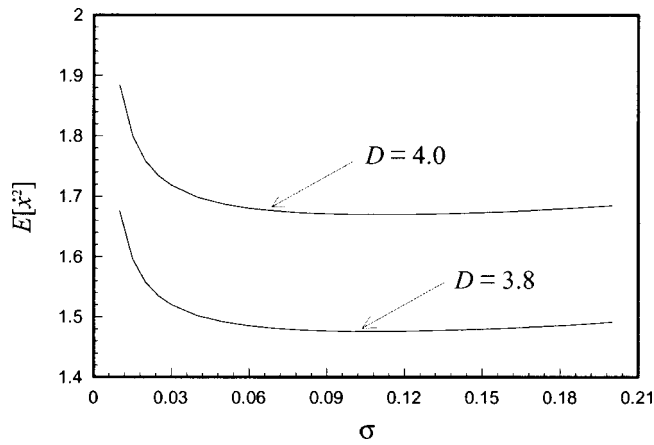


Fig. 10 Mean square velocity versus weighting parameter  $\sigma$

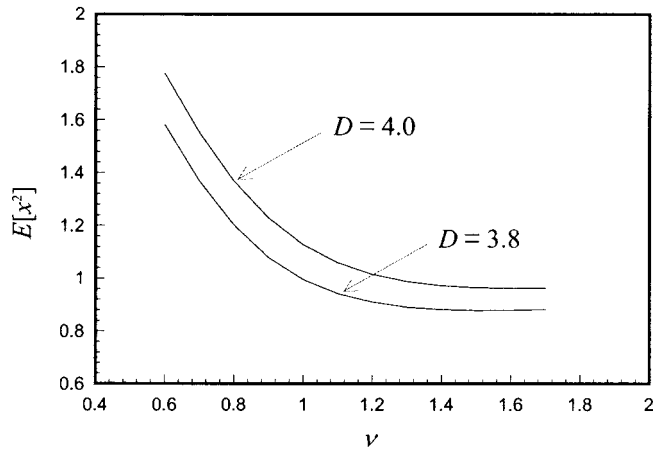


Fig. 11 Mean square displacement versus weighting parameter  $\nu$

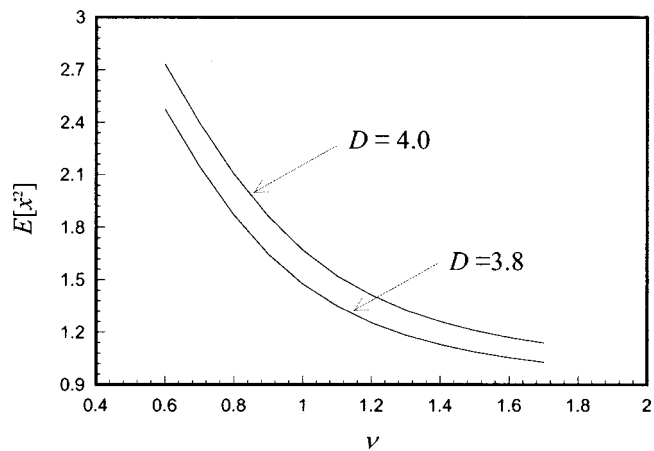


Fig. 12 Mean square velocity versus weighting parameter  $\nu$

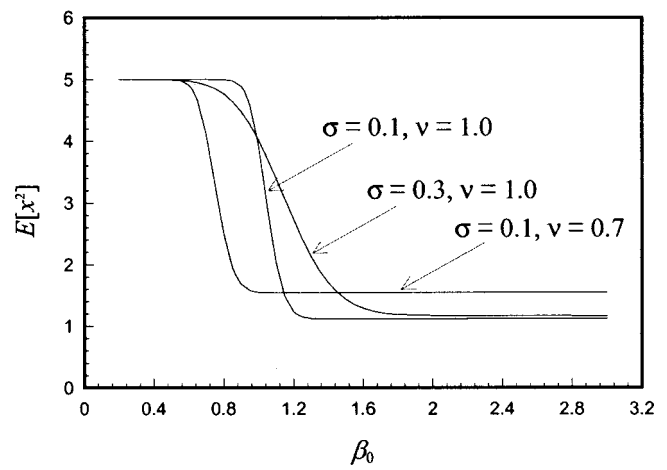


Fig. 13 Mean square displacement versus weighting parameter  $\beta_0$

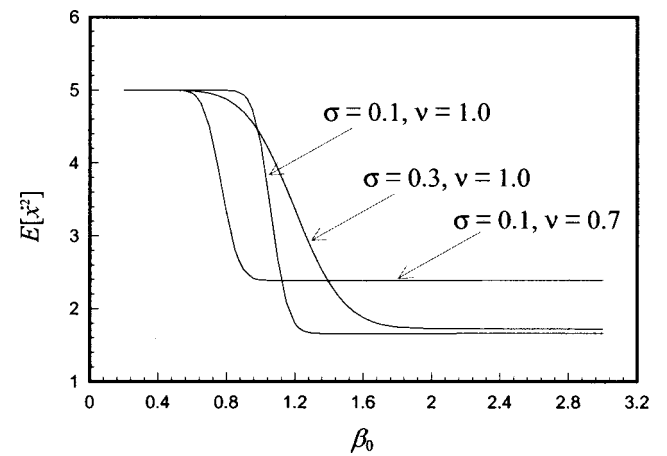


Fig. 14 Mean square velocity versus weighting parameter  $\beta_0$

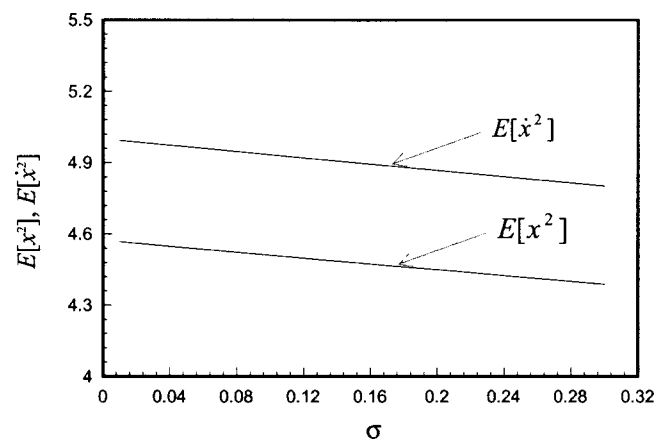


Fig. 15 Mean square response versus weighting parameter  $\sigma(\nu=0)$

velocity. Figures 13 and 14 show the mean square responses versus the weighting parameter  $\beta_0$  under different combination of the parameters  $\sigma$  and  $\nu$ . It is seen that there exists a sudden drop in the mean square responses with the increase of the parameter  $\beta_0$ . In the case of  $\sigma=0.1$  and  $\nu=1.0$ , the mean square responses tend to a low constant value when  $\beta_0$  is greater than 1.2. In the degener-

ated case of the weighting parameter  $\nu=0$ , as shown in Fig. 15, the mean square responses decrease slowly with the increase of the weighting parameter  $\sigma$ . Figure 16 shows that the mean square displacement drops sharply and then trends to a constant value, while the mean square velocity varies smoothly.

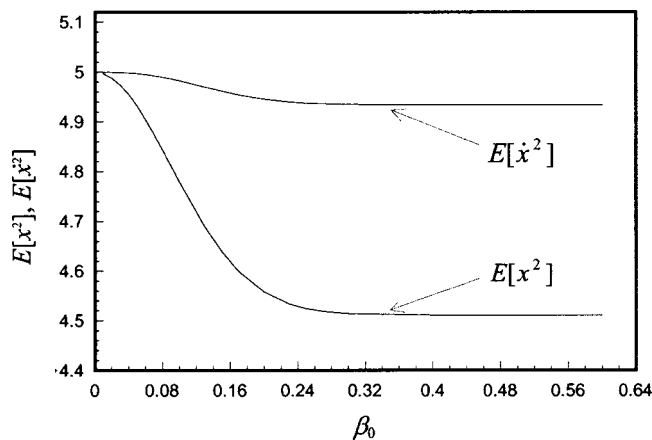


Fig. 16 Mean square response versus weighting parameter  $\beta_0$  ( $\nu=0$ )

## 5 Conclusions

The Preisach model has been shown great promise for modeling the nonlinear constitutive relation of hysteretic materials and devices. In this paper, a new method for analyzing nonlinear random dynamic response of the Preisach hysteretic system under stationary Gaussian white noise excitation was developed. The proposed method is based on covariance and switching probability analysis in considering the integral form of the Preisach constitutive relationship. Simplified formulas for evaluating the correlation coefficients of hysteretic restoring force with response were derived for the symmetric Preisach weighting function based on the approximation of equal "up" and "down" switching probabilities. Although this study addressed only the single-degree-of-freedom Preisach hysteretic system subjected to stationary random excitation, the proposed method can be extended to analyze multi-degree-of-freedom Preisach systems under stationary or nonstationary excitation. An example of the Preisach hysteretic system with the Gaussian distribution weighting function was given to evaluate the mean square responses by using the proposed method and to verify the validity of the derived formulas. A good agreement was observed between the predicted values of the correlation coefficients using the simplified formulas and using digital simulation. The numerical results also showed that the mean square responses of the Preisach hysteretic system decrease with the increase of linear stiffness and viscous damping, and in general, are more sensitive to the weighting parameter  $\nu$  than to the weighting parameter  $\sigma$  and the weighting range  $\beta_0$  (or  $\alpha_0$ ). It was found that the mean square responses suffer a sharp drop with the increase of the parameter  $\beta_0$  and are affected only in a certain range of the Preisach weighting function.

## Acknowledgments

This study was supported by the Hong Kong Polytechnic University under the grant G-YW29 and through the Area of Strategic Development (ASD) Program in Structural Engineering. These supports are gratefully acknowledged.

## References

- [1] Preisach, F., 1935, "Über die Magnetische Nachwirkung," *Z. Phys.*, **94**, pp. 277–302 (in German).
- [2] Krasnoselskii, M. A., and Pokrovskii, A. V., 1989, *Systems With Hysteresis*, Springer, Berlin.
- [3] Mayergoyz, I. D., 1991, *Mathematical Models of Hysteresis*, Springer-Verlag, New York.
- [4] Visintin, A., 1994, *Differential Models of Hysteresis*, Springer-Verlag, Berlin.
- [5] Hughes, D., and Wen, J. T., 1995, "Preisach Modeling and Compensation for Smart Material Hysteresis," *Active Materials and Smart Structures*, Vol. 2427, G. L. Anderson and D. C. Lagoudas, eds., SPIE, Bellingham, WA, pp. 50–64.
- [6] Ni, Y. Q., Ko, J. M., and Wong, C. W., 1999, "Nonparametric Identification of Nonlinear Hysteretic Systems," *J. Eng. Mech.*, **125**, pp. 206–215.
- [7] Freeman, A. R., and Joshi, S. P., 1996, "Numerical Modeling of PZT Nonlinear Electromechanical Behavior," *Smart Structures and Materials 1996: Mathematics and Control in Smart Structures*, Vol. 2715, V. V. Varadan and J. Chandra, eds., SPIE, Bellingham, WA, pp. 602–613.
- [8] Bertotii, G., and Basso, V., 1993, "Considerations on the Physical Interpretation of the Preisach Model of Ferromagnetic Hysteresis," *J. Appl. Phys.*, **73**, pp. 5827–5829.
- [9] Sreeram, P. N., and Naganathan, N. G., 1994, "Hysteresis Prediction for Piezoceramic Actuator Systems Using Preisach Models," *Smart Structures and Materials 1994: Smart Materials*, Vol. 2189, V. V. Varadan, ed., SPIE, Bellingham, WA, pp. 14–25.
- [10] Ge, P., and Jouaneh, M., 1995, "Modeling Hysteresis in Piezoceramic Actuators," *Precis. Eng.*, **17**, pp. 211–221.
- [11] Hughes, D., and Wen, J. T., 1997, "Preisach Modeling of Piezoceramic and Shape Memory Alloy Hysteresis," *Smart Mater. Struct.*, **6**, pp. 287–300.
- [12] Lagoudas, D. C., and Bhattacharyya, A., 1997, "On the Correspondence Between Micromechanical Models for Isothermal Pseudoelastic Response of Shape Memory Alloys and the Preisach Model for Hysteresis," *Math. Mech. Solids*, **2**, pp. 405–440.
- [13] Adly, A. A., Mayergoyz, I. D., and Bergqvist, A., 1991, "Preisach Modeling of Magnetostrictive Hysteresis," *J. Appl. Phys.*, **69**, pp. 5777–5779.
- [14] Schafer, J., and Janocha, H., 1995, "Compensation of Hysteresis in Solid-State Actuators," *Sens. Actuators A*, **49**, pp. 97–102.
- [15] Lubarda, V. A., Sumarac, D., and Krajcinovic, D., 1993, "Preisach Model and Hysteretic Behaviour of Ductile Materials," *Eur. J. Mech. A/Solids*, **12**, pp. 445–470.
- [16] Sumarac, D., and Stosic, S., 1996, "The Preisach Model for the Cyclic Bending of Elasto-Plastic Beams," *Eur. J. Mech. A/Solids*, **15**, pp. 155–172.
- [17] Wang, J. Y., Ni, Y. Q., and Ko, J. M., 1999, "Transient Dynamic Response of Preisach Hysteretic Systems," *A New Advance in Seismic Isolation, Energy Dissipation and Control of Structures*, F. Zhou and B. F. Spencer, Jr., eds., Seismological Press, Beijing, China, pp. 378–385.
- [18] Ni, Y. Q., Wang, J. Y., and Ko, J. M., 1999, "Advanced Method for Modelling Hysteretic Behaviour of Semi-Rigid Joints," *Advances in Steel Structures*, Vol. 1, S. L. Chan and J. G. Teng, eds., Elsevier Science Ltd., Oxford, UK, pp. 331–338.
- [19] Lo, H. R., Hammond, J. K., and Sainsbury, M. G., 1988, "Nonlinear System Identification and Modelling with Application to an Isolator with Hysteresis," *Proceedings of the 6th International Modal Analysis Conference*, Vol. 2, Society of Experimental Mechanics, Bethel, CT, pp. 1453–1459.
- [20] Mayergoyz, I. D., and Korman, C. E., 1991, "Preisach Model With Stochastic Input as a Model for Viscosity," *J. Appl. Phys.*, **69**, pp. 2128–2134.
- [21] Mayergoyz, I. D., and Korman, C. E., 1994, "The Preisach Model With Stochastic Input as a Model for Aftereffect," *J. Appl. Phys.*, **75**, pp. 5478–5480.
- [22] Korman, C. E., and Mayergoyz, I. D., 1997, "Review of Preisach Type Models Driven by Stochastic Inputs as a Model for After-Effect," *Physica B*, **233**, pp. 381–389.
- [23] Verdi, C., and Visintin, A., 1989, "Numerical Approximation of the Preisach Model for Hysteresis," *Math. Modell. Numer. Anal.*, **23**, pp. 335–356.
- [24] Yu, Y., Xiao, Z., Lin, E.-B., and Naganathan, N., 1999, "Wavelet Implementation of Preisach Model of Hysteresis," *Smart Structures and Materials 1999: Mathematics and Control in Smart Structures*, Vol. 3667, V. V. Varadan, ed., SPIE, Bellingham, WA, pp. 776–784.
- [25] Wen, Y. K., 1980, "Equivalent Linearization for Hysteretic Systems Under Random Excitation," *ASME J. Appl. Mech.*, **47**, pp. 150–154.
- [26] Korman, C. E., and Mayergoyz, I. D., 1995, "Switching as an Exit Problem," *IEEE Trans. Magn.*, **31**, pp. 3545–3547.
- [27] Ni, Y. Q., Ying, Z. G., and Ko, J. M., 2000, "Nonlinear Random Vibration of Preisach Hysteretic Systems," *Proceedings of the International Conference on Advanced Problems in Vibration Theory and Applications*, J. H. Zhang and X. N. Zhang, eds., Science Press, Beijing, China, pp. 568–574.
- [28] Galinaitis, W. S., and Rogers, R. C., 1997, "Compensation for Hysteresis Using Bivariate Preisach Models," *Smart Structures and Materials 1997: Mathematics and Control in Smart Structures*, Vol. 3039, V. V. Varadan and J. Chandra, eds., SPIE, Bellingham, WA, pp. 538–647.
- [29] Torre, E. D., and Vajda, F., 1997, "Effect of Apparent Reversibility on Parameter Estimation," *IEEE Trans. Magn.*, **33**, pp. 1085–1092.



**E. Scarpetta**

D.I.I.M.A.,  
University of Salerno,  
84084 Fisciano (SA), Italy

**M. A. Sumbatyan**

Research Institute of Mechanics  
and Applied Mathematics,  
Stachki Prospect 200/1,  
Rostov-on-Don 344090, Russia

# In-Plane Wave Propagation Through Elastic Solids With a Periodic Array of Rectangular Defects

*In the context of wave propagation in damaged (elastic) solids, an analytical approach is developed to study normal penetration of a longitudinal plane wave into a periodic array of rectangular defects. Reducing the problem to some integral equations holding over the base and height of the openings, a direct numerical method is applied to give a complete solution for various exact or approximated forms. Several figures show the peculiarities of the structure and lead to physical conclusions. [DOI: 10.1115/1.1430235]*

## 1 Introduction

In the frame of wave propagation through (solid) continuous media with irregular distributed defects, many researches have been devoted to study the reflection and transmission properties of the given lattice with respect to some incident wave. For regular (periodic) distributions in a two-dimensional context, which are those contemplated in the present paper, there are mainly two types of approach to the scattering problem. The first one, more often used, resorts to well-known numerical algorithms for solving certain integral equations based on the length or the surface of the defects and originated from natural boundary conditions. This line of research is deeply concerned in the numerous papers performed by Achenbach et al. (see, e.g., [1–5]), where several geometric configurations, for not too high frequency, are taken into account.

The other type of approach is more analytical. Along with the important results obtained in ([6–11]), we would also mention our previous papers ([12–16]), in which a new—quite general—analytical method has been introduced for various scattering problems in the *one-mode* range of frequency. Starting from integral equations based on the opening between neighboring defects and originated by continuity assumptions, we were able to put down explicit formulas for the relevant parameters by means of a mild (uniform) approximation valid in that range. In many cases, we also solved analytically the main integral equations, thus arriving at the complete solution of the problem.

Of course, the geometrical form of the defects is crucial for all scattering problems, whatever be the method of approach. It would be preferable to consider more and more irregular forms (even unknown), until now being considered rather simple forms such as slit-type, circular, and rectangular defects. The latter case has been fully treated by numerical methods (of engineering type) in an acoustic context ([17,18]), and only recently by analytical methods for a scalar problem in elastic context ([16]). In this paper we aim to carry on, as analytically as possible, the study of rectangular scatterers in an elastic context, and precisely to consider the vector problem for the normal incidence of a longitudinal plane wave onto a periodic (vertical) array of rectangular defects

in an elastic medium. Of course, this is equivalent to considering regular openings periodically distributed in a vertical screen of finite thickness inside the medium. Assuming the dependence on time of the harmonic type, we will employ both continuity and boundary conditions to lay down some (systems of) integral equations that hold over the base and the height of such openings, and whose unknowns turn out to provide a complete analytical representation of the scattered field in the whole structure, including the reflection and transmission coefficients. A direct numerical method will then be applied to solve such integral equations in exact form (as they arise) as well as in various approximated forms. Finally, several figures reflecting the numerical results will permit us to evaluate the influence of the physical and geometrical parameters on the wave properties of the structure, and some interesting remarks will be derived.

It should be finally noted that the incidence of a longitudinal wave in a two-dimensional medium gives rise to the so-called *in-plane* problem for the propagation of the SV- and P-type waves ([19]). This problem in connection with periodically distributed rectangular defects is here tackled analytically for the first time.

## 2 Formulation of the Problem: Boundary Conditions

The geometrical structure is quite similar to that considered in ([16]): We have an unbounded two-dimensional elastic medium in which there is an infinite, periodic array of rectangular defects (see Fig. 1). The period of the grating is  $2a$ , the opening, i.e., the distance between two neighboring defects is  $2b$  (around  $|y| = 0, 2a, 4a, \dots$ ) and the length of the horizontal side of the rectangles is  $2l$  (around  $x = 0$ ).

In the assumed harmonic regime, the time-dependence implies the common factor  $e^{-i\omega t}$  in all the field variables; we omit throughout this indication, and prefer to express the displacement field  $\mathbf{u} \equiv (u_x, u_y)$  by means of the following (Green-Lamé type) representation:

$$u_x = \frac{\partial \varphi}{\partial x} + \frac{\partial \psi}{\partial y}, \quad u_y = \frac{\partial \varphi}{\partial y} - \frac{\partial \psi}{\partial x} \quad (2.1)$$

in which the *displacement potentials*  $\varphi(x, y)$  and  $\psi(x, y)$  satisfy throughout the Helmholtz equations:

$$\partial^2 \varphi / \partial x^2 + \partial^2 \varphi / \partial y^2 + k_1^2 \varphi = 0, \quad \partial^2 \psi / \partial x^2 + \partial^2 \psi / \partial y^2 + k_2^2 \psi = 0.$$

Above,  $\omega$  is the circular frequency, and  $k_1, k_2$  denote the longitudinal and transverse wave numbers; of course,  $\omega/k_1 \equiv c_1$  and  $\omega/k_2 \equiv c_2$  give the respective wave speeds of the material in concern ( $c_1 > c_2$ ).

Contributed by the Applied Mechanics Division of THE AMERICAN SOCIETY OF MECHANICAL ENGINEERS for publication in the ASME JOURNAL OF APPLIED MECHANICS. Manuscript received by the ASME Applied Mechanics Division, April 2, 2001; final revision, August 6, 2001. Associate Editor: A. K. Mal. Discussion on the paper should be addressed to the Editor, Professor Lewis T. Wheeler, Department of Mechanical Engineering, University of Houston, Houston, TX 77204-4792, and will be accepted until four months after final publication of the paper itself in the ASME JOURNAL OF APPLIED MECHANICS.

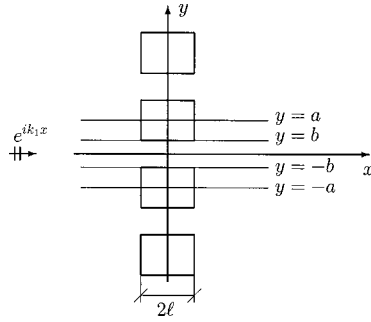


**Fig. 1 Normal penetration of a longitudinal plane wave into a periodic array of rectangular defects  $2l \times 2(a-b)$**

The following (linear) constitutive equations for the relevant stress components hold throughout:

$$\tau_{xy} = \tau_{yx} = c_2^2 \left( 2 \frac{\partial^2 \varphi}{\partial x \partial y} - \frac{\partial^2 \psi}{\partial x^2} + \frac{\partial^2 \psi}{\partial y^2} \right) \quad (2.2a)$$

$$\sigma_x = c_1^2 \left( \frac{\partial^2 \varphi}{\partial x^2} + \frac{\partial^2 \varphi}{\partial y^2} \right) - 2c_2^2 \left( \frac{\partial^2 \varphi}{\partial y^2} - \frac{\partial^2 \psi}{\partial x \partial y} \right) \quad (2.2b)$$

$$\sigma_y = c_1^2 \left( \frac{\partial^2 \varphi}{\partial x^2} + \frac{\partial^2 \varphi}{\partial y^2} \right) - 2c_2^2 \left( \frac{\partial^2 \varphi}{\partial x^2} + \frac{\partial^2 \psi}{\partial x \partial y} \right) \quad (2.2c)$$

(putting the constant density equal to 1).

In the considered structure, an incident longitudinal plane wave of the form

$$\varphi_{\text{inc}} = e^{ik_1 x}, \quad \psi_{\text{inc}} = 0$$

is entering from  $-\infty$ , giving rise to scattered fields in the left ( $x < -l$ ), central ( $|x| < l$ ), and right ( $x > l$ ) parts. Thanks to the natural symmetry and periodicity along  $y$ , the problem can be obviously restricted to the typical layer  $|y| < a$  with a narrowing  $|y| < b$  of length  $2l$ . By the same token, we can represent the potentials in the left and right parts of this layer as follows:

$$\varphi_{\text{left}}(x, y) = e^{ik_1(x+l)} + \text{Re}^{-ik_1(x+l)} + \sum_{n=1}^{\infty} A_n e^{q_n(x+l)} \cos(\pi n y / a) \quad (2.3a)$$

$$\psi_{\text{left}}(x, y) = \sum_{n=1}^{\infty} B_n e^{r_n(x+l)} \sin(\pi n y / a) \quad (x < -l, |y| < a), \quad (2.3b)$$

$$\varphi_{\text{right}}(x, y) = T e^{ik_1(x-l)} + \sum_{n=1}^{\infty} C_n e^{-q_n(x-l)} \cos(\pi n y / a) \quad (2.4a)$$

$$\psi_{\text{right}}(x, y) = \sum_{n=1}^{\infty} D_n e^{-r_n(x-l)} \sin(\pi n y / a) \quad (x > l, |y| < a), \quad (2.4b)$$

where it holds that

$$q_n = \sqrt{(\pi n / a)^2 - k_1^2}, \quad r_n = \sqrt{(\pi n / a)^2 - k_2^2}, \quad n = 1, 2, 3, \dots, \quad (2.5)$$

in order for the Helmholtz equations to be trivially solved by each term of the above series.

Note that such representations identically satisfy the natural boundary conditions at the edges of the two semilayers:

$$u_y(x, \pm a) = \tau_{xy}(x, \pm a) \sim \sin(\pi n y / a)|_{y=\pm a} = 0, \quad |x| > l.$$

Moreover, the *one-mode assumption* for frequency, namely

$$0 < k_1 < k_2 < (\pi / a), \quad (2.6)$$

assures that all  $q_n$ s and  $r_n$ s are real and positive; as a consequence, constants  $R$  and  $T$  can attain their full meaning as *reflection* and *transmission* coefficients, respectively, since at large distances from the defects' array only the terms containing them, with the given (longitudinal) wave number, will remain nonvanishing in the scattered field of Eqs. (2.3), (2.4).

In the central (rectangular) part  $|x| < l$ ,  $|y| < b$ , we begin by writing the potentials as superpositions of their even and odd components (with respect to  $x$ )

$$\varphi_{\text{cent}} = \varphi_{\text{cent}}^+ + \varphi_{\text{cent}}^-, \quad \psi_{\text{cent}} = \psi_{\text{cent}}^- + \psi_{\text{cent}}^+$$

and then represent them in the following manner:

$$\begin{aligned} \varphi_{\text{cent}}^+(x, y) = & E_0^+ \cos(k_1 x) + \sum_{n=1}^{\infty} E_n^+ \text{ch}(p_n x) \cos(\pi n y / b) \\ & + F_0^+ \cos(k_1 y) + \sum_{n=1}^{\infty} F_n^+ \text{ch}(v_n y) \cos(\pi n x / l), \end{aligned} \quad (2.7a)$$

$$\begin{aligned} \varphi_{\text{cent}}^-(x, y) = & E_0^- \sin(k_1 x) + \sum_{n=1}^{\infty} E_n^- \text{sh}(p_n x) \cos(\pi n y / b) \\ & + \sum_{n=1}^{\infty} F_n^- \text{ch}(v_n y) \sin(\pi n x / l), \end{aligned} \quad (2.7b)$$

$$\begin{aligned} \psi_{\text{cent}}^+(x, y) = & \sum_{n=1}^{\infty} P_n^+ \text{sh}(s_n x) \sin(\pi n y / b) \\ & + \sum_{n=1}^{\infty} Q_n^+ \text{sh}(w_n y) \sin(\pi n x / l), \end{aligned} \quad (2.8a)$$

$$\begin{aligned} \psi_{\text{cent}}^-(x, y) = & \sum_{n=1}^{\infty} P_n^- \text{ch}(s_n x) \sin(\pi n y / b) + Q_0^- \sin(k_1 y) \\ & + \sum_{n=1}^{\infty} Q_n^- \text{sh}(w_n y) \cos(\pi n x / l) \quad (|x| < l, |y| < b), \end{aligned} \quad (2.8b)$$

where it holds

$$\begin{aligned} p_n = & \sqrt{(\pi n / b)^2 - k_1^2}, \quad v_n = \sqrt{(\pi n / l)^2 - k_1^2}, \\ s_n = & \sqrt{(\pi n / b)^2 - k_2^2}, \quad w_n = \sqrt{(\pi n / l)^2 - k_2^2} \end{aligned} \quad (2.9)$$

for the same reason as before.

In the sequel, we will find convenient to put

$$a_n = \pi n / a, \quad b_n = \pi n / b, \quad l_n = \pi n / l.$$

Further, where needed, all field variables will be labeled as *left*, *cent(ral)* or *right* according to the region in which they are considered. For all fields involved in the central region, we will also distinguish, by proper labels (+ or -), between the components coming from  $\varphi_{\text{cent}}^+$ ,  $\psi_{\text{cent}}^+$  and those coming from  $\varphi_{\text{cent}}^-$ ,  $\psi_{\text{cent}}^-$  (via Eqs. (2.1) or (2.2)). In this connection, note that, with respect to  $x$ ,  $u_{x-}^{\text{cent}}$ ,  $u_{y+}^{\text{cent}}$ ,  $\tau_{xy-}^{\text{cent}}$ ,  $\sigma_{x+}^{\text{cent}}$  are even functions, while  $u_{x+}^{\text{cent}}$ ,  $u_{y-}^{\text{cent}}$ ,  $\tau_{xy+}^{\text{cent}}$ ,  $\sigma_{x-}^{\text{cent}}$  are odd.

Of course, the sides of the defects cannot sustain stresses, that implies the following boundary conditions to hold in the typical layer:

$$\begin{aligned} \tau_{xy}^{\text{left}}(-l, y) = & \sigma_x^{\text{left}}(-l, y) \\ = & \tau_{xy}^{\text{right}}(l, y) = \sigma_x^{\text{right}}(l, y) = 0, \quad b < |y| < a; \end{aligned} \quad (2.10)$$

$$\sigma_y^{\text{cent}}(x, \pm b) = 0, \quad \tau_{xy}^{\text{cent}}(x, \pm b) = 0, \quad |x| < l. \quad (2.11)$$

All the capital letters in the above representations of the total wave field denote unknown constants. Following the guidelines of our analytical approach, the next task is to introduce some new (unknown) functions in terms of which all these constants can be expressed. In this connection, if we put

$$\tau_{xy}^{\text{left}}(-l, y) \equiv \begin{cases} g_1^\tau(y), & |y| < b \\ 0, & b < |y| < a, \end{cases}$$

$$\sigma_x^{\text{left}}(-l, y) \equiv \begin{cases} g_1^\sigma(y), & |y| < b \\ 0, & b < |y| < a \end{cases} \quad (2.12)$$

$$\tau_{xy}^{\text{right}}(l, y) \equiv \begin{cases} g_2^\tau(y), & |y| < b \\ 0, & b < |y| < a, \end{cases}$$

$$\sigma_x^{\text{right}}(l, y) \equiv \begin{cases} g_2^\sigma(y), & |y| < b \\ 0, & b < |y| < a \end{cases} \quad (2.13)$$

(recall Eqs. (2.10)), then an assumption of continuity between neighboring regions leads to

$$g_1^\tau(y) = \tau_{xy}^{\text{cent}}(-l, y) = -\tau_{xy+}^{\text{cent}}(l, y) + \tau_{xy-}^{\text{cent}}(l, y),$$

$$g_2^\tau(y) = \tau_{xy}^{\text{cent}}(l, y), \quad (2.14)$$

$$g_1^\sigma(y) = \sigma_x^{\text{cent}}(-l, y) = \sigma_{x+}^{\text{cent}}(l, y) - \sigma_{x-}^{\text{cent}}(l, y),$$

$$g_2^\sigma(y) = \sigma_x^{\text{cent}}(l, y), \quad |y| < b. \quad (2.15)$$

We also put

$$u_{y+}^{\text{cent}}(x, b) \equiv g_u^+(x), \quad u_{y-}^{\text{cent}}(x, b) \equiv g_u^-(x), \quad |x| < l. \quad (2.16)$$

These equations are the starting point of our procedure. In them, functions  $g_{1,2}^\tau$  and  $g_{1,2}^\sigma$  are physically related to the stress components along the borderlines; the geometrical symmetry implies they are odd and even functions, respectively. Of course,  $g_u^+$  is even and  $g_u^-$  is odd.

### 3 Analytical Representations

We now aim to derive formulas for all unknown constants of the total field in terms of the six functions  $g$  just introduced. For the sake of clarity, let us begin by calculating all fields involved in Eqs. (2.11)<sub>2</sub>–(2.16). In view of constitutive Eqs. (2.2) and wave field representations (2.1), (2.3), (2.4), (2.7), and (2.8), we have

$$\tau_{xy}^{\text{left}}(-l, y) = c_2^2 \sum_{n=1}^{\infty} [-2q_n a_n A_n - (2a_n^2 - k_2^2) B_n] \sin a_n y, \quad (3.1a)$$

$$\tau_{xy}^{\text{right}}(l, y) = c_2^2 \sum_{n=1}^{\infty} [2q_n a_n C_n - (2a_n^2 - k_2^2) D_n] \sin a_n y, \quad (3.1b)$$

$$\sigma_x^{\text{left}}(-l, y) = -c_1^2 k_1^2 (1 + R) + c_2^2 \sum_{n=1}^{\infty} [(2a_n^2 - k_2^2) A_n + 2a_n r_n B_n] \cos a_n y, \quad (3.1c)$$

$$\sigma_x^{\text{right}}(l, y) = -c_1^2 k_1^2 T + c_2^2 \sum_{n=1}^{\infty} [(2a_n^2 - k_2^2) C_n - 2a_n r_n D_n] \cos a_n y, \quad (3.1d)$$

$$\tau_{xy+}^{\text{cent}}(l, y) = c_2^2 \sum_{n=1}^{\infty} [-2p_n b_n \text{sh}(p_n l) E_n^+ - (2b_n^2 - k_2^2) \text{sh}(s_n l) P_n^+] \sin(b_n y), \quad (3.1e)$$

$$\sigma_{x+}^{\text{cent}}(l, y) = c_2^2 \left\{ -k_2^2 E_0^+ \cos(k_1 l) + (2k_1^2 - k_2^2) F_0^+ \cos(k_1 y) + \sum_{n=1}^{\infty} [(2b_n^2 - k_2^2) \text{ch}(p_n l) E_n^+ + 2b_n s_n \text{ch}(s_n l) P_n^+] \cos(b_n y) + \sum_{m=1}^{\infty} (-1)^m \times [(-2v_m^2 - k_2^2) F_m^+ \text{ch}(v_m y) + 2l_m w_m Q_m^+ \text{ch}(w_m y)] \right\}, \quad (3.1f)$$

$$\tau_{xy-}^{\text{cent}}(l, y) = c_2^2 \left\{ \sum_{n=1}^{\infty} [-2p_n b_n \text{ch}(p_n l) E_n^- - (2b_n^2 - k_2^2) \text{ch}(s_n l) P_n^-] \sin(b_n y) + \sum_{m=1}^{\infty} (-1)^m [2v_m l_m F_m^- \text{sh}(v_m y) + (2l_m^2 - k_2^2) Q_m^- \text{sh}(w_m y)] \right\}, \quad (3.1g)$$

$$\sigma_{x-}^{\text{cent}}(l, y) = c_2^2 \left\{ -k_2^2 E_0^- \sin(k_1 l) + \sum_{n=1}^{\infty} [(2b_n^2 - k_2^2) \text{sh}(p_n l) E_n^- + 2b_n s_n \text{sh}(s_n l) P_n^-] \cos b_n y \right\}, \quad (3.1h)$$

$$\tau_{xy+}^{\text{cent}}(x, \pm b) = \pm c_2^2 \sum_{n=1}^{\infty} [-2l_n v_n \text{sh}(v_n b) F_n^+ + (2l_n^2 - k_2^2) \text{sh}(w_n b) Q_n^+] \sin(l_n x), \quad (3.1i)$$

$$\tau_{xy-}^{\text{cent}}(x, \pm b) = \pm c_2^2 \sum_{n=1}^{\infty} [2l_n v_n \text{sh}(v_n b) F_n^- + (2l_n^2 - k_2^2) \text{sh}(w_n b) Q_n^-] \cos(l_n x) \mp c_2^2 Q_0^- k_1^2 \sin(k_1 b), \quad (3.1l)$$

$$u_{y+}^{\text{cent}}(x, b) = \sum_{n=1}^{\infty} [v_n \text{sh}(v_n b) F_n^+ - l_n \text{sh}(w_n b) Q_n^+] \cos(l_n x) - k_1 \sin(k_1 b) F_0^+, \quad (3.1m)$$

$$u_{y-}^{\text{cent}}(x, b) = \sum_{n=1}^{\infty} [v_n \text{sh}(v_n b) F_n^- + l_n \text{sh}(w_n b) Q_n^-] \sin(l_n x). \quad (3.1n)$$

From Eq. (2.11)<sub>2</sub>, in view of (3.1i,l), we get

$$-2l_n v_n \text{sh}(v_n b) F_n^+ + (2l_n^2 - k_2^2) \text{sh}(w_n b) Q_n^+ = 0, \quad (3.2a)$$

$$2l_n v_n \text{sh}(v_n b) F_n^- + (2l_n^2 - k_2^2) \text{sh}(w_n b) Q_n^- = 0, \quad (3.2b)$$

$$Q_0^- = 0. \quad (3.2c)$$

From Eqs. (2.16), in view of (3.1m,n), by simple integration over  $|x| < l$  we get

$$F_0^+ = \frac{-1}{2lk_1 \sin(k_1 b)} \int_{-l}^l g_u^+(\xi) d\xi \quad (3.3)$$

(and  $\int_{-l}^l g_u^-(\xi) d\xi = 0$ , that is obvious since  $g_u^-$  is odd), while by integration after multiplying (2.16)<sub>1</sub> by  $\cos l_m x$  and (2.16)<sub>2</sub> by  $\sin l_m x$  ( $m=1,2,\dots$ ), we get further, respectively (by orthogonality):

$$v_n \operatorname{sh}(v_n b) F_n^+ - l_n \operatorname{sh}(w_n b) Q_n^+ = \frac{1}{l} \int_{-l}^l g_u^+(\xi) \cos(l_n \xi) d\xi, \quad (3.4a)$$

$$v_n \operatorname{sh}(v_n b) F_n^- + l_n \operatorname{sh}(w_n b) Q_n^- = \frac{1}{l} \int_{-l}^l g_u^-(\xi) \sin(l_n \xi) d\xi. \quad (3.4b)$$

The following values can be easily deduced from (3.2a,b), (3.4):

$$F_n^+ = Q_n^+ \frac{(2l_n^2 - k_2^2) \operatorname{sh}(w_n b)}{2l_n v_n \operatorname{sh}(v_n b)} = -\frac{2l_n^2 - k_2^2}{lk_2^2 v_n \operatorname{sh}(v_n b)} \int_{-l}^l g_u^+(\xi) \cos(l_n \xi) d\xi, \quad (3.5a)$$

$$F_n^- = -Q_n^- \frac{(2l_n^2 - k_2^2) \operatorname{sh}(w_n b)}{2l_n v_n \operatorname{sh}(v_n b)} = -\frac{2l_n^2 - k_2^2}{lk_2^2 v_n \operatorname{sh}(v_n b)} \int_{-l}^l g_u^-(\xi) \sin(l_n \xi) d\xi. \quad (3.5b)$$

From Eqs. (2.12), in view of (3.1a,c), by integration over  $|y| < a$  we get  $\int_{-b}^b g_1^\tau(\eta) d\eta = 0$  (obvious) and  $-2ac_1^2 k_1^2 (1+R) = \int_{-b}^b g_1^\sigma(\eta) d\eta$ , whence:

$$R = -1 - \frac{1}{2ac_1^2 k_1^2} \int_{-b}^b g_1^\sigma(\eta) d\eta. \quad (3.6)$$

On repeating the integration after multiplying (2.12)<sub>1</sub> and (2.12)<sub>2</sub> by  $\sin a_m y$  and  $\cos a_m y$  ( $m=1,2,\dots$ ), respectively, we also get the following  $2 \times 2$  linear system (by orthogonality):

$$\begin{cases} -2q_n a_n A_n - (2a_n^2 - k_2^2) B_n = \frac{1}{ac_2^2} \int_{-b}^b g_1^\tau(\eta) \sin(a_n \eta) d\eta \\ (2a_n^2 - k_2^2) A_n + 2r_n a_n B_n = \frac{1}{ac_2^2} \int_{-b}^b g_1^\sigma(\eta) \cos(a_n \eta) d\eta \end{cases}$$

that gives

$$A_n = \frac{2r_n a_n}{ac_2^2 \Delta_n} \int_{-b}^b g_1^\tau(\eta) \sin(a_n \eta) d\eta + \frac{2a_n^2 - k_2^2}{ac_2^2 \Delta_n} \int_{-b}^b g_1^\sigma(\eta) \cos(a_n \eta) d\eta, \quad (3.7a)$$

$$B_n = -\frac{2a_n^2 - k_2^2}{ac_2^2 \Delta_n} \int_{-b}^b g_1^\tau(\eta) \sin(a_n \eta) d\eta - \frac{2a_n q_n}{ac_2^2 \Delta_n} \int_{-b}^b g_1^\sigma(\eta) \cos(a_n \eta) d\eta, \quad (3.7b)$$

where  $\Delta_n = (2a_n^2 - k_2^2)^2 - 4a_n^2 q_n r_n$  is the well-known Rayleigh function ([19]).

From Eqs. (2.13), by analogous procedure (in view of (3.1b,d)), we get  $\int_{-b}^b g_2^\tau(\eta) d\eta = 0$  and

$$T = -\frac{1}{2ac_1^2 k_1^2} \int_{-b}^b g_2^\sigma(\eta) d\eta, \quad (3.8)$$

$$C_n = -\frac{2r_n a_n}{ac_2^2 \Delta_n} \int_{-b}^b g_2^\tau(\eta) \sin(a_n \eta) d\eta + \frac{2a_n^2 - k_2^2}{ac_2^2 \Delta_n} \int_{-b}^b g_2^\sigma(\eta) \cos(a_n \eta) d\eta, \quad (3.9a)$$

$$D_n = -\frac{2a_n^2 - k_2^2}{ac_2^2 \Delta_n} \int_{-b}^b g_2^\tau(\eta) \sin(a_n \eta) d\eta + \frac{2a_n q_n}{ac_2^2 \Delta_n} \int_{-b}^b g_2^\sigma(\eta) \cos(a_n \eta) d\eta. \quad (3.9b)$$

From Eqs. (2.14) and (2.15), by difference and summation, respectively, we get

$$(g_2^\tau - g_1^\tau)(y) = 2\tau_{xy}^{\text{cent}}(l, y), \quad (g_1^\sigma + g_2^\sigma)(y) = 2\sigma_{x+}^{\text{cent}}(l, y), \quad |y| < b. \quad (3.10)$$

See Eqs. (3.1e,f): The first equation above involves constants  $E_n^+$  and  $P_n^+$ ; the second one, besides these and  $E_0^+$ , involves  $F_0^+$ ,  $F_n^+$ ,  $Q_n^+$ , which are known (in terms of  $g_u^+$ ) and can be substituted from Eqs. (3.3) and (3.5a). Made this, a simple integration of Eq. (3.10)<sub>2</sub> over  $|y| < b$  gives

$$E_0^+ = -\frac{1}{2bk_2^2 \cos(k_1 l)} \left[ \frac{1}{2c_2^2} \int_{-b}^b (g_1^\sigma + g_2^\sigma)(\eta) d\eta + \frac{2k_1^2 - k_2^2}{k_1 \sin(k_1 l)} \int_{-l}^l g_u^+(\xi) \cos(k_1 \xi) d\xi \right]. \quad (3.11)$$

Further, on multiplying Eqs. (3.10)<sub>1</sub> and (3.10)<sub>2</sub> by  $\sin b_m y$  and  $\cos b_m y$  ( $m, \nu=1,2,\dots$ ), respectively, and then integrating over  $|y| < b$ , we get the following  $2 \times 2$  linear system (by orthogonality):

$$\begin{cases} -2p_n b_n \operatorname{sh}(p_n l) E_n^+ - (2b_n^2 - k_2^2) \operatorname{sh}(s_n l) P_n^+ = \frac{1}{2bc_2^2} \int_{-b}^b (g_2^\tau - g_1^\tau)(\eta) \sin(b_n \eta) d\eta, \\ (2b_n^2 - k_2^2) \operatorname{ch}(p_n l) E_n^+ + 2s_n b_n \operatorname{ch}(s_n l) P_n^+ = \frac{1}{2bc_2^2} \int_{-b}^b (g_1^\sigma + g_2^\sigma)(\eta) \cos(b_n \eta) d\eta \\ + \frac{2(-1)^n}{bk_2^2} \int_{-l}^l g_u^+(\xi) \left[ \frac{(2b_n^2 - k_2^2)(-2p_n^2 - k_2^2)}{2p_n \operatorname{sh}(p_n l)} \operatorname{ch}(p_n \xi) + \frac{2b_n^2 s_n}{\operatorname{sh}(s_n l)} \operatorname{ch}(s_n \xi) \right] d\xi, \end{cases}$$

that gives

$$E_n^+ = \frac{s_n b_n \text{ch}(s_n l)}{\Pi_n^+ b c_2^2} \int_{-b}^b (g_2^\tau - g_1^\tau)(\eta) \sin(b_n \eta) d\eta + \frac{(2b_n^2 - k_2^2) \text{sh}(s_n l)}{\Pi_n^+} \left\{ \frac{1}{2b c_2^2} \int_{-b}^b (g_1^\sigma + g_2^\sigma)(\eta) \cos(b_n \eta) d\eta + \frac{2(-1)^n}{b k_2^2} \int_{-l}^l g_u^+(\xi) \left[ \frac{(2b_n^2 - k_2^2)(-2p_n^2 - k_2^2)}{2p_n \text{sh}(p_n l)} \text{ch}(p_n \xi) + \frac{2b_n^2 s_n}{\text{sh}(s_n l)} \text{ch}(s_n \xi) \right] d\xi \right\}, \quad (3.12a)$$

$$P_n^+ = -\frac{(2b_n^2 - k_2^2) \text{ch}(p_n l)}{\Pi_n^+ 2b c_2^2} \int_{-b}^b (g_2^\tau - g_1^\tau)(\eta) \sin(b_n \eta) d\eta - \frac{2p_n b_n \text{sh}(p_n l)}{\Pi_n^+} \left\{ \frac{1}{2b c_2^2} \int_{-b}^b (g_1^\sigma + g_2^\sigma)(\eta) \cos(b_n \eta) d\eta + \frac{2(-1)^n}{b k_2^2} \int_{-l}^l g_u^+(\xi) \left[ \frac{(2b_n^2 - k_2^2)(-2p_n^2 - k_2^2)}{2p_n \text{sh}(p_n l)} \text{ch}(p_n \xi) + \frac{2b_n^2 s_n}{\text{sh}(s_n l)} \text{ch}(s_n \xi) \right] d\xi \right\}, \quad (3.12b)$$

where we put

$$\prod_n^+ = (2b_n^2 - k_2^2)^2 \text{sh}(s_n l) \text{ch}(p_n l) - 4b_n^2 p_n s_n \text{sh}(p_n l) \text{ch}(s_n l).$$

To obtain formulas (3.11), (3.12) we used some results from series' tables:

$$\sum_{m=1}^{\infty} (-1)^m \frac{\cos(mx)}{b^2 m^2 + a^2} = \frac{1}{2} \left[ \frac{\pi}{ab} \frac{\text{ch}(ax/b)}{\text{sh}(\pi a/b)} - \frac{1}{a^2} \right], \quad (3.13)$$

$$\sum_{m=1}^{\infty} (-1)^m \cos(mx) = -1/2, \quad \sum_{m=1}^{\infty} (-1)^m m^2 \cos(mx) = 0,$$

and needed to calculate the following summations:

$$\sum_{m=1}^{\infty} (-1)^m \frac{-2v_m^2 - k_2^2}{v_m^2} (2l_m^2 - k_2^2) \cos(l_m \xi) = \frac{(2k_1^2 - k_2^2) k_2^2}{2} \left[ \frac{l}{k_1} \frac{\cos(k_1 \xi)}{\sin(k_1 l)} - \frac{1}{k_1^2} \right], \quad (3.14a)$$

$$\sum_{m=1}^{\infty} (-1)^m \frac{-2v_m^2 - k_2^2}{l_m^2 + p_n^2} (2l_m^2 - k_2^2) \cos(l_m \xi) = \frac{(2b_n^2 - k_2^2)(-2p_n^2 - k_2^2) l}{2p_n} \frac{\text{ch}(p_n \xi)}{\text{sh}(p_n l)} + \frac{(2k_1^2 - k_2^2) k_2^2}{2p_n^2}, \quad (3.14b)$$

$$\sum_{m=1}^{\infty} (-1)^m \frac{l_m^2 w_m^2}{l_m^2 + s_n^2} \cos(l_m \xi) = \frac{b_n^2 l s_n}{2} \frac{\text{ch}(s_n \xi)}{\text{sh}(s_n l)}.$$

Of course, the above results should be interpreted in the sense of *generalized summations* of the Abel-Poisson type ([20]).

There remains  $E_0^-$ ,  $E_n^-$ ,  $P_n^-$  to be calculated. Parallel to Eq. (3.10), by summation of Eqs. (2.14) and the difference of (2.15), we get, respectively

$$(g_1^\tau + g_2^\tau)(y) = 2\tau_{xy}^{\text{cent}}(l, y), \quad (g_2^\sigma - g_1^\sigma)(y) = 2\sigma_x^{\text{cent}}(l, y), \quad |y| < b. \quad (3.15)$$

In the first of these equations, the values for  $F_n^-$ ,  $Q_n^-$  (see Eq. (3.1g)) in terms of  $g_u^-$  can be substituted from Eqs. (3.5b). A simple integration of Eq. (3.15)<sub>2</sub> over  $|y| < b$  gives, in view of (3.1h)

$$E_0^- = \frac{-1}{4b c_2^2 k_2^2 \sin(k_1 l)} \int_{-b}^b (g_2^\sigma - g_1^\sigma)(\eta) d\eta, \quad (3.16)$$

while, on multiplying Eqs. (3.15)<sub>1</sub> and (3.15)<sub>2</sub> by  $\sin b_n y$  and  $\cos b_m y$  ( $v, m = 1, 2, \dots$ ), respectively, and integrating over  $|y| < b$ , we get the following  $2 \times 2$  linear system (by orthogonality):

$$\begin{cases} -2p_n b_n \text{ch}(p_n l) E_n^- - (2b_n^2 - k_2^2) \text{ch}(s_n l) P_n^- = \frac{1}{2b c_2^2} \int_{-b}^b (g_1^\tau + g_2^\tau)(\eta) \sin(b_n \eta) d\eta + \frac{2b_n(-1)^n}{b k_2^2} (2p_n^2 + k_2^2) \\ \quad \times \int_{-l}^l g_u^-(\xi) \left[ \frac{\text{sh}(s_n \xi)}{\text{sh}(s_n l)} - \frac{\text{sh}(p_n \xi)}{\text{sh}(p_n l)} \right] d\xi, \\ (2b_n^2 - k_2^2) \text{sh}(p_n l) E_n^- + 2s_n b_n \text{sh}(s_n l) P_n^- = \frac{1}{2b c_2^2} \int_{-b}^b (g_2^\sigma - g_1^\sigma)(\eta) \cos(b_n \eta) d\eta, \end{cases}$$

that gives

$$E_n^- = \frac{(2b_n^2 - k_2^2) \text{ch}(s_n l)}{2b c_2^2 \Pi_n^-} \int_{-b}^b (g_2^\sigma - g_1^\sigma)(\eta) \cos(b_n \eta) d\eta + \frac{2s_n b_n \text{sh}(s_n l)}{\Pi_n^-} \left\{ \frac{1}{2b c_2^2} \int_{-b}^b (g_1^\tau + g_2^\tau)(\eta) \sin(b_n \eta) d\eta + \frac{2b_n(-1)^n}{b k_2^2} (2p_n^2 + k_2^2) \int_{-l}^l g_u^-(\xi) \left[ \frac{\text{sh}(s_n \xi)}{\text{sh}(s_n l)} - \frac{\text{sh}(p_n \xi)}{\text{sh}(p_n l)} \right] d\xi \right\}, \quad (3.17a)$$

where we put

$$P_n^- = -\frac{2p_n b_n \text{ch}(p_n l)}{2b c_2^2 \Pi_n^-} \int_{-b}^b (g_2^\sigma - g_1^\sigma)(\eta) \cos(b_n \eta) d\eta - \frac{(2b_n^2 - k_2^2) \text{sh}(p_n l)}{\Pi_n^-} \left\{ \frac{1}{2b c_2^2} \int_{-b}^b (g_1^\tau + g_2^\tau)(\eta) \sin(b_n \eta) d\eta + \frac{2b_n(-1)^n}{b k_2^2} (2p_n^2 + k_2^2) \int_{-l}^l g_u^-(\xi) \left[ \frac{\text{sh}(s_n \xi)}{\text{sh}(s_n l)} - \frac{\text{sh}(p_n \xi)}{\text{sh}(p_n l)} \right] d\xi \right\}, \quad (3.17b)$$



$$\prod_n = (2b_n^2 - k_2^2)^2 \text{sh}(p_n l) \text{ch}(s_n l) - 4b_n^2 p_n s_n \text{sh}(s_n l) \text{ch}(p_n l).$$

To obtain formulas (3.17), we used these results from series' tables:

$$\sum_{m=1}^{\infty} (-1)^m \frac{m \sin(mx)}{b^2 m^2 + a^2} = -\frac{\pi}{2b^2} \frac{\text{sh}(ax/b)}{\text{sh}(\pi a/b)},$$

$$\sum_{m=1}^{\infty} (-1)^m m \sin(mx) = 0, \quad (3.18)$$

and needed to calculate the following summations (see the remark after Eqs. (3.14)):

$$\sum_{m=1}^{\infty} (-1)^m \frac{l_m (2l_m^2 - k_2^2)}{l_m^2 + p_n^2} \sin(l_m \xi) = \frac{l}{2} (2p_n^2 + k_2^2) \frac{\text{sh}(p_n \xi)}{\text{sh}(p_n l)},$$

$$\sum_{m=1}^{\infty} (-1)^m \frac{l_m (2l_m^2 - k_2^2)}{l_m^2 + s_n^2} \sin(l_m \xi) = \frac{l}{2} (2p_n^2 + k_2^2) \frac{\text{sh}(s_n \xi)}{\text{sh}(s_n l)}.$$

This derivation completes the aim of the present section.

#### 4 Reduction to Integral Equations

As field equations (along the edges of the central part of the layer), we will employ continuity assumptions for the displacement field between neighboring regions, namely

$$u_x^{\text{left}}(-l, y) = u_x^{\text{cent}}(-l, y), \quad u_x^{\text{right}}(l, y) = u_x^{\text{cent}}(l, y), \quad (4.1)$$

$$u_y^{\text{cent}}(-l, y) = u_y^{\text{cent}}(-l, y), \quad u_y^{\text{right}}(l, y) = u_y^{\text{cent}}(l, y), \quad |y| < b, \quad (4.2)$$

and the (traction-free) boundary condition (2.11)<sub>1</sub> as follows:

$$\sigma_{y+}^{\text{cent}}(x, b) = 0, \quad \sigma_{y-}^{\text{cent}}(x, b) = 0, \quad |x| < l. \quad (4.3)$$

Due to convenience for further calculations, we prefer to derive from these six equations two (disjoint) 3×3 systems of integral equations: one, involving the plus components (+) of the central fields, for the unknown functions  $(g_1^\sigma + g_2^\sigma)(y)$ ,  $(g_2^\tau - g_1^\tau)(y)$ ,  $g_u^+(x)$ , - and one, involving the minus components (-), for the unknown functions  $(g_2^\sigma - g_1^\sigma)(y)$ ,  $(g_1^\tau + g_2^\tau)(y)$ ,  $g_u^-(x)$ .

Then, by taking the difference of (4.1) and summation of (4.2), we get the following two equations, respectively,

$$u_x^{\text{right}}(l, y) - u_x^{\text{left}}(-l, y) = 2u_{x+}^{\text{cent}}(l, y), \quad (4.4)$$

$$u_y^{\text{right}}(l, y) + u_y^{\text{left}}(-l, y) = 2u_{y+}^{\text{cent}}(l, y), \quad (4.5)$$

which, in view of Eqs. (2.1), (2.3), (2.4), (2.7), (2.8), imply

$$\sum_{n=1}^{\infty} \{2[p_n \text{sh}(p_n l) E_n^+ + b_n \text{sh}(s_n l) P_n^+] \cos(b_n y) + [q_n (A_n + C_n) + a_n (B_n - D_n)] \cos(a_n y)\}$$

$$= ik_1 (T - 1 + R) (2k_1 \sin(k_1 l) E_0^+, \quad |y| < b, \quad (4.6)$$

$$\sum_{n=1}^{\infty} \{2[b_n \text{ch}(p_n l) E_n^+ + s_n \text{ch}(s_n l) P_n^+] \sin(b_n y) - [a_n (A_n + C_n) + r_n (B_n - D_n)] \sin(a_n y) - 2[F_n^+ v_n \text{sh}(v_n y) - Q_n^+ l_n \text{sh}(w_n y)] (-1)^n\} + 2k_1 F_0^+ \sin(k_1 y) = 0, \quad |y| < b. \quad (4.7)$$

From Eq. (4.3)<sub>1</sub>, in view of Eqs. (2.2c), (2.7), (2.8), we also get

$$\sum_{n=1}^{\infty} \{[(2l_n^2 - k_2^2) \text{ch}(v_n b) F_n^+ - 2w_n l_n \text{ch}(w_n b) Q_n^+] \times \cos(l_n x) - (-1)^n [(2p_n^2 + k_2^2) E_n^+ \text{ch}(p_n x) + 2s_n b_n P_n^+ \text{ch}(s_n x)]\} + (2k_1^2 - k_2^2) E_0^+ \cos(k_1 x) = k_2^2 F_0^+ \cos(k_1 b), \quad |x| < l. \quad (4.8)$$

Now, by substituting in the above three equations the values for all (capital) constants involved from the formulas of the previous section, we obtain the first 3×3 system of integral equations in the unknowns  $(g_1^\sigma + g_2^\sigma)$ ,  $(g_2^\tau - g_1^\tau)$ ,  $g_u^+$ , that can be written as follows:

$$\int_{-b}^b K_{11}^+(\eta - y) (g_1^\sigma + g_2^\sigma)(\eta) d\eta + \int_{-b}^b K_{12}^+(\eta - y) (g_2^\tau - g_1^\tau)(\eta) d\eta + \int_{-l}^l K_{13}^+(\xi, y) g_u^+(\xi) d\xi = -2ik_1, \quad |y| < b, \quad (4.9a)$$

$$\int_{-b}^b K_{21}^+(\eta - y) (g_1^\sigma + g_2^\sigma)(\eta) d\eta + \int_{-b}^b K_{22}^+(\eta - y) (g_2^\tau - g_1^\tau)(\eta) d\eta + \int_{-l}^l K_{23}^+(\xi, y) g_u^+(\xi) d\xi = 0, \quad |y| < b, \quad (4.10a)$$

$$\int_{-b}^b K_{31}^+(x, \eta) (g_1^\sigma + g_2^\sigma)(\eta) d\eta + \int_{-b}^b K_{32}^+(x, \eta) (g_2^\tau - g_1^\tau)(\eta) d\eta + \int_{-l}^l K_{33}^+(x, \xi) g_u^+(\xi) d\xi = 0, \quad |x| < l, \quad (4.11a)$$

if we define the kernels

$$K_{11}^+(y) = \frac{a \tan(k_1 l) + ib}{2abk_1 c_1^2} - \frac{k_2^2}{ac_2^2} \sum_{n=1}^{\infty} \frac{q_n}{\Delta_n} \cos(a_n y) - \frac{k_2^2}{bc_2^2} \sum_{n=1}^{\infty} \frac{p_n \text{sh}(p_n l) \text{sh}(s_n l)}{\Pi_n^+} \cos(b_n y), \quad (4.9b)$$

$$K_{12}^+(y) = \frac{1}{ac_2^2} \sum_{n=1}^{\infty} \frac{2a_n^2 - k_2^2 - 2q_n r_n}{\Delta_n} a_n \sin(a_n y) + \frac{1}{bc_2^2} \times \sum_{n=1}^{\infty} \frac{2s_n p_n \text{sh}(p_n l) \text{ch}(s_n l) - (2b_n^2 - k_2^2) \text{ch}(p_n l) \text{sh}(s_n l)}{\Pi_n^+} b_n \times \sin(b_n y), \quad (4.9c)$$

$$K_{13}^+(x, y) = \frac{2c_2^2 - c_1^2}{bc_1^2 \cos(k_1 l)} \cos(k_1 x) - \frac{4}{b} \sum_{n=1}^{\infty} \frac{p_n \text{sh}(p_n l) \text{sh}(s_n l)}{\Pi_n^+} (-1)^n \left[ \frac{2b_n^2 s_n}{\text{sh}(s_n l)} \text{ch}(s_n x) - \frac{(2b_n^2 - k_2^2)(2p_n^2 + k_2^2)}{2p_n \text{sh}(p_n l)} \text{ch}(p_n x) \right] \cos(b_n y), \quad (4.9d)$$

$$K_{21}^+(y) = K_{12}^+(y), \quad (4.10b)$$

$$K_{22}^+(y) = \frac{k_2^2}{bc_2^2} \sum_{n=1}^{\infty} \frac{s_n \text{ch}(p_n l) \text{ch}(s_n l)}{\Pi_n^+} \cos(b_n y) + \frac{k_2^2}{ac_2^2} \sum_{n=1}^{\infty} \frac{r_n}{\Delta_n} \cos(a_n y), \quad (4.10c)$$

$$K_{23}^+(x, y) = \frac{2}{lk_2^2} \sum_{n=1}^{\infty} \left[ \frac{2l_n^2 - k_2^2}{\text{sh}(v_n b)} \text{sh}(v_n y) - \frac{2l_n^2}{\text{sh}(w_n b)} \text{sh}(w_n y) \right] (-1)^n \cos(l_n x) - \frac{\sin(k_1 y)}{l \sin(k_1 b)}$$

$$- \frac{4}{bk_2^2} \sum_{n=1}^{\infty} \frac{2s_n p_n \text{sh}(p_n l) \text{ch}(s_n l) - (2b_n^2 - k_2^2) \text{ch}(p_n l) \text{sh}(s_n l)}{\Pi_n^+} \left[ \frac{2b_n^2 s_n}{\text{sh}(s_n l)} \text{ch}(s_n x) - \frac{(2b_n^2 - k_2^2)(2p_n^2 + k_2^2)}{2p_n \text{sh}(p_n l)} \text{ch}(p_n x) \right]$$

$$\times (-1)^n b_n \sin(b_n y), \quad (4.10d)$$

$$K_{31}^+(x, y) = -\frac{1}{4c_2^2} K_{13}^+(x, y), \quad (4.11b)$$

$$\sum_{n=1}^{\infty} \{2[b_n \text{sh}(p_n l) E_n^- + s_n \text{sh}(s_n l) P_n^-] \sin(b_n y) + [a_n(A_n - C_n) + r_n(B_n + D_n)] \sin(a_n y)\} = 0, \quad |y| < b; \quad (4.15)$$

$$K_{32}^+(x, y) = \frac{1}{bc_2^2} \sum_{n=1}^{\infty} \frac{(-1)^n}{\Pi_n^+} [(2b_n^2 - k_2^2) \text{ch}(p_n l) \text{ch}(s_n x) - (2p_n^2 + k_2^2) \text{ch}(s_n l) \text{ch}(p_n x)] s_n b_n \sin(b_n y), \quad (4.11c)$$

$$\sum_{n=1}^{\infty} \{[(2l_n^2 - k_2^2) \text{ch}(v_n b) F_n^- + 2w_n l_n \text{ch}(w_n b) Q_n^-] \sin(l_n x) - (-1)^n [(2p_n^2 + k_2^2) E_n^- \text{sh}(p_n x) + 2s_n b_n P_n^- \text{sh}(s_n x)] + (2k_1^2 - k_2^2) E_0^- \sin(k_1 x)\} = 0, \quad |x| < l. \quad (4.16)$$

$$K_{33}^+(x, \xi) = \frac{k_2 c_1}{2lc_2} \cot(k_1 b) - \frac{(2c_2^2 - c_1^2)^2 k_1}{bc_1^2 c_2^2 \sin(2k_1 l)} \cos[k_1(x - \xi)]$$

$$+ \frac{1}{lk_2^2} \sum_{n=1}^{\infty} \left[ 4l_n^2 w_n \text{cth}(w_n b) - \frac{(2l_n^2 - k_2^2)^2}{v_n} \text{cth}(v_n b) \right] \cos[l_n(x - \xi)]$$

$$+ \frac{2}{bk_2^2} \sum_{n=1}^{\infty} \frac{1}{\Pi_n^+} \left[ \frac{2b_n^2 s_n}{\text{sh}(s_n l)} \text{ch}(s_n \xi) - \frac{(2b_n^2 - k_2^2)(2p_n^2 + k_2^2)}{2p_n \text{sh}(p_n l)} \text{ch}(p_n \xi) \right]$$

$$\times [4b_n^2 p_n s_n \text{sh}(p_n l) \text{ch}(s_n x) - (2b_n^2 - k_2^2)(2p_n^2 + k_2^2) \text{sh}(s_n l) \text{ch}(p_n x)], \quad (4.11d)$$

and recall the evenness or oddness properties of functions  $g$ .

Parallely, by taking the summation of (4.1) and the difference of (4.2), we get, respectively,

$$u_x^{\text{right}}(l, y) + u_x^{\text{left}}(-l, y) = 2u_{x-}^{\text{cent}}(l, y), \quad (4.12)$$

$$u_y^{\text{right}}(l, y) - u_y^{\text{left}}(-l, y) = 2u_{y-}^{\text{cent}}(l, y), \quad (4.13)$$

which, together with Eq. (4.3)<sub>2</sub>, lead us to the following three equations:

$$\sum_{n=1}^{\infty} \{2[p_n \text{ch}(p_n l) E_n^- + b_n \text{ch}(s_n l) P_n^-] \cos(b_n y) - [q_n(A_n - C_n) + a_n(B_n + D_n)] \cos(a_n y) + 2[F_n^- l_n \text{ch}(v_n y) + Q_n^- w_n \text{ch}(w_n y)] (-1)^n\} = ik_1(T + 1 - R) - 2k_1 \cos(k_1 l) E_0^-, \quad |y| < b; \quad (4.14)$$

Substitution of the involved constants (as before) finally gives rise to the following  $3 \times 3$  system of integral equations in the unknowns  $(g_2^\sigma - g_1^\sigma)$ ,  $(g_1^\tau + g_2^\tau)$ ,  $g_u^-$ :

$$\int_{-b}^b K_{11}^-(\eta - y)(g_2^\sigma - g_1^\sigma)(\eta) d\eta + \int_{-b}^b K_{12}^-(\eta - y) \times (g_1^\tau + g_2^\tau)(\eta) d\eta + \int_{-l}^l K_{13}^-(\xi, y) g_u^-(\xi) d\xi = 2ik_1, \quad |y| < b, \quad (4.17a)$$

$$\int_{-b}^b K_{21}^-(\eta - y)(g_2^\sigma - g_1^\sigma)(\eta) d\eta + \int_{-b}^b K_{22}^-(\eta - y)(g_1^\tau + g_2^\tau)(\eta) d\eta + \int_{-l}^l K_{23}^-(\xi, y) g_u^-(\xi) d\xi = 0, \quad |y| < b, \quad (4.18a)$$

$$\int_{-b}^b K_{31}^-(x, \eta)(g_2^\sigma - g_1^\sigma)(\eta) d\eta + \int_{-b}^b K_{32}^-(x, \eta)(g_1^\tau + g_2^\tau)(\eta) d\eta + \int_{-l}^l K_{33}^-(x, \xi) g_u^-(\xi) d\xi = 0, \quad |x| < l, \quad (4.19a)$$

where we put

$$K_{11}^-(y) = \frac{ib - a \cot(k_1 l)}{2abk_1 c_1^2} - \frac{k_2^2}{ac_2^2} \sum_{n=1}^{\infty} \frac{q_n}{\Delta_n} \cos(a_n y) - \frac{k_2^2}{bc_2^2} \sum_{n=1}^{\infty} \frac{p_n \text{ch}(p_n l) \text{ch}(s_n l)}{\Pi_n^-} \cos(b_n y), \quad (4.17b)$$

$$K_{12}^-(y) = \frac{1}{ac_2^2} \sum_{n=1}^{\infty} \frac{2a_n^2 - k_2^2 - 2q_n r_n}{\Delta_n} a_n \sin(a_n y) + \frac{1}{bc_2^2} \sum_{n=1}^{\infty} \frac{2s_n p_n \operatorname{ch}(p_n l) \operatorname{sh}(s_n l) - (2b_n^2 - k_2^2) \operatorname{ch}(s_n l) \operatorname{sh}(p_n l)}{\Pi_n^-} b_n \sin(b_n y), \quad (4.17c)$$

$$K_{13}^-(x, y) = \frac{4}{bk_2^2} \sum_{n=1}^{\infty} (2p_n^2 + k_2^2) \left[ \frac{\operatorname{sh}(s_n x)}{\operatorname{sh}(s_n l)} - \frac{\operatorname{sh}(p_n x)}{\operatorname{sh}(p_n l)} \right] b_n^2 \cos(b_n y) \frac{2s_n p_n \operatorname{sh}(s_n l) \operatorname{ch}(p_n l) - (2b_n^2 - k_2^2) \operatorname{ch}(s_n l) \operatorname{sh}(p_n l)}{\Pi_n^-} (-1)^n \\ + \frac{2}{lk_2^2} \sum_{n=1}^{\infty} \left[ \frac{2w_n \operatorname{ch}(w_n y)}{\operatorname{sh}(w_n b)} - \frac{(2l_n^2 - k_2^2) \operatorname{ch}(v_n y)}{v_n \operatorname{sh}(v_n b)} \right] (-1)^n l_n \sin(l_n x), \quad (4.17d)$$

$$K_{21}^-(y) = K_{12}^-(y), \quad (4.18b)$$

$$K_{22}^-(y) = \frac{k_2^2}{bc_2^2} \sum_{n=1}^{\infty} \frac{\operatorname{sh}(p_n l) \operatorname{sh}(s_n l) s_n}{\Pi_n^-} \cos(b_n y) \\ + \frac{k_2^2}{ac_2^2} \sum_{n=1}^{\infty} \frac{r_n}{\Delta_n} \cos(a_n y), \quad (4.18c)$$

$$K_{23}^-(x, y) = \frac{4}{b} \sum_{n=1}^{\infty} (-1)^n \frac{(2p_n^2 + k_2^2)}{\Pi_n^-} [\operatorname{sh}(p_n l) \operatorname{sh}(s_n x) \\ - \operatorname{sh}(s_n l) \operatorname{sh}(p_n x)] s_n b_n \sin(b_n y), \quad (4.18d)$$

$$K_{31}^-(x, y) = \frac{1}{2bc_2^2} \sum_{n=1}^{\infty} \frac{(-1)^n}{\Pi_n^-} [4b_n^2 p_n s_n \operatorname{ch}(p_n l) \operatorname{sh}(s_n x) \\ - (2b_n^2 - k_2^2)(2p_n^2 + k_2^2) \operatorname{ch}(s_n l) \operatorname{sh}(p_n x)] \cos(b_n y) \\ - \frac{2c_2^2 - c_1^2}{4bc_2^2 c_1^2} \sin(k_1 x), \quad (4.19b)$$

$$K_{32}^-(x, y) = \frac{1}{bc_2^2} \sum_{n=1}^{\infty} \frac{(-1)^n}{\Pi_n^-} [(2b_n^2 - k_2^2) \operatorname{sh}(p_n l) \operatorname{sh}(s_n x) \\ - (2p_n^2 + k_2^2) \operatorname{sh}(s_n l) \operatorname{sh}(p_n x)] s_n b_n \sin(b_n y), \quad (4.19c)$$

$$K_{33}^-(x, \xi) = \frac{4}{bk_2^2} \sum_{n=1}^{\infty} \frac{b_n^2 s_n}{\Pi_n^-} [(2b_n^2 - k_2^2)(2p_n^2 + k_2^2) \operatorname{sh}(p_n l) \operatorname{sh}(s_n x) \\ - (2p_n^2 + k_2^2)^2 \operatorname{sh}(s_n l) \operatorname{sh}(p_n x)] \left[ \frac{\operatorname{sh}(s_n \xi)}{\operatorname{sh}(s_n l)} - \frac{\operatorname{sh}(p_n \xi)}{\operatorname{sh}(p_n l)} \right] \\ + \frac{1}{lk_2^2} \sum_{n=1}^{\infty} \left[ 4l_n^2 w_n \operatorname{cth}(w_n b) \right. \\ \left. - \frac{(2l_n^2 - k_2^2)^2}{v_n} \operatorname{cth}(v_n b) \right] \cos[l_n(x - \xi)]. \quad (4.19d)$$

Once given a solution to the above systems, the scattered fields would directly follow from the equations of Sections 2 and 3; note this in particular for the reflection and transmission coefficients given by Eqs. (3.6) and (3.8), respectively.

In this connection, we conclude the analytical development by applying a standard *low-frequency* approximation to the integral systems in order to derive formulas for the quoted coefficients in which the dependence on frequency appears explicitly. To this aim, we can consider only Eqs. (4.9) and (4.17) (that are related to the continuity of  $u_x$  through the borderlines  $x = \pm l$ ), and in them we keep as main asymptotic terms the first fraction of  $K_{11}^+$  for Eq. (4.9), and the first fraction of  $K_{11}^-$  for Eq. (4.17) (see Eqs. (4.9b), (4.17b)). Thus, Eqs. (4.9), (4.17) attain the following simple forms:

$$\int_{-b}^b (g_1^\sigma + g_2^\sigma)(\eta) d\eta = -2ik_1 \frac{2abk_1 c_1^2}{a \tan(k_1 l) + ib}, \quad (4.20a)$$

$$\int_{-b}^b (g_2^\sigma - g_1^\sigma)(\eta) d\eta = 2ik_1 \frac{2abk_1 c_1^2}{ib - a \cot(k_1 l)}, \quad (4.20b)$$

from which, by Eqs. (3.6), (3.8) the searched (explicit) formulas for the low-frequency approximation are easily derived:

$$R = \frac{b^2 - a^2}{a^2 + b^2 + 2iab \cot(2k_1 l)},$$

$$T = \frac{2iab}{(a^2 + b^2) \sin(2k_1 l) + 2iab \cos(2k_1 l)}. \quad (4.21)$$

## 5 Numerical Analysis and Physical Remarks

In order to investigate the wave properties of the structure in concern with respect to the involved geometrical and physical parameters, we have developed a direct numerical algorithm for solving the two (disjoint) systems of integral Eqs. (4.9), (4.10), (4.11) and (4.17), (4.18), (4.19). This algorithm is based upon the classical *co-location* technique of the *Boundary Element Methods* (see [21]). We have focused our attention to formulas (3.6) and (3.8) for the reflection and transmission coefficients, respectively, and along all computations we have always verified that the *balance of rates of energies* ([19])

$$|R|^2 + |T|^2 = 1 \quad (5.1)$$

actually holds; that is what is commonly made to control the precision of some numerical results (cf. [1–5]). Note that formulas (4.21) for the low-frequency case identically satisfy this balance. The elastic material taken into account is the *aluminum*: for it,  $c_1 = 6200$  m/s and  $c_2 = 3080$  m/s.

First of all, we have studied the influence on the reflection properties of the physical variables  $(g_1^\sigma \pm g_2^\sigma)(y)$ ,  $(g_1^\tau \mp g_2^\tau)(y)$ ,  $g_u^\pm(x)$ , which represent the normal and tangential stresses along the borderlines  $x = \pm l$ , and the amplitude of the normal vibration along the traction-free surface  $y = b$ . A typical example of the computations is shown in Fig. 2, where the behavior of the reflection coefficient versus the frequency parameter is displayed for a particular (square) geometry ( $l/a = b/a = 0.5$ ). Line 1 is related to the exact solution of the two  $3 \times 3$  systems, which amounts to a full consideration of all the quoted variables, while line 2 and line 3 are obtained by assuming  $g_u^\pm \approx 0$  and  $g_1^\tau, g_2^\tau, g_u^\pm \approx 0$ , respectively. To neglect the normal vibration along  $y = b$  requires of course not to consider the field equations originating from the traction-free boundary conditions (4.3), so that the second case is treated by solving only the two  $2 \times 2$  systems (4.9), (4.10), and (4.17), (4.18) with  $g_u^\pm = 0$ . Analogously, to neglect the tangential stresses along  $x = \pm l$  requires not to consider the field equations originating from the continuity conditions (4.2) on the vertical component of the displacement, so that the third case is treated by solving only the two equations (4.9), (4.17) with  $g_1^\tau, g_2^\tau, g_u^\pm = 0$ .

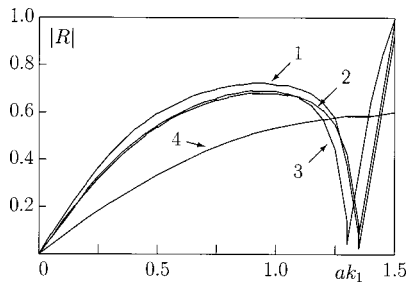


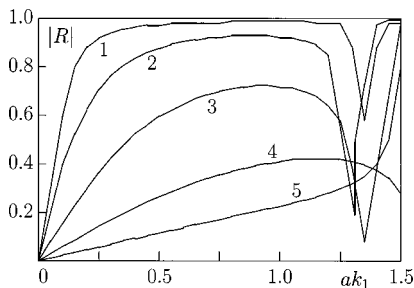
**Fig. 2 Reflection coefficient  $|R|$  versus frequency parameter  $ak_1$  ( $c_2/c_1=0.497$ ,  $b/a=l/a=0.5$ ). Line 1: exact solution (from  $3\times 3$  systems (4.9), (4.10), (4.11), (4.17), (4.18), (4.19)); line 2: approximated solution  $g_u^\pm \approx 0$  (from  $2\times 2$  systems (4.9), (4.10), (4.17), (4.18)); line 3: approximated solution  $g_u^\pm, g_{1,2}^\pm \approx 0$  (from Eqs. (4.9), (4.17)); line 4; low-frequency approximation (from formula (4.21)).**

Recall that such equations are related to the continuity conditions (4.1) on the horizontal component of the displacement.

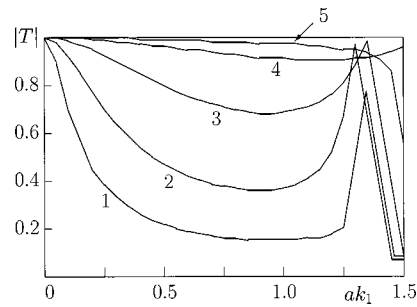
We can observe that line 2 is very close to line 1, that means a weak influence of functions  $g_u^\pm$  (i.e., of normal vibration) on the reflection properties; line 3 is less close to line 1, and this implies a slightly greater, but not significant, influence of functions  $g_1^\pm$  and  $g_2^\pm$  (i.e., of tangential stresses).

Figure 2 also shows an interesting feature of the structure, namely the existence of a (short) range of frequency in which the reflection coefficient is very small; this means that the considered structure admits a *passing band* of frequencies around the value  $ak_1 \approx 1.3$ , very close to the end of the one-mode interval (actually,  $ak_1 = ak_2 c_2/c_1 \approx 0.5ak_2 < 0.5\pi \approx 1.5$ ). For comparison, we have also reported, as line 4, the graph of the function  $|R|$  versus  $ak_1$  from Eq. (4.21): it is evident that it is a rough precision of the classical low-frequency approximation even for a small frequency.

In Fig. 3 the behavior of  $|R|$  versus the frequency parameter is again displayed from an exact solution of the full  $3\times 3$  systems, but for different values of the relative opening  $b/a$  ( $l/a=0.5$ ). Besides the general remark that an arbitrary (periodic) structure of obstacles cannot provide any wave reflection in the limit of vanishing frequency, we can first observe that “closed” structures suddenly attenuate the transmission as soon as frequency begins to increase (see the great initial slopes of lines 1 and 2), and keep quasi-locked the waveguide for greater frequencies. Reflection properties generally increase with increasing frequency and obstacles; however, this figure shows that even for very small openings there are still sharp peaks, with a sudden decrease of the reflection, just in the neighborhood of the same critical value  $ak_1 \approx 1.3$ . The existence of such a passing band seems to be excluded for lines 4 and 5, depicting larger and larger openings (however, in the first case, it could be located just out of the



**Fig. 3 Reflection coefficient  $|R|$  versus frequency parameter  $ak_1$  ( $c_2/c_1=0.497$ ,  $l/a=0.5$ ). Line 1:  $b/a=0.1$ ; line 2:  $b/a=0.25$ ; line 3:  $b/a=0.5$ ; line 4:  $b/a=0.75$ ; line 5:  $b/a=0.9$ .**



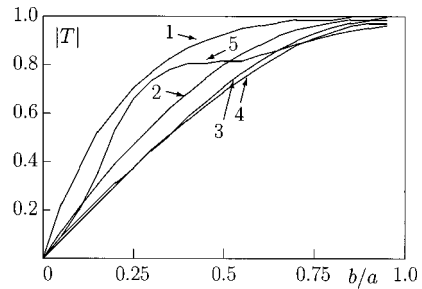
**Fig. 4 Transmission coefficient  $|T|$  versus frequency parameter  $ak_1$  ( $c_2/c_1=0.497$ ,  $l/a=0.5$ ). Line 1:  $b/a=0.1$ ; line 2:  $b/a=0.25$ ; line 3:  $b/a=0.5$ ; line 4:  $b/a=0.75$ ; line 5:  $b/a=0.9$ .**

one-mode regime; in the second case, due to the smallness of the obstacle, one would actually expect a more smooth behavior of the reflection properties).

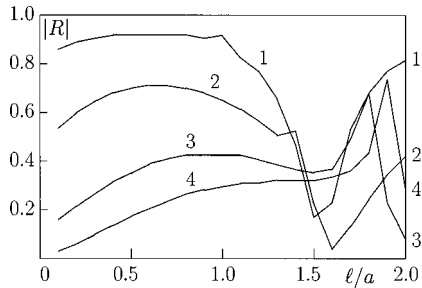
Anyway, we note that, perhaps excluding line 4, the reflection coefficient tends to the maximum value when the frequency approaches the end of the one-mode regime even for a limited wide opening; in fact, the limiting case  $b/a=1$  does not imply the absence of obstacles at all, since in every case there remains a periodic array of slit-type cracks parallel to the direction of the incident longitudinal wave. The free crack faces cannot sustain the normal stress  $\sigma_y$  (which obviously is not trivial), and therefore the wavefield is quite different from what it would be in a noncracked medium.

Figure 4 merely repeats the contents of Fig. 3, but making reference to the transmission coefficient; a good satisfaction of Eq. (5.1) is evident.

The remaining figures also are related to exact solutions of the full systems. Figure 5 shows the behavior of the transmission coefficient with respect to the relative opening  $b/a$ , for different values of frequency ( $l/a=0.5$ ). For not high frequencies, one



**Fig. 5 Transmission coefficient  $|T|$  versus relative opening  $b/a$  ( $c_2/c_1=0.497$ ,  $l/a=0.5$ ). Line 1:  $ak_1=0.25$ ; line 2:  $ak_1=0.5$ ; line 3:  $ak_1=0.75$ ; line 4:  $ak_1=1.0$ ; line 5:  $ak_1=1.25$ .**



**Fig. 6 Reflection coefficient  $|R|$  versus relative length of rectangles  $l/a$  ( $c_2/c_1=0.497$ ,  $ak_1=0.75$ ). Line 1:  $b/a=0.25$ ; line 2:  $b/a=0.5$ ; line 3:  $b/a=0.75$ ; line 4:  $b/a=0.9$ .**

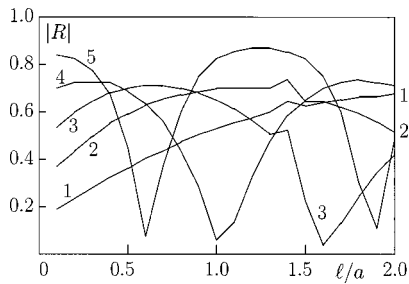


**Fig. 7 Reflection coefficient  $|R|$  versus relative length of rectangles  $l/a$  ( $c_2/c_1=0.497$ ,  $b/a=0.5$ ). Line 1:  $ak_1=0.25$ ; line 2:  $ak_1=0.5$ ; line 3:  $ak_1=0.75$ ; line 4:  $ak_1=1.0$ ; line 5:  $ak_1=1.25$ .**

would expect a (monotonic) increase of the transmission properties with the opening increasing, and this is actually reflected in lines 1–4. For higher frequencies, the response of the structure on the incident wave becomes more complex, and this probably explains the nonmonotonic behavior of line 5.

Finally, Figs. 6 and 7 display the influence on the reflection coefficient of the relative length of the obstacles. Note that the values of the physical and geometrical parameters involved are such that, in the one-mode regime, the longitudinal wavelength  $\lambda_1=2\pi/k_1$  keeps always greater than  $2l$  (of course, it holds throughout  $\lambda_2>2a\geq 2b$ ). In Fig. 6 we have four lines for different values of the opening  $b/a$  and a fixed frequency; unexpectedly, the behavior is nonmonotonic: in fact, lines 1 and 2, reflecting a more closed structure, point out a short range of the length in which the reflection properties suddenly decrease; and lines 3 and 4 show an opposite property. However, exceeding some critical values of  $l/a$ , the reflection coefficient seems to become again smaller for larger openings. In Fig. 7 there are five lines for different values of the frequency and a fixed opening. Some similar remarks as above also apply to this figure; it is worth noting that higher frequencies appear to imply a periodic behavior of  $|R|$  versus  $l/a$ .

## Acknowledgment

This paper has been written under the auspices of G.N.F.M. of the Italian I.N.D.A.M.

## References

- [1] Achenbach, J. D., and Kitahara, M., 1987, "Harmonic Waves in a Solid With a Periodic Distribution of Spherical Cavities," *J. Acoust. Soc. Am.*, **81**, pp. 595–599.
- [2] Angel, Y. C., and Achenbach, J. D., 1987, "Harmonic Waves in an Elastic Solid Containing a Doubly Periodic Array of Cracks," *Wave Motion*, **9**, pp. 377–385.
- [3] Achenbach, J. D., and Li, Z. L., 1986, "Reflection and Transmission of Scalar Waves by a Periodic Array of Screens," *Wave Motion*, **8**, pp. 225–234.
- [4] Angel, Y. C., and Achenbach, J. D., 1985, "Reflection and Transmission of Elastic Waves by a Periodic Array of Cracks," *ASME J. Appl. Mech.*, **52**, pp. 33–41.
- [5] Achenbach, J. D., and Li, Z. L., 1986, "Propagation of Horizontally Polarized Transverse Waves in a Solid With a Periodic Distribution of Cracks," *Wave Motion*, **8**, pp. 371–379.
- [6] Malin, V. V., 1963, "Theory of Strip Grating of Finite Period," *Radio Eng. Electron. Phys.*, **8**, pp. 185–193.
- [7] Jones, D. S., 1986, *Acoustic and Electromagnetic Waves*, Clarendon Press, Oxford.
- [8] Collin, R. E., 1991, *Field Theory of Guided Waves*, 2nd Ed., IEEE Press, New York.
- [9] Lewin, L., 1975, *Theory of Waveguides*, Butterworth, London.
- [10] Twersky, V., 1986, "On the Scattering of Waves by an Infinite Grating," *IEEE Trans. Antennas Propag.*, **4**, pp. 330–345.
- [11] Miles, J. W., 1982, "On Rayleigh Scattering by a Grating," *Wave Motion*, **4**, pp. 285–292.
- [12] Scarpetta, E., and Sumbatyan, M. A., 1995, "Explicit Analytical Results for One-Mode Normal Reflection and Transmission by a Periodic Array of Screens," *J. Math. Anal. Appl.*, **195**, pp. 736–749.
- [13] Scarpetta, E., and Sumbatyan, M. A., 1996, "Explicit Analytical Results for One-Mode Oblique Penetration Into a Periodic Array of Screens," *IMA J. Appl. Math.*, **56**, pp. 109–120.
- [14] Scarpetta, E., and Sumbatyan, M. A., 1997, "On Wave Propagation in Elastic Solids With a Doubly Periodic Array of Cracks," *Wave Motion*, **25**, pp. 61–72.
- [15] Scarpetta, E., and Sumbatyan, M. A., 2000, "On the Oblique Wave Penetration in Elastic Solids With a Doubly Periodic Array of Cracks," *Q. Appl. Math.*, **58**, pp. 239–250.
- [16] Scarpetta, E., and Sumbatyan, M. A., "Wave Penetration Through Elastic Solids With a Periodic Array of Rectangular Flaws," *MECCANICA*, in press.
- [17] Shenderov, Ye. L., 1970, "Propagation of Sound Through a Screen of Arbitrary Wave Thickness With Gaps," *Sov. Phys. Acoust.*, **16**, No. 1.
- [18] Solokin, N. V., and Sumbatyan, M. A., 1994, "Artificial Layer," *Res. Nondestruct. Eval.*, **6**, pp. 19–34.
- [19] Achenbach, J. D., 1973, *Wave Propagation in Elastic Solids*, North-Holland, Amsterdam.
- [20] Gel'fand, L. M., and Shilov, G. E., 1964, *Generalized Functions*, Vol. 1, Academic Press, San Diego.
- [21] Banerjee, P. K., and Butterfield, R., 1981, *Boundary Element Methods in Engineering Sciences*, McGraw-Hill, New York.



# Low Reynolds Number Slip Flow in a Curved Rectangular Duct

C. Y. Wang

Professor,  
Departments of Mathematics and  
Mechanical Engineering,  
Michigan State University,  
East Lansing, MI 48824  
Mem. ASME

*The radially symmetric, steady, slow viscous slip flow through a curved duct of rectangular cross section is studied. The Stokes equation is solved using eigenfunction expansions and Navier's slip condition. As slip is increased, the location of the maximum velocity moves from near center to the outer wall. The minimum velocity occurs at the inside corners. It is found that both slip and curvature promote the flow rate but not necessarily the mean velocity. [DOI: 10.1115/1.1445142]*

## Introduction

The flow in a curved duct is a fundamental fluid dynamic problem studied by numerous authors (e.g. [1]). Invariably the no-slip condition between the fluid and the duct wall is assumed. However, there are cases where partial slip does occur and the no-slip condition must be relaxed. The fluoroplastic covering, such as Teflon, resists adhesion. Some surfaces are coated with a thin layer of another fluid, be it a lubricant, mucous, or injectant. Some surfaces are rough or porous which are modelled by a smooth surface with some equivalent slip. Lastly, the fluid may be particulate. As a whole it behaves as a continuum, but on a solid boundary slip may occur. Examples include blood flow in moderately small vessels, where near the boundary the blood is red-cell free. Also there is a hydrodynamic slip regime for rarefied gasses when the Knudsen number is nonzero but small ([2]).

In all of these partial slip cases, the bulk of the fluid may be regarded as Newtonian and the no-slip condition is supplanted by the leading order expansion relating slip with the shear stress

$$u' = N \frac{\partial u'}{\partial n} \quad (1)$$

where  $u'$  is the tangential velocity,  $n$  is the normal direction to the surface pointing into the fluid, and  $N > 0$  is the slip coefficient. The condition Eq. (1) has been attributed to Beavers and Joseph, but it is more appropriately called the Navier condition since Navier [3] had proposed it a century earlier. If  $N = 0$ , it is the same as the no-slip condition and if  $N$  is infinite, it is a stress-free condition.

Although the Navier condition seems to be a simple extension of the classical no-slip condition, due to its inherent difficulty, analytic solutions are rare. The only known fundamental geometries which yield analytic partial-slip flow solutions are the Stokes flow past a sphere ([4]), parallel flows in a circular tube, parallel plates, annular, and rectangular ducts ([5]). The literature to date considered either these geometries or perturbations of these geometries. The present paper studies a new fundamental geometry which describes slip flow in a curved rectangular duct. We shall obtain analytic solutions for low Reynolds numbers which is true for most aforementioned applications. Since the Reynolds number is very small, nonlinear terms such as inertial or centrifugal forces are absent.

Contributed by the Applied Mechanics Division of THE AMERICAN SOCIETY OF MECHANICAL ENGINEERS for publication in the ASME JOURNAL OF APPLIED MECHANICS. Manuscript received by the ASME Applied Mechanics Division, Apr. 16, 2001; final revision, Sept. 6, 2001. Associate Editor: D. A. Siginer. Discussion on the paper should be addressed to the Editor, Professor Lewis T. Wheeler, Department of Mechanical Engineering, University of Houston, Houston, TX 77204-4792, and will be accepted until four months after final publication of the paper itself in the ASME JOURNAL OF APPLIED MECHANICS.

## Solution

Figure 1 shows the cross section of the rectangular duct whose centerline has a radius of curvature of  $R$ . The duct has dimensions  $2aR$  in width and  $2bR$  in height. Fully developed flow is assumed, since for low Reynolds numbers the entrance length is limited to one width. Thus the present results also apply to a finite section of a curved duct, connected by straight ducts. The governing equation is the Stokes equation

$$v_{rr} + \frac{1}{r} v_r - \frac{v}{r^2} + v_{zz} = -\frac{1}{r} \quad (2)$$

where  $v$  is the azimuthal velocity normalized by the pressure gradient factor  $(-Rp_\theta/\mu)$ ,  $(r, \theta, z)$  are cylindrical coordinates normalized by  $R$  and  $\mu$  is the viscosity. The pressure gradient  $p_\theta$  is constant due to azimuthal symmetry and is negative if the  $\theta$ -direction velocity  $v$  is to be positive. For Stokes flow the other velocity components and the other momentum equations are identically zero. The boundary conditions are the Navier condition Eq. (1) applied to the four walls.

Due to symmetry about  $z = 0$ , the solution of Eq. (2) can be expressed in terms of the even infinite series

$$v(r, z) = \sum_{n=1}^{\infty} f_n(r) \cos(\beta_n z) \quad (3)$$

where  $\beta_n$  is an eigenvalue. The slip boundary condition on  $z = b$  is

$$v(r, b) = -\bar{\mu} \frac{\partial v}{\partial z}(r, b) \quad (4)$$

where  $\bar{\mu} \equiv N/R$  is a nondimensional parameter representing the importance of slip. Since Eq. (3) is even, the boundary condition at  $z = -b$  is automatically satisfied. Equation (4) yields the eigenvalue relation

$$\cos \alpha_n = \lambda \alpha_n \sin \alpha_n \quad (5)$$

Here  $\alpha_n \equiv b\beta_n$  and  $\lambda \equiv \bar{\mu}/b$ . Equation (5) is solved in the Appendix for given  $\lambda$ . One can show that the eigenfunctions  $\cos(\beta_n z)$  are complete and orthogonal in  $[0, b]$ . In order to take into account the nonhomogeneous term in Eq. (2), we can make an even extension of unity in  $[0, b]$ , and construct the even Fourier series

$$1 = \sum_{n=1}^{\infty} A_n \cos(\beta_n z) \quad (6)$$

where the Fourier coefficients  $A_n$  can be inverted by multiplying  $\cos(\beta_n z)$  and integrating from 0 to  $b$ ,

$$A_n = \frac{2 \sin \alpha_n}{\alpha_n + \sin \alpha_n \cos \alpha_n} \quad (7)$$

Equation (2) then reduces to

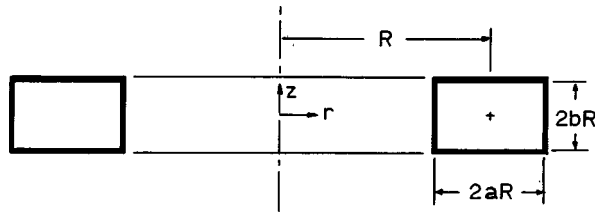


Fig. 1 Cross section of the curved rectangular duct

$$f_n''(r) + \frac{1}{r} f_n' - \left( \beta_n^2 + \frac{1}{r^2} \right) f_n = -\frac{A_n}{r} \quad (8)$$

The solution is

$$f_n(r) = \frac{A_n}{\beta_n^2 r} + C_{1n} K_1(\beta_n r) + C_{2n} I_1(\beta_n r) \quad (9)$$

where  $K$  and  $I$  are modified Bessel functions. The constants  $C_{1n}$  and  $C_{2n}$  are determined from the slip conditions

$$f_n = \bar{\mu}(f_n' - f_n/r) \text{ on } r = 1 - a \quad (10)$$

$$f_n = -\bar{\mu}(f_n' - f_n/r) \text{ on } r = 1 + a \quad (11)$$

where  $(f' - f/r)$  is the appropriate form for the shear stress on a radial surface. With the aid of a computer with symbolic capabilities we find

$$C_{1n} = 2A_n \left[ a - 1 - 2\bar{\mu} + \frac{2(a^2 - 1)L_1}{(1 + a)^2 L_2} \right] / L_3 \quad (12)$$

$$C_{2n} = \frac{2A_n L_4}{(1 - a^2)\beta_n^2 L_5} \quad (13)$$

where

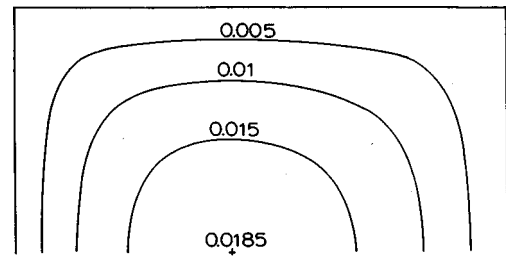
$$L_1 = 2(a^2 - 1) \left[ \left( 1 - \frac{\bar{\mu}}{a - 1} \right) I_1^- - \frac{\beta_n \bar{\mu}}{2} (I_0^- + I_2^-) \right] \\ \times \{ (1 + a)(a - 1 - 2\bar{\mu})[2(1 + a - \bar{\mu})K_1^+ \\ - (1 + a)\beta_n \bar{\mu}(K_0^+ + K_2^+)] + (a - 1)(1 + a - 2\bar{\mu}) \\ \times [2(a - 1 - \bar{\mu})K_1^- + (a - 1)\beta_n \bar{\mu}(K_0^- + K_2^-)] \} \quad (14)$$

$$L_2 = [2(1 + a + \bar{\mu})I_1^- + (a - 1)\beta_n \bar{\mu}(I_0^- + I_2^-)][2(1 + a - \bar{\mu})K_1^+ \\ - (1 + a)\beta_n \bar{\mu}(K_0^+ + K_2^+)] \\ + [2(1 + a - \bar{\mu})I_1^+ + (1 + a)\beta_n \bar{\mu}(I_0^+ + I_2^+)] \\ \times [2(a - 1 - \bar{\mu})K_1^- + (a - 1)\beta_n \bar{\mu}(K_0^- + K_2^-)] \quad (15)$$

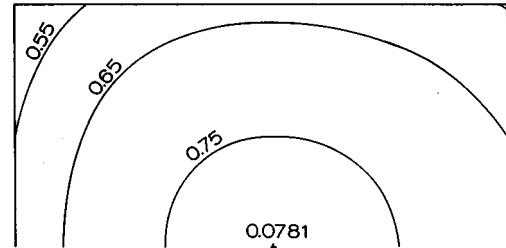
$$L_3 = (a - 1)\beta_n^2 [2(a - 1 - \bar{\mu})K_1^- + (a - 1)\beta_n \bar{\mu}(K_0^- + K_2^-)] \quad (16)$$

$$L_4 = (1 + a)(a - 1 - 2\bar{\mu})[2(1 + a - \bar{\mu})K_1^+ - (1 + a)\beta_n \bar{\mu}(K_0^+ \\ + K_2^+)] + (a - 1)(1 + a - 2\bar{\mu})[2(a - 1 - \bar{\mu})K_1^- \\ + (a - 1)\beta_n \bar{\mu}(K_0^- + K_2^-)] \quad (17)$$

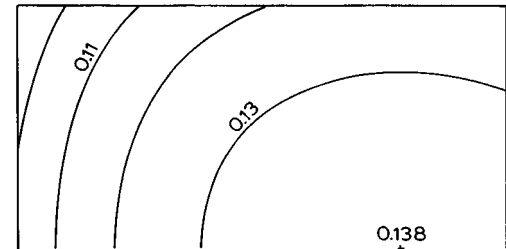
$$L_5 = [2(1 + a + \bar{\mu})I_1^- + (a - 1)\beta_n \bar{\mu}(I_0^- + I_2^-)][2(1 + a - \bar{\mu})K_1^+ \\ - (1 + a)\beta_n \bar{\mu}(K_0^+ + K_2^+)] + [2(1 + a - \bar{\mu})I_1^+ \\ + (1 + a)\beta_n \bar{\mu}(I_0^+ + I_2^+)] [2(a - 1 - \bar{\mu})K_1^- \\ + (a - 1)\beta_n \bar{\mu}(K_0^- + K_2^-)] \quad (18)$$



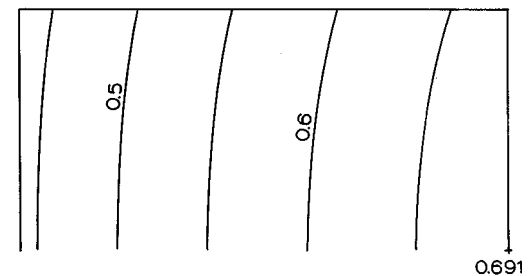
(a)



(b)



(c)



(d)

Fig. 2 Equivelocity lines for the  $a=b=0.5$  duct. (a)  $\bar{\mu}=0$ , (b)  $\bar{\mu}=0.5$ , (c)  $\bar{\mu}=1$ , (d)  $\bar{\mu}=5$ . Only the top halves are shown. Values are for  $v(r, z)$ .

and the plus and minus superscripts represent evaluation at  $\beta_n(1 + a)$  and  $\beta_n(1 - a)$ , respectively. We find the series converge very fast. Four-digit accuracy in velocity is guaranteed when the first five terms in the series are retained.

Typical equivelocity lines (only the top half is shown) are shown in Fig. 2 for the square duct ( $a=b=0.25$ ). In Fig. 2(a), there is no slip on the boundary ( $\bar{\mu}=0$ ). Notice the location of the maximum velocity is slightly to the left of the center of the cross section. When there is slip, the velocity on the boundary is no longer zero, but local minima occur at the corners (Fig. 2(b)). The maximum velocity also moves toward the outside boundary (Fig. 2(c)). For high slip coefficients the equivelocity lines tend to be parallel to the side walls (Fig. 2(d)).

After the velocity is obtained, the flow rate, represented by the mean velocity, is given by

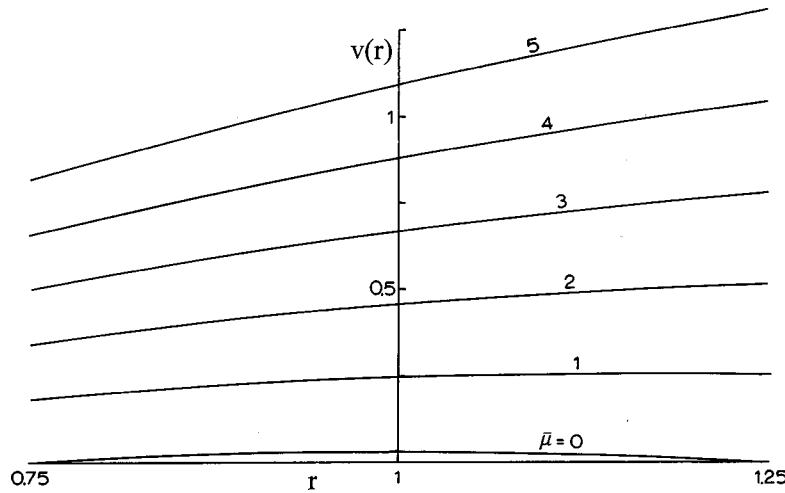


Fig. 3 Velocity distribution for azimuthal flow through an annulus

$$\begin{aligned}\bar{v} &= \frac{1}{2ab} \int_{1-a}^{1+a} \int_0^b v dz dr \\ &= \frac{1}{2ab} \sum_{n=1}^{\infty} \left\{ \frac{A_n}{\beta_n} \ln \left( \frac{1+a}{1-a} \right) \right. \\ &\quad \left. - C_{1n} (K_0^+ - K_0^-) + C_{2n} (I_0^+ - I_0^-) \right\} \frac{\sin \alpha_n}{\beta_n^2}. \quad (19)\end{aligned}$$

### Flow Through a Curved Channel

We have solved the slow slip flow through a curved rectangular duct. The solutions, however, do not apply to the case where the height  $b$  is infinite, i.e., the curved channel. This special case is considered here. The results are also exact solutions of the Navier-Stokes since the Reynolds numbers need not be small. Because the velocity is independent of  $z$ , the governing equation is

$$v''(r) + \frac{1}{r} v' - \frac{v}{r^2} = -\frac{1}{r}. \quad (20)$$

Using the slip boundary conditions the solution is

$$v(r) = -\frac{1}{2} r \ln r + C_1 r + \frac{C_2}{r} \quad (21)$$

where

$$\begin{aligned}C_1 &= \frac{1}{8} [2\bar{\mu}(1-a^2+4a\bar{\mu}) - (1-a)^3(1+a-2\bar{\mu})\ln(1-a) \\ &\quad + (1+a)^3(1-a+2\bar{\mu})\ln(1+a)] / (a-a^3+\bar{\mu}+3a^2\bar{\mu})\end{aligned} \quad (22)$$

$$\begin{aligned}C_2 &= -\frac{1}{8} (1-a^2)^2 \left[ 2\bar{\mu} + (1-a^2) \ln \left( \frac{1+a}{1-a} \right) \right] / \\ &\quad (a-a^3+\bar{\mu}+3a^2\bar{\mu}). \quad (23)\end{aligned}$$

Some velocity profiles for  $a=0.25$  are shown in Fig. 3. We note that for large slip or large  $\bar{\mu}$ , the coefficient  $C_1$  dominates and the velocity is approximately linear as reflected in Fig. 3.

$$v \approx \frac{a}{1+3a^2} \bar{\mu} r \quad (24)$$

The mean velocity is

$$\begin{aligned}\bar{v} &= \frac{1}{8a} \left[ (1-a)^2 \ln(1-a) - (1+a)^2 \ln(1+a) + 2(1+4C_1)a \right. \\ &\quad \left. + 4C_2 \ln \left( \frac{1+a}{1-a} \right) \right]. \quad (25)\end{aligned}$$

### Results and Discussion

The flow conductance is best represented by the normalized mean velocity instead of the friction factor-Reynolds number product which does not exist for Stokes flow. Figure 4(a) shows the mean velocity for a square ( $b=a$ ) curved duct. Since lengths are normalized with respect to radius of curvature  $R$ , the larger the value of  $a$  the larger the normalized curvature of the turn. In general the mean velocity rises with  $a$  and with the slip factor  $\bar{\mu}$ , except for large curvature and large constant slip factors, probably due to the unevenness of the wall shear. (The wall shear, being proportional to the slip velocity, can be obtained from the wall velocities in Fig. 2(b-d).) Even if the mean velocity decreases slightly it is more than off set by the increase in area such that the total flow still increases with  $a$ . The classical solution for the flow in a straight rectangular duct with no slip ( $\bar{\mu}=0$ ) is

$$\bar{v}_0 = c_1 a^2 \quad (26)$$

where  $c_1=0.14058$  for the square duct (see, e.g., [6]). This solution compare very well with our curved duct solution, showing the curvature effects are minimal when there is no slip. Also shown in Fig. 4(a) are the results of Ebert and Sparrow [5] who considered the straight rectangular duct with slip. Their semi-empirical formula in our variables is

$$\bar{v} = \left( 1 + \frac{c_2 \bar{\mu}}{2b} \right) \bar{v}_0 \quad (27)$$

where  $c_2$  is a coefficient depending on the aspect ratio. For a square,  $c_2=7.567$ . We see from Fig. 4(a) that Eq. (27) is valid only for very small  $a$  values, showing curvature effects are important if slip is not close to zero. Figure 4(b) shows the results for aspect ratio of 0.5 ( $c_1=0.05717$ ,  $c_2=6.306$ ). In the no slip case the straight duct has slightly smaller flow than the curved duct. The results for aspect ratio of 2 are shown in Fig. 4(c) ( $c_1=0.2287$ ,  $c_2=12.612$ ). In order to compare the flow for the same cross section, the value of  $a$  is doubled compared to that of Fig. 4(b). We note that if slip is not zero, the flow in a duct curving about the long side (inset of Fig. 4(c)) is always larger than that curving about the short side (inset of Fig. 4(b)). Figure 5 shows

the large aspect ratio cases. The infinite aspect ratio results (flow in an annulus) are given by Eq. (25). Figure 6 shows the approach of the finite aspect ratio solution Eq. (19) to the infinite aspect ratio solution for increasing  $b$ . It is seen that the effect of slip is to delay this approach to higher aspect ratios. Although the curves are for  $a=0.5$  the results for other values of  $a$  show a similar behavior. In the case of large slip (infinite  $N$  or  $\bar{\mu}$ ) the boundaries are stress free. From force balance the fluid can flow without a pressure gradient. The azimuthal velocity, satisfying all the

boundary conditions, can be shown to be proportional to the radius  $r$ , i.e., a rigid rotation. This is also reflected in Eq. (24) for large  $\bar{\mu}$ .

Of interest is the location of the velocity maximum which we noted (Fig. 2(a)) is off centered towards the inner wall. In order to show that this phenomenon is a property of neither Stokes flow nor slip flow, consider the infinite aspect ratio solution which is also an exact solution of the Navier-Stokes equations (valid for all Reynolds numbers). Using Eq. (21) and no slip ( $\bar{\mu}=0$ ), we find

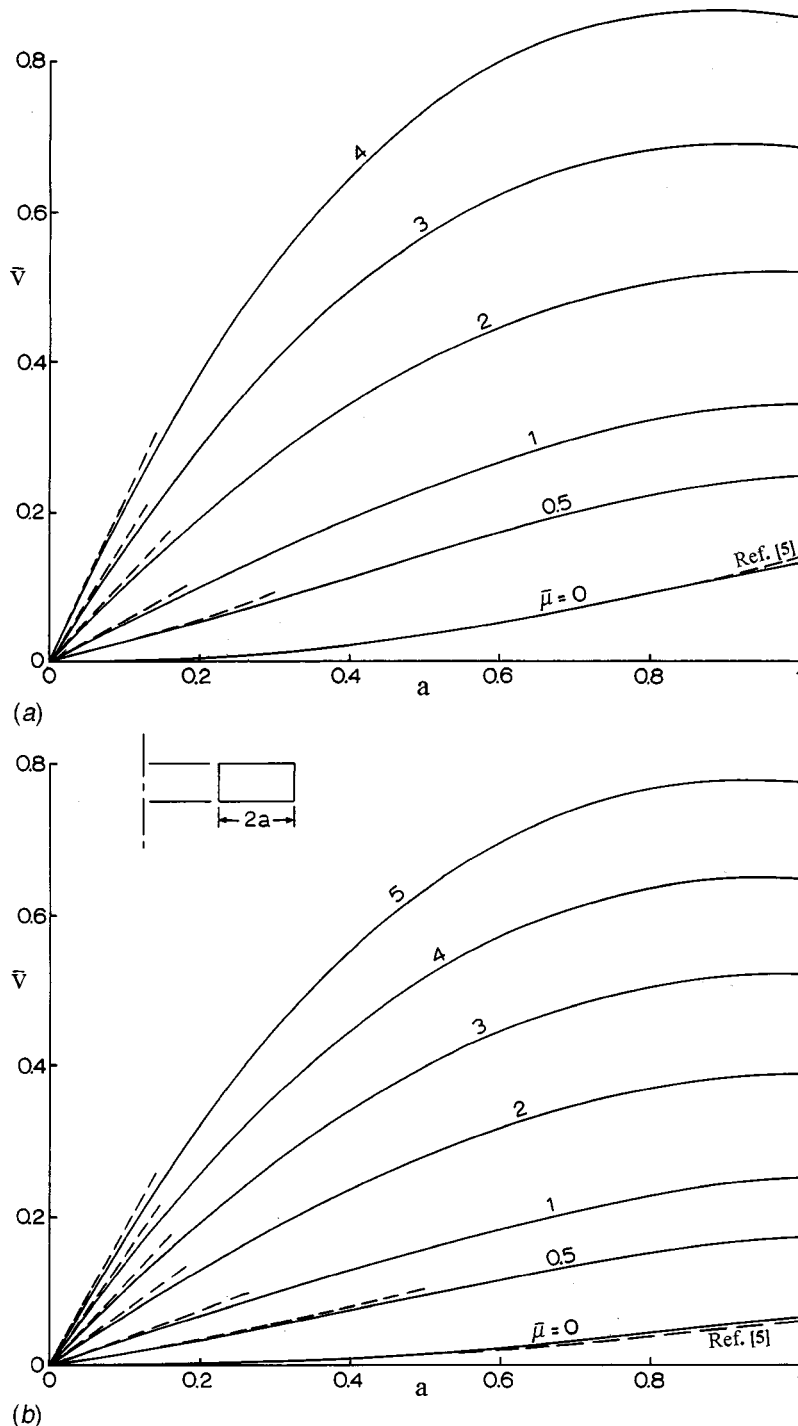


Fig. 4 Normalized mean velocity as a function of  $a$  for various constant slip factor  $\bar{\mu}$ . Unless otherwise noted, dashed lines are from [5] or Eq. (27). (a)  $b = a$ , (b)  $b = 0.5a$ , (c)  $b = 2a$ .

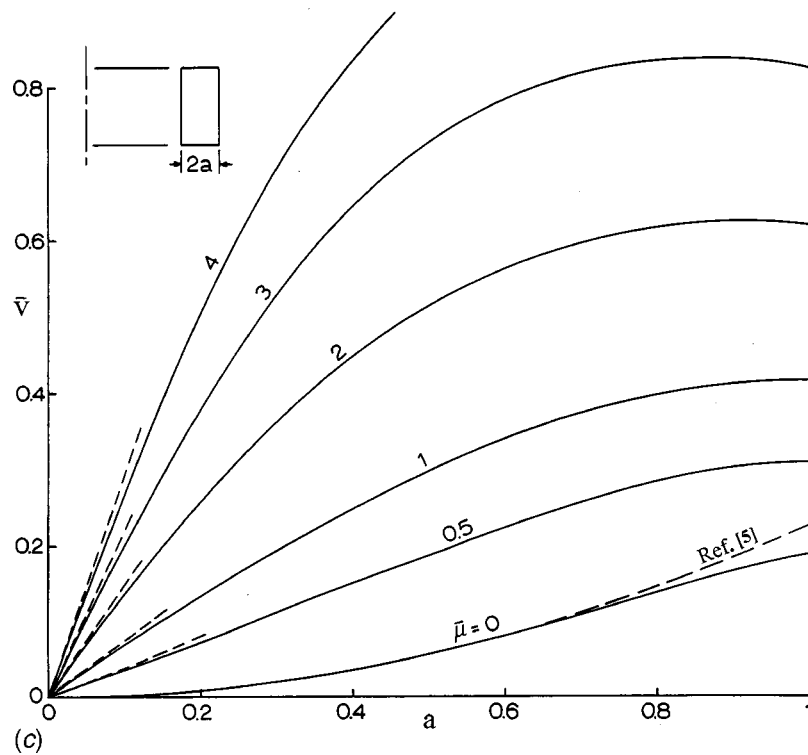


Fig. 4 (continued)

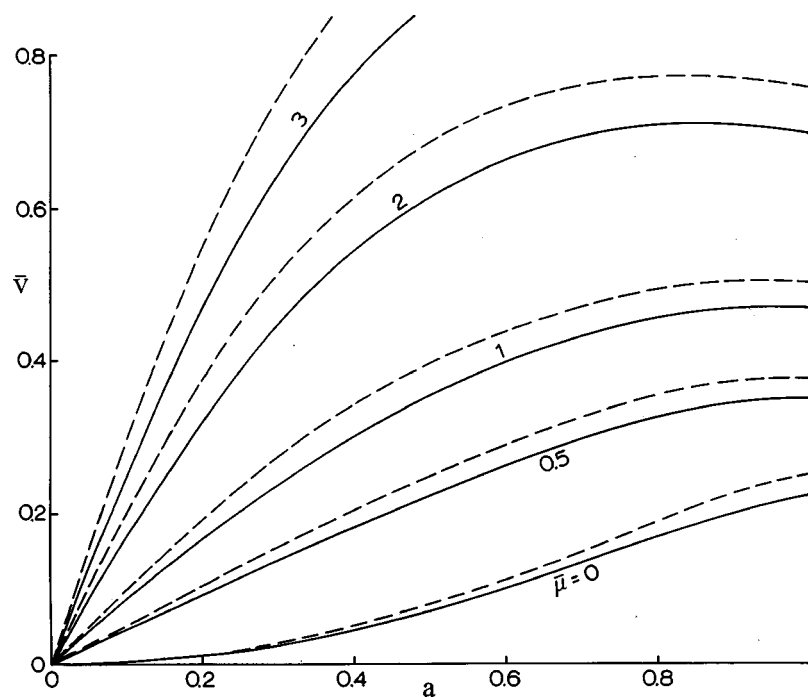


Fig. 5 Normalized mean velocity for high aspect-ratio ducts. Continuous lines are when  $b=5a$ . Dashed lines are from Eq. (25)  $b=\infty$ .

the velocity maximum is always closer to the inner wall, especially when the normalized curvature is large ( $r=2/e=0.7358 < 1$  for  $a=1$ ). When slip is increased, the velocity maximum moves towards the outer wall (Figs. 2(b), 2(c), 2(d), and 3). In general, the flow in a curved duct is governed by both the curvature and the Reynolds number (or Dean number). The reason current literature failed to report a velocity maximum closer to the

inner wall is due to the fact that small curvature and large Dean numbers were assumed, the latter is known to promote a maximum velocity towards the outer wall ([1]).

Analytical slip flow solutions are even more scarcer than no-slip solutions due to the inseparability of the Robbins type boundary conditions in most coordinate systems. We find slip flow on a curved tube dramatically changes the velocity distribution, from



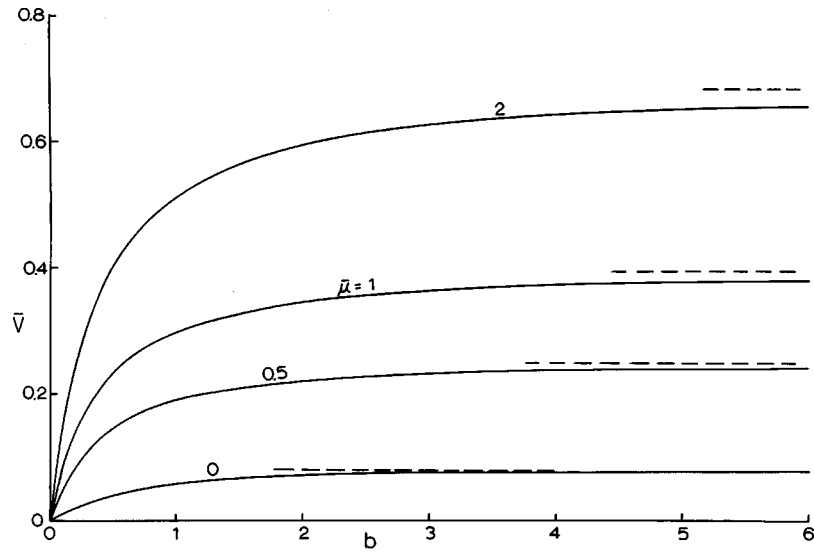


Fig. 6 The mean velocity as a function of height  $b$  for  $a=0.5$  and given slip factor  $\bar{\mu}$ . Dashed lines are the  $b=\infty$  results from Eq. (25).

Table 1 Values of  $\alpha_n$  for various  $\lambda$

$\lambda$ ( $n$ )	0.2		0.5		1		2	
	Num.	Eq. (28)	Num.	Eq. (28)	Num.	Eq. (28)	Num.	Eq. (28)
1	1.3138		1.0769		0.8603		0.6533	
2	4.0336	2.5830	3.6436	3.5632	3.4256	3.4277	3.2923	3.2913
3	6.9096	6.8102	6.5783	6.5746	6.4373	6.4383	6.3616	6.3616
4	9.8928	9.8757	9.6296	9.6290	9.5293	9.5297		
5	12.935	12.931	12.722	12.723	12.645	12.645		
6	16.011	16.010						

concentric equivelocity lines to parallel equivelocity lines. Both slip and curvature enhances the flow rate, although nonlinearly.

Depending on the application, other factors such as twist, non-zero Reynolds numbers, non-Newtonian effects, compressibility, etc., may be included. The present paper then serves as a basis for these more involved situations.

## Acknowledgment

This work is partially supported by NIH grant RR01243.

## Appendix

The eigenvalues of Eq. (5) can be evaluated numerically, but one can obtain an asymptotic formula for large  $n$ . Such a formula greatly facilitates the velocity evaluations. Using a perturbation about  $(n-1)\pi$ , we find

$$\alpha_n \approx (n-1)\pi + \frac{1}{\lambda(n-1)\pi} - \frac{\lambda + (1/3)}{\lambda^3(n-1)^3\pi^3} + O((n-1)^{-5}). \quad (28)$$

If  $\lambda=0$  the exact solution is  $\alpha_n = (n-0.5)\pi$ . Equation (28) is compared with the exact numerical values in Table 1.

We see that Eq. (28) is quite accurate especially for large  $n$  and large  $\lambda$ . In fact for  $\lambda \geq 1$  the asymptotic formula gives five-digit accuracy for all  $n \geq 2$ .

## References

- [1] Berger, S. A., Talbot, L., and Yao, L. S., 1983, "Flow in Curved Tubes," *Annu. Rev. Fluid Mech.*, **15**, pp. 461–512.
- [2] Sharipov, F., and Seleznev, V., 1998, "Data on Internal Rarefied Gas Flows," *J. Phys. Chem. Ref. Data*, **27**, pp. 657–706.
- [3] Navier, C. L. M., 1827, "Sur les lois du mouvement des fluides," *C. R. Acad. Sci.*, **6**, pp. 389–440.
- [4] Happel, J., and Brenner, H., 1991, *Low Reynolds Number Hydrodynamics*, 2nd Ed., Kluwer, Dordrecht, The Netherlands.
- [5] Ebert, W. A., and Sparrow, E. M., 1965, "Slip Flow in Rectangular and Annular Ducts," *J. Basic Eng.*, **87**, pp. 1018–1024.
- [6] Shah, R. K., and London, A. L., 1978, *Laminar Flow Forced Convection in Ducts*, Academic Press, San Diego, CA.

A Brief Note is a short paper that presents a specific solution of technical interest in mechanics but which does not necessarily contain new general methods or results. A Brief Note should not exceed 1500 words or equivalent (a typical one-column figure or table is equivalent to 250 words; a one line equation to 30 words). Brief Notes will be subject to the usual review procedures prior to publication. After approval such Notes will be published as soon as possible. The Notes should be submitted to the Editor of the JOURNAL OF APPLIED MECHANICS. Discussions on the Brief Notes should be addressed to the Editorial Department, ASME International, Three Park Avenue, New York, NY 10016-5990, or to the Editor of the JOURNAL OF APPLIED MECHANICS. Discussions on Brief Notes appearing in this issue will be accepted until two months after publication. Readers who need more time to prepare a Discussion should request an extension of the deadline from the Editorial Department.

## Some Properties of $J$ -Integral in Plane Elasticity

**Y. Z. Chen**

Division of Engineering Mechanics, Jiangsu University,  
Zhenjiang, Jiangsu 212013, P. R. China

**K. Y. Lee**

Department of Mechanical Engineering, Yonsei  
University, Seoul 120-749, South Korea

*Some properties of the  $J$ -integral in plane elasticity are analyzed. An infinite plate with any number of inclusions, cracks, and any loading conditions is considered. In addition to the physical field, a derivative field is defined and introduced. Using the Betti's reciprocal theorem for the physical and derivative fields, two new path-independent  $D_1$  and  $D_2$  are obtained. It is found that the values of  $J_k(k=1,2)$  on a large circle are equal to the values of  $D_k(k=1,2)$  on the same circle. Using this property and the complex variable function method, the values of  $J_k(k=1,2)$  on a large circle is obtained. It is proved that the vector  $J_k(k=1,2)$  is a gradient of a scalar function  $P(x,y)$ . [DOI: 10.1115/1.1432663]*

### 1 Introduction

The well-known  $J$ -integral of elastic fracture mechanics was introduced by several researchers [1–3]. The integral was related to potential energy-release rate associated with crack extension. Budiansky and Rice [4] showed that some path independent integrals discovered by Knowles and Sternberg [5] were related to energy-release rates associated with cavity or crack rotation and expansion. In some particular cases, the  $J$ -integral can be integrated in a closed form [3]. The relations between the path-independent integrals and the stress intensity factors were analyzed [6–9]. Chen and Hasebe [10] investigated the consistency check of the  $J$ -integral in the multiple crack problems. Recently, the vanishing condition of the  $J_1$  value on a large circle was addressed without a rigorous proof [11].

In this paper, some properties of the  $J$ -integral in plane elastic-

ity are analyzed. An infinite plate with any number of inclusions, cracks, and any loading conditions is considered (Fig. 1). A derivative field is defined and introduced. Using the Betti's reciprocal theorem for the physical and the derivative fields we introduce two path-independent integrals  $D_1$  and  $D_2$ . It is proved that the  $D_k(k=1,2)$  values are equal to the  $J_k(k=1,2)$  values on the large circle. Using the complex variable method, the  $J_k(k=1,2)$  values on the large circle are obtainable. It is found that the  $J_1$  and  $J_2$  becomes a vector, and it may be expressed in a gradient of a scalar function  $P(x,y)$ .

### 2 $J_k$ Integrals and the Derivative Stress Field

In the literature, the  $J_k(k=1,2)$  integrals are defined by

$$J_1(L) = \int_{(x_o, y_o), (L)}^{(x, y)} \left( W n_1 - \frac{\partial u_i}{\partial x} \sigma_{ij} n_j \right) ds \quad (1)$$

$$J_2(L) = \int_{(x_o, y_o), (L)}^{(x, y)} \left( W n_2 - \frac{\partial u_i}{\partial y} \sigma_{ij} n_j \right) ds \quad (2)$$

where  $W$  denotes the strain energy density,  $u_i$  the displacements,  $\sigma_{ij}$  the displacements, and  $n_j$  the direction cosines. In plane elasticity, the strain energy density can be expressed as

$$W = u_{i,j} \sigma_{ij} / 2 \quad (3)$$

where  $u_{i,j} = \partial u_i / \partial x_j$ . In Eqs. (1) and (2), the path “ $L$ ” is generally defined as a path with the starting point  $(x_o, y_o)$  and the end point  $(x, y)$  (Fig. 1).

Meantime, the relevant integrals are defined on a closed path “CH” (Fig. 1)

$$J_1(\text{CH}) = \oint_{(\text{CH})} \left( W n_1 - \frac{\partial u_i}{\partial x} \sigma_{ij} n_j \right) ds \quad (4)$$

$$J_2(\text{CH}) = \oint_{(\text{CH})} \left( W n_2 - \frac{\partial u_i}{\partial y} \sigma_{ij} n_j \right) ds. \quad (5)$$

In Eqs. (4) and (5), if there are some holes, cracks, or inclusions in a closed contour, the contour is defined as the type “CH” (Fig. 1).

In the following analysis, two stress fields are introduced. The first field is the physical field, which is defined from the geometry and the loading condition shown in Fig. 1, and it is called the  $\alpha$ -field hereafter. Clearly, for the  $\alpha$ -field we can write

$$u_{i(\alpha)} = u_i, \quad \sigma_{ij(\alpha)} = \sigma_{ij}. \quad (6)$$

The second field is defined as a derivative field. It is called the  $\beta$ -field and may be written as

Contributed by the Applied Mechanics Division of THE AMERICAN SOCIETY OF MECHANICAL ENGINEERS for publication in the ASME JOURNAL OF APPLIED MECHANICS. Manuscript received by the ASME Applied Mechanics Division, Apr. 24, 2001; final revision, Sep. 6, 2001. Associate Editor: J. R. Barber.

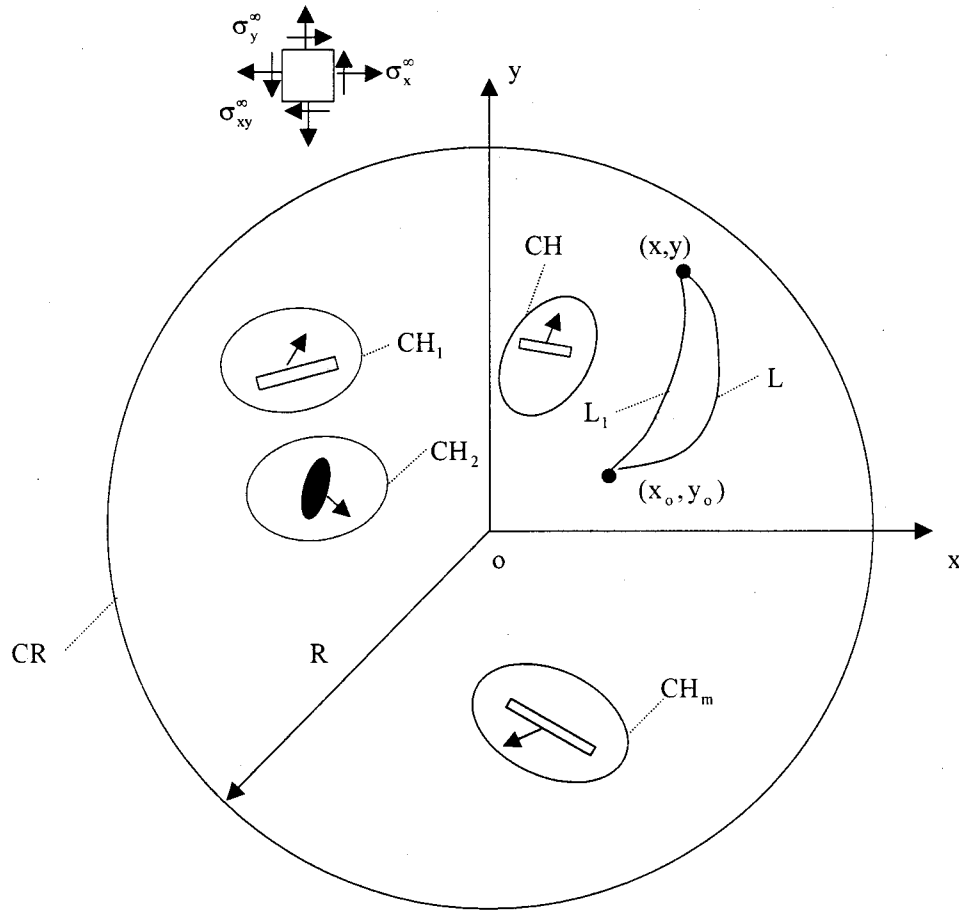


Fig. 1 An infinite plate containing cracks, holes, and inclusions

$$u_{i(\beta)} = \frac{\partial u_i}{\partial x}, \quad \sigma_{ij(\beta)} = \frac{\partial \sigma_{ij}}{\partial x}. \quad (7)$$

It is easy to prove that the components  $u_{i(\beta)}$  and  $\sigma_{ij(\beta)}$  satisfy all the governing equations of elasticity.

Similar to Eq. (1), we can define

$$\begin{aligned} D_1(L) &= \int_{(x_o, y_o), (L)}^{(x, y)} \frac{1}{2} (u_{i(\alpha)} \sigma_{ij(\beta)} - u_{i(\beta)} \sigma_{ij(\alpha)}) n_j ds \\ &= \int_{(x_o, y_o), (L)}^{(x, y)} \frac{1}{2} \left( u_i \frac{\partial \sigma_{ij}}{\partial x} - \frac{\partial u_i}{\partial x} \sigma_{ij} \right) n_j ds. \end{aligned} \quad (8)$$

Clearly, from the Betti's reciprocal theorem in elasticity  $D_1(L)$  is also a path-independent integral. In addition, similar to Eq. (4), the following integral is defined:

$$D_1(\text{CH}) = \oint_{(\text{CH})} \frac{1}{2} \left( u_i \frac{\partial \sigma_{ij}}{\partial x} - \frac{\partial u_i}{\partial x} \sigma_{ij} \right) n_j ds. \quad (9)$$

A relation between  $J_1$  and  $D_1$  has been found, and it reads

$$J_1(\text{CH}) = D_1(\text{CH}). \quad (10)$$

In fact, instead of Eq. (10), it is equivalent to prove the following equality:

$$\oint_{(\text{CH})} \left( u_i \frac{\partial \sigma_{ij}}{\partial x} + \frac{\partial u_i}{\partial x} \sigma_{ij} \right) n_j ds = 2 \oint_{(\text{CH})} W dy. \quad (11)$$

Clearly, for the first term on the left-hand side of Eq. (11), we have

$$\begin{aligned} d_1 &= \oint_{(\text{CH})} u_i \frac{\partial \sigma_{ij}}{\partial x} n_j ds \\ &= \oint_{(\text{CH})} u \left( \frac{\partial \sigma_x}{\partial x} dy - \frac{\partial \sigma_{xy}}{\partial x} dx \right) + \oint_{(\text{CH})} v \left( \frac{\partial \sigma_{xy}}{\partial x} dy - \frac{\partial \sigma_y}{\partial x} dx \right) \\ &= \oint_{(\text{CH})} u \left( -\frac{\partial \sigma_{xy}}{\partial y} dy - \frac{\partial \sigma_{xy}}{\partial x} dx \right) \\ &\quad + \oint_{(\text{CH})} v \left( -\frac{\partial \sigma_y}{\partial y} dy - \frac{\partial \sigma_y}{\partial x} dx \right) \\ &= \oint_{(\text{CH})} (-u d\sigma_{xy} - v d\sigma_y) \\ &= \oint_{(\text{CH})} \sigma_{xy} \left( \frac{\partial u}{\partial x} dx + \frac{\partial u}{\partial y} dy \right) + \sigma_y \left( \frac{\partial v}{\partial x} dx + \frac{\partial v}{\partial y} dy \right). \end{aligned} \quad (12)$$

In addition, for the second term on the left-hand side of Eq. (11), we have

$$\begin{aligned} d_2 &= \oint_{(\text{CH})} \frac{\partial u_i}{\partial x} \sigma_{ij} n_j ds \\ &= \oint_{(\text{CH})} \frac{\partial u}{\partial x} (\sigma_x dy - \sigma_{xy} dx) + \frac{\partial v}{\partial x} (\sigma_{xy} dy - \sigma_y dx). \end{aligned} \quad (13)$$

Finally, from Eqs. (3), (12), and (13), the equality shown by Eq.

(11) is proved. Thus, the equality Eq. (10) is also proved. The identity shown by Eq. (10) is implicit in Eshelby's work [12].

Alternatively, the second stress field, the  $\beta$ -field and may be defined as

$$u_{i(\beta)} = \frac{\partial u_i}{\partial y}, \quad \sigma_{ij(\beta)} = \frac{\partial \sigma_{ij}}{\partial y}. \quad (14)$$

It is easy to prove that the components  $u_{i(\beta)}$  and  $\sigma_{ij(\beta)}$  satisfy all the governing equations of elasticity. Similar to the previous case, we can define

$$D_2(L) = \int_{(x_o, y_o), (L)}^{(x, y)} \frac{1}{2} (u_{i(\alpha)} \sigma_{ij(\beta)} - u_{i(\beta)} \sigma_{ij(\alpha)}) n_j ds \\ = \int_{(x_o, y_o), (L)}^{(x, y)} \frac{1}{2} \left( u_i \frac{\partial \sigma_{ij}}{\partial y} - \frac{\partial u_i}{\partial y} \sigma_{ij} \right) n_j ds. \quad (15)$$

$$D_2(\text{CH}) = \oint_{(\text{CH})} \frac{1}{2} \left( u_i \frac{\partial \sigma_{ij}}{\partial y} - \frac{\partial u_i}{\partial y} \sigma_{ij} \right) n_j ds. \quad (16)$$

where  $D_2(L)$  is also a path independent integral. Similarly, we can prove

$$J_2(\text{CH}) = D_2(\text{CH}) \quad (17)$$

### 3 $J_k$ Integrals on a Large Circle

In the following analysis "CR" denotes a sufficient large circle in which all the cracks and inclusions are enclosed (Fig. 1). Since the equality Eq. (10) is proved, and the closed path "CR" is a particular type of "CH", thus, we have

$$J_1(\text{CR}) = D_1(\text{CR}) \quad (18)$$

where

$$J_1(\text{CR}) = \oint_{(\text{CR})} \left( W n_1 - \frac{\partial u_i}{\partial x} \sigma_{ij} n_j \right) ds \quad (19)$$

$$D_1(\text{CR}) = \oint_{(\text{CR})} \frac{1}{2} \left( u_i \frac{\partial \sigma_{ij}}{\partial x} - \frac{\partial u_i}{\partial x} \sigma_{ij} \right) n_j ds. \quad (20)$$

Equation (18) shows that instead of evaluating the integral  $J_1(\text{CR})$  we can evaluate its equivalent value  $D_1(\text{CR})$ .

The following analysis depends on the complex variable function method in plane elasticity [13]. In the method, the stresses  $(\sigma_x, \sigma_y, \sigma_{xy})$ , the resultant forces  $(X, Y)$  and the displacements  $(u, v)$  are expressed in terms of two complex potentials  $\phi(z)$  and  $\psi(z)$  such that

$$\sigma_x + \sigma_y = 4\text{Re}\phi'(z) \\ \sigma_y - \sigma_x + 2i\sigma_{xy} = 2[\bar{z}\phi''(z) + \psi'(z)] \quad (21)$$

$$f = -Y + iX = \phi(z) + z\overline{\phi'(z)} + \overline{\psi(z)} \quad (22)$$

$$2G(u + iv) = \kappa\phi(z) - z\overline{\phi'(z)} - \overline{\psi(z)} \quad (23)$$

where  $G$  is the shear modulus of elasticity,  $\kappa = (3 - \nu)/(1 + \nu)$  is for the plane stress problem,  $\kappa = 3 - 4\nu$  is for the plane-strain problem, and  $\nu$  is the Poisson's ratio. The following equations in the polar coordinate are also introduced [13]:

$$\sigma_r + i\sigma_{r\theta} = \phi'(z) + \overline{\phi'(z)} - \frac{R^2}{z^2} [z\overline{\phi''(z)} + \overline{\psi'(z)}] \quad (24)$$

$$2G(u_r - iu_\theta) = \frac{z}{R} [\kappa\overline{\phi(z)} - \bar{z}\phi'(z) - \overline{\psi(z)}]. \quad (25)$$

For the physical field, the complex potentials  $\phi(z)$  and  $\psi(z)$  in the remote place can be expressed in the general form [13]

$$\phi(z) = A_1 z + A_2 \log z + \sum_{k=1}^{\infty} \frac{a_k}{z^k} \quad (26a)$$

$$\psi(z) = B_1 z + B_2 \log z + \sum_{k=1}^{\infty} \frac{b_k}{z^k} \quad (26b)$$

where

$$A_1 = \frac{\sigma_x^\infty + \sigma_y^\infty}{4}, \quad B_1 = \frac{\sigma_y^\infty - \sigma_x^\infty}{2} + i\sigma_{xy}^\infty \quad (27a)$$

$$A_2 = -\frac{(F_x + iF_y)}{2\pi(\kappa + 1)}, \quad B_2 = -\frac{\kappa(F_x - iF_y)}{2\pi(\kappa + 1)}. \quad (27b)$$

In Eq. (27b),  $F_x$  and  $F_y$  are the resultant forces applied on the finite region of the infinite plate. Also, the coefficient  $a_k$  and  $b_k$  ( $k = 1, 2, \dots$ ) in Eq. (26) will be determined from a concrete solution.

For the  $\alpha$ -field, we simply write the complex potentials in the form

$$\phi_{(\alpha)}(z) = \phi(z), \quad \psi_{(\alpha)}(z) = \psi(z). \quad (28)$$

If the  $\beta$ -field is defined by Eq. (7), we obtain the following:

$$(\sigma_x + \sigma_y)_{(\beta)} = \frac{\partial}{\partial x} (\sigma_x + \sigma_y) = 4\text{Re}\phi''(z),$$

$$(\sigma_y - \sigma_x + 2i\sigma_{xy})_{(\beta)} = \frac{\partial}{\partial x} (\sigma_y - \sigma_x + 2i\sigma_{xy}) \\ = 2[\bar{z}\phi'''(z) + \phi''(z) + \psi''(z)] \quad (29)$$

$$2G(u + iv)_{(\beta)} = 2G \frac{\partial}{\partial x} (u + iv) \\ = \kappa\phi'(z) - z\overline{\phi''(z)} - \overline{\phi'(z)} - \overline{\psi'(z)}. \quad (30)$$

Comparing Eqs. (21) and (23) with Eqs. (29) and (30), the complex potentials for the  $\beta$ -field are obtained,

$$\phi_{(\beta)}(z) = \phi'(z) = A_1 + \frac{A_2}{z} - \sum_{k=1}^{\infty} \frac{ka_k}{z^{k+1}} \quad (31a)$$

$$\psi_{(\beta)}(z) = \phi'(z) + \psi'(z) = A_1 + B_1 + \frac{A_2 + B_2}{z} - \sum_{k=1}^{\infty} \frac{k(a_k + b_k)}{z^{k+1}}. \quad (31b)$$

Obviously, it is natural to rewrite the  $D_1(\text{CR})$  integral in the form

$$D_1(\text{CR}) = \oint_{(\text{CR})} \frac{1}{2} \left( u_i \frac{\partial \sigma_{ij}}{\partial x} - \frac{\partial u_i}{\partial x} \sigma_{ij} \right) n_j ds \\ = \text{Re} \oint_{(\text{CR})} \frac{1}{2} ((u_r - iu_\theta)_{(\alpha)} (\sigma_r + i\sigma_{r\theta})_{(\beta)} \\ - (u_r - iu_\theta)_{(\beta)} (\sigma_r + i\sigma_{r\theta})_{(\alpha)}) ds \quad (32)$$

where the terms  $(u_r - iu_\theta)_{(\alpha)}$ ,  $(\sigma_r + i\sigma_{r\theta})_{(\beta)}$ ,  $(u_r - iu_\theta)_{(\beta)}$  and  $(\sigma_r + i\sigma_{r\theta})_{(\alpha)}$  can be evaluated by using Eqs. (24) and (25).

It is easy to see that there are some relations on the large circle "CR"

$$z = R \exp(i\theta), \quad \bar{z} = R^2/z, \quad dz = izd\theta, \quad ds = Rd\theta = -i \frac{Rdz}{z} \\ \text{(for } z \text{ on CR).} \quad (33)$$

The substitutions shown by Eq. (33) reveals that the integral involved in right side of Eq. (32) (after "Re") may be changed into an integral of complex variable function of the form  $\oint_{(\text{CR})} f(z) dz$ .

By using the residue theorem in complex variable analysis for the integral  $\oint_{(CR)} f(z) dz$ , from Eq. (32) the final result is obtainable:

$$J_1(CR) = D_1(CR) = \frac{1}{8G} [(\kappa - 1)(\sigma_x^\infty + \sigma_y^\infty)F_x - 2(\sigma_y^\infty - \sigma_x^\infty)F_y + 4\sigma_{xy}^\infty F_y]. \quad (34)$$

From Eq. (34) we can see the following points:

(a) The  $J_1(CR)$  ( $=D_1(CR)$ ) value is not equal to zero in general.

(b) The  $J_1(CR)$  ( $=D_1(CR)$ ) value solely depends on the remote stresses  $\sigma_x^\infty$ ,  $\sigma_y^\infty$ , and  $\sigma_{xy}^\infty$  and the resultant forces  $F_x$  and  $F_y$ . It does not depend on the coefficients  $a_k$  and  $b_k$  ( $k=1, 2, \dots$ ). Previously, the vanishing condition of  $J_1(CR)$  was studied without a rigorous proof [11].

Similarly, if the  $\beta$ -field is defined by Eq. (14), the relevant complex potentials take the form

$$\phi_{(\beta)}(z) = i\phi'(z) = i \left[ A_1 + \frac{A_2}{z} - \sum_{k=1}^{\infty} \frac{ka_k}{z^{k+1}} \right] \quad (35a)$$

$$\psi_{(\beta)}(z) = i[-\phi'(z) + \psi'(z)] = i \left[ B_1 - A_1 + \frac{B_2 - A_2}{z} - \sum_{k=1}^{\infty} \frac{k(b_k - a_k)}{z^{k+1}} \right]. \quad (35b)$$

As before, similar derivation will yield

$$J_2(CR) = D_2(CR) = \frac{1}{8G} [(\kappa - 1)(\sigma_x^\infty + \sigma_y^\infty)F_y + 2(\sigma_y^\infty - \sigma_x^\infty)F_x + 4\sigma_{xy}^\infty F_x] \quad (36)$$

where

$$J_2(CR) = \oint_{(CR)} \left( Wn_2 - \frac{\partial u_i}{\partial y} \sigma_{ij} n_j \right) ds \quad (37)$$

$$D_2(CR) = \oint_{(CR)} \frac{1}{2} \left( u_i \frac{\partial \sigma_{ij}}{\partial y} - \frac{\partial u_i}{\partial y} \sigma_{ij} \right) n_j ds. \quad (38)$$

#### 4 Scalar Field Defined From the $J_k$ Integrals

It is easy to see that for a given point in the infinite plate the  $J_1$  or  $J_2$  generally takes a multiply value. Clearly, if one takes a cut from all cracks or inclusions, a  $(J_1, J_2)$  field with single value is obtained. From the definition shown by Eqs. (1) and (2), we find the following:

$$\frac{\partial J_1}{\partial y} = \frac{\partial J_2}{\partial x} = \frac{1}{2} \left( \frac{\partial u}{\partial y} \sigma_{xy} + \frac{\partial v}{\partial y} \sigma_y - \frac{\partial u}{\partial x} \sigma_x - \frac{\partial v}{\partial x} \sigma_{xy} \right). \quad (39)$$

Therefore, we can define a function

$$P(x, y) = \int_{(x_0, y_0)}^{(x, y)} J_1 dx + J_2 dy. \quad (40)$$

Alternatively speaking, the  $J_1$  and  $J_2$  integrals become the gradient of a scalar function

$$J_1 = \frac{\partial P}{\partial x}, \quad J_2 = \frac{\partial P}{\partial y}. \quad (41)$$

These relations reveal that  $J_1$  and  $J_2$  become vectors, and an invariant can be defined:

$$J_{in} = \sqrt{J_1^2 + J_2^2}. \quad (42)$$

It can also be proved that the  $D_1(L)$  and  $D_2(L)$  integrals defined by Eqs. (8) and (15) also become vectors.

#### 5 Conclusion

The introduction of the derivative field plays an important role in the present study. It is worthy to explain why this field is introduced. In fact, the second term in the  $J_1$  integral is composed of two factors  $\partial u_i / \partial x$  and  $\sigma_{ij} n_j ds$ . Physically, the terms  $(\partial u_i / \partial x)(\sigma_{ij} n_j ds)$  represent the work along a segment  $ds$ , which is done by the traction of the physical field and the displacement of the derivative field. This situation helps people to get an idea to use the Betti's reciprocal theorem between the physical field and the derivative field. Therefore, a path-independent integral  $D_1(L)$  is obtainable.

In addition, after equality  $J_1(CH) = D_1(CH)$ , or  $J_1(CR) = D_1(CR)$  is proved, and the realization  $\bar{z} = R^2/z$  on the large circle is used, the final result of  $J_1(CR)$  is obtained.

#### References

- [1] Rice, J. R., 1968, *Fracture: An Advanced Treatise*, Vol. 2, H. Liebowitz, ed., Academic Press, San Diego, CA.
- [2] Rice, J. R., 1968, "A Path-Independent Integral and the Approximate Analysis of Strain Concentration by Notches and Cracks," *ASME J. Appl. Mech.*, **35**, pp. 379–386.
- [3] Cherepanov, G. P., 1979, *Mechanics of Brittle Fracture*, McGraw-Hill, New York.
- [4] Budiansky, B., and Rice, J. R., 1973, "Conservation Laws and Energy-Release Rates," *ASME J. Appl. Mech.*, **40**, pp. 201–203.
- [5] Knowles, J. K., and Sternberg, E., 1972, "On a Class of Conservation Laws in Linearized and Finite Elastostatics," *Arch. Ration. Mech. Anal.*, **44**, pp. 187–211.
- [6] Freund, L. B., 1978, "Stress Intensity Factor Calculation Based on a Conservation Integral," *Int. J. Solids Struct.*, **14**, pp. 241–250.
- [7] Herrmann, A. G., and Herrmann, G., 1981, "On Energy-Release Rates for a Plane Crack," *ASME J. Appl. Mech.*, **48**, pp. 525–530.
- [8] Chen, Y. Z., 1985, "New Path Independent Integrals in Linear Elastic Fracture Mechanics," *Eng. Fract. Mech.*, **22**, pp. 673–686.
- [9] Chen, Y. Z., and Hasebe, Norio, 1994, "Eigenfunction Expansion and Higher Order Weight Functions of Interface Cracks," *ASME J. Appl. Mech.*, **61**, pp. 843–849.
- [10] Chen, Y. H., and Hasebe, Norio, 1998, "A Consistency Check for Strongly Interaction Multiple Crack Problems in Isotropic, Bimaterial, and Orthotropic Bodies," *Int. J. Fract.*, **89**, pp. 333–353.
- [11] Chen, Y. H., 2001, "M-Integral Analysis for Two Dimensional Solids With Strongly Interacting Microcracks. Part I: In an Infinite Brittle Solid," *Int. J. Solids Struct.*, **38**, pp. 3193–3212.
- [12] Eshelby, J. D., 1951, "The Force on an Elastic Singularity," *Philos. Trans. R. Soc. London, Ser. A*, **A244**, pp. 87–112.
- [13] Muskhelishvili, N. I., 1953, *Some Basic Problems of Mathematical Theory of Elasticity*, Noordhoff, The Netherlands.

### Orthotropic Hyperelasticity in Terms of an Arbitrary Molecular Chain Model

**J. E. Bischoff**  
Mem. ASME

**E. M. Arruda**  
Mem. ASME

**K. Grosh**  
Mem. ASME

Department of Mechanical Engineering and Applied Mechanics, University of Michigan, Ann Arbor, MI 48109-2125



There are many statistical mechanical models of long-chain models, two of which are the freely jointed chain model and the wormlike chain model. A continuum constitutive law for hyperelastic orthotropic materials has recently been developed using the freely jointed chain model as its basis. In this note, the continuum strain energy function is recast in general terms allowing for the incorporation of an arbitrary macromolecular constitutive model. In particular, the orthotropic constitutive model is recast using the wormlike chain model in place of the freely jointed chain model and the effects of this alternation are examined. [DOI: 10.1115/1.1432664]

## 1 Introduction

A micromechanical model for orthotropic hyperelastic materials has recently been developed from an orthotropic unit cell with eight constituent chains [1]. This model can be applied to collagenous soft tissue such as skin and hear tissue, in which the presence of an anisotropic collagen network within the tissue dominates the elastic response of the material and results in nonlinear orthotropic constitutive behavior. In this model, the response of a single chain in the representative unit cell is calculated by considering the chain to be freely jointed; that is, each chain is composed of a number  $N$  of rigid links each of length  $l$ . The strain energy  $w(\rho)$  for such a chain is given by

$$w(\rho) = k\Theta N \left( \frac{\rho}{N} \beta + \ln \frac{\beta}{\sinh \beta} \right) \quad (1)$$

where  $\rho$  is the length of the chain normalized by the rigid link length  $l$ ;  $k$  is Boltzmann's constant;  $\Theta$  is absolute temperature; and  $\beta = \mathcal{L}^{-1}(\rho/N)$  where  $\mathcal{L}(x) = \coth x - 1/x$  is the Langevin function. The continuum strain energy function  $W$  developed from considering an orthotropic unit cell with eight such chains forming a junction at the center of the unit cell and terminating at its corners is given by

$$W = W_0 + \frac{nk\Theta}{4} \left\{ \frac{N}{2} \sum_{i=1}^4 \left[ \frac{\rho^{(i)}}{N} \beta^{(i)} + \ln \frac{\beta^{(i)}}{\sinh \beta^{(i)}} \right] - \frac{\beta_p}{\sqrt{N}} \ln(\lambda_a^2 \lambda_b^2 \lambda_c^2) \right\} + B[\cosh(J-1) - 1] \quad (2)$$

where  $W_0$  is a constant related to the strain energy of the undeformed continuum;  $n$  is a free parameter that reflects the unit cell (or chain) density; the superscript  $(i)$  represents the  $i$ th chain in the unit cell;  $\beta_p = \mathcal{L}^{-1}(P/N)$  where  $P$  is the initial normalized length of a chain;  $\lambda_a, \lambda_b$ , and  $\lambda_c$  are stretches and  $\mathbf{a}, \mathbf{b}$ , and  $\mathbf{c}$  are the normalized unit cell dimensions along the three orthonormal material axes  $\mathbf{a}$ ,  $\mathbf{b}$ , and  $\mathbf{c}$ , respectively;  $B$  is a free parameter that governs the bulk compressibility of the material; and  $J = \det \mathbf{F}$  is the volume change accompanying deformation normalized by the undeformed volume where  $\mathbf{F}$  is the deformation gradient. Only four chains act independently because of symmetry.

Statistical representations of macromolecules other than the freely jointed chain (FJC) model can be considered within the framework of a unit cell to develop a continuum constitutive law, such as a freely jointed chain model with steric constraints, the wormlike chain (WLC) model, or the extensible wormlike chain model. Each of these models prescribes a unique strain energy function for the chain and will result in a unique continuum strain energy function. To incorporate other chain models, the orthotropic constitutive model given in Eq. (2) will be recast in terms of an arbitrary chain strain energy function  $w(\rho)$ . Using this general

formulation, an orthotropic continuum constitutive law based on the WLC model will be developed and compared to the previously developed model based on the FJC model.

## 2 Constitutive Model Development

Let  $w(\rho)$  be the strain energy function of a single chain where  $\rho$  is the length of the chain normalized by a length scale originating from the statistical model. Following the approach in Bischoff et al. [1], the strain energy function for an orthotropic unit cell with eight of these chains is

$$w = \frac{n}{4} \left\{ \left[ \sum_{i=1}^4 w(\rho^{(i)}) \right] - \frac{1}{P} \left( \frac{dw(\rho)}{d\rho} \right)_{\rho=P} \ln(\lambda_a^2 \lambda_b^2 \lambda_c^2) \right\} + B[\cosh(J-1) - 1]. \quad (3)$$

The components  $S_{jk}$  of the second Piola-Kirchhoff stress tensor calculated from  $W$  are

$$S_{jk} = \frac{n}{4} \left\{ \left[ \sum_{i=1}^4 \frac{P_j^{(i)} P_k^{(i)}}{\rho^{(i)}} \left( \frac{dw(\rho)}{d\rho} \right)_{\rho=\rho^{(i)}} \right] - \frac{1}{P} \left( \frac{dw(\rho)}{d\rho} \right)_{\rho=P} \left( \frac{a^2 a_j a_k}{\lambda_a^2} + \frac{b^2 b_j b_k}{\lambda_b^2} + \frac{c^2 c_j c_k}{\lambda_c^2} \right) \right\} + B \sinh(J-1) \frac{\partial J}{\partial E_{jk}} \quad (4)$$

where  $P_j^{(i)}$  are components of the undeformed chain vector for the  $i$ th chain and  $E_{jk}$  are components of the Lagrangian strain tensor. When the freely jointed chain model is used, together with the assumption that the undeformed (reference) length of each chain is its rms length such that  $P = \sqrt{N}$ , then  $dw(\rho)/d\rho = k\Theta \mathcal{L}^{-1}(\rho/N)$  and the stress-strain relationship given in [1] is recovered.

The WLC model considers a macromolecule to be a flexible rod characterized by a total contour length  $L$  and a persistence length  $A$  (the characteristic distance over which significant deviations in the tangent vector of the chain arise). An interpolation formula for the force-stretch response of a wormlike chain is

$$\frac{fA}{k\Theta} = \frac{r}{L} + \frac{1}{4(1-r/L)^2} - \frac{1}{4} \quad (5)$$

where  $f$  is the applied force and  $r$  is the deformed length of the chain [2]. Using the persistence length as a normalized factor, the strain energy for a wormlike chain can be found by integrating Eq. (5), giving

$$w(\rho) = k\Theta \left( \frac{\rho^2}{2\Lambda} + \frac{\Lambda}{4} \frac{1}{1-\rho/\Lambda} - \frac{\rho}{4} \right); \quad \rho \leq \Lambda \quad (6)$$

where  $\rho = r/A$  and  $\Lambda = L/A$ . (Note that a singularity exists in Eq. (6) at the fully extended length  $\rho = \Lambda$ , beyond which ( $\rho > \Lambda$ ) a finite value of  $w(\rho)$  is returned from the strain energy function even though these deformed lengths are not physically permissible.) The undeformed length of a chain is typically given as its end-to-end root-mean-squared distance  $R = \sqrt{2AL}$  [2], and thus the normalized undeformed length used here is  $P = \sqrt{2\Lambda}$ . From this relation, when  $\Lambda \leq 2$  then  $P \geq \Lambda$ , meaning the undeformed length of each chain is greater than its contour length. Clearly that is not physical and  $\Lambda$  must therefore be greater than two when using this model. Using the undeformed length  $P$  and  $w(\rho)$  in Eq. (6), the strain energy function and the associated stressed for the orthotropic continuum model using the WLC approximation can be determined from Eqs. (3) and (4).

## 3 Simulations

To examine the differences associated with using the WLC model in place of the FJC model within the framework of the orthotropic continuum model, simulations of uniaxial tension have been performed. For simplicity, the material axes are aligned with the principal stretches, such that  $\mathbf{a} = [1, 0, 0]$ ,  $\mathbf{b} = [0, 1, 0]$ , and  $\mathbf{c}$

Contributed by the Applied Mechanics Division of THE AMERICAN SOCIETY OF MECHANICAL ENGINEERS for publication in the ASME JOURNAL OF APPLIED MECHANICS. Manuscript received by the ASME Applied Mechanics Division, May 8, 2001; final revision, Oct. 5, 2001. Associate Editor: L. T. Wheeler.

$= [0, 0, 1]$ . By virtue of this alignment no shear stresses are generated and the stress-stretch relations in the three principal directions in terms of the chain strain energy  $w(\rho)$  are

$$\begin{aligned} T_{11} &= \frac{na^2}{4J} \left[ \frac{\lambda_1^2}{\rho} \frac{dw(\rho)}{d\rho} - \frac{1}{P} \left( \frac{dw(\rho)}{d\rho} \right)_{\rho=P} \right] + B \sinh(J-1) \\ T_{22} &= \frac{nb^2}{4J} \left[ \frac{\lambda_2^2}{\rho} \frac{dw(\rho)}{d\rho} - \frac{1}{P} \left( \frac{dw(\rho)}{d\rho} \right)_{\rho=P} \right] + B \sinh(J-1) \\ T_{33} &= \frac{nc^2}{4J} \left[ \frac{\lambda_3^2}{\rho} \frac{dw(\rho)}{d\rho} - \frac{1}{P} \left( \frac{dw(\rho)}{d\rho} \right)_{\rho=P} \right] + B \sinh(J-1) \quad (7) \end{aligned}$$

where  $T_{ii}$  are the principal Cauchy stresses,  $\lambda_i$  are the principal stretches, and the deformed chain length is  $\rho = \sqrt{a^2\lambda_1^2 + b^2\lambda_2^2 + c^2\lambda_3^2}/2$ . To simulate uniaxial tension along the  $x_i$ -axis,  $T_{22}=T_{33}=0$  and the second two equations in Eq. (7) can be solved for the transverse stretches  $\lambda_2$  and  $\lambda_3$  given an applied stretch  $\lambda_1$ . Note that  $a$  and  $b$  are free parameters, but after specifying these parameters and the chain parameters ( $n$  and  $N$  for the FJC model,  $n$  and  $\Lambda$  for the WLC model), then  $c$  is fixed by

$$c = \sqrt{4N - a^2 - b^2} \quad (8)$$

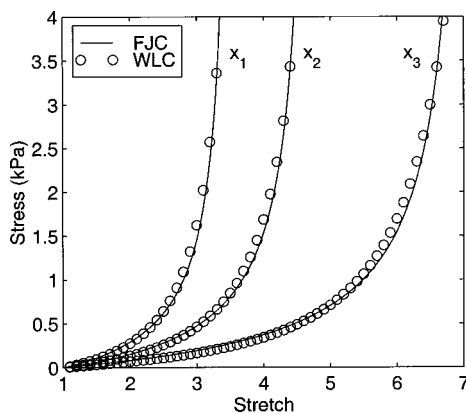
if the FJC model is used or by

$$c = \sqrt{8\Lambda - a^2 - b^2} \quad (9)$$

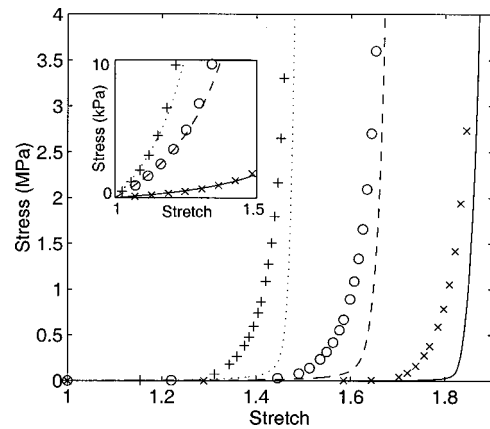
if the WLC model is used.

Figure 1 shows results of simulations using the FJC or WLC model for uniaxial tension along each of the three material axes (denoted  $x_1, x_2, x_3$  in the figure). For the FJC simulations,  $a=4, b=3, c=2, N=7.25$ , and  $n=1 \cdot 10^{22}/\text{m}^3$ . WLC simulation parameters were selected to match the results from the corresponding FJC simulation while preserving the relative values of the aspect ratios; the resulting parameters are  $a=9, b=6.75, c=4.5, \Lambda=18.35$ , and  $n=0.7 \cdot 10^{22}/\text{m}^3$ . For all simulations  $B=0$  MPa. Though not shown here, at low stretches ( $<1.5$ ) or stretches well into the locking regime (corresponding to stresses above 5 kPa), differences between simulations using the FJC model versus as the WLC model become significant, indicating that the initial modulus and final locking stretch predicting by the two models are different.

To examine the ability of the continuum model using the WLC model to capture the initial modulus and locking stretch of simulations using the FJC model, a series of simulations was per-



**Fig. 1 Simulations of uniaxial tension along each of the three material axes ( $x_1, x_2, x_3$ ) using the freely jointed chain (FJC) or the wormlike chain (WLC) model in the orthotropic constitutive model. Parameters used for the FJC simulations are  $a=4, b=3, c=2, N=7.25, n=1 \cdot 10^{22}/\text{m}^3$ , and  $B=0.1$  MPa. Parameters used for the WLC simulations are  $a=9, b=6.75, c=4.5, \Lambda=18.35, n=0.7 \cdot 10^{22}/\text{m}^3$ , and  $B=0.1$  MPa.**



**Fig. 2 Simulations of uniaxial tension along the  $x_1$ -axis using the freely jointed chain (FJC) model (represented by lines) or the wormlike chain (WLC) model (symbols) in the orthotropic constitutive model. The locking stretch was set to be  $\lambda^L=1.5, 1.7$ , or  $1.9$ . Parameters are given in Table 1.**

formed in which the locking stretch  $\lambda^L$  was set a priori to be 1.9, 1.7, and 1.5 with aspect ratios of  $a=2.5$  and  $b=1$  when possible. Results are shown in Fig. 2; parameters used in these simulations are given in Table 1. For uniaxial deformation along the  $x_1$ -axis, the WLC model predicts locking to occur at  $\lambda^L=2\Lambda/a$ , thus setting  $\Lambda$  as a function of  $\lambda^L$  and  $a$ . However, when  $\lambda^L=1.5$  and when  $a=2.5$  this relations gives  $\Lambda < 2$  in violation of the physical basis of the WLC model. Thus, for this locking stretch,  $a$  was calculated with  $\Lambda=2.125$ . The FJC model predicts locking under uniaxial tension along the  $x_1$ -axis to occur at  $\lambda^L=2N/a$ . The parameters for the curves using the FJC model were determined by matching the initial modulus and locking stretch of the corresponding WLC simulation. As seen in Fig. 2, the initial behavior (inset) and the locking stretch of the two models are matched well, but the curvatures of the constitutive responses in the intermediate regime deviate significantly from each other.

Figures 1 and 2 suggest that differences in the response of the continuum constitutive model when different molecular models are used (in this case the FJC model versus the WLC model) can be attributed primarily to the differences between the molecular models themselves. It is known that the locking behavior predicted by the FJC model for a single chain occurs more sharply than that predicted by the WLC model [2] and this is reflected in the continuum responses examined here (Fig. 2). However, the orthotropy of the material response predicted by the general continuum model in Eq. (3) relates directly to the orthotropic aspect ratios of the unit cell itself and thus the orthotropy is not affected by the selection of a particular chain constitutive model (Fig. 1). Additionally, a change in the aspect ratio of the unit cell affects the predicted continuum response in a consistent fashion regardless of the particular molecular model (Fig. 2), provided the physical bases for the molecular models are not violated. These results suggest that the orthotropy of the continuum model using the FJC model that has previously been seen to match the orthotropic re-

**Table 1 Parameters used to generate the curves in Fig. 2. For all simulations  $b=1$  and  $B=0.1$  MPa.**

$\lambda^L$	Wormlike Chain (WLC)			Freely Jointed Chain (FJC)		
	$a$	$\Lambda$	$n/(\text{m}^3)$	$a$	$N$	$n/(\text{m}^3)$
1.9	2.5	2.375	$4 \cdot 10^{21}$	2.5	2.375	$5 \cdot 10^{22}$
1.7	2.5	2.125	$4 \cdot 10^{21}$	2.5	2.125	$3 \cdot 10^{23}$
1.5	2.83	2.125	$4 \cdot 10^{21}$	2.5	1.875	$3.5 \cdot 10^{23}$

sponse of certain biological tissues [1] will also be predicted using a different chain model such as the WLC since the orthotropy is largely attributable to the unit cell rather than the constituent chains; however, the nonlinear nature of the resulting fits (i.e., the degree of locking) will be altered due to differences between the chain models.

## References

- [1] Bischoff, J. E., Arruda, E. M., and Grosh, K., 2001, "A Microstructurally Based Orthotropic Hyperelastic Constitutive Law," *ASME J. Appl. Mech.*, to appear.
- [2] Marko, J. F., and Siggia, E. D., 1995, "Stretching DNA," *Macromolecules* **28**, pp. 8759–8770.